REXTRAP

Ion Accumulation, Cooling, and Bunching for REX-ISOLDE

Dissertation
zur Erlangung des Grades
“Doktor der Naturwissenschaften”
am Fachbereich Physik
der Johannes Gutenberg-Universität
in Mainz

vorgelegt von:
Pit Schmidt
geboren in Wurzen

Mainz 2001

Dekan:

1. Gutachter:

2. Gutachter:

3. Gutachter:

Tag der mündlichen Prüfung: 18. Dezember 2001

To all the Happy Trappers:

Sketch by Georges Boixader

Every computer program has at least one bug and can be shortened by at least one instruction – from which, by induction, one can deduce that every program can be reduced to one instruction which doesn't work.

(Programmers Wisdom)

This can easily be extended to any thesis: Each thesis has at least one misspelling and can be shortened by at least one word. . .

(T.S., November 2000)

Abbreviations

AC	—	**A**lternate **C**urrent
ADC	—	**A**nalogue **D**igital **C**onverter
CCD	—	**C**harged **C**oupled **D**evice
CMOS	—	**C**omplementary **M**etal **O**xide **S**emiconductor
CPU	—	**C**entral **P**rocessing **U**nit
DAC	—	**D**igital **A**nalogue **C**onverter
DC	—	**D**irect **C**urrent
EBIS	—	**E**lectron **B**eam **I**on **S**ource
ECR	—	**E**lectron **C**yclotron **R**esonance
FWHM	—	**F**ull **W**idth at **H**alf **M**aximum
GPIB	—	**G**eneral **P**urpose **I**nterface **B**us
GPS	—	**G**eneral **P**urpose **S**eparator
HRS	—	**H**igh **R**esolution **S**eparator
HV	—	**H**igh **V**oltage
IJTF	—	**I**nternational **J**ournal of **T**ools and **F**ools
ISOLDE	—	**I**sotope **S**eparation **O**n-**L**ine **DE**
IH-structure	—	**I**nter digital **H** structure
JYFL	—	**J**yväskylän **y**liopiston **f**ysiikan **l**aitos
LINAC	—	**Li**near **Ac**celerator
MCP	—	**M**icro-**C**hannel **P**lates
NMR	—	**N**uclear **M**agnetic **R**esonance
OLM	—	**O**ptical **L**ink **M**odule
OLP	—	**O**ptical **L**ink **P**lug
PPAC	—	**P**arallel **P**late **A**valanche **C**ounter
PROFIBUS	—	**Pro**cess **Fi**eld **Bus**
REX-ISOLDE	—	**R**adioactive Beam **Ex**periment at **ISOLDE**
RF	—	**R**adio **F**requency
RFQ	—	**R**adio **F**requency **Q**uadrupole
TCP/IP	—	**T**ransmission **C**ontrol **P**rotocol/**I**nternet **P**rotocol
TOF	—	**T**ime-**O**f-**F**light
TTL	—	**T**ransistor-**T**ransistor **L**ogic
VME	—	**V**irtual **M**emory **E**xtension
WITCH	—	**W**eak **I**nteraction **T**rap for **Ch**arged Particles

All fundamental physical constants used in this work are the generally recommended values taken from ref. [Moh00].

Contents

List of Tables

List of Figures

Introduction

Much of what we know about the properties of "nucleonic matter" has been learned from nuclear reactions. Nuclear isotopes produced in reactions with stable nuclei are generally, with a few exceptions, limited to regions near the valley of stability. The study of species far from stability has through the years revealed a rich variety of genuine nuclear phenomena, e.g. halo nuclei, proton radioactivity, or exotic shell effects. Furthermore it provides the unique opportunity to compose a nuclear probe as desired, i.e. to choose a composition of protons and neutrons required by the experiment. This potential of using radioactive beams for studying, in the laboratory, novel aspects of nuclear structure as well as key reactions relevant for nucleosynthesis, has triggered interest world wide in the upgrade and construction of radioactive ion beam facilities (RIB) and accelerators to generate the high-quality beams of short-lived nuclei required.

Over the past thirty years the large number of about 600 beams of different radioactive isotopes from more than 60 elements have been produced at the **ISOLDE** (**I**sotope **S**eparation **O**nline) facility at CERN near Geneva (Switzerland). ISOLDE is an ISOL-type facility, where radioactive isotopes are produced by nuclear reactions in a thick target induced by the impact of a high energetic proton beam. The reaction products are on-line ionised, accelerated to 60 keV, and mass-analysed and being distributed to several different beam ports. The long experience and know-how in the production of low-energetic radioactive beams and the already existing infrastructure predestinate ISOLDE as place for a post accelerator facility. The first goal of REX-ISOLDE (**R**adioactive Beam **EX**periment at **ISOLDE**) project is to prove an efficient new concept of bunching, charge-breeding and post-accelerating of low energetic radioactive ion beams from an ISOL-facility to energies somewhat below the Coulomb barrier.

The system has to be efficient in order not to waste the valuable radioactive ions. The final energy of the system should be sufficiently high for the physics addressed. The most pricy part of REX-ISOLDE is the accelerator structure. To keep this part short and at reasonable costs a charge breeding device has been introduced before the accelerator chain due to the fact that the final energy of an accelerated particle is proportional to its charge state. For REX-ISOLDE an **E**lectron **B**eam **I**on **S**ource (**EBIS**) has been chosen due to the high charge states and the excellent quality of the extracted ion bunches. An efficient EBIS operation, i.e. not to waste the costly produced radioactive ions, requires low-emittance ion bunches.

Within this thesis REXTRAP, a large gas-filled Penning trap, has been developed. It has been successfully commissioned to serve for accumulation, emittance improving, and bunching of the continuous ISOLDE ion beam. Properties of REXTRAP have been systematically investigated and intensively verified by numerical simulations. The report starts with a brief overview of the REX-ISOLDE project, explaining the concept of the post-accelerator. Special attention is given to its dedication to new physics. The next part deals with the theory necessary to understand REXTRAP in detail. An extensive chapter describes the setup, followed by the major parts of this thesis characterising the system by discussing results obtained within simulations and experimentally. A comparison with other cooling and bunching techniques, outlook, summary, and appendix establish the final part.

1 REX-ISOLDE

1.1 The On-line Mass Separator ISOLDE

At ISOLDE [Kug92] radioactive isotopes are generated in a thick target by nuclear reactions between relativistic protons and target nuclei. The pulsed proton beam with an energy of 1–1.4 GeV is delivered by the smallest CERN ring accelerator — the Proton Synchrotron Booster (PSB) [Jon93, All92]. The produced isotopes are diffusing out of a thick target matrix into an ion source. Depending on the desired ion species they become singly charged by ionization in surface, plasma, or laser ion sources [Rav74, Rav76, Sun92, Mis93, Let98]. After acceleration to an energy of 60 keV the ions are mass analysed and then distributed to several experimental places via a set of electrostatic beam lines. The ISOLDE facility, as illustrated in Fig. 1.1, houses two target-separator units. The general-purpose separator (GPS) has a mass resolving power of about 2400. Experiments requiring a larger value may utilise the high-resolution separator (HRS) which provides resolving power of about 7000 in low and up to 30000 in high-resolution mode.

1.2 Experimental Setup

The post-accelerator REX-ISOLDE will deliver radioactive ion beams with energies up to 2.2 MeV/u. For this purpose a Penning trap and an electron beam ion source (REXEBIS) are

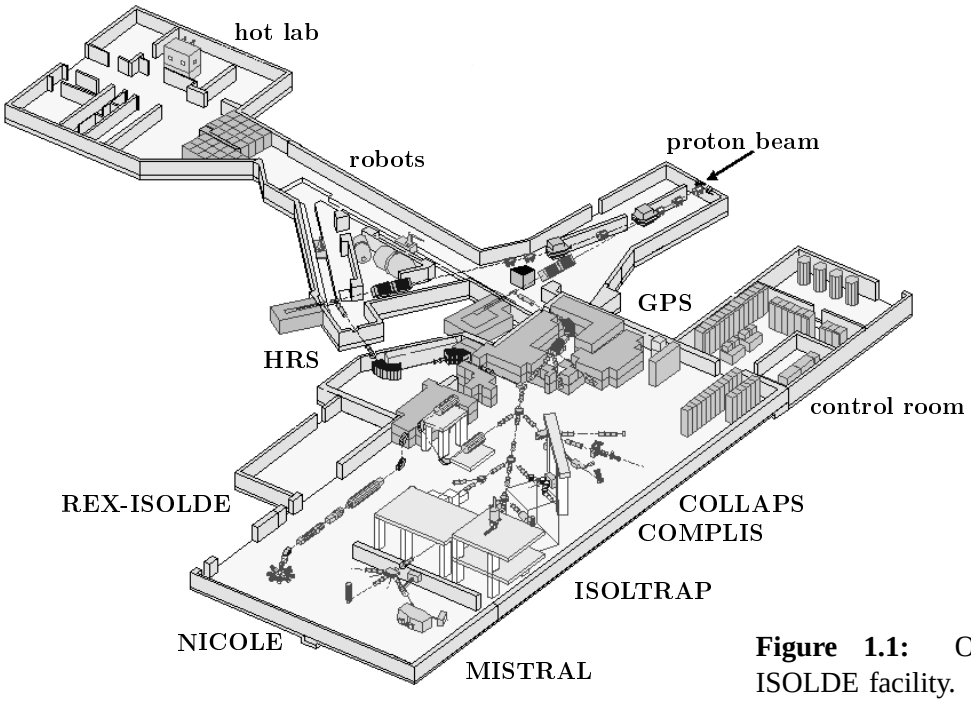

Figure 1.1: Overview of the ISOLDE facility. Important experiments and installations are labelled.

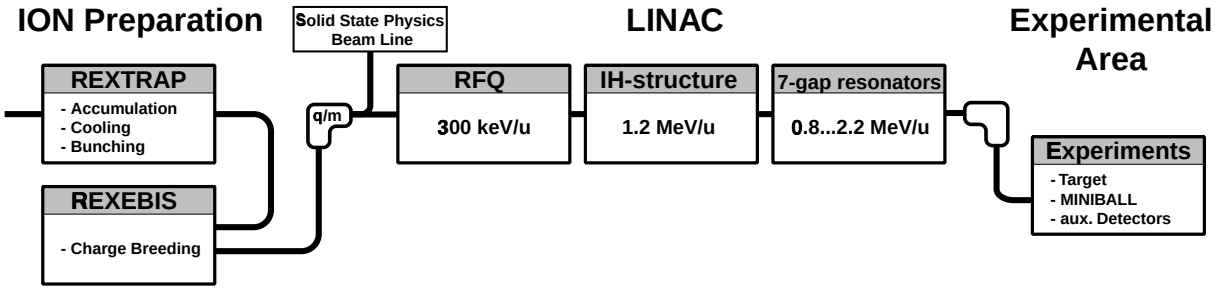

Figure 1.2: Flow Chart of the REX-ISOLDE setup.

combined with a linear accelerator. In Fig. 1.2 the principle of the post-accelerator is illustrated. Fig. 1.3 shows a drawing of the complete system as it will be installed in the ISOLDE experimental hall. The continuous beam of singly charged 60 keV ions is decelerated and accumulated in a gas-filled Penning trap (REXTRAP). The ions are cooled and released as bunches. After re-acceleration they are transferred to REXEBIS where the charge state is increased. A magnetic q/m separator selects the desired charge state for injection into the accelerator. The latter consists of a **R**adio **F**requency **Q**uadrupole (**RFQ**), an **I**nterdigital **H**-type structure (**IH**) and three 7-gap resonators. This concept, utilising an accumulation device with buffer gas for cooling and bunching, and a charge breeder is the first of its kind and is designed for high efficiency, which is extremely important when handling valuable and rare exotic nuclei.

In the following the individual stages of the experiment will be described in detail.

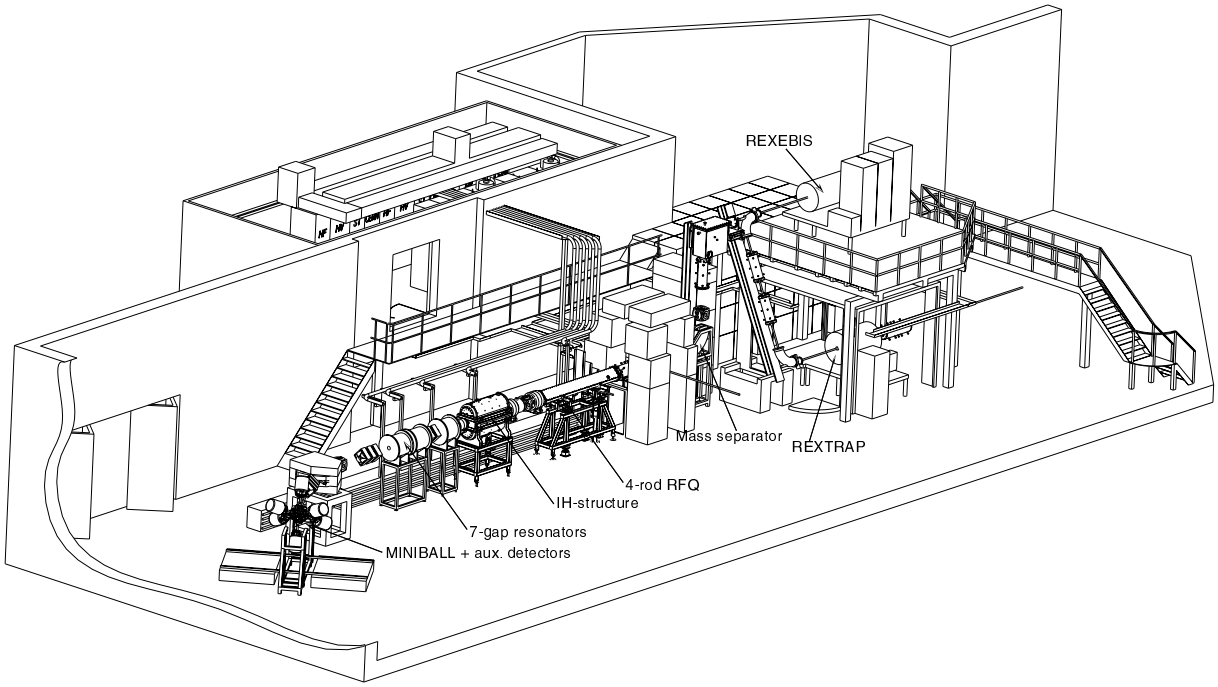

Figure 1.3: Three-dimensional view of the REX-ISOLDE setup.

1.2.1 REXTRAP

The first stage of the ion preparation part of REX-ISOLDE is REXTRAP, a large gas-filled Penning trap. It accumulates and bunches the incoming continuous ISOLDE ion beam. The ions are confined in radial direction by the action of a strong magnetic field and in longitudinal direction by a static quadrupole electrical potential. During their passage through the system they lose energy by collisions with the buffer gas and are finally trapped in the potential minimum. The dissipating force provided by the buffer gas combined with a special rf-sideband cooling technique [Bol90, Sav91, Kön95] leads to an overall phase space reduction of the injected ion beam. Finally, all ions are cooled and collected in the trap centre. From there they can be extracted as short ion bunches by sudden lowering of the electrostatic potential well at the trap exit.

1.2.2 REXTRAP-REXEBIS Transfer Beam Line

The beam transport beam line to REXEBIS (Fig. 1.4) has to fulfil several demands. Firstly, it has to transfer the ion bunches delivered by REXTRAP without loss to REXEBIS bridging the difference in height and position between both parts of REX-ISOLDE. Secondly, it has to prevent the flooding of the EBIS with buffer gas from the trap.

A system consisting of two 90° spherical benders and additional quadrupole triplets has been chosen, which provides an achromatic and symmetric transport system. Several small diaphragms at beam focal positions form a a multi-stage differential pumping system. Thus reducing the buffer gas pressure by several orders of magnitude along the transfer beam line. Such a scheme avoids contamination of the EBIS ion bunches by ionised buffer gas atoms diffusing out of REXTRAP.

Beam diagnostic units are placed at the beam transport entrance, in the middle of the system, and at its exit. Each of these units is composed of a Faraday cup, and a beam viewing system consisting of a multi-channel plate with a phosphor screen and an associated CCD camera. This allows the measurement of beam currents, as well as the determination of beam position and intensity profile.

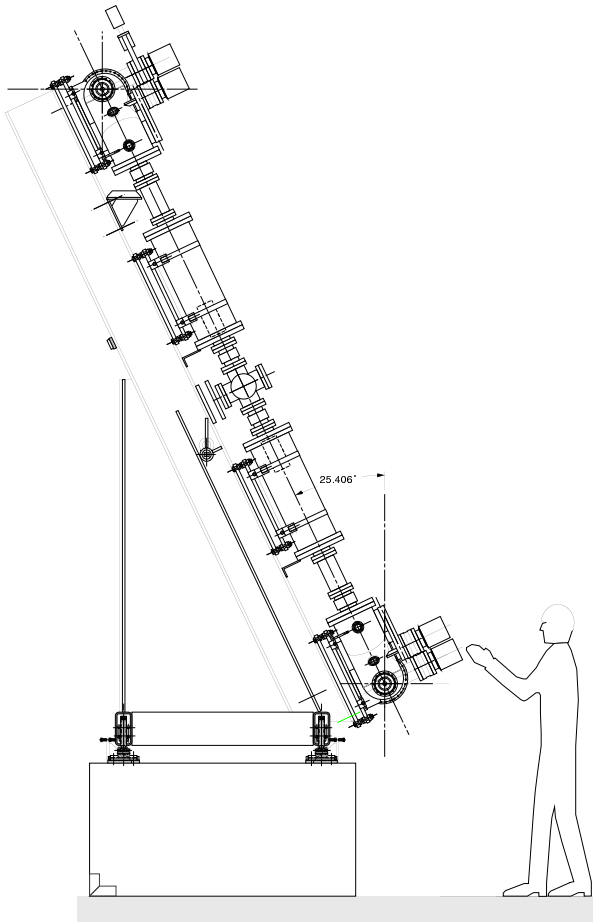

Figure 1.4: Schematic of the beam transport system connecting REXTRAP to REXEBIS.

A complete description and analysis of the beam transport system is not the intention of this thesis. It will be given in [For01].

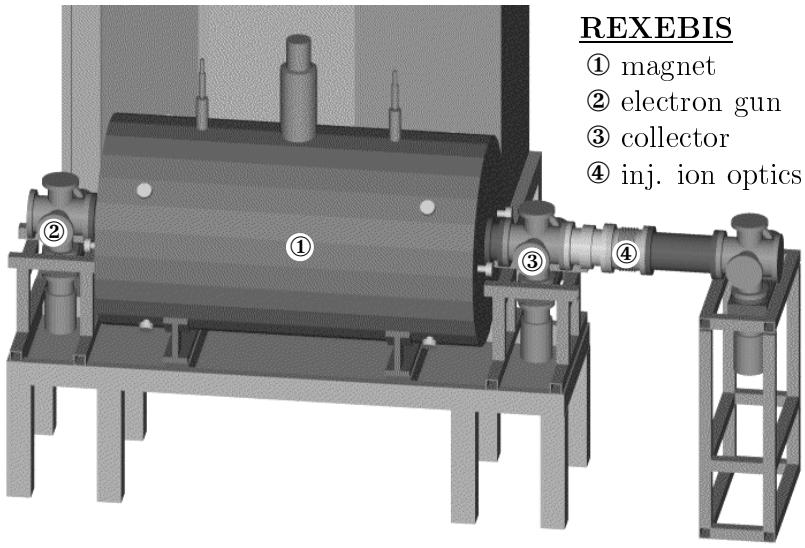

element	charge-state
$_{8}$O	7^+
$_{11}$Na	9^+
$_{12}$Mg	9^+
$_{18}$Ar	9^+
$_{19}$K	11^+
$_{20}$Ca	12^+
$_{36}$Kr	16^+
$_{37}$Rb	18^+
$_{51}$Sb	19^+
$_{54}$Xe	21^+
$_{82}$Pb	22^+
$_{92}$U	22^+

Solenoid	
magnetic field	up to 2 T
homogeneity	0.25 % over ±400 mm
field straightness	< 0.1mm over ±800 mm
Inner structure	
trap length	100 . . . 798 mm
trap capacity	$6 \cdot 10^{10}$ charges
electron beam energy	5 keV
electron beam radius	0.25 mm
electron current density	> 200 A/cm^2

Electron gun	
cathode material	LaB_6 310 crystal
cathode lifetime	1 year
electron beam current	0.48 A

Ion beam properties	
acceptance	3π mm mrad (@ 60 kV)
emittance	< 19π mm mrad (@ 20 kV)

Figure 1.5: View of the REXEBIS system. The right table gives the peak of the charge state distribution for a breeding time of 20 ms for different element species. A compilation of important REXEBIS parameters is given in the lower table.

1.2.3 REXEBIS

In the REXEBIS charge breeder (Fig. 1.5) the charge state of the ions delivered by REXTRAP will be increased to a charge-to-mass ratio of $\frac{q}{m} \geq \frac{1}{4.5}$ [Wen98, Rao98, Axe99].

The EBIS concept is most suitable for REX-ISOLDE since it delivers the highest possible charge states in comparison to other charge breeding techniques [Sor95, Has96]. An EBIS makes use of a dense electron beam that is compressed to a high density by a strong magnetic field. This electron beam creates a radial potential well for the ions while the longitudinal confinement is provided by electric potentials created by cylindrical electrodes surrounding the electron beam. Trapped low-charged ions undergo stepwise ionization via electron impact collisions. The final charge state distribution is determined by the element and the product of confinement time and electron beam current density (see the table in Fig. 1.5).

REXEBIS uses an electron current of 0.5 A and 5 keV beam energy. This beam is compressed by the magnetic field to yield a current density of more than 200 $\frac{A}{cm^2}$. This results in breeding times between 5 and 20 ms for most of the interesting ion species. Due to the charge state distribution of the multiply charged ions an efficiency of 30 % seems to be realistic for the

REXEBIS setup.

During the delivery of pulses from REXTRAP the EBIS is operated at a potential of 60 kV. The potential is lowered to 20 kV while charge breeding in order to match the ion energy to the velocity acceptance value of the following RFQ resonator. After extraction it is rapidly brought back to be able to accept the following ion bunch from REXTRAP.

1.2.4 Mass Separator

The number of residual gas ions in an ion bunch coming from REXEBIS can be several orders of magnitude larger than the number of rare radioactive ions. Therefore, an efficient q/m selection is necessary prior to the injection of the ion beam into the LINAC. For this purpose a mass separator has been introduced in the system [Rao99]. Its components are an electrostatic and a magnetic bender. Monte Carlo simulations show that the mass resolving power of about 150 is sufficient to ensure that less than 0.01 % of the particles passing trough the mass slit are residual gas ions.

1.2.5 LINAC

The linear accelerator of REX-ISOLDE consists of three different acceleration stages following succesful concepts already realized. The components used for REX-ISOLDE are further developments of cavities used at the GSI-HLI LINAC [Ble89], the CERN LINAC 3 [War93], and the high-current injector at the MPI für Kernphysik in Heidelberg [Hah92, Sch88, Fri91, Kle92]. An overview including important parameters and photographs of the different parts of the LINAC is shown in Fig. 1.6.

The 4-rod RFQ

The efficient acceleration of low energetic ion beams using RFQs is well established [Sch85]. Therefore, such a system has been chosen for the first accelerating stage of REX-ISOLDE.

The 4-rod RFQ consists of four electrodes to which alternating voltages are applied. The rf quadrupole field provides transverse focusing for the low energy ions while an aperture modulation of the four rods performs smooth bunching of the injected beam and acceleration. The RFQ tank is 3 m long and has a diameter of 0.32 m. It accelerates the radioactive ions from 5 keV/u to 300 keV/u.

The conservative design allows ions to be accelerated with charge-to-mass ratios down to $\frac{q}{m} = \frac{1}{6.5}$. This is of special interest for future experiments on heavier ions.

The IH-Structure

The IH structure is an efficient accelerating drift-tube structure [Nol79]. Inside the resonator tank cylindrical cavity drift tubes of varying length (according to the velocity of the particles) are mounted alternating on opposite sides. The magnetic field lines, created by the radiofrequency field, are parallel to the beam axis and the induced currents flow azimuthally on the wall producing electric fields of alternating direction between the drift tubes. This field forces the ions forward.

After a first accelerating part the ions are transversally focused by a quadrupole triplet in the REX-ISOLDE IH-structure. The beam is rebunched in the first three gaps behind the triplet followed by a second accelerating stage. The IH structure has 20 gaps distributed over a length of 1.5 m. A fine tuning of the final energy between 1.1 and 1.2 MeV/u can be achieved by adjusting the gap voltage distribution using two capacitive plungers and changing the rf-power level in the resonator.

The 7-gap Resonators

The final section of the LINAC consists of three 7-gap resonators. These special types of split ring resonators are optimized for synchronous particle velocities of $\beta = 5.4$ %, 6.0 % and 6.6 % [Pod98, Pod99a, Pod99b]. Each resonator has a single resonance structure, consisting of a copper half shell and three arms attached two both sides of the shell. An additional quadrupole doublet between the first and second resonator allows transverse focusing. The final energy of the accelerator can easily be adjusted between 0.8 and 2.2 MeV/u by tuning rf power and phase of the three active resonators.

1.2.6 Target and Detectors

The first series of experiments to be carried out with REX-ISOLDE will make use of Coulomb excitation and nucleon transfer reactions [REX94]. Such experiments demand high experimental efforts. This includes sophisticated targets, the effcient detection of γ-rays, as well as particle identification. All the equipment needed will be described in the following.

The Target Chamber

A target chamber has been constructed according to the special requirements of the germanium detector array MINIBALL, which is described further down. It is a compromise between the minimum volume necessary to house all the needed equipment and the maximum volume that can be easily surrounded by the Ge detectors. The chamber is made from thin aluminium to minimize γ-absorbtion and scattering. It houses a turnable wheel with target holders, a Faraday cup, a beam collimator and a segmented silicon strip detector, described later.

The Parallel Plate Avalanche Counter

The Parallel Plate Avalanche Counter (PPAC) was developed serving as an efficient and spatially sensitive forward angle detector to monitor the radioactive particle beam behind the target [Cub00]. It has a compact design with a low effective thickness to prevent the radioactive ions from being stopped and to avoid large angle scattering. This reduces the background of other detectors in the target area. The detector is operated with a small gas flow of 4 to 10 mbar of isobuthane and with voltages of about 600 V. The spatial resolution of about 1.6 mm is mainly determined by the width of the aluminium coated mylar strips inside the detector. To cover a large dynamic range of counting rates the PPAC supports two modes of operation. At low countrates ($< 10^6\,\mathrm{s}^{-1}$ per strip) the signals can be read out from the end of the delay lines event-by-event, whereas at intensities above this the current measured on all anode strips is recorded. With a rise time of the detector signals of about 5 ns in the event-by-event read-out mode the PPAC may even serve as a fast trigger.

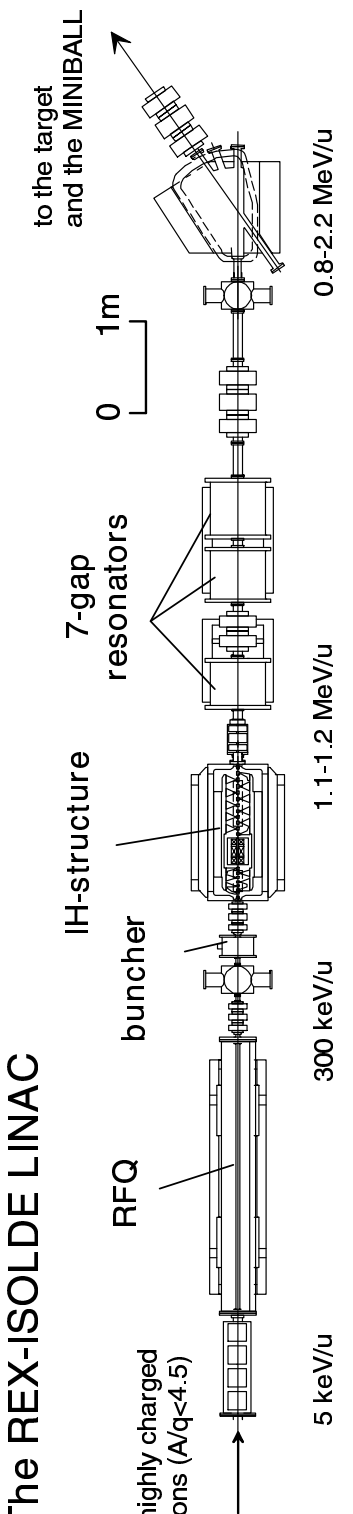

	Radio Frequency Quadrupole	Interdigital H-Structure	7-Gap-Resonators
	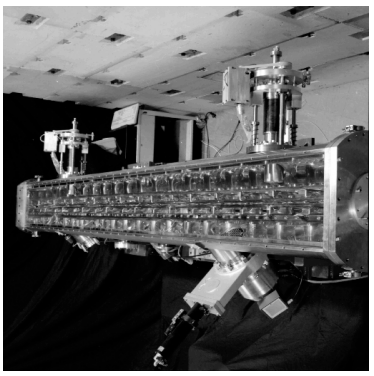	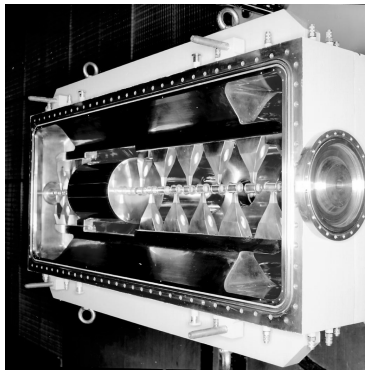	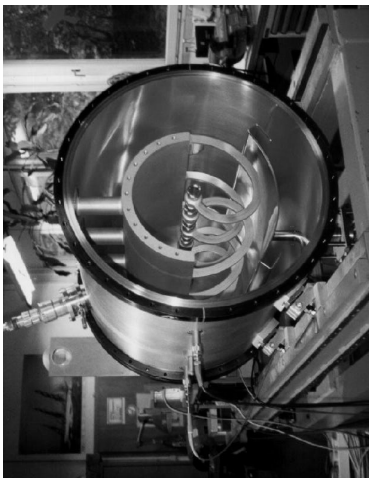
length	3 m	1.5 m	2.4 m
input energy	5 keV/u	300 kV/u	1.1. . .1.2 MeV/u
output energy	300 kV/u	1.1. . .1.2 MeV/u	0.8. . .2.2 MeV/u
rod voltage	42 kV	5.1 MV	1.8 MV
power consumption	53 kW	63 kW	90 kW
acceptance	0.63π mm mrad	0.60π mm mrad	1.3π mm mrad
emittance	0.68π mm mrad	0.63π mm mrad	

Figure 1.6: Overview of the REX-ISOLDE LINAC. The table shows photographs of open resonator tanks and technical parameters for each acceleration stage.

The MINIBALL Detector

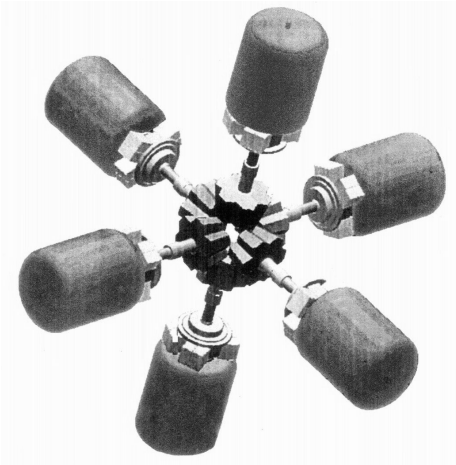

Figure 1.7: The MINIBALL detector.

The efficient detection of γ-rays will be one of the most important tasks for the envisaged experiments at REX-ISOLDE. To utilize the valuable radioactive beams in the most effective way a new germanium detector array is currently being assembled. The so called MINIBALL is optimized to gain highest full-energy peak efficiency. It consists of a new generation of six-fold encapsulated segmented Ge-detectors in a compact configuration without Anti-Compton shielding [Ebe96, Hab97]. In its final implementation the array will consist of 40 Ge-detectors. Subgroups of 3 and 4 detectors in one common cryostat allow flexible geometrical arrangements to meet specific experimental requirements.

Top of the art instrumentation with flash analogue-digital converters and digital-signal processing will give the MINIBALL the energy resolution of conventional analogue high-resolution spectroscopy electronics at substantially higher count rates. Together with the new data aquisition system [MAR00] basing on the GSI frontend system MBS [MBS00] and the ROOT framework from CERN [ROO00] this will provide a high-performance data aquisition and analysis system for the REX-ISOLDE user community.

The Compact Disc Detector Array

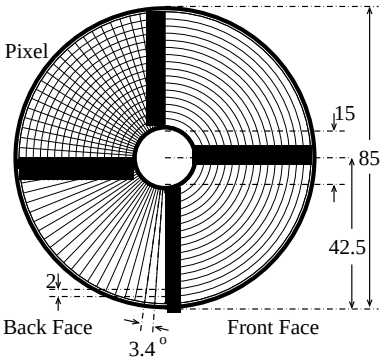

Figure 1.8: The Compact Disc detector.

The purpose of particle detection inside the MINIBALL is to gain information about the doppler shift of the γ-rays by measuring the momentum of their source. Therefore a position sensitive silicon detector based on the Double-Sided Silicon Strip Detector technology (DSSSD) detects scattered particles in the relevant solid angle [Sel91]. The front is segmented in 16 annular p-doped strips per quadrant at 2 mm pitch, while the back consists of 24 n-doped sector strips at 3.5° pitch. These 160 discrete detector elements provide an effective area of 93 % out of the total 5000 mm^2. Depending on the application (as energy loss or total kinetic energy detector) the wafer thickness varies between 35 µm and 1000 µm.

1.3 Physics Program

The REX-ISOLDE pilot experiment [REX94] aims to probe whether the magic numbers N=20 and N=28 are conserved when going to very neutron-rich nuclei by using Coulomb excitation and transfer reaction experiments. The steadily growing number of proposals and letters of intent [Sch99, Axe98, Jon98a, Ost97, Bec99, Wie97, Cam97, And97, Haa94, Wey94, For94]

for the use of REX-ISOLDE show clearly that it will allow to perform a variety of new experiments in several physics fields. In the following the physics relevance of REX-ISOLDE will be reviewed.

1.3.1 Nuclear Structure Physics

A large share of the experiments carried out with REX-ISOLDE will be dedicated to nuclear structure physics. Some key aspects are discussed in the following.

Studies of Nuclei Close to the Semimagic Shells of N=20 and 28

Quite different predictions from nuclear shell models [Dob94, Sha94] are obtained when one leaves the valley of stability towards neutron-rich nuclei. This clearly reflects the uncertainty in predicting nuclear forces, in particular, their isospin dependence. In [Dob94] the change of the nuclear potential from a Woods-Saxon potential to a more parabolic harmonic potential is predicted. This results in a lowering of the low-l single-particle energies and an increase in energy of the high-l levels, finally leading to a change in the magic numbers and hence to new predictions of the regions of nuclear deformation. On the other hand, relativistic mean field calculations [Sha94] do not confirm these changes. Furthermore, information on semimagic nuclei is of particular importance for the determination of the monopole component of the nuclear interaction as their simple structure allows relativistic calculations. Thus a study of the level structure and the quadrupole deformations of neutron-rich nuclei near neutron shell closures of great importance.

An additional phenomenon makes the situation even more interesting. The strong neutron-proton interaction implies a strong core polarization near closed shells, resulting in low-lying intruder states [Hey92a, Hey92b, Woo92]. These strongly deformed 2p2h configurations coexists besides the more spherical configurations and may even become the ground state. A pilot experiment confirmed this [Mot95]. This triggered further Coulomb excitation experiments [Sch96, Gla97], which identified a new region of well-deformed nuclei at and near the N=28 shell closure. The importance of intruder configurations has been shown in a systematic study of the chain of neutron-rich Si-isotopes [Ibb98] as well as for neutron-rich Ne and Mg isotopes [Pri99].

All of the previous experiments have been performed with NaI scintillators and are therefore limited in energy resolution. The MINIBALL as an efficient, high resolution γ-detection setup will greatly enhance the possibility to make a precise study of these complex nuclei in order to obtain detailed level schemes, information about vibration states, and nuclear deformation. In particular for odd-A nuclei only sparse knowledge is available [Ibb99].

Studies of Nuclei Close to the Drip-Line

Studies of light nuclei in the dripline regions continue to attract a large interest world-wide. The loose binding near the border of stability and the large excess of protons or neutrons give rise to phenomena such as forming of halo states, clustering and new shell structures. The steady progress on experimental and theoretical side is summarized in recent review articles [Han95, Jon98b, Tan96]. Unfortunately the analysis of available experimental data, as well as

future experiments are hampered by the lack of information about the quantum characteristics of their nuclear states. The normal way to obtain this kind of information is to produce the needed nuclear species in some kind of nuclear reactions. In the case of dripline nuclei, where both the involved target and beam nuclei are far from stability, the application of this technique becomes rather difficult. Almost unknown reaction schemes, small cross sections and large background are only a few drawbacks making the interpretation of experimental results rather difficult. A possible method of choice to overcome such problems is the use of radioactive beams combined with simple, well understood reactions to populate the desired nuclear states [Axe96]. In the following a few techniques and the desired reactions relevant for REX-ISOLDE are listed.

The understanding of ^{11}Li, one of the most well-known halo nuclei with a long tradition [Pos66, Thi75, Han87], depends strongly upon the structure of the low-energy states in ^{10}Li being an unbound two-body subsystem of ^{11}Li. The beams becoming available with REX-ISOLDE give rather unique opportunities to collect more precise spectroscopic data for ^{10}Li. The most favourable reactions for proton resonance scattering are d(^{9}Li,p)^{10}Li and ^{9}Be(^{9}Li,^{8}Be)^{10}Li [Axe98].

The clusterization of the unbound nucleus ^{7}He is not fully understood. The question if that nucleus is best described as a α+3n or a ^{6}He+n system has to be solved [AS88, Nil96]. A better knowledge of ^{7}He will also be important for the further unterstanding of ^{8}He, which can best be described as a five-body α+4n system for the moment [Zhu94]. For that purpose the simple one-neutron pick-up reaction ^{9}Be(^{9}Li,^{8}Be)^{7}He will be used at REX-ISOLDE [Jon98a].

The heaviest known one-neutron halo nucleus is ^{19}C. A systematic study of the momentum distribution of charged fragments after one-neutron breakup of ^{15,17,19}C has already been performed [Bau98]. However, the spin of the ground state of these nuclei, one important key-piece for interpreting the data, is still missing. With the present REX-ISOLDE energies one can get information about the spin of the ^{17}C ground state. The investigation of the T $= \frac{5}{2}$ analogue states in ^{17}N via the reaction ^{16}C will provide the relevant information [Axe98].

1.3.2 Nuclear Astrophysics

A second important share of REX-ISOLDE experiments will deal with astrophysical questions. Two important fields will be shortly reviewed.

Nucleosynthesis

Radioactive ion beam experiments offer a unique opportunity to extend the experimental study of astrophysical nucleosynthesis processes towards unstable, short-lived nuclei. A detailed knowledge of the nuclear-structure parameters of the involved nuclei is essential to understand these processes taking place in such unhabitable environments like supernovae (the final collapse of massive stars), novae (explosive hydrogen burning on the surface of white dwarfs) or X-ray bursts (explosive hydrogen burning on the surface of neutron stars) [Kra98b].

The r-process proceeds on the neutron-rich side of the line of stability and is mainly determined by an equilibrium of neutron captures and (γ,n) reactions. The most important parameter which enter are nuclear masses, β-decay halflives and β-delayed properties, e.g. neutron emission and possibly fission. The onset of the r-process depends on the competition of (α,n)-reactions and neutron captures. Especially the understanding of the change from α-induced reactions to neutron captures is from great interesst [Kra92, Kra95, Kra96, Thi98]. An experimental investigation of the size of α-induced and neutron capture reactions of neutron rich

nuclei, e.g. ^{82}Ge(α,n) ^{80}Zn(d,p) would be desirable [Kra98a].

Explosive hydrogen burning on the surface of white dwarfs and neutron stars leads to the rp-process, a sequence of rapid proton captures and associated β^+-decays. At higher material densities and temperatures it undergoes a transistion and is then dominated by (α,p)-reactions [Thi94]. Elements as heavy as sulfur and argon can be produced in novae, and up to krypton and beyond in X-ray bursts. The understanding of the rp-process path, which is located at the proton rich side of the chart of nuclei, requires a detailed knowledge of the involved (p,γ)-, (p,α)-, and (α,p)-reactions and β^+-decays. It turns out that the reaction is determined almost entirely by only a finite number of key reactions. For example, at temperatures above $3 \cdot 10^8$ K the rp-process flux proceeds through the bottleneck ^{35}Ar(p,γ), the breakout point of the S-Cl-Ar-cycle [Sch97]. The investigation of this reaction as one of the key reactions of the rp-process is proposed as on of the first astrophysics experiments at REX-ISOLDE [Wie97].

The Solar Neutrino Puzzle

The absolute cross section σ(E) of the reaction ^{7}Be(p,γ)^{8}B plays an important role in the understanding of the high energy flux of solar neutrinos [Bah92, Bah98]. Preliminary values were derived from the β-delayed α-decay of ^{8}Be after bombarding ^{7}Be targets with high energy protons. Unfortunately these values differ significantly. This is believed to be due to the different target stoichiometry of the ^{7}Be targets produced via hot chemistry. Thus, direct measurements of this cross section will improve the accuracy of the value and help to solve the solar neutrino puzzle. This will be done by studying the reaction H(^{7}Be,γ)^{8}B in inverse kinematic, i.e. the ^{7}Be beam will be guided into a windowless gas target system filled with hydrogen gas. The ^{8}B residual nuclides will be implanted together with the ^{7}Be beam into a beam stopper, which is periodically moved in front of a particle detector to observe the β-delayed α-decay of ^{8}B [Cam97].

1.3.3 "Low" Energy Experiments at REX-ISOLDE

As it has been shown in the previous sections, REX-ISOLDE provides radioactive beam experiments at higher energies. Nevertheless, it also opens up interesting opportunities at the "low" energy side. The reduction of the beam size as well as of beam divergence by REXTRAP could help several experiments to use the potential of ISOLDE more efficient. For example experiments with collinear spectroscopy [Gei97] could gain efficiency since the overlap of the laser beam with the ion beam will be increased. Spectroscopy experiments can become more sensitive since it is possible to determine the background better for pulsed beams. Precision experiments using further trap setups for laser or electron spectroscopy are also imaginable.

A few examples of projects, which use the low-energy part of REX-ISOLDE are described in the following.

The WITCH Experiment

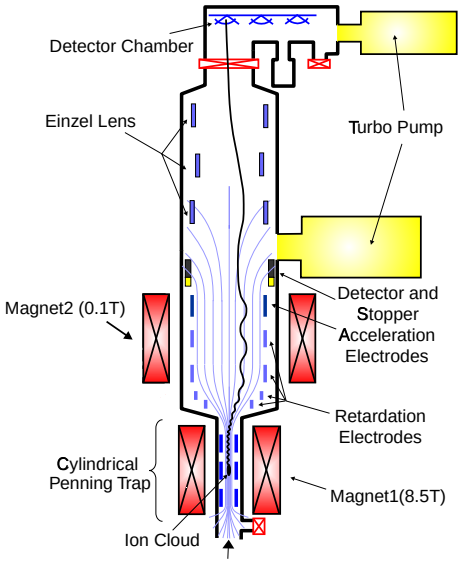

Figure 1.9: The WITCH retardation spectrometer.

The WITCH (**W**eak **I**nteraction **T**rap for **CH**arged particles) experiment is a retardation spectrometer coupled to a Penning trap system. It will be placed behind REXTRAP [Bec99, Bec00] (see Fig. 1.9). By measuring the recoil energy spectrum of suitable ion species (e.g. ^{35}Ar, ^{46}V) undergoing a β-decay one hopes to gain information about the nature of the electroweak interaction. The present form of the Standard Model describes the nuclear weak process in terms of vector (V) and axial vector (A) type interactions. Although all experimental results today can be explained with a V-A form of the charged weak current, the possible presence of scalar and tensor type interactions are not yet ruled out. The experimental limit to distinguish between both types is mainly determined by the knowledge of the beta-neutrino correlation coeffizient. It can be deduced from the angular correlation between the β-particle and the neutrino. The neutrino is rather difficult to detect, i.e. the determination of the correlation has to be done indirectly. One possibility is the measurement of the recoil energy spectrum of β-decayed ions, since the energy of the ion is influenced by the relative emission angle of the β-particle and the neutrino. The systematic errors of most of preliminary experiments [Boo84, Ade93a, Ade93b, Sch93, Glü98] was limited by particle scattering in the source and the intermediate medium between the source and the detectors. The reduction of these problems will be one of the main advantages of the WITCH retardation spectrometer. The trap permits storage of cool ions for an extended period of time, providing a strongly localized source of radioactive ions with almost zero thickness. REXTRAP will serve for that experiment as beam cooler and buncher.

Solid State Physics

Solid state physics at ISOLDE has a long tradition. The combination of a great variety of isotopically clean radioactive ion beams, rather high intensities, and the opportunity to implant on-line has attracted a continuously increasing number of materials research projects, particular in the field of semiconductor physics. The higher ion energies made possible by REX-ISOLDE will continue this development, simply due to the advantage of deeper implantations and the vanishing problem of surface “dirt” [For99].

In addition, a new beam line planned leading from behind the REX-ISOLDE mass separator towards an existing high-voltage platform. It allows ions to be post-accelerated up to 300 kV per charge state [Lin95, Haa97]. The platform will be mainly used for experiments needing deep implantation of radioactive ions into solid states, as well as polarized beams with the tilted-foil method [Lin95, Lin97].

2 REXTRAP — An Overview

Ion sources at ISOL facilities like ISOLDE are optimised to achieve the highest ionization efficiency, i.e. highest yield, rather than to achieve the lowest beam emittance. In fact, the transversal emittance of the ISOLDE beam is about one order of magnitude larger then the transversal acceptance of the REXEBIS. Furthermore, the highest capture efficiency in an EBIS can be achieved if a bunched beam is injected. Although there are studies on the way to set up a pulsed ISOLDE ion source [Seb96] ISOLDE delivers a continuous ion beam by now. Therefore a technique was looked for that allows to improve the ISOLDE beam emittance by beam cooling and to convert the continuous beam into ion bunches.

Because cooling is mediated by a repeated interaction of the particle with a "cooling medium" it can only be carried out for particles which are stored for an appropriate time. This can be achieved in ion storage rings or ion traps. The beam energy of ISOLDE is not suitable for a storage ring, however as it will be shown it is capable for an ion trap. In addition, ion traps allow controlled ion extraction, i.e. to form ion bunches, necessary to operate traps as beam buncher, as it s necessary for REX-ISOLDE.

There exist mainly two different kind of traps, Penning [Pen36, Pie48, Deh67, Deh69] and Paul [Pau58, Fis59] traps. Several cooling techniques [Ita95] have been developed and successfully applied to both kinds of traps. For example, resistive cooling [Cor89] is widely applicable with cooling times of a few seconds achieved so far. However, it has been mainly applied to very light or highly charged ions. Ion temperatures in the sub-Kelvin range can be reached by laser cooling [Win79, Dyc85, Asp86, Bro86, Let88, Cor89, Dal89, Met99], but it requires an appropriate optical transition available only in certain elements. Collisional cooling methods are generally applicable to all ion types [Maj68, Kni79, Sch81, Ved83, Cut85, Cut86, Gab89, Pre91, Mor92, Yod92, Kud98, Fuj97, Pen97]. This includes as collision partners electrons, positrons, laser cooled ions, and buffer gas atoms. The latter as cooling reservoir ensure short cooling times, as they are necessary for the operation of REXTRAP. The drawbacks, i.e. the possibility of charge exchange, can be made negligible for most cases by using noble gases as buffer gas.

There exist several attempts to use ion traps as efficient beam buncher and cooler. From earlier tests with a buffer gas filled Paul trap as a beam buncher for the ISOLTRAP experiment [Moo92] it was hoped that an increase in size would also improve the capture efficiency. Unfortunately, this could not be confirmed [Sch98]. The maximum efficiency, achieved so far, has been in the order of 0.1 % which is a completely unacceptable value with regard to REX-ISOLDE. On the other hand an efficient buffer-gas assisted capturing of low energy ions into a cylindrical Penning trap [Ste94, Rai97] has been demonstrated by the same group. Estimations, and projections on the basis of the experiences gained during that project indicated that a large gas-filed Penning trap could act as an efficient beam cooler and buncher for the REX-ISOLDE project — the idea of REXTRAP was born.

In a Penning trap ions are confined in radial direction by the action of a strong magnetic field and in longitudinal direction by a quadrupole electrical potential. Such a potential can be created either by hyperboloidal shaped electrodes or by a stack of cylindrical electrodes. There are two possibilities of injecting external particles into a gas-filled Penning trap as it is

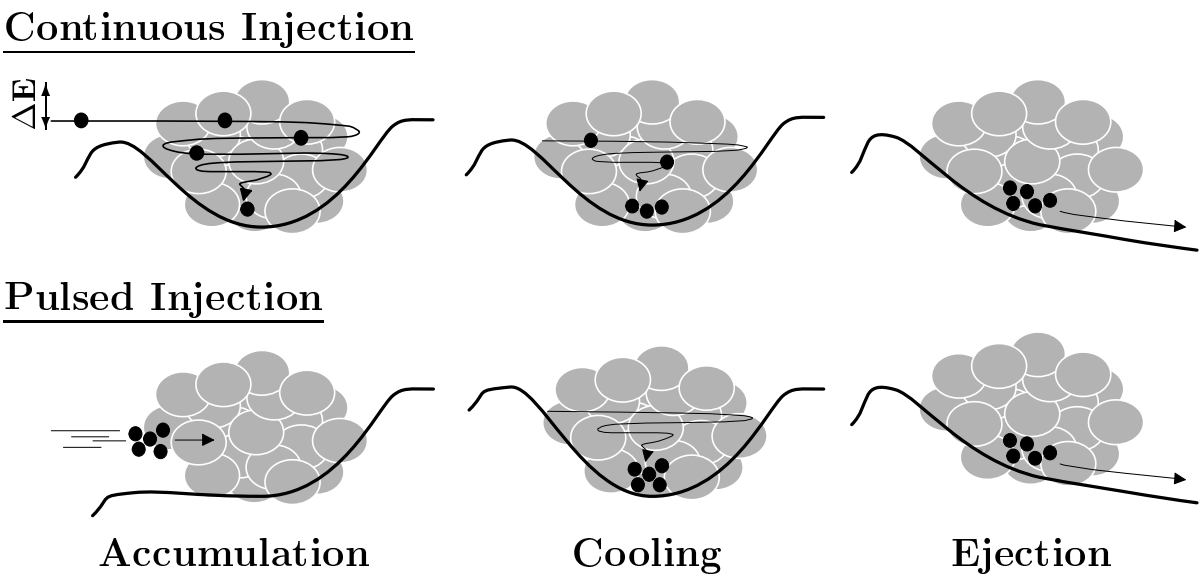

Figure 2.1: Operation Principles of a Penning trap: continuous and pulsed injection, cooling, and pulsed ejection.

illustrated in Fig. 2.1.

For continuous injection the potential well at the trap entrance is set slightly below the energy of the incoming ions. They pass that well and are reflected at the second potential well. Trapping can be achieved if the energy loss during one passage through the trap is larger then the initial energy difference. This method is naturally chosen for continuous incident beams, whereas for pre-bunched beams dynamical injection is suitable. Thereby the potential hill at the trap entrance is lowered for a short time. After the bunch has entered the trap region it is raised again. REXTRAP has to be operated with the continuous injection scheme since ISOLDE delivers a continuous beam.

During their passage through the system the ions will lose energy by collisions with the buffer gas and finally be trapped in the potential minimum. The dissipating force provided by the buffer gas leads to a reduction of the kinetic energy of the injected ions. The combination of magnetic and electrostatic field in a Penning trap causes three eigen motions for the ions: an oscillation parallel to the direction of the magnetic field and two radial oscillations perpendicular to it, the reduced cyclotron motion and the magnetron motion [Bro86]. The latter has a particular feature: its energy decreases with increasing amplitude. Due to the energy dissipation the amplitudes of the axial and the reduced cyclotron motion decrease whereas the amplitude of the unstable magnetron motion increases. This can be circumvented by a mass selective side band cooling technique, which is described in detail in Sec. 3.3.2. As a result ions are finally cooled and collected in the trap centre. From there they can be extracted as short ion bunches by lowering the electrostatic potential well at the trap exit.

For the work presented here REXTRAP was mainly used as stand alone, i.e. the timing of the system was not synchronised neither with ISOLDE nor with the further stages of REX-ISOLDE. However, such a synchronisation will be required for the operation of the post accelerator in connection with ISOLDE.

The very first experiments planned with REX-ISOLDE will deal with very short lived ion

species (see Sec. 1.3). These species are shortly released after the proton bunch impact at the target. Therefore, it is necessary to synchronise the trap operation with the primary proton bunches delivered by the PSB. For this case the trap can be operated with the following timing scheme The trap will be opened for the target release time of the desired ion species. The cooling process is started simultaneously. After closing the trap it must be proceeded for an additional period in order to allow also the latest injected ions to be cooled. The minimal time distance between two proton pulses from the PSB is about one second. The length of trap cooling time will be about a few tenth of milli-seconds. Therefore, ion losses are only expected due to the decay of the desired species during this period.

The release of ion species with longer half-lives, as for instance used for solid state physics experiments, is not that strongly correlated to the primary proton bunches. The ion beam is practically uniform. A certain dead time of the trap system must be taken into account for this case since during the final cooling period no ions are accepted from ISOLDE.

It is obvious that the operation of the following stages of REXTRAP must be synchronised with the trap cycle. This affects mainly the ion injection into the REXEBIS. For the coordination of all stages two scenarios could be implemented. Firstly, trigger impulses could be handed directly from one stage to next or secondly a main clock could be set up. It has not yet decided which will be favoured.

3 Theoretical Background

The following chapter gives an overview of the motion of a charged particle in a Penning trap with respect to the operation of REXTRAP. This includes the influence of damping forces, radiofrequency dipole and quadrupole fields. An additional section is dedicated to the theory of buffer gas cooling.

3.1 Principle of Storage in a Penning Trap

In a Penning trap ions are confined in radial direction by the action of a strong axial magnetic field $\mathbf{B} = B \cdot \hat{\mathbf{e}}_\mathbf{z}$ and in longitudinal direction by a quadrupole electrical potential

$$\Phi = \frac{U_0}{4d^2}(2z^2 - x^2 - y^2) \; . \tag{3.1}$$

There are a number possibilities to produce this potential, two very common ones are illustrated in Fig. 3.1.

The equipotential surfaces of a quadrupole potential are of hyperboloidal revolution. A Penning trap can therefore be made of a ring electrode and two end caps of hyperbolic shape. U_0 in Eq. (3.1) denotes the voltage between the electrodes. The characteristic trap parameter d is a function of r_0 and z_0, the distances of the ring electrode and the end caps from the trap centre, respectively. It is given by

$$d = \sqrt{\frac{1}{2}\left[z_0^2 + \frac{r_0^2}{2}\right]} \; . \tag{3.2}$$

Alternatively the quadrupolar shaped electrical potential can be approximated by a superposition of the potentials of a stack of cylindrical electrodes. This structure is named cylindrical Penning trap. The parameter d looses its special meaning. However U_0/d^2 remains a meaningful parameter that describes the depth of the potential well.

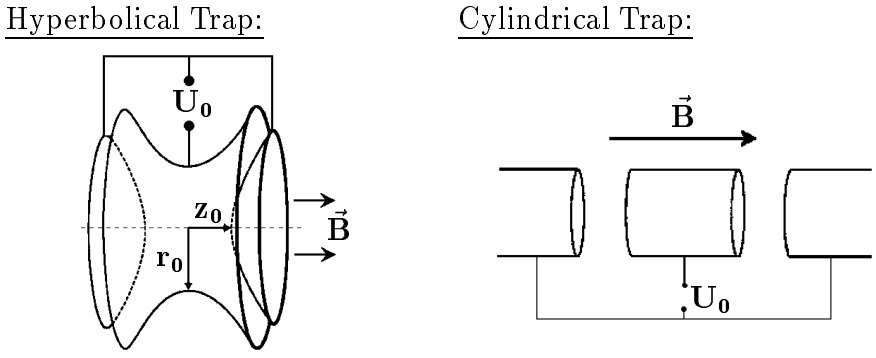

Figure 3.1: Most common types of Penning traps. **Left:** Hyperbolic Penning trap. **Right:** Simple cylindrical Penning trap.

3.2 Equation of Motion in an Ideal Penning Trap

The equation of motion for a particle with charge q and mass m in an electrical potential according to Eq. (3.1) and an axial magnetic field is given by

$$\ddot{\mathbf{r}} = \frac{q}{m}\left(\dot{\mathbf{r}} \times \mathbf{B} - \nabla\Phi\right) \qquad \Longleftrightarrow \qquad \begin{pmatrix} \ddot{x} \\ \ddot{y} \\ \ddot{z} \end{pmatrix} = \begin{pmatrix} \dot{x} \\ \dot{y} \\ \dot{z} \end{pmatrix} \times \begin{pmatrix} 0 \\ 0 \\ \omega_c \end{pmatrix} + \frac{\omega_z^2}{2} \begin{pmatrix} x \\ y \\ -2z \end{pmatrix}$$

$$\text{with} \quad \omega_c = \frac{q}{m}B \quad \text{and} \quad \omega_z = \sqrt{\frac{qU_0}{md^2}}\,. \tag{3.3}$$

One immediately realizes that the axial and radial motion decouple. The axial part of Eq. (3.3), $\ddot{z} + \omega_z^2 z = 0$, describes a harmonic oscillation with the frequency ω_z along the z-axis

$$z(t) = \sqrt{z(0)^2 + \frac{\dot{z}(0)^2}{\omega_z^2}}\,\sin(\omega_z t + \varphi_z) \qquad \text{with} \qquad \tan\varphi_z = -\frac{\omega_z z(0)}{\dot{z}(0)}\,. \tag{3.4}$$

The radial part of Eq. (3.3) is most commonly solved* by introducing the velocity vectors $\mathbf{V}^{\pm} = \dot{\mathbf{r}} - \omega_{\mp}\,\mathbf{r} \times \hat{\mathbf{e}}_\mathbf{z}$ according to [Bro86]. $\mathbf{V}^+$ and $\mathbf{V}^-$ are the velocities in coordinate systems which are moving with velocities $\omega_-\mathbf{r} \times \hat{\mathbf{e}}_\mathbf{z}$ and $\omega_+\mathbf{r} \times \hat{\mathbf{e}}_\mathbf{z}$, respectively. Please note that $\mathbf{V}^-$ rotates backwards with respect to $\mathbf{V}^+$. One obtains the two decoupled differential equation systems

$$\dot{\mathbf{V}}^{\pm} = \omega_{\pm}\mathbf{V}^{\pm} \times \hat{\mathbf{e}}_\mathbf{z} \qquad \text{with} \qquad \omega_{\pm} = \frac{1}{2}(\omega_c \pm \sqrt{\omega_c^2 - 2\omega_z^2})\,. \tag{3.5}$$

*For an alternative method to solve Eq. (3.3), refer to Sec. 3.3.1

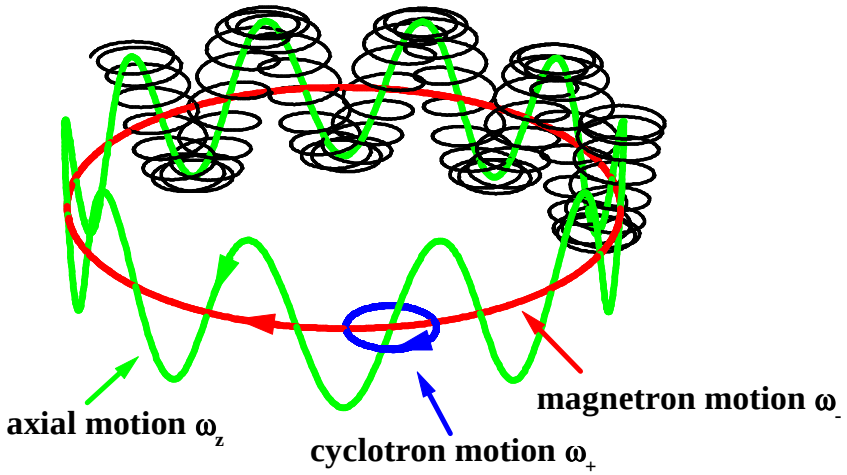

Figure 3.2: The motion of an ion in an ideal Penning trap is a superposition of two circular radial motions, the reduced cyclotron motion (ω_+) and the magnetron motion (ω_-), and a harmonic oscillation (ω_z) in axial direction.

The solutions are

$$\begin{aligned} V_x^{\pm} &= V_x^{\pm}(0)\cos(\omega_{\pm}t) + V_y^{\pm}(0)\sin(\omega_{\pm}t) \\ V_y^{\pm} &= V_y^{\pm}(0)\cos(\omega_{\pm}t) - V_x^{\pm}(0)\sin(\omega_{\pm}t)\ . \end{aligned} \tag{3.6}$$

Back transformation into Cartesian space via $x = -\frac{V_y^+ - V_y^-}{\omega_+ - \omega_-}$ and $y = \frac{V_x^+ - V_x^-}{\omega_+ - \omega_-}$ gives

$$\begin{aligned} x &= R^+\sin(\omega_+ t + \varphi_+) - R^-\sin(\omega_- t + \varphi_-) \\ y &= R^+\cos(\omega_+ t + \varphi_+) - R^-\cos(\omega_- t + \varphi_-) \end{aligned} \tag{3.7}$$

$$\text{with} \quad R^{\pm} = \frac{\sqrt{V_x^{\pm}(0)^2 + V_y^{\pm}(0)^2}}{\omega_+ - \omega_-} \qquad \tan\varphi_{\pm} = -\frac{V_y^{\pm}(0)}{V_x^{\pm}(0)}\ .$$

Therefore, the radial motion is a superposition of two circular motions, named magnetron and reduced cyclotron motion. They are characterised by the magnetron frequencies ω_- and the cyclotron frequency ω_+ and the radii R^- and R^+, respectively. Please note the following frequency relations

$$\omega_+ + \omega_- = \omega_c \qquad \omega_+^2 + \omega_-^2 + \omega_z^2 = \omega_c^2 \qquad \omega_+\omega_- = \frac{1}{2}\omega_z^2 \qquad \omega_- < \omega_z < \omega_+\ . \tag{3.8}$$

Fig. 3.2 illustrates the superposition of the two radial and the axial motion in an ideal Penning trap.

3.3 The Influence of Additional Forces on the Ion Motion

In the following the influence of additional forces on the ion motion in a Penning trap is discussed. In connection with REXTRAP buffer gas induced damping forces and forces resulting from azimuthal radiofrequency fields are from special interest.

In earlier approaches to solve the equation of motion for an ion in a Penning trap under the influence of a damping force it has always been assumed that the ion eigen frequencies ω_+, ω_-, and ω_z, remain constant. However, from the harmonic oscillator it is known, that its frequency shifts for an additional damping force. Therefore, in the first sub-section the ion motion in a Penning trap under the influence of a damping force is discussed in detail.

During the commissioning phase of REXTRAP an unpredicted behaviour was observed in the case of exciting the ion motion with dipole fields. In order to understand this phenomenon better the equation of motion for an ion in a Penning under the influence of an azimuthal rf dipole field and a damping force has been solved analytically for the first time. In addition the ion motion under the influence of an azimuthal rf quadrupole field is shortly reviewed, as a basis for the understanding of the working principle of REXTRAP.

3.3.1 Frictional Damping

For low ion velocities the damping of the ion motion is caused by the long-ranged interaction between the ion and the buffer gas atoms, polarised by the ion (see Sec. 3.4). In such a case the damping force

$$\mathbf{F_D} = -\sigma\, m\, \dot{\mathbf{r}}\ . \tag{3.9}$$

is proportional to the ion velocity. In order to describe the ion motion under the influence of damping and azimuthal radio frequency fields it is necessary to express $\mathbf{F_D}$ in units of $\mathbf{V}^{\pm}$. This transformation can be done via

$$\dot{x} = \frac{\omega_+ V_x^+ - \omega_- V_x^-}{\omega_+ - \omega_-} \qquad \text{and} \qquad \dot{y} = \frac{\omega_+ V_y^+ - \omega_- V_y^-}{\omega_+ - \omega_-} \; . \tag{3.10}$$

The equation of motion in Cartesian coordinates becomes

$$\begin{aligned} \ddot{x} - \omega_c \dot{y} - \frac{1}{2}\omega_z^2 x + \sigma \dot{x} &= 0 \\ \ddot{y} + \omega_c \dot{x} - \frac{1}{2}\omega_z^2 y + \sigma \dot{y} &= 0 \\ \ddot{z} - \frac{1}{2}\omega_z^2 z + \sigma \dot{z} &= 0 \; . \end{aligned} \tag{3.11}$$

The axial motion

The axial motion along the z-axis is still decoupled and behaves like an ordinary damped oscillator

$$z(t) \;=\; \mathrm{e}^{-\frac{\sigma}{2}t} \sqrt{z(0)^2 + \left(\frac{\dot{z}(0)}{\omega_z'} - \frac{\sigma}{2\omega_z'} z(0) \right)^2} \sin(\omega_z' t + \varphi_z') \tag{3.12}$$

$$\text{with} \quad \omega_z' = \sqrt{\omega_z^2 - \frac{1}{4}\sigma^2} \qquad \tan\varphi_z' = -\frac{\omega_z' z(0)}{\dot{z}(0) - \frac{\sigma}{2} z(0)} \; .$$

The radial motion

The radial part of Eq. (3.11) can be combined with the substitution $u = x + iy$ to

$$\ddot{u} + (i\omega_c + \sigma)\dot{u} - \frac{\omega_z^2}{2} u = 0 \; . \tag{3.13}$$

This homogeneous differential equation with constant coefficients is most commonly solved via the ansatz $u = \mathrm{e}^{i(\omega t + \alpha)}$, leading to the following quadratic equation for the exponent

$$\omega^2 + (\omega_c - i\sigma)\omega + \frac{\omega_z^2}{2} = 0 \; . \tag{3.14}$$

The solution of Eq. (3.13) is a superposition of the two solutions of Eq. (3.14)

$$u = A_1 \mathrm{e}^{i(\omega_1 t + \alpha_1)} + A_2 \mathrm{e}^{i(\omega_2 t + \alpha_2)} \tag{3.15}$$

$$\text{with} \qquad \omega_{1/2} = \frac{1}{2}\left(i\sigma - \omega_c \pm \sqrt{(i\sigma - \omega_c)^2 - 2\omega_z^2} \right) \; .$$

By splitting u into real and imaginary part, one obtains the following equations for the motion of an ion in an ideal Penning trap incorporating a damping force proportional to the ion velocity

$$\begin{array}{rcrcl} x &=& R^- \mathrm{e}^{\alpha_- t} \cos(\omega_- t + \varphi_-) &+& R^+ \mathrm{e}^{\alpha_+ t} \cos(\omega_+' t + \varphi_+) \\ y &=& -R^- \mathrm{e}^{\alpha_- t} \sin(\omega_- t + \varphi_-) &-& R^+ \mathrm{e}^{\alpha_+ t} \sin(\omega_+' t + \varphi_+) \end{array} \tag{3.16}$$

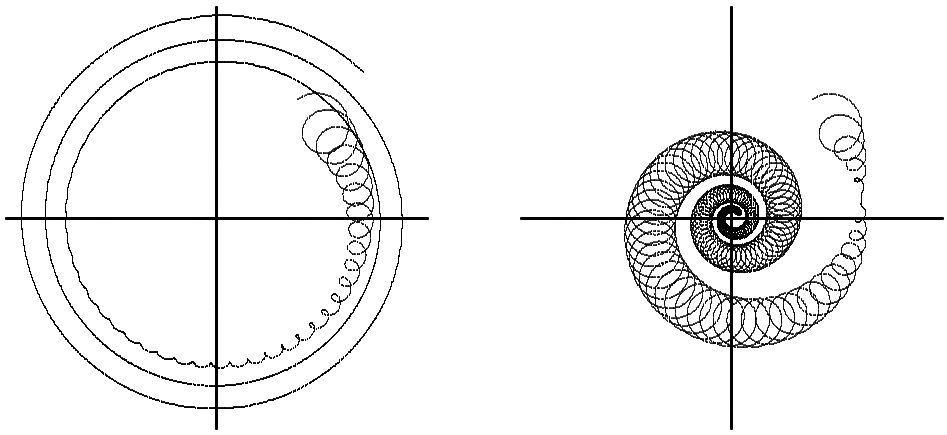

Figure 3.3: The radial motion of a particle in a Penning trap under the influence of a damping force only (left) and an additional azimuthal quadrupole excitation field (right). In the first case the particle is lost due to the increase of the magnetron radius, whereas in the second case it is finally centred.

$$\text{with} \quad \omega'_{\pm} = \frac{1}{2}(\omega_c \pm \sqrt{\omega_{c^2} - 2\omega_z^2}) \pm \Delta\omega \qquad \Delta\omega = \frac{\sigma^2}{16} \cdot \frac{8\omega_z^2 + \sigma^2}{(\omega_c^2 - 2\omega_z^2)^{\frac{3}{2}}}$$

$$\alpha_{\pm} = -\frac{\sigma}{2}\left(1 \pm \left[1 + \frac{1}{8} \cdot \frac{8\omega_z^2 + \sigma^2}{\omega_c^2 - 2\omega_z^2}\right]\right) .$$

Therefore, the radial motion is a superposition of two circular motions with the frequencies ω'_+ and ω'_- which are shifted down and up, respectively, by $\Delta\omega$ from the unperturbed frequencies ω_+ and ω_-. However, by incorporating real trap operation parameters, one realizes that these frequency shifts are very small and can be neglected in most cases. The radius of the reduced cyclotron motion decays exponentially with a time constant $\alpha_+ \approx -\sigma$ whereas the slow magnetron motion radius increases exponentially with a considerable smaller time constant of $\alpha_- \approx \frac{\sigma}{2}\frac{\omega_z^2}{\omega_c^2}$. This behaviour is illustrated in the left part of Fig. 3.3. Consequently, a particle under the influence of a damping force in a Penning trap will eventually be lost due to the steady increase of its magnetron radius. However, this ion loss mechanism can be overcome by an appropriate coupling of magnetron and reduced cyclotron motion. The result is shown in the right part of Fig. 3.3 and will be discussed in detail in Sec. 3.3.2.

3.3.2 The Influence of Azimuthal RF-Fields on the Ion Motion

In order to be able to manipulate the ion motion in a Penning trap azimuthal radio frequency dipole and quadrupole fields are of special interest. Such fields can be generated approximately by applying alternating voltages on a segmented central trap electrode. The principle is illustrated in Fig. 3.4.

The application of two voltages U_D phase shifted by 180° to opposite half-electrodes results in a dipole potential near the trap centre

$$V_D = a\, U_D \cdot \frac{x}{r_0} . \tag{3.17}$$

A quadrupolar shaped potential is obtained by applying voltages U_Q with a phase shift of 180° to neighbouring electrodes of a four-fold split centre electrode. The potential is characterised by

$$V_Q = a\,U_Q \cdot \frac{x^2 - y^2}{r_0^2}\ . \tag{3.18}$$

The parameter r_0 denotes the distance of the electrodes from the trap centre. The geometry factor a is introduced to describe to deviation from an ideal dipole or quadrupole potential caused by the non-ideal shape of the electrodes.

Dipole Excitation

Under the influence of an azimuthal electrical dipole field as described by Eq. (3.17) with $U_D = U_d \cdot \cos(\omega_{rf} t + \varphi_{rf})$ and a damping force according to Eq. (3.9) the radial part of Eq. (3.5) becomes

$$\begin{array}{rcrcrcl} \dot{V}_x^{\pm} & = & \omega_{\pm} V_y^{\pm} & - & \gamma\,(\omega_+ V_x^+ - \omega_- V_x^-) & & \\ \dot{V}_y^{\pm} & = & -\omega_{\pm} V_x^{\pm} & - & \gamma\,(\omega_+ V_y^+ - \omega_- V_y^-) & + & k_0 \cos(\omega_{rf} t + \varphi_{rf}) \end{array} \tag{3.19}$$

$$\text{with} \qquad k_0 = a\,\frac{q}{m}\frac{U_d}{r_0} \qquad \gamma = \frac{\sigma}{\omega_+ - \omega_-}\ .$$

The axial motion of the particle is not influenced and fully described by Eq. (3.12).

For the radial motion one expects resonance effects at the magnetron and reduced cyclotron frequency. Therefore, in the following excitation frequencies $\omega_{rf} \approx \omega_+$ and $\omega_{rf} \approx \omega_-$ are discussed. As been discussed in Sec. 3.3.1 a damping force has no remarkable effect on the eigen frequencies ω_- and ω_+. Thus, the differential equation system (Eq. (3.19)) can be solved via the ansatz $\mathbf{V}^{\pm}(t) = \mathbf{A}^{\pm}(t) \cdot \mathrm{e}^{\pm i(\omega_{\pm} t + \varphi_{\pm})}$, following the procedure in [Bol90], where it has been applied only to the case of quadrupole excitation. Doing so, one observes a slow change of

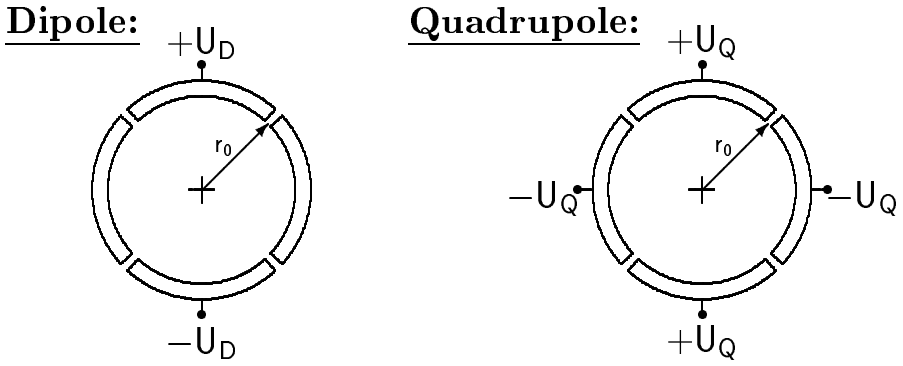

Figure 3.4: Principle of generating an azimuthal electrical dipole (left) and quadrupole field (right) in the central part of a Penning trap by using split centre electrodes.

the amplitudes $\mathbf{A}^{\pm}(t)$ with additional fast modulations. Neglecting these high frequency terms (rotating wave approximation) leads to

$$\begin{aligned}
\dot{A_x^{\pm}} &= \mp i\omega_{\pm}A_x^{\pm} + \omega_{\pm}A_y^{\pm} \mp \gamma\omega_{\pm}A_x^{\pm} \\
&\underline{\omega_{rf} \approx \omega_- :} \\
\dot{A_y^{+}} &= -i\omega_{+}A_y^{+} - \omega_{+}A_x^{+} - \gamma\omega_{+}A_y^{+} \\
\dot{A_y^{-}} &= i\omega_{-}A_y^{-} - \omega_{-}A_x^{-} + \gamma\omega_{+}A_y^{-} + \tfrac{k_0}{2}\mathrm{e}^{-i\left[(\omega_{rf}-\omega_-)t+(\varphi_{rf}-\varphi_-)\right]} \\
&\underline{\omega_{rf} \approx \omega_+ :} \\
\dot{A_y^{+}} &= -i\omega_{+}A_y^{+} - \omega_{+}A_x^{+} - \gamma\omega_{+}A_y^{+} + \tfrac{k_0}{2}\mathrm{e}^{i\left[(\omega_{rf}-\omega_+)t+(\varphi_{rf}-\varphi_+)\right]} \\
\dot{A_y^{-}} &= i\omega_{-}A_y^{-} - \omega_{-}A_x^{-} + \gamma\omega_{+}A_y^{-} \quad .
\end{aligned} \tag{3.20}$$

Under the assumption that the ion motions are still circular ($A_y^{\pm} = \pm iA_x^{\pm} = \pm iA^{\pm}$) this reduces to

$$\begin{aligned}
&\underline{\omega_{rf} \approx \omega_- :} \quad \dot{A^{+}} = -\gamma\omega_{+}A^{+} \\
&\qquad\qquad\qquad\quad \dot{A^{-}} = \gamma\omega_{-}A^{-} + \tfrac{ik_0}{2}\mathrm{e}^{-i\left[(\omega_{rf}-\omega_-)t+(\varphi_{rf}-\varphi_-)\right]} \\
&\underline{\omega_{rf} \approx \omega_+ :} \quad \dot{A^{-}} = \gamma\omega_{-}A^{-} \\
&\qquad\qquad\qquad\quad \dot{A^{+}} = -\gamma\omega_{+}A^{+} - \tfrac{ik_0}{2}\mathrm{e}^{i\left[(\omega_{rf}-\omega_+)t+(\varphi_{rf}-\varphi_+)\right]} \; .
\end{aligned} \tag{3.21}$$

The first of each pair of equation describes the normal decay and growth of the cyclotron and magnetron radius, as it has already been discussed in Sec. 3.3.1. It can be seen that in the case of dipole excitation both radial motions remain uncoupled. An excitation frequency $\omega_{rf} \approx \omega_-$ only affects the magnetron motion, whereas for $\omega_{rf} \approx \omega_+$ only the cyclotron motion is influenced. In the following, these cases are called magnetron and cyclotron excitation, respectively. The second equations are discussed now. A minus sign describes the evolution of the magnetron motion for $\omega_{rf} \approx \omega_-$, while a plus sign refers to the cyclotron motion for $\omega_{rf} \approx \omega_+$.

With the abbreviations

$$\alpha_{\pm} = \mp\gamma\omega_{\pm} \qquad k^{\pm} = \mp k_0\,\mathrm{e}^{\pm i(\varphi_{rf}-\varphi_{\pm})} \qquad \Delta\omega_{\pm} = \pm(\omega_{rf}-\omega_{\pm}) \tag{3.22}$$

Eq. (3.21) can be written as

$$\dot{A^{\pm}} - \alpha_{\pm}A^{\pm} = \frac{i\,k^{\pm}}{2}\,\mathrm{e}^{i\Delta\omega_{\pm}t} \tag{3.23}$$

Please note that $\alpha_{\pm}$ corresponds to that obtained in Sec. 3.3.1.

The solution of Eq. (3.23) can be found via standard techniques, i.e. Laplace transformation [Arf71]. This leads to

$$A^{\pm}(s)[s-\alpha_{\pm}] = A^{\pm}(0) + \frac{i\,k^{\pm}}{2}\frac{1}{(s-i\Delta\omega_{\pm})} \; . \tag{3.24}$$

A partial fraction expansion

$$A^{\pm}(s) = \frac{A^{\pm}(0)}{(s-\alpha_{\pm})} - \frac{i\,k^{\pm}}{2(\alpha_{\pm}-i\Delta\omega_{\pm})}\left[\frac{1}{(\alpha_{\pm}-s)} + \frac{1}{(s-i\Delta\omega_{\pm})}\right] \tag{3.25}$$

allows back transformation and one obtains

$$A^{\pm}(t) = A^{\pm}(0)\,\mathrm{e}^{\alpha_{\pm}t} + \frac{k^{\pm}}{2}\left(\frac{\mathrm{e}^{\alpha_{\pm}t} - \mathrm{e}^{i\Delta\omega_{\pm}t}}{\Delta\omega_{\pm} + i\alpha_{\pm}}\right) . \tag{3.26}$$

The radii are calculated via $R^{\pm}(t) = \frac{1}{\omega_+ - \omega_-} \cdot \Re\left\{A^{\pm}(t) \cdot \mathrm{e}^{\pm i(\omega_{\pm}t + \varphi_{\pm})}\right\}$,

$$R^{\pm}(t) = \frac{1}{\omega_+ - \omega_-}\sqrt{\left[A^{\pm}(0)\,\mathrm{e}^{\alpha_{\pm}t} + \frac{k_0}{2}\cdot\frac{\zeta_{\pm}}{\kappa_{\pm}}\right]^2 + \left[\frac{k_0}{2}\cdot\frac{\xi_{\pm}}{\kappa_{\pm}}\right]^2} \tag{3.27}$$

with

$$\begin{aligned}
A^{\pm}(0) &= (\omega_+ - \omega_-)R^{\pm}(0) \\
\kappa_{\pm} &= \Delta\omega_{\pm}^2 + \alpha_{\pm}^2 \qquad \Delta\varphi_{\pm} = \varphi_{rf} - \varphi_{\pm} \\
\zeta_{\pm} &= \Delta\omega_{\pm}\{\pm\cos\Delta\varphi_{\pm}[\mathrm{e}^{\alpha_{\pm}t} - \cos(\Delta\omega_{\pm}t)] + \sin\Delta\varphi_{\pm}\sin(\Delta\omega_{\pm}t)\} + \\
&\quad \alpha_{\pm}\{\quad \sin\Delta\varphi_{\pm}[\mathrm{e}^{\alpha_{\pm}t} - \cos(\Delta\omega_{\pm}t)] \mp \cos\Delta\varphi_{\pm}\sin(\Delta\omega_{\pm}t)\} \\
\xi_{\pm} &= \Delta\omega_{\pm}\{\mp\sin\Delta\varphi_{\pm}[\mathrm{e}^{\alpha_{\pm}t} - \cos(\Delta\omega_{\pm}t)] + \cos\Delta\varphi_{\pm}\sin(\Delta\omega_{\pm}t)\} + \\
&\quad \alpha_{\pm}\{\mp\cos\Delta\varphi_{\pm}[\mathrm{e}^{\alpha_{\pm}t} - \cos(\Delta\omega_{\pm}t)] - \sin\Delta\varphi_{\pm}\sin(\Delta\omega_{\pm}t)\} \ .
\end{aligned}$$

The evolution of the radii $R^{\pm}$ will be discussed now starting with the simple cases $\alpha_{\pm} = 0$ or $k_0 = 0$ end ending with the more complex one $\alpha_{\pm} \neq 0$, $k_0 \neq 0$.

- $\underline{\alpha_{\pm} \neq 0,\ k_0 = 0}$

  In the case of damping only Eq. (3.27) reduces to

  $$R^{\pm}(t) = R^{\pm}(0)\,\mathrm{e}^{\alpha_{\pm}t} , \tag{3.28}$$

  which describes the normal growth and decay of the magnetron and cyclotron motion as it was already discussed in Sec. 3.3.1.

- $\underline{\alpha_{\pm} = 0,\ k_0 \neq 0}$

  In the case of excitation only one obtains from Eq. (3.27)

  $$\begin{aligned}
  R^{\pm}(t) &= \frac{1}{\omega_+ - \omega_-}\Big[A^{\pm}(0)^2 + \frac{k_0^2}{\Delta\omega_{\pm}^2}\sin^2(\tfrac{\Delta\omega_{\pm}}{2}t) \\
  &\quad + A^{\pm}(0)\frac{k_0}{\Delta\omega_{\pm}}\left\{\pm 2\cos\Delta\varphi_{\pm}\sin^2(\tfrac{\Delta\omega_{\pm}}{2}t) + \sin\Delta\varphi_{\pm}\sin(\Delta\omega_{\pm}t)\right\}\Big]^{\frac{1}{2}} .
  \end{aligned} \tag{3.29}$$

  Therefore, $R^{\pm}(t)$ is the sum of a constant term $R^{\pm}(0)$ and a term modulated with the frequency $\frac{1}{2}\Delta\omega_{\pm}$ and $\Delta\omega_{\pm}$.
  In Fig. 3.5 the evolution of the cyclotron radius $R^{+}(t)$ as a function of $\Delta\omega_{+}$ is shown for two different initial phase shifts $\Delta\varphi_{+}$. The magnetron motion performs similar. Therefore it is not treated in an extra figure. The amplitude of the oscillation becomes larger with increasing excitation amplitude k_0 and with smaller frequency detuning $\Delta\omega_{\pm}$. The starting phase has a small influence and does not change the general behaviour. For the

resonance case one notes a linear increase of the radius, which can be deduced from Eq. (3.29),

$$\lim_{\Delta\omega_\pm \to 0} R^\pm(t) = \frac{1}{\omega_+ - \omega_-}\sqrt{A^\pm(0)^2 + \frac{k_0^2}{4}t^2 + A^\pm(0)k_0 t\sin\varphi}\,. \tag{3.30}$$

If the ions start at rest ($R^\pm(0) = 0$), then $R^\pm(t)$ looses its phase dependency and shows a simple oscillation,

$$R^\pm(t) = \left|\frac{k_0}{\Delta\omega_\pm}\sin(\frac{\Delta\omega_\pm}{2}t)\right|\,. \tag{3.31}$$

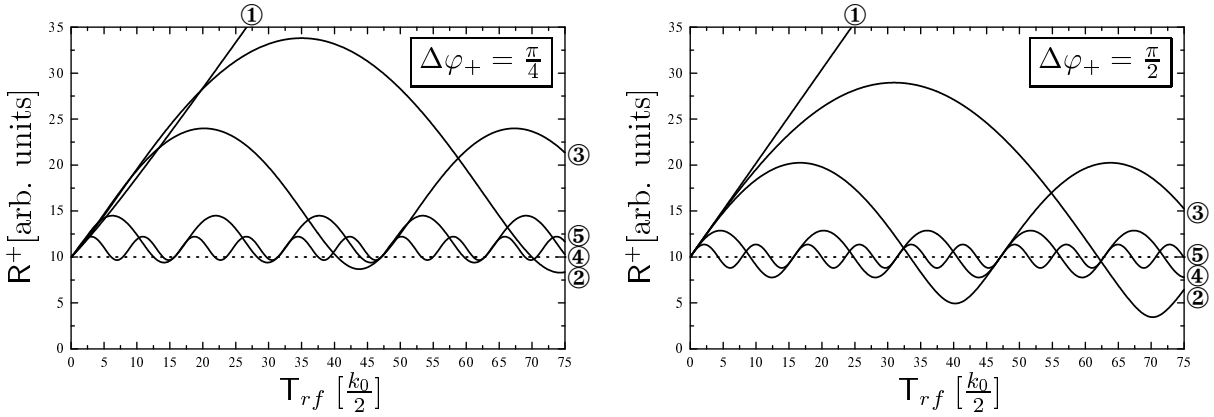

Figure 3.5: The amplitude of the cyclotron motion $R^+(t)$ for dipole excitation as a function of the excitation time T_{rf} (in units of $\frac{k_0}{2}$) for different values of $\Delta\omega_+$ (①: 0, ②: $\frac{1}{500}\omega_+$, ③: $\frac{1}{300}\omega_+$, ④: $\frac{1}{100}\omega_+$, ⑤: $\frac{1}{50}\omega_+$) and an initial phase shift $\Delta\varphi_+ = \frac{\pi}{4}$ (left) and $\Delta\varphi_+ = \frac{\pi}{2}$ (right). Parameters used in these calculations are $\omega_+ = 1$, $\omega_- = \frac{1}{50}$, $\gamma = 0$, $k_0 = \frac{1}{1000}\omega_+$, and $R^+(0) > 0$.

- $\alpha_\pm \neq 0,\ k_0 \neq 0$

  As seen in the previous case also here a phase shift between initial ion motion and excitation field does not change the general behaviour of the motion. Therefore, $\Delta\varphi_\pm = 0$ is used in the following.

  Eq. (3.27) can be written as

$$R^\pm(t) = \frac{1}{\omega_+ - \omega_-}\sqrt{\left[A^\pm(0)\,\mathrm{e}^{\alpha_\pm t} + \frac{k_0}{2}\cdot\frac{\zeta}{\kappa}\right]^2 + \left[\frac{k_0}{2}\cdot\frac{\xi}{\kappa}\right]^2} \tag{3.32}$$

$$\begin{aligned}\zeta &= \alpha_\pm\sin(\Delta\omega_\pm t) + \Delta\omega_\pm\left[\mathrm{e}^{\alpha_\pm t} - \cos(\Delta\omega_\pm t)\right]\\ \xi &= \Delta\omega_\pm\sin(\Delta\omega_\pm t) + \alpha_\pm\left[\mathrm{e}^{\alpha_\pm t} - \cos(\Delta\omega_\pm t)\right]\,.\end{aligned}$$

  Already here one recognises an important characteristic of the motion. For damping values $\gamma > 0$ and $t \to \infty$ the magnetron radius grows to infinity, whereas the cyclotron motion radius approaches a maximum value which is independent of all other initial conditions.

In the upper part of Fig. 3.6 the evolution of the magnetron radius for different detuning values ($\Delta\omega_-$) is shown. Oscillations with a frequency of $\frac{\Delta\omega_-}{2}$ are clearly visible, on top of the already mentioned exponential increase. The time constant of the latter is not affected by the detuning. It depends only on the damping coefficient as can be seen in the bottom of Fig. 3.6.
The cyclotron radius approaches for $t \to \infty$ a limit of

$$R^+(\infty) = \frac{k_0}{2(\omega_+ - \omega_-)\sqrt{\alpha_+^2 + \Delta\omega_+^2}} \,. \tag{3.33}$$

Accordingly, an increase of the frequency detuning ($\Delta\omega_+$) as well as the damping coefficient (α_+) will decrease $R^+(\infty)$. This can easily be seen in Fig. 3.7. Also in these cases one observes oscillations with a frequency $\frac{\Delta\omega_-}{2}$. An initial radius $R^+(0)$ has no influence on the final radius.

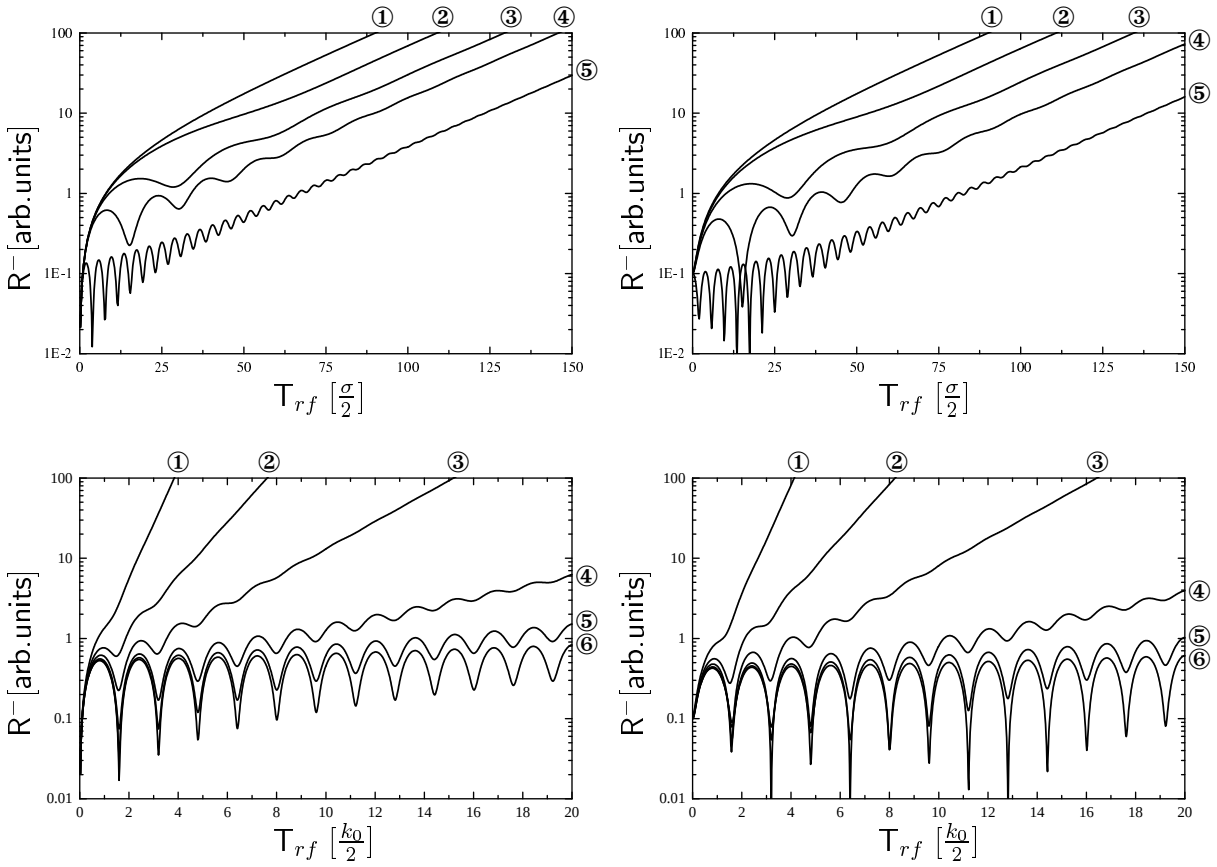

Figure 3.6: The amplitude of the magnetron motion $R^-(t)$ for dipole excitation as a function of the dipole excitation time T_{rf} for the parameters frequency detuning $\Delta\omega_-$ (top), damping coefficient γ (bottom) and initial radii $R^-(0) = 0$ (left), $R^-(0) \neq 0$ (right).
Numbers used in this calculations are $\omega_+ = 1$, $\omega_- = \frac{1}{50}$; Top: $k_0 = \gamma\omega_c$, $\Delta\omega_- =$ ①: 0, ②: $\frac{1}{50}\omega_-$, ③: $\frac{1}{20}\omega_-$, ④: $\frac{1}{10}\omega_-$, ⑤: $\frac{2}{5}\omega_-$, $\gamma = \frac{1}{500}$; Bottom: $k_0 = \frac{1}{1000}\omega_c$, $\Delta\omega_- = \frac{1}{50}\omega_-$, $\gamma =$ ①: 0, ②: $\frac{1}{1000}$, ③: $\frac{1}{500}$, ④: $\frac{1}{250}$, ⑤: $\frac{1}{100}$, ⑥: $\frac{1}{50}$.

Quadrupole Excitation

The manipulation of the ion motion in a Penning trap using azimuthal electrical quadrupole fields has been discussed in great detail in ref. [Bol90, Sav91, Kön95]. Its importance for the working principle of REXTRAP makes it necessary to discuss it here briefly.

An azimuthal electrical quadrupole field as described by Eq. (3.18) with $U_Q = U_q \cdot \cos(\omega_{rf} t + \varphi_{rf})$ and a damping force according to Eq. (3.9) changes the radial part of Eq. (3.5) to

$$\begin{array}{rcrcrcl} \dot{V}_x^{\pm} & = & \omega_{\pm} V_y^{\pm} & + & k\,(V_x^{+} - V_x^{-}) & - & \gamma\,(\omega_{+} V_x^{+} - \omega_{-} V_x^{-}) \\ \dot{V}_y^{\pm} & = & -\omega_{\pm} V_x^{\pm} & + & k\,(V_y^{+} - V_y^{-}) & - & \gamma\,(\omega_{+} V_y^{+} - \omega_{-} V_y^{-}) \end{array} \tag{3.34}$$

$$\text{with} \qquad k = k_0 \cos(\omega_{rf} t + \varphi_{rf}) \qquad k_0 = \frac{a}{\omega_{+} - \omega_{-}} \frac{q}{m} \frac{U_q}{2 r_0^2} \; .$$

The axial motion of the particle is not influenced and fully described by Eq. (3.12).

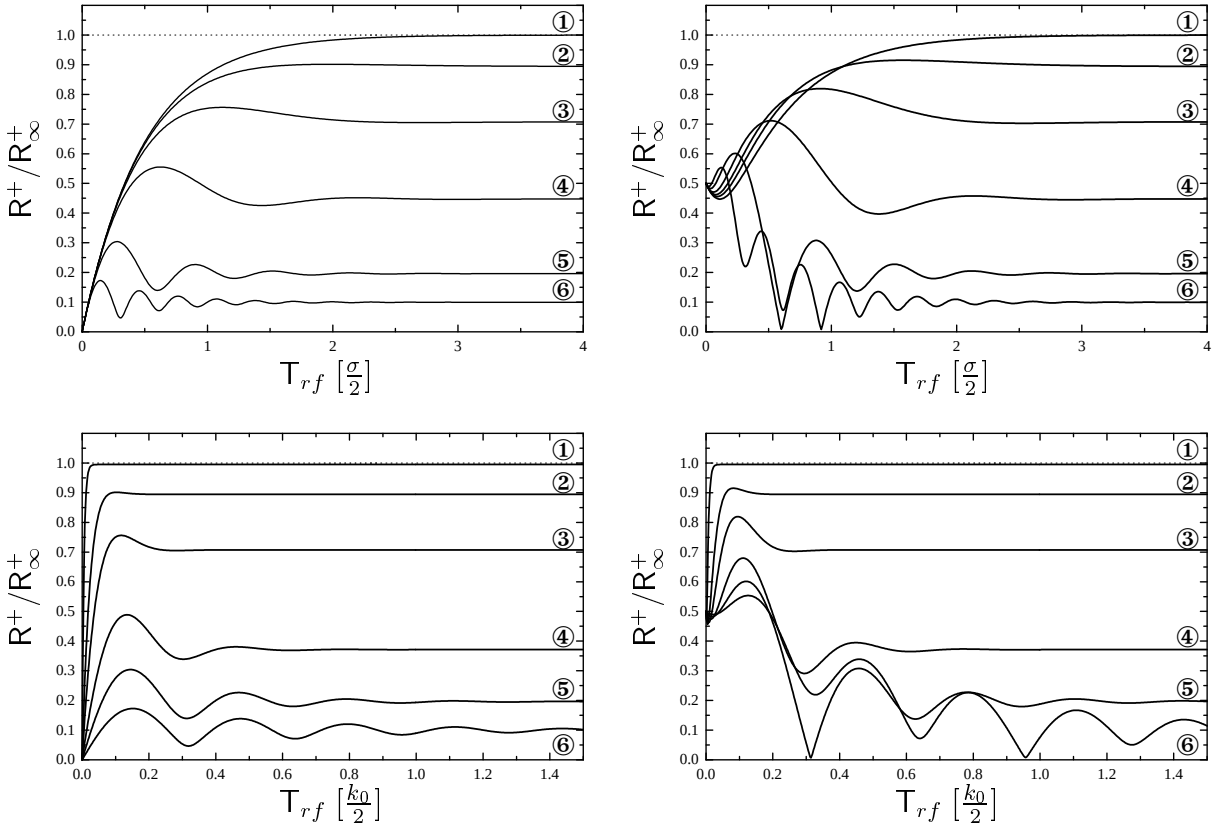

Figure 3.7: The amplitude of the cyclotron motion $R^{+}(t)$ normalised by $R_{\infty}^{+} = R^{+}(\infty, \Delta\omega_{+} \to 0) = \frac{k}{2\sigma\omega_{+}}$ for dipole excitation as a function of the excitation time T_{rf} for the parameters frequency detuning $\Delta\omega_{+}$ (top), damping coefficient γ (bottom) and initial radii $R^{+}(0) = 0$ (left), $R^{+}(0) = \frac{1}{2} R_{\infty}^{+}$ (right). Numbers used in this calculations are $\omega_{+} = 1$, $\omega_{-} = \frac{1}{50}$; Top: $k_0 = \gamma\omega_c$, $\Delta\omega_{+} =$ ①: 0, ②: $\frac{1}{1000}\omega_{+}$, ③: $\frac{1}{500}\omega_{+}$, ④: $\frac{1}{250}\omega_{+}$, ⑤: $\frac{1}{100}\omega_{+}$, ⑥: $\frac{1}{50}\omega_{+}$, $\gamma = \frac{1}{500}$; Bottom: $k_0 = \frac{1}{1000}\omega_c$, $\Delta\omega_{+} = \frac{1}{50}\omega_{+}$, $\gamma =$ ①: 0, ②: $\frac{1}{1000}$, ③: $\frac{1}{500}$, ④: $\frac{1}{250}$, ⑤: $\frac{1}{100}$, ⑥: $\frac{1}{50}$.

The solution of this differential equation system can be found following the same way as it has been done for the case of dipole excitation in Sec. 3.3.2. For an excitation frequency $\omega_{rf} \approx \omega_c$ and under the assumption that the magnetron and reduced cyclotron motion remain circular with the unperturbed frequencies ω_+ and ω_-, one finds for the radii

$$R^{\pm}(t) = \Re\left\{f^{\pm}(t)\mathrm{e}^{\pm\frac{i}{2}\Delta\omega t}\right\}\mathrm{e}^{-\frac{\sigma}{2}t} \tag{3.35}$$

$$\begin{aligned} f^{\pm}(t) &= R^{\pm}(0)\cosh(\Delta t) \mp \frac{(\gamma\omega_c + i\Delta\omega)R^{\pm}(0) + k_0^{\pm}R^{\mp}(0)}{2\Delta}\sinh(\Delta t) \\ \Delta &= \frac{1}{2}\sqrt{(\gamma\omega_c + i\Delta\omega)^2 - k_0^2} \\ \Delta\omega &= \omega_{rf} - \omega_c \qquad k_0^{\pm} = k_0\mathrm{e}^{\pm i\Delta\varphi} \qquad \Delta\varphi = \varphi_{rf} - (\varphi_+ + \varphi_-)\,. \end{aligned}$$

In the following the resonance case $\omega_{rf} = \omega_c$ will be discussed starting from the simple cases $k = 0$ and $\sigma = 0$ and ending with the more complex ones $k \neq 0$, $\sigma \neq 0$.

- $\underline{k = 0,\ \sigma \neq 0}$

  For the case of damping only Eq. (3.35) reduces to

  $$R^{\pm}(t) = R^{\pm}(0)\mathrm{e}^{\alpha_{\pm}t}\,, \tag{3.36}$$

  which is equivalent to Eq. (3.16) and described there.

- $\underline{k \neq 0,\ \sigma = 0}$

  For the case of excitation only Eq. (3.35) becomes:

  $$R^{\pm}(t) = R^{\pm}(0)\cos(\frac{k_0}{2}t) \mp R^{\mp}(0)\cos\Delta\varphi\sin(\frac{k_0}{2}t). \tag{3.37}$$

  As can be seen, the azimuthal quadrupole excitation leads to a coupling of the cyclotron and magnetron motion. The initial phase shift determines how complete the transfer of the motions into each other will be.

- $\underline{k \neq 0,\ \sigma \neq 0}$

  It has been shown in Sec. 3.3.1 that the cyclotron motion decays much faster than the magnetron motion grows under the influence of an damping force. A sufficiently strong coupling of both motions should therefore prevent the increase of the magnetron radius, allowing a reduction of the amplitude of both motions. In the case of resonance Eq. (3.35) changes to

  $$R^{\pm}(t) = \mathrm{e}^{-\frac{\sigma}{2}t}\left[R^{\pm}(0)\cosh(\Delta t) \mp \frac{\gamma\omega_c R^{\pm}(t) + k_0^{\pm}R^{\mp}(0)}{2\Delta}\sinh(\Delta t)\right] \tag{3.38}$$

  The general behaviour of $R^{\pm}(t)$ is determined by the size of Δ, i.e. the ratio of the damping rate ($\gamma\omega_c$) to the excitation amplitude (k_0). Fig. 3.8 shows the amplitudes of the magnetron and cyclotron motion as a function of the excitation time (T_{rf}) for different values of k_0 (marked with ①..⑥). As a general trend one observes an exponential increase or decrease of the amplitudes. The corresponding time constant α is displayed in Fig. 3.9. An detailed description of these cases is given in the following.

①..③ $\underline{k_0 < \gamma\omega_c}$: Here, Δ is real and the time constant for the amplitudes is given by $\alpha = -\frac{\sigma}{2} + \Delta$. Accordingly, the radii increase for $\Delta < \frac{\sigma}{2}$, they remain constant for $\Delta = \frac{\sigma}{2}$, or else they decrease. This behaviour is illustrated in the cases ①, ②, and ③, respectively. Thereby it has been used that $\Delta \gtreqless -\frac{\sigma}{2}$ corresponds to $k_0 \gtreqless \sqrt{2}\cdot\gamma\omega_z$.

④..⑥ $\underline{k_0 \geq \gamma\omega_c}$: For $k_0 \geq \gamma\omega_c$ Δ becomes complex and one obtains for the radii:

$$R^{\pm}(t) = \mathrm{e}^{-\frac{\sigma}{2}t}\left[R^{\pm}(0)\cos(|\Delta|t) \mp \frac{\gamma\omega_c R^{\pm}(0) + k_0\cos\Delta\varphi R^{\mp}(0)}{2|\Delta|}\sin(|\Delta|t)\right], \tag{3.39}$$

observing a steady decrease of both amplitudes with an additional periodic beating between them. The time constant α has reached its maximum negative value of $-\frac{\sigma}{2}$. An increase of k_0 above $\gamma\omega_c$ does not change α further. It only raises the beating frequency between the two motions. This behaviour is clearly visible in the cases ④, ⑤, and ⑥ in Fig. 3.8 and Fig. 3.9.

As shown above, for a damping force acting on the ion and sufficiently strong coupling of magnetron and cyclotron motion via an azimuthal rf quadrupole field with a frequency of ω_c one can achieve a reduction of both motions. In this way one can counteract the increase of the magnetron radius found for the damping case only and finally centre an ion in a Penning trap. This is illustrated in Fig. 3.3.

3.4 Buffer Gas Cooling

In Sec. 2 it has been discussed that the reduction of the phase space occupied by the ion swarm via cooling, is essential for an operation of REXTRAP as emittance improvement and bunching device. Buffer gas cooling in combination with rf sideband excitation ensures short cooling

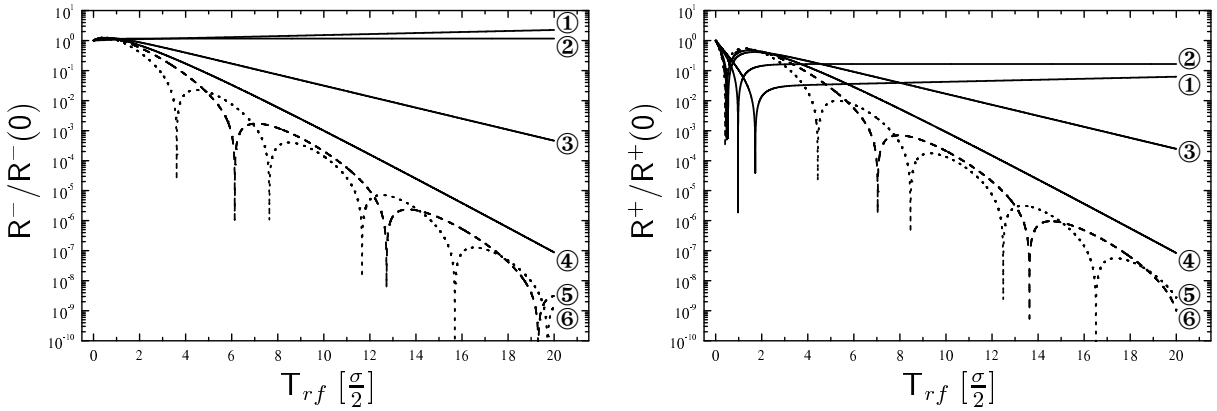

Figure 3.8: Amplitudes R^- of the magnetron (left) and R^+ of the cyclotron motion (right) with quadrupole excitation as function of the excitation time T_{rf} (in units of $\frac{\sigma}{2}$) for different excitation amplitudes: ① $k = \frac{1}{5}\sqrt{2}\gamma\omega_z$, ② $k = \sqrt{2}\gamma\omega_z$, ③ $k = 3\sqrt{2}\gamma\omega_z$, ④ $k = \gamma\omega_c$, ⑤, ⑥ $k = \frac{11}{10}\gamma\omega_c$ – dashed, $k = \frac{5}{4}\gamma\omega_c$ – dotted. The numbers used in these calculations are $\omega_+ = 1$, $\omega_- = \frac{1}{50}$, $R^+(0) = R^-(0) > 0$.

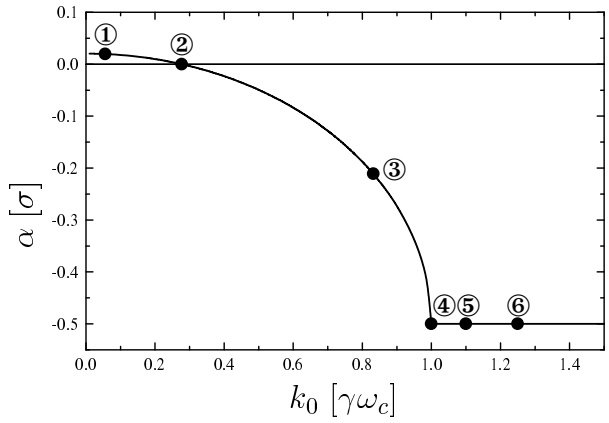

excitation amplitudes

① $k = \frac{1}{5}\sqrt{2}\gamma\omega_z$
② $k = \sqrt{2}\gamma\omega_z$
③ $k = 3\sqrt{2}\gamma\omega_z$
④ $k = \gamma\omega_c$
⑤ $k = \frac{11}{10}\sqrt{2}\gamma\omega_c$
⑥ $k = \frac{5}{4}\sqrt{2}\gamma\omega_c$

Figure 3.9: Time constants $\alpha_\pm$ (in units of σ) as function of the radio frequency amplitude k_0 (in units of $\gamma\omega_c$). The numbered points correspond to the curves shown in Fig. 3.8.

times. It is applicable to all ion species and in comparison to other techniques relatively easy to perform.

In the following a short introduction to important topics of buffer gas cooling with respect to the operation of REXTRAP is presented.

3.4.1 Damping and Ion Mobility

The equation of motion for an ion in a Penning trap under the influence of a damping force was extended by a damping term (see Sec. 3.3.1)

$$\mathbf{F_D} = -\sigma\, m\, \dot{\mathbf{r}}\ . \tag{3.40}$$

Realistic damping constants are obtained from measurements of the ion mobility in the according buffer gas. The drift velocity $\mathbf{v_d}$ of the ion is measured when dragging the ion through the gas via an applied electrical field $\mathbf{E_d}$. The relationship between drift velocity and electric field is given by

$$\mathbf{v_d} = K\, \mathbf{E_{el}}\ , \tag{3.41}$$

where K denotes the ion mobility. By comparing the stationary limit

$$\dot{\mathbf{v}}_\mathbf{d} + \sigma \mathbf{v_d} = \frac{q}{m}\mathbf{E_{el}} \qquad\qquad \lim_{t\to\infty} \dot{\mathbf{v}}_\mathbf{d} = 0 \tag{3.42}$$

with Eq. (3.41) one obtains for the damping constant σ

$$\sigma = \frac{q}{m}\frac{1}{K}\ . \tag{3.43}$$

Since the ion mobility scales with the gas temperature T and pressure p it is normally tabulated as reduced mobility K_0, i.e. normalised to standard atmospheric pressure and temperature

$$K_0 = K\,\frac{273.16\,\text{Kelvin}}{T}\,\frac{p}{1013\,\text{mbar}}\ . \tag{3.44}$$

A compilation of nearly all available ion mobility data can be found in [Ell76, Ell78, Ell84, Vie95]. These data cover mostly the energy range up to a few electron volts. In this regime

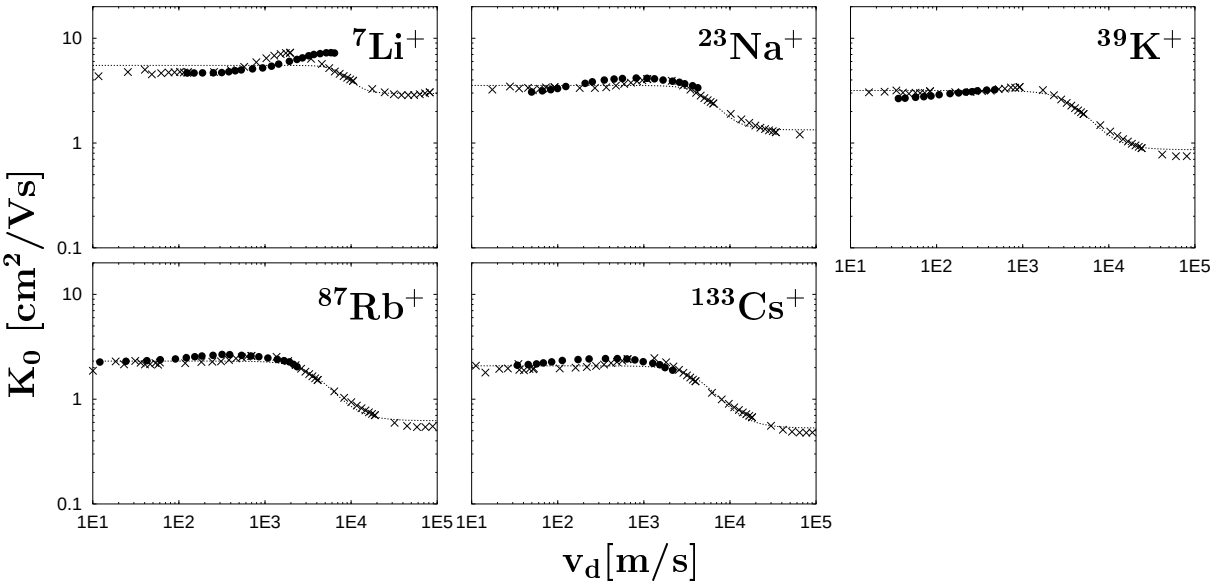

Figure 3.10: The reduced ion mobility as function of the ion velocity for ^{7}Li, ^{23}Na, ^{39}K, ^{87}Rb, and ^{133}Cs in a argon buffer gas atmosphere. (• – experimental values from [Ell76, Ell78, Ell84, Vie95], $\times$ – simulated values, dashed line – parametric function according to Eq. (3.45))

the ion mobility can be treated as constant for a certain ion buffer gas combination. For higher ion energies in the order of a few hundred electron volts, no experimental data are available. Unfortunately, this range is interesting for the simulation of ion injection into REXTRAP and of the energy loss of the ions while passing through the trap. Therefore, it was necessary to calculate the ion mobility for the interesting velocity range.

Ion simulations have been performed using a method already applied in [Sch98]. In this simulations ions are dragged through a buffer gas by an applied electrical field. Collisions with the neutrals of the gas are treated in a "realistic" way, i.e. by employing known ion-neutral interaction potentials. For a detailed description of this procedure please refer to Sec. A. The results of the calculations are depicted for several ion-neutral combinations in Fig. 3.10. The experimental values of the ion mobility are well reproduced for the low energy range. At higher energies, where no experimental data are available, the mobility decreases and for even higher energies it approaches a stationary limit. This trend can be understood since for higher ion energies the nature of the collisions changes from those dominated by soft Van-der-Waals-interaction to hard-sphere collisions due to the strong repelling part of the interaction potential.

For the ion motion simulations in REXTRAP it has been desirable to have a parametric function available that describes the complete shape of the curve. The following heuristic formula was found to describe well the ion mobility as a function of the ion velocity

$$K_0(v_d) = \frac{K_0^0 - K_0^\infty}{1 + \left(\frac{v_d}{v_\kappa}\right)^\kappa} + K_0^\infty \ . \tag{3.45}$$

For lower velocities ($v_d \to 0$) K_0 takes the value K_0^0, whereas it becomes K_0^∞ for higher values ($v_d \to \infty$). The slope of the drop in between these extreme cases can be controlled by v_κ and κ. The results of fitting Eq. (3.45) to the calculated values are given in Table 3.1. As it can be seen

ion/buffer gas	K_0^0 $\left[\frac{\text{cm}^2}{\text{Vs}}\right]$	K_0^∞ $\left[\frac{\text{cm}^2}{\text{Vs}}\right]$	v_κ $\left[\frac{\text{m}}{\text{s}}\right]$	κ
$^7Li^+$—Ar	5.50	2.97	8963.64	4.32
$^{23}Na^+$—Ar	3.54	1.34	6220.35	3.04
$^{39}K^+$—Ar	3.17	0.86	4700.73	2.39
$^{87}Rb^+$—Ar	2.31	0.62	4647.07	2.39
$^{133}Cs^+$—Ar	2.08	0.53	5485.78	2.34

Table 3.1: Parameters for Eq. (3.45) in order to reproduce the ion mobility as a function of the ion velocity for several ion-neutral combinations.

in Fig. 3.10, this parametric function reproduces the experimental and calculated ion mobility quite well over the complete velocity rrange shown.

3.4.2 Cooling Limit

The cooling process, as it was considered until now, would lead to zero amplitudes of the ion motion since the finite temperature of the cooling medium was neglected. It is obvious that phase space reduction will only take place until the system has reached a thermodynamic equilibrium state, i.e. until the temperature of the ion swarm is equal to the buffer gas temperature. The cooling limit will be discussed in the following.

The phase space density of a collection of interacting particles in the thermal equilibrium is represented by the relation

$$\text{phase space density} = \text{constant} \times \exp\left(\frac{H}{kT}\right) \tag{3.46}$$

where H is the energy and kT is a constant which defines the temperature of the ensemble in terms of the Boltzmann constant k. Expressing Eq. (3.46) in symbolic form gives

$$\frac{\mathrm{d}^6\mathrm{n}(H)}{\mathrm{dx\,dy\,dz\,dp}_x\,\mathrm{dp}_y\,\mathrm{dp}_z} \sim \exp\left(\frac{H}{kT}\right) \tag{3.47}$$

where x, y, and z denotes the spatial coordinates, p_x, p_y, and p_z are the associated momentum coordinates.

Both, axial and radial motion, contribute to the Hamiltonian H for a particle in a Penning trap. Since it contains no mixing terms (radial and axial motion are decoupled) Eq. (3.47) decomposes and axial and radial motion can be treated separately.

The Axial Motion

The axial motion is a harmonic oscillation (see Eq. (3.4)) along the z-axis. Therefore the Hamiltonian is given by

$$H = \frac{m}{2}\omega_z^2\, z_0^2 \qquad \text{with} \quad z_0 = \sqrt{z(0)^2 + \frac{\dot{z}(0)^2}{\omega_z^2}}\,. \tag{3.48}$$

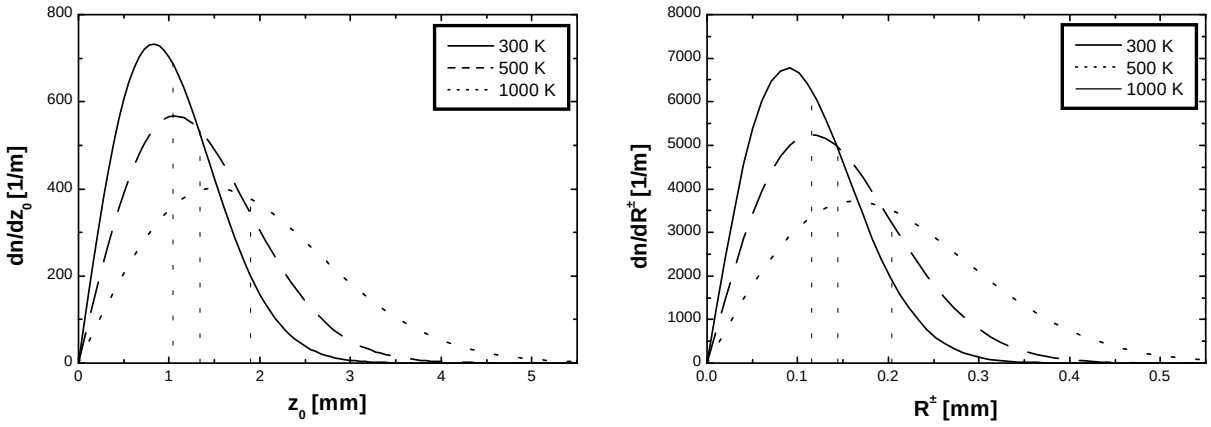

Figure 3.11: The longitudinal (left) and radial (right) ion density for the coupled case as a function of displacement for several equilibrium temperatures. Please note the different scales.

In the case of thermodynamic equilibrium the part of Eq. (3.47) describing the axial motion becomes

$$\frac{\mathrm{d}^2 n}{\mathrm{d}z \mathrm{d}\dot{z}} \sim \exp\left\{-\frac{H}{kT}\right\} = \exp\left\{-\frac{m}{2kT}\,\omega_z^2\, z_0^2\right\}\ . \tag{3.49}$$

Integration over $\mathrm{d}\dot{z}$ and normalisation leads to

$$\frac{\mathrm{d}n}{\mathrm{d}z_0} = \frac{m\omega_z^2}{kT}\, z_0\, \exp\left\{-\frac{m\omega_z^2}{2kT}\, z_0^2\right\}\ . \tag{3.50}$$

Using the frequency relations of Eq. (3.8) allow this to be simplified further

$$\frac{\mathrm{d}n}{\mathrm{d}z_0} \approx \frac{2qB\omega_-}{kT}\, z_0 \exp\left\{-\frac{qB\omega_-}{kT}\, z_0^2\right\}\ . \tag{3.51}$$

An important characteristic of such a distribution is the mean radius given by

$$\langle z_0 \rangle = \int_0^\infty z_0\, \mathrm{d}n = \int_0^\infty z_0 \left(\frac{\mathrm{d}n}{\mathrm{d}z_0}\right) \mathrm{d}z_0 = \frac{1}{\omega_z}\sqrt{\frac{\pi kT}{2m}} \approx \frac{1}{2}\sqrt{\frac{\pi kT}{qB\omega_-}}\ . \tag{3.52}$$

Therefore, the shape of the axial spatial distribution is mainly determined by the temperature. An increase of the temperature broadens it. This is illustrated in Fig. 3.11. It should be noted that the distribution is not mass dependent.

The Radial Motion

The ion density function for the radial motion can be found in a similar way [Sch00].

- Magnetron and cyclotron motion without quadrupole excitation (without coupling)

  The Hamiltonian for this uncoupled case is given by

$$H = \frac{m}{2}(\omega_+ - \omega_-)(\omega_+ R^+ - \omega_- R^-) \tag{3.53}$$

Since the magnetron motion is unbound (denoted by the "$-$" sign) it is only meaningful to give a distribution function for the cyclotron motion

$$\frac{\mathrm{d}n}{\mathrm{d}R^+} = \frac{m\,\omega_+(\omega_+ - \omega_-)}{kT}\,R^+\,\exp\left\{-\frac{m\,\omega_+(\omega_+ - \omega_-)}{2kT}R^{+2}\right\}\,, \tag{3.54}$$

which can be further reduced to

$$\frac{\mathrm{d}n}{\mathrm{d}R^+} \approx \frac{q^2B^2}{mkT}\,R^+\,\exp\left\{-\frac{q^2B^2}{2mkT}R^{+2}\right\}\,. \tag{3.55}$$

Averaging gives the mean radii

$$\begin{aligned}\langle R^+\rangle_{uncoupled} &= \sqrt{\frac{\pi kT}{2m\omega_+(\omega_+ - \omega_-)}} \approx \frac{1}{\omega_+}\sqrt{\frac{\pi kT}{2m}} = \frac{1}{qB}\sqrt{\frac{\pi mkT}{2}} \\ \langle R^-\rangle_{uncoupled} &= \infty \quad \text{for} \quad t \to \infty\,.\end{aligned} \tag{3.56}$$

Therefore, the final distribution is mainly determined by the temperature of the buffer gas. In contrast to the axial case it is mass dependent. Higher temperature or larger ion mass leads to broader distributions.

• Magnetron and cyclotron motion with quadrupole excitation (coupling)

As been shown in Sec. 3.3.2 magnetron and cyclotron motion can be coupled via a radial quadrupole field with the frequency $\omega_{rf} = \omega_c$. Then the Hamilton becomes

$$H = \frac{m}{4}(\omega_+ - \omega_-)^2(R^{+2} + R^{-2})\,, \tag{3.57}$$

which leads to the following density function

$$\begin{aligned}\frac{\mathrm{d}n}{\mathrm{d}R^\pm} &= \frac{m(\omega_+ - \omega_-)^2}{2kT}\,R^\pm \exp\left\{-\frac{m(\omega_+ - \omega_-)^2}{4kT}\,R^{\pm 2}\right\} \\ &\approx \frac{q^2B^2}{2kTm}\,R^\pm \exp\left\{-\frac{q^2B^2}{4kTm}\,R^{\pm 2}\right\}\,.\end{aligned} \tag{3.58}$$

For the mean radii one obtains

$$\langle R^\pm\rangle_{coupled} = \sqrt{\frac{\pi kT}{2m\omega_+(\omega_+ - \omega_-)}} \approx \frac{1}{qB}\sqrt{\pi mkT} = \sqrt{2}\,\langle R^+\rangle_{uncoupled}\,. \tag{3.59}$$

The final radii distributions for both motions are identical. They are broadened by a factor of $\sqrt{2}$ compared to the coupled case.

Simulation of Equilibrium Distributions

In order to prove the calculated relations and to obtain reasonable input data to investigate the characteristics of ejected ion bunches from REXTRAP, thermal equilibrium distributions of several ion buffer gas combinations have been simulated.

Different distributions have been obtained by placing an ion swarm consisting of a few ten thousand ions into a virtual Penning trap with buffer gas and track its motion until an equilibrium state has been reached. The simulation has been performed using the program *PennDamp*

described in Sec. 5.2. The input parameter set for the program has been chosen to meet real operation parameters of REXTRAP as close as possible. The collisions of the ions with the buffer gas were treated as hard sphere collisions with a rate corresponding to a helium buffer gas atmosphere of $p_{He} = 1 \cdot 10^{-5}$ mbar and a temperature $T = 300\,K$. The equilibrium state was normally reached after a few seconds, indicated by the fact that the mean radii show no significant change between two iterations.

In Fig. 3.12 the differences between uncoupled and coupled magnetron and cyclotron motion for $^{133}Cs^+$ is presented. The plots show histograms of the radii of the different motion and the corresponding theory functions. A nearly perfect agreement of the simulations with theory can be noted.

Similar plots in Fig. 3.13 illustrate the mass dependence of the amplitude distribution for the different motion in the case of coupled magnetron and cyclotron motion. Again, perfect agreement of the simulation with theory can be seen for the case of $^{133}Cs^+$. If the mass ratio of the collision partners becomes smaller, i.e. for $^{39}K^+$ and $^{23}Na^+$ the distributions of magnetron and cyclotron radii broaden slightly, which can be attributed to a slightly higher temperature of these motions. A similar phenomenon, rf-heating, has been found in Paul traps. Due to the collisions with the buffer gas atoms the ions run out of phase with the applied coupling quadrupole rf-field, which results in heating of the radial motion. Accordingly, it is not noticeable for the axial motion.

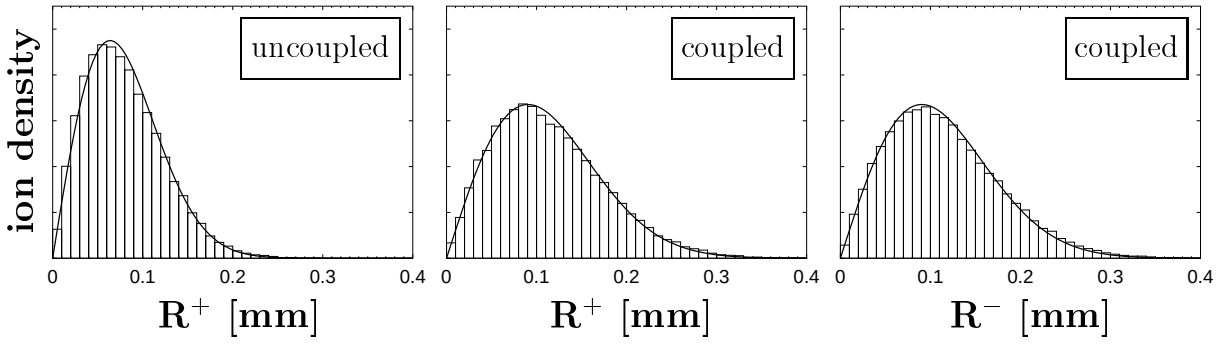

Figure 3.12: Equilibrium distributions for $^{133}Cs^+$ in a Penning trap with Helium buffer gas at a temperature of 300 K. The histograms are the result of a simulation. The line plots correspond to the theory functions. **Left:** Distribution of cyclotron radii R^+ for uncoupled magnetron and cyclotron motion. **Middle and Right:** Distribution of magnetron radii R^- and cyclotron radii R^+ for coupled magnetron and cyclotron motion.

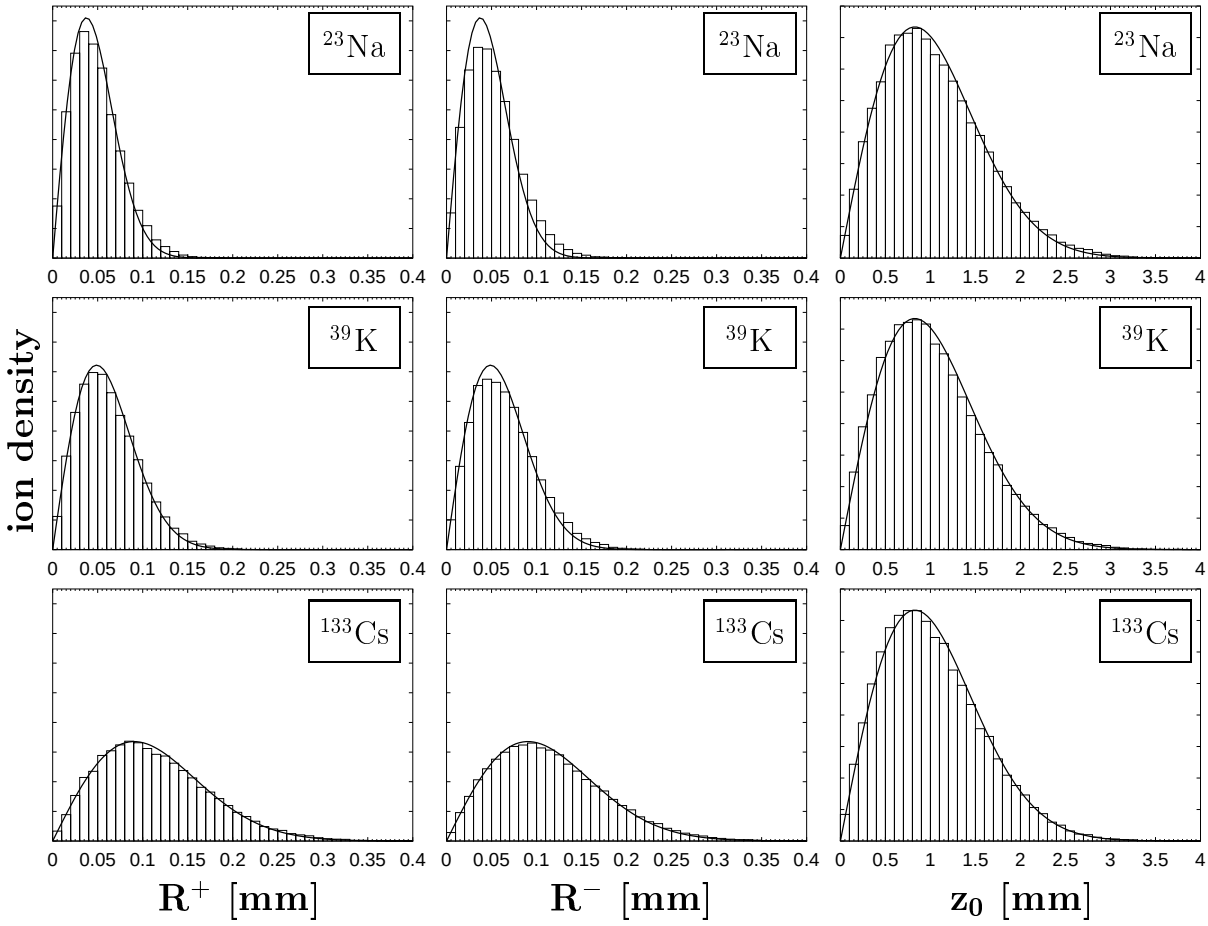

Figure 3.13: Equilibrium distributions of cyclotron radii R^+ (left), magnetron radii R^- (right), and maximum amplitudes of the axial motion z_0 for $^{23}Na^+$, $^{39}K^+$, and $^{133}Cs^+$ in a Penning trap with Helium buffer gas at a temperature of 300 K for coupled magnetron and cyclotron motion. The histograms are the result of simulation. The line plots correspond to the theory functions.

4 Experimental Set-up

The planned performance of the REX-ISOLDE post accelerator, together with the limits set by REXEBIS and by the beam properties of ISOLDE define the boundary conditions for REX-TRAP design. Due to the few and costly produced radioactive ions the device has to be efficient, i.e. the injection and extraction efficiency should be close to 100 %. The acceptance should be equal or larger than the ISOLDE beam emittance of 35 πmm mrad (@ 60 keV). The EBIS requests ion bunches that fit into a narrow acceptance phase space with values of 3 πmm mrad (@ 60 keV) radially and and 100 µs eV (@ 60 keV) longitudinally [Wen98, Wen00]. Cycle times of 20 ms should be reached in order to match the accelerators timing scheme [Hab00]. Furthermore, the device has to be reliable since it is a part of a complex accelerator chain.

The experimental set-up of REXTRAP (Fig. 4.1), built to meet these requirements, is described in detail in this chapter. The set-up, the control system as well as important operation parameters and schemes will be discussed.

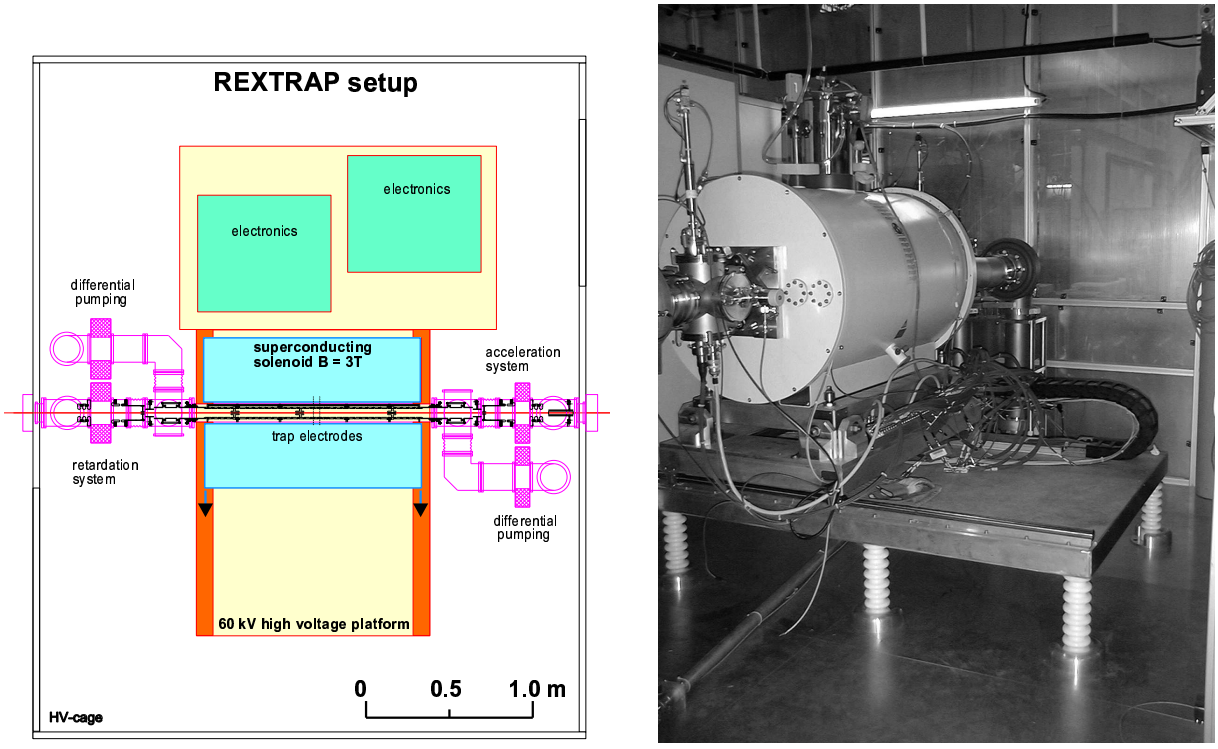

Figure 4.1: The experimental set-up of REXTRAP. **Left:** Schematical top view of the system. Nearly the complete space inside the Faraday cage is taken by a high voltage platform. The magnet system that houses the trap structure and two racks containing the elctronic for trap operation are placed on the platform. **Right:** Photograph of the system. The high voltage platform rests on large insulators and the magnet can be easily pinpointed in the foreground. Parts of the injection and ejection ion optics are visible in front and behind the magnet.

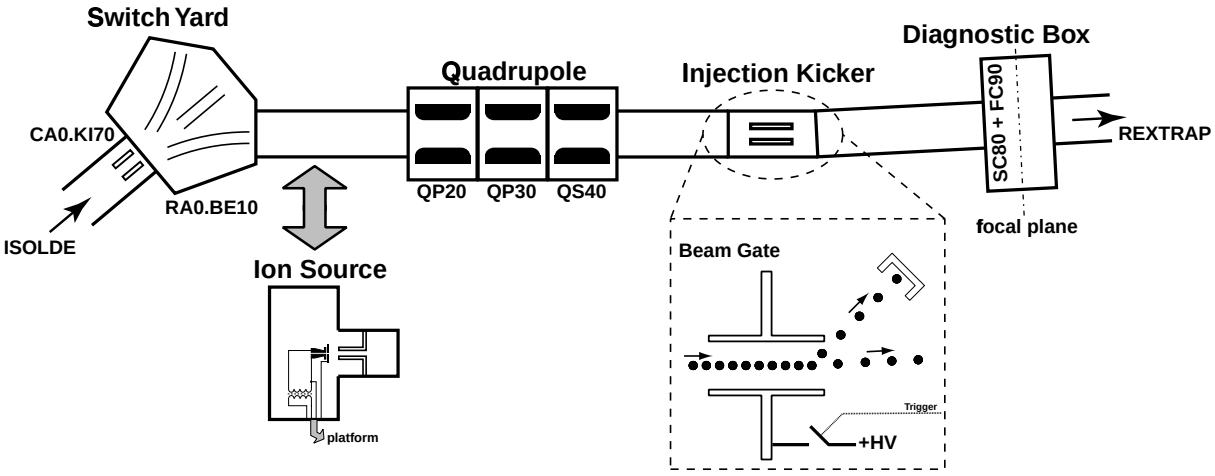

Figure 4.2: Overview of the RA0 beam line leading towards REXTRAP. The insertion of the off-line ion source into the beam line and the principal of the REXTRAP beam gate are schematically shown.

4.1 Beam Transport to REXTRAP

The injection beam line of REXTRAP, i.e. the RA0 section of the ISOLDE beam line system, branches off the central beam line at the end of section CA0 to the right. A sketch of the beam line is shown in Fig. 4.2. It consists of a standard ISOLDE quadrupole triplet, a beam kicker, and a standard ISOLDE diagnostic box.

The beam tube between the switch yard and the quadrupole can be removed. In the gap the test ion source is inserted to carry out off-line measurements.

The injection kicker has been introduced in order to correct a 3° misfit between the kicker-bender system at the end of the CA0-beam line and the optical axis of REX-ISOLDE. The kicker consists of two parallel electrodes for horizontal and vertical deflection, respectively. The vertical plates are used as beam gate for REXTRAP, which allows the control of the number of ions to be injected and stored in the trap. This functionality is achieved by applying a pulsed high voltage to one of the vertical kicker plates, which deflects the ion beam into the sidewall of the beam line.

4.2 The Off-Line Ion Source

In order to carry out off-line measurements for commissioning of REXTRAP and further stages of REX-ISOLDE a compact ion source for alkali ions has been developed using a concept described in ref. [Dez96].

In Fig. 4.3 a detailed sketch of the source is shown. Additionally, pictures of the complete system and a detailed view are given. The heart of the system is a conically shaped cylindrical hollow heater made from graphite and filled up with an alkali-zeolite. It is direct current heated and builds up a temperature gradient from the thinnest part in front to the thicker part at the end. The gradient provides a steadily flow of alkali atoms from the back part of the zeolite reservoir to its front. There the atoms are ionised at some pieces of tungsten wire incorporated in the zeolite material. The ions are accelerated in the field between the ioniser at high voltage and an electrode at ground potential. The beam shape can be influenced by an additional extraction

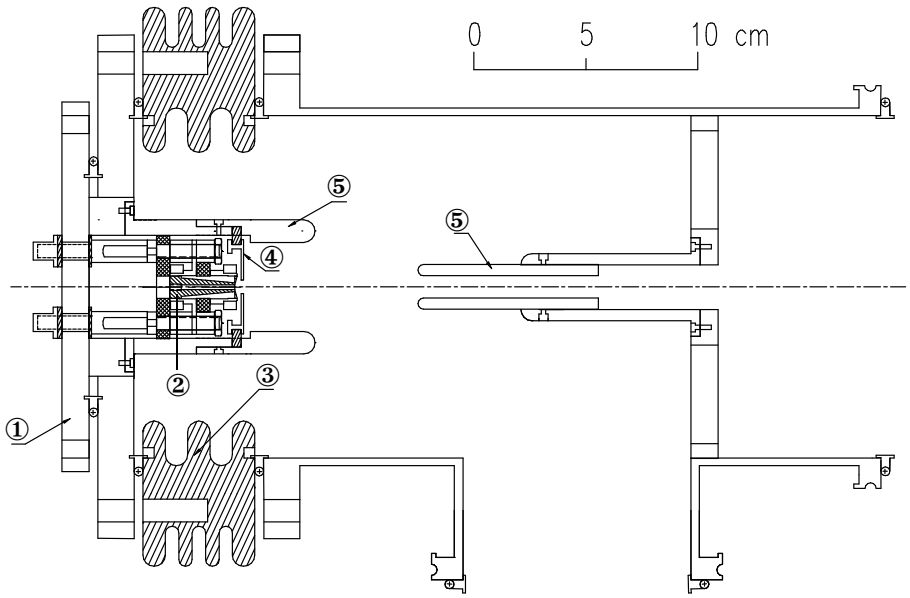

Parts list:

① base flange at HV
② ionizer unit
③ insulator
④ skimmer plates
⑤ extraction lenses

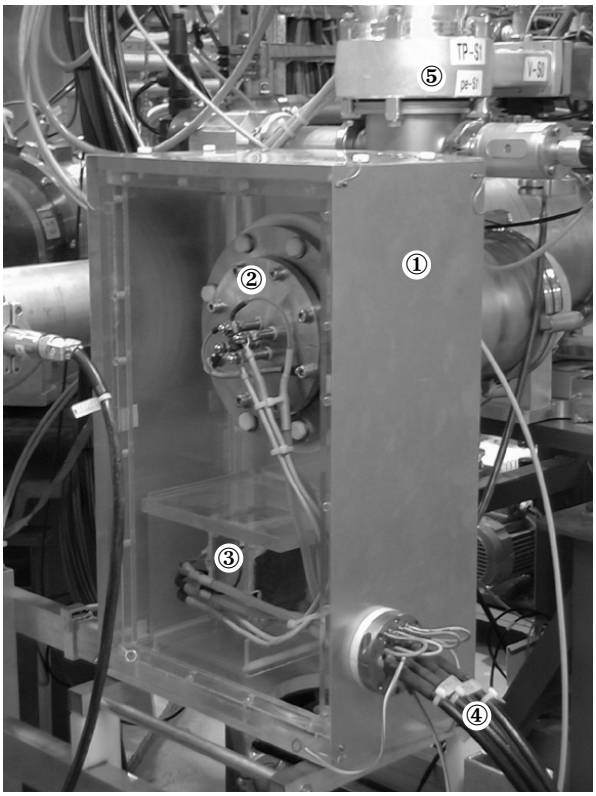

Overview

① housing
② base flange
③ transformer
④ power cables
⑤ vacuum pump

Detailed View

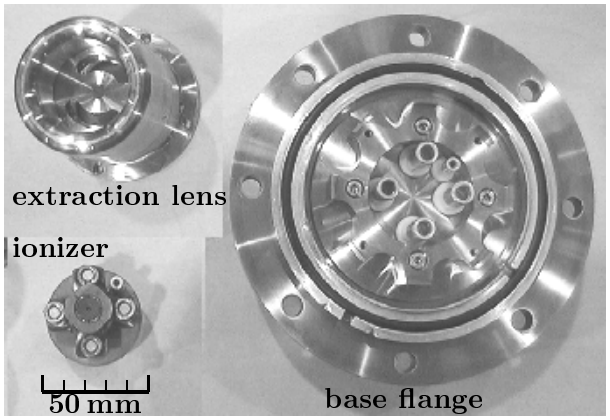

Figure 4.3: The REXTRAP test ion source. **Top:** Sectional view of the system. **Bottom left:** Photograph of the open Faraday cage. **Bottom right:** The inner part taken in pieces.

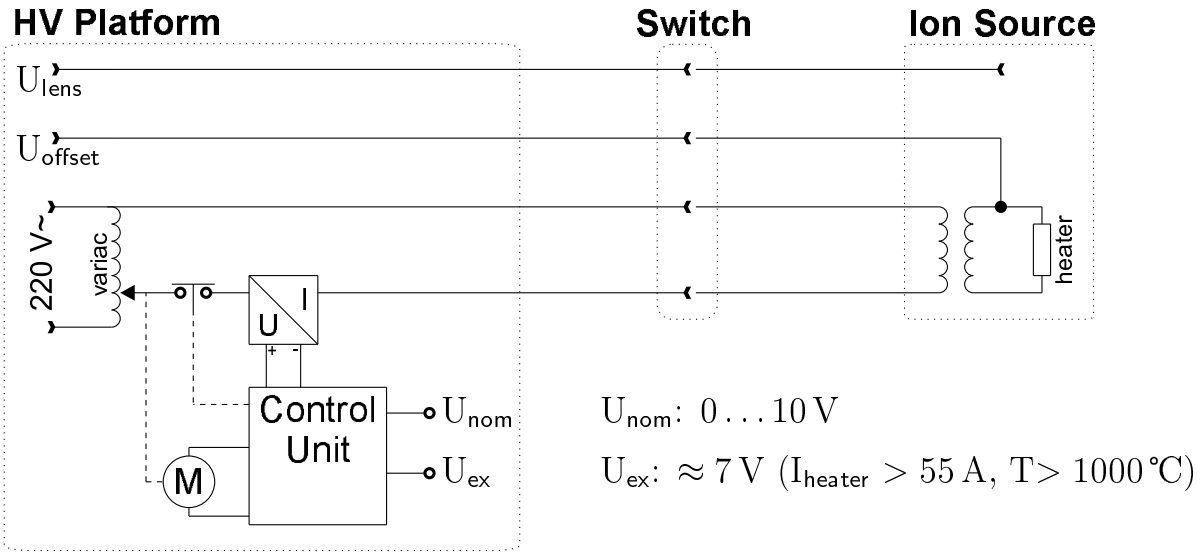

Figure 4.4: Block diagram of the REXTRAP test ion source.

electrode.

The system was constructed to ensure easy maintenance. It fits completely on a vacuum flange of 150 mm in diameter. For servicing the ioniser, i.e. to refill the zeolite material, two screws fixing the extraction lens system to the base flange have to be unfastened to remove that part. The electrical contacts of the ioniser unit establish plugs which fit into sockets formed by the vacuum feed troughs mounted at the base flange. This allows an easy removal of the ioniser.

All current and voltage supplies for operation are provided by a set of cables directly from the high voltage platform of REXTRAP. For on-line operation, i.e. when the ion source unit is moved out of the beam line, the cable connection is disconnected. A principle sketch of the ion source circuit is given in Fig. 4.4.

In order to keep the ion current from the source constant it is necessary to stabilise the temperature of the ioniser. This is achieved by regulating the primary current of the heater transformer by a motor driven variac placed on the high voltage platform. The variac is controlled by an external regulation circuit consisting of a current-to-voltage converter and a main control unit. The circuit compares in principle a signal derived from the primary heater current with a nominal voltage set remotely by the user. In addition, the control unit incorporates a safety circuit which opens the circuit of the primary heating current in the case of malfunction.

Due to the limited space between the ISOLDE switch yard and the quadrupole RA0 the Faraday cage of the ion source withstands only high voltages up to 50 kV without frequent sparks. For most of the test measurements a high voltage of 30 kV was chosen, ensuring almost trouble free operation.

The test ion source has been found to be very reliable over the time it was used to get REXTRAP operational. Depending on which zeolite was used ion beams of $^{133}Cs^{+}$, $^{87}Rb^{+}$, $^{39}K^{+}$, and $^{23}Na^{+}$ with stable currents up to a few nA can be produced over several weeks without refilling the source.

4.3 The REXTRAP Solenoid

The magnet constitutes the largest individual part of the REXTRAP system when it comes to weight and cost. It provides the magnetic field needed for the radial ion confinement.

The solenoid, manufactured by MAGNEX, is of superconducting type. It is an unshielded system with a warm bore, i.e. the inner cylinder containing a vacuum tube with the trap structure is kept at room temperature and thermally decoupled from the cryostats. Superconducting systems have two advantages. They provide high stability and need no on-line power supply. On the other hand the magnet coils must be cooled to liquid helium temperature. Depending on the season the REXTRAP magnet needs to be refilled every 6 weeks with liquid helium (100 l). The outer liquid nitrogen cryostat has to be filled every week (70 l).

A compilation of important data of the REXTRAP magnet can be found in Table 4.1.

4.3.1 The High Voltage Platform

The magnet is placed on a high voltage platform inside a Faraday cage. It abuts on rails which allow a sidewise displacement of about one metre. This ensures easy access to the trap structure for maintenance.

The REXTRAP high voltage platform rests on ten insulators made of Delrin. The insulation of the vacuum line is provided by large disc-shaped polyethylene insulators which are carved at their in- and outside in order to extend the creepage distance.

4.3.2 The Magnetic Field

The magnetic field of the REXTRAP solenoid is produced by a pair of Helmholtz coils. A number of additional small shim windings allows fine tuning of the field parameters and the compensation of field deforming due to the influence of the surrounding environment. A plot of the magnetic field strength along the central axis is given in Fig. 4.5. It was obtained by calculations using the nominal coil current and the geometrical data provided by the manufacturer. The field is relatively flat in the centre part, rises to its maximum at the position of the coils while dropping fast further out.

manufacturer: Magnex Scientific Limited	
maximum central field: 3 T	nominal coil current: 200.3 A
shim coils: Z1, Z2, X, Y, ZX, ZY, X2-Y2, XY	
central field homogeneity	
axially over 20 mm: < 2 ppm	radially over 20 mm: < 10 ppm
length of cryostat: 1300 mm	overall diameter: 890 mm
clear bore: 120 mm	overall height: 1328 mm
hold time	
liquid helium: 6 weeks (60 cm^3/h)	liquid nitrogen: 7 days (330 cm^3/h)

Table 4.1: Compilation of important properties of the REXTRAP solenoid.

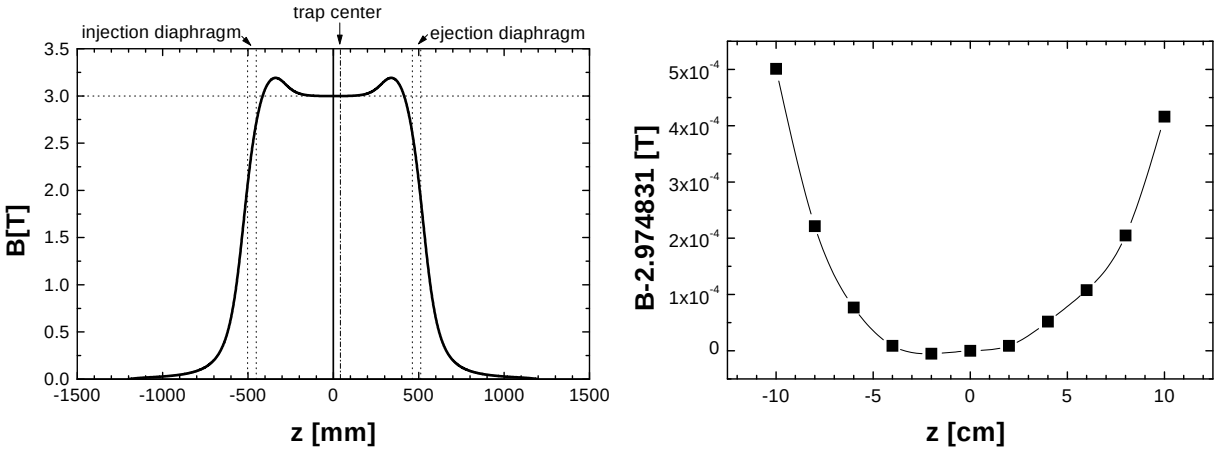

Figure 4.5: The magnetic field of the REXTRAP solenoid. **Left:** Field plot along the magnet axis obtained from calculations using the nominal current and geometrical data provided by the manufacturer. **Right:** Axial magnetic field strength measured at the magnet centre.

The field homogeneity at the centre of the magnet was specified to be axially over 20 mm less than 2 ppm and radially over 20 mm less than 10 ppm. This was checked using a NMR probe and found to be slightly violated (Fig. 4.5). However, this should not affect the operation of REXTRAP significantly and was therefore not reclaimed.

Although the stray fields of the magnet are smaller than 5 G outside the Faraday cage, they influenced the beam transport of the central beam line of ISOLDE remarkably, since this beam line runs a long distance nearly in parallel with the field lines. Therefore, it was necessary to shield this part of the beam line in order to prevent unwanted beam displacement.

4.3.3 Vacuum Tube Alignment

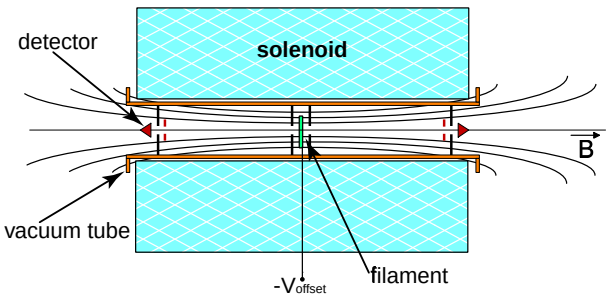

Figure 4.6: The set-up used for aligning the vacuum tube housing the trap structure with respect to the field lines of the REXTRAP magnet.

The manufacturer did not guarantee that the axis of the magnetic field is identical with the geometrical axis of the magnet case. Therefore, the vacuum tube inside the magnet bore is mounted with a special fixation allowing the alignment of the tube with respect to the magnetic field lines.

The alignment procedure was carried out using low energy electrons produced in the magnet centre. The experimental set-up of this procedure is shown in Fig. 4.6. The electrons emitted by a current-heated tantalum foil and accelerated by a small offset voltage of about -200 V must pass through two small pinhole at each side ensuring low emittance electron beams to both sides. The electrons travel along the magnetic field lines and hit segmented catcher electrodes at both ends of the solenoid. From the current distribution at the different electrode segments one can extract the position of

the vacuum tube according to the magnetic field lines and correct it until the electron current is maximised at the central segment. This procedure is very sensitive and it is assumed that the REXTRAP vacuum tube is adjusted better than 0.1 mm with respect to the magnetic field of the solenoid.

The REXTRAP magnet was delivered in 1996 and has been found very reliable and robust. It passed its first practical test soon after installation. The whole potential this magnet provides was shown by capturing one of the heaviest particle stored in a Penning trap device ever. Already at this early stage one major problem of REXTRAP arose. During the injection procedure, one has to bewail losses in the order of a few 10 %. However, once passed the entrance diaphragm, no further losses could be noted. This was confirmed by scattering experiments of visible photons (Fig. 4.7). Since the charge-to-mass ratio of the trapped particle tends to be close to zero, it was not possible to eject the super heavy in the common way by lowering the axial electrical potential. Instead, the magnetic field had to be lowered until it could be easily extracted. For the physics relevance of this unique event please refer to the included article from the IJTF at page 123.

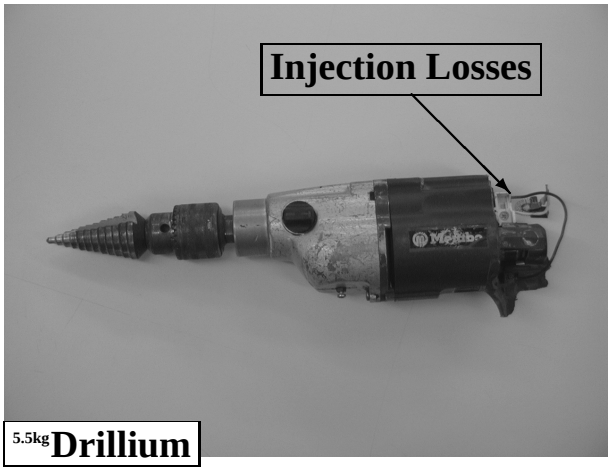

Figure 4.7: Spectrum of the first Super Heavy Particle of $^{5.5kg}$Drillium trapped in REXTRAP using visible photons after particle extraction. Losses that occurred during the injection process are marked.

4.4 The Electrode Structure

The electrode structure of the REXTRAP set-up is shown in Fig. 4.8. The system was cut into its three functional sections for a better visualisation. Every ion-optical element is named according to the name of the device which it is connected to.

The ejection and acceleration stage of REXTRAP is similar to the deceleration and injection part, except that it is mirrored with respect to the trap centre. The electrodes needed for these stages are fixed inside of vacuum tubes and chambers. These are connected to the tube inside the magnet bore and to support structures on ground potential. All these electrodes are machined of stainless steel. Alumina or glass ceramics (Macor) are used for the insulating parts. All electrodes but the kicker and steerer ones are cylindrical shaped. The latter consists of two pairs of parallel plates mounted in horizontal and vertical direction, respectively. Such a construction allows beam steering by application of different voltages to facing electrodes.

The middle section, the trap structure itself, consists of about 40 electrodes with a diameter of 50 mm. The centre electrode is four-fold split in order to generate electrical quadrupole and dipole fields in the trap centre. The electrodes are assembled in five sub-units (Fig. 4.9 top right). Ceramic spacers (Macor) between the electrodes provide electrical insulation. The insulators fit in special slots of the electrodes. These sandwich-like-structures are hold together by an outside support structure. All sub-units are combined to the complete trap structure, which

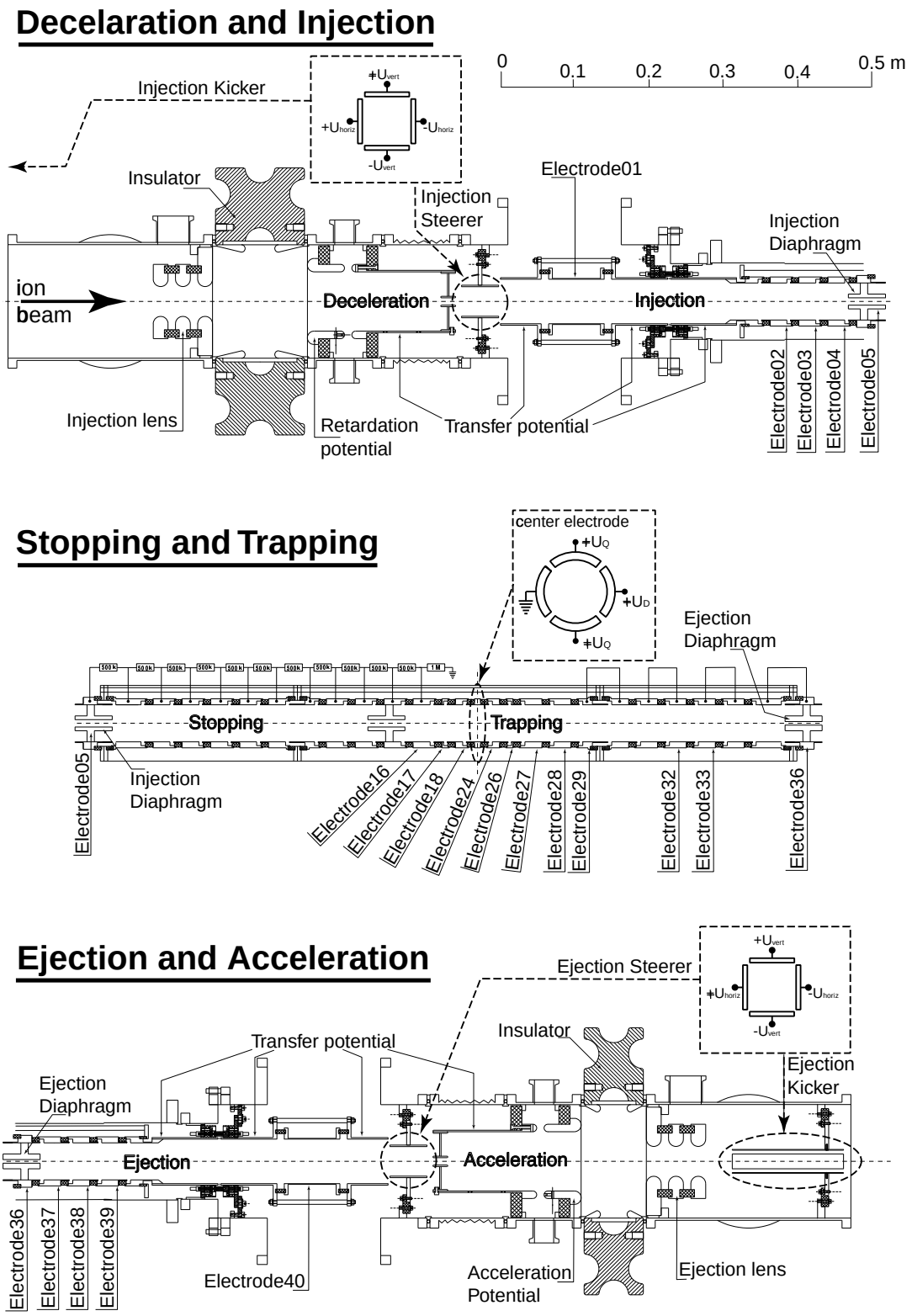

Figure 4.8: The electrode structure of the REXTRAP set-up. The linear structure of the system has been cut into three functional units for better visualisation. Every ion-optical element is named according to the name of the device which it is connected to.

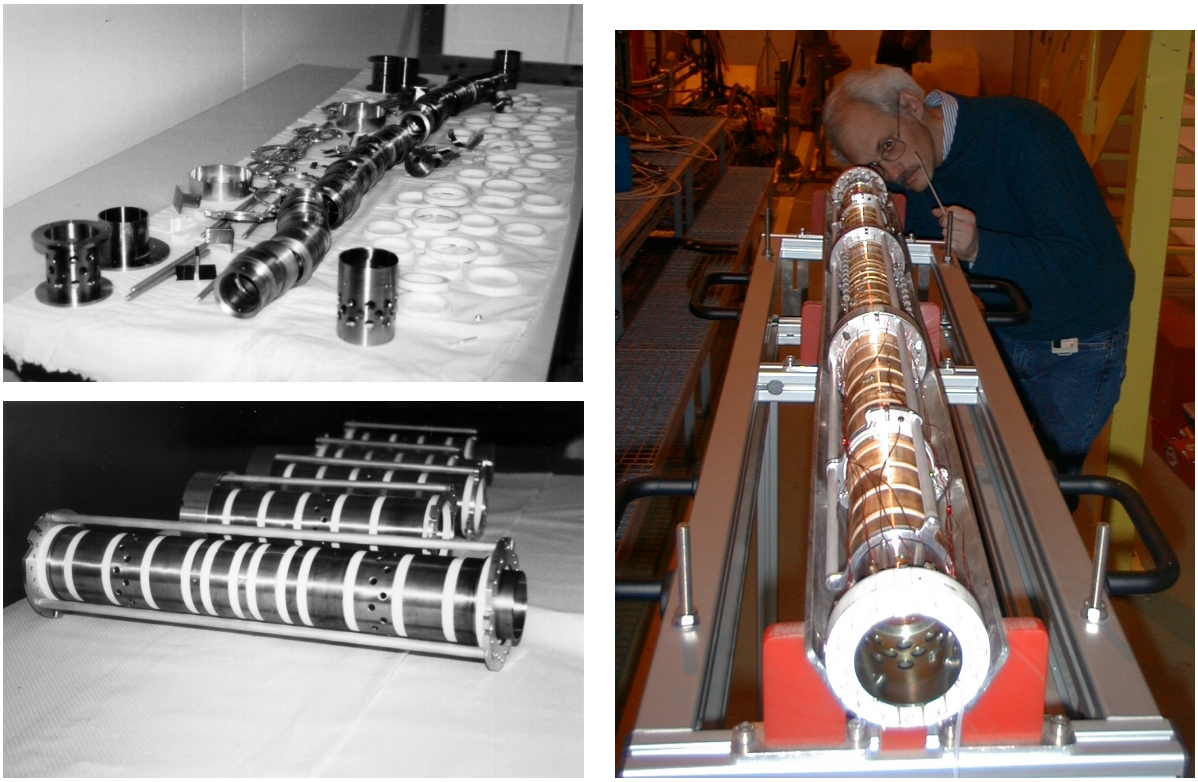

Figure 4.9: Photographs of the trap structure of REXTRAP. **Top Left:** The jigsaw puzzle of all parts waiting to be assembled. **Bottom Left:** The different sections complete assembled.
Right: The trap structure completely assembled and cabled resting at its support trolley.

has an overall length of about 1.30 m. The completely assembled and cabled trap is shown in Fig. 4.9. A large Macor disc is mounted at the outer parts on both sides of the structure which contains sockets for electrical connection. Similar counterparts with appropriate plugs are fixed in vacuum cross pieces. This “plug and play” system provides, in contrast to its computer equivalent, an easy maintenance of the complete system. Dismounting and mounting times of the system are typically in the order of ten minutes.

The trap structure is situated in the vacuum tube inside the bore of the solenoid. The tube material is a special stainless steel with an extra low magnetic susceptibility and has been especially checked not to contain magnetic enclosures. All trap electrodes are made from oxygen-free copper, which is gold-plated for an excellent finish quality. The use of materials with low magnetic activity, which also includes washers and screws for trap assembling, ensures a minimum of magnetic field distortions. Small aluminium wheels allow an easy insertion of the complete trap structure into the vacuum tube when the magnet is moved into its outside position.

4.5 Vacuum System

An schematic overview of the vacuum and gas inlet system of REXTRAP is shown in Fig. 4.10. The vacuum system that houses the ion optical part discussed above consists of a tube inside the bore of the solenoid and several vacuum chambers mostly of DN 160 ISO size connected to the

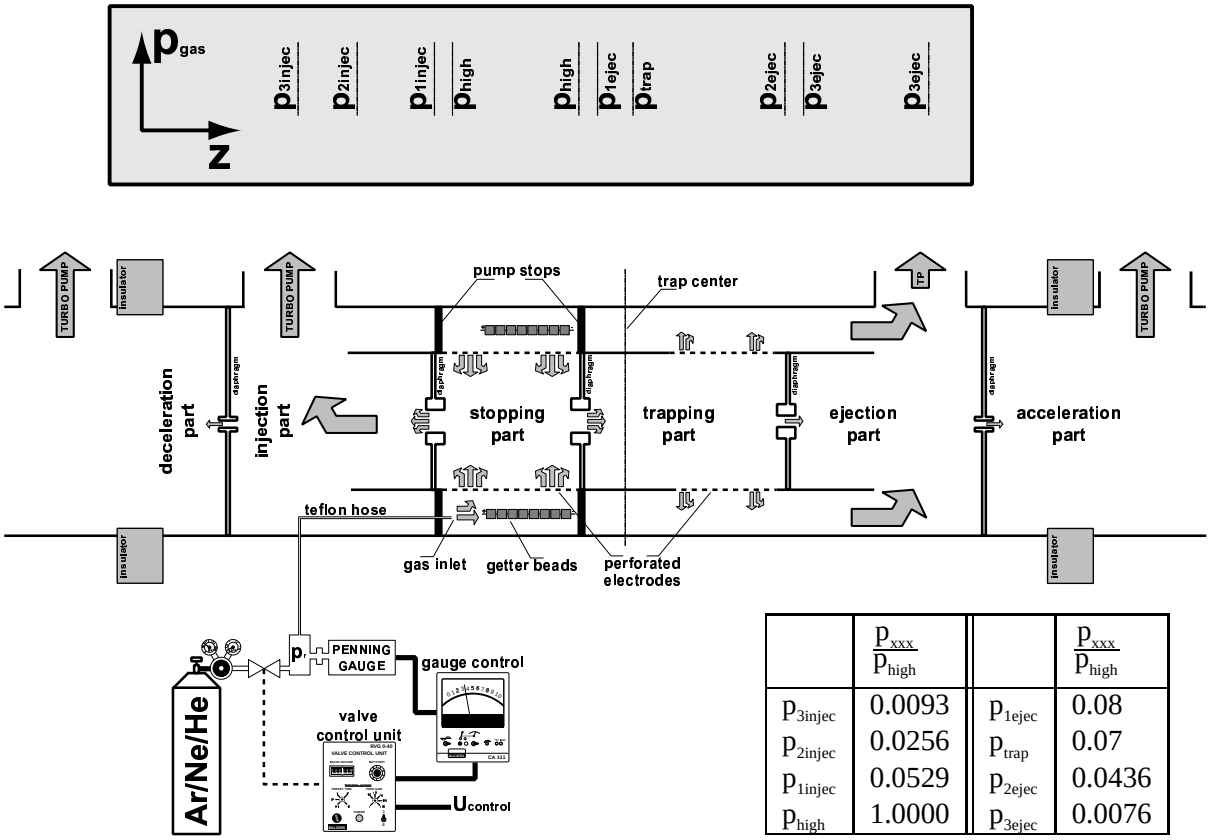

	$\frac{p_{xxx}}{p_{high}}$		$\frac{p_{xxx}}{p_{high}}$
p_{3injec}	0.0093	p_{1ejec}	0.08
p_{2injec}	0.0256	p_{trap}	0.07
p_{1injec}	0.0529	p_{2ejec}	0.0436
p_{high}	1.0000	p_{3ejec}	0.0076

Figure 4.10: Overview of the REXTRAP vacuum and gas inlet system. The molecular gas flow is indicated by arrows. The vertical axis has been stretched by a factor of 5 for a better visualisation. The table gives the buffer gas pressure normalised by the pressure in the stopping part for argon according to gas flow calculations. The points correspond to the scale shown on top.

tube. Two turbo pumps (Alcatel 400 l/s) at each side of the set-up are connected to REXTRAP. These pumps are backed by one 33 m^3/h roughing pump (Alcatel 2033D). The inner part of the trap is mainly pumped through the injection and ejection diaphragms. Differential pumping in between the trap sections is accomplished by a number of diaphragms, ensuring a good quality vacuum towards the ISOLDE beam line and the beam transport system to REXEBIS.

An important point of concern are gas impurities in the system, i.e. the rest gas pressure. It should be kept low, in order to minimise charge exchange reactions and ion losses inside the trap structure. The vacuum tube and the contained trap structure is only moderately bakeable (up to 80 °C), since the surrounding superconducting magnet is heat sensitive for obvious reasons. Furthermore, the inner part of the trap structure is only pumped through the differential pumping diaphragms, resulting in a relative high rest gas pressure. Beads of non-evaporable getter materials (SAES St 172 type) have been installed in the space between vacuum tube and trap electrodes to compensate this lack of pumping speed and to clean the buffer gas from impurities. This beads are normally activated by direct current heating after the system has been pumped down.

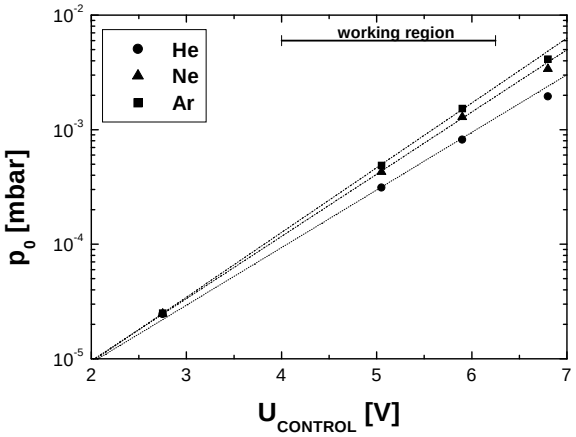

$$p_{0[\mathrm{mbar}]} = \exp\left\{\overline{U} \cdot U_{\mathrm{control\,[V]}} - \overline{p}\right\}$$

	$\overline{U}$	$\overline{p}$
He	1.158	13.912
Ne	1.250	14.053
Ar	1.301	14.177

Figure 4.11: The buffer gas pressure p_0 in the stopping part of REXTRAP as a function of the control voltage applied to the buffer gas control unit $U_{control}$ for different gases. In the working area this dependency can expressed according to Eq. (4.1) using the constants given in the table.

Buffer Gas Supply

The buffer gas pressure in the trap, namely argon, neon, or helium, is kept at a stationary pressure distribution by stabilising the pressure of a small gas reservoir outside. This reservoir is formed by a small vacuum T-piece. The buffer gas inlet is controlled via a needle valve connected to a pressure controller unit (Balzers RME010 + RVG040). The reading of a full-range pressure gauge (Alcatel P3C + CA111) fixed to the reservoir serves as input for the controller unit. The gas is guided to the inner part of the trap via a long teflon hose. This capillary tube releases the gas at the space in between the vacuum tube and the electrode structure. This outer part is shielded against injection and trapping part by diffusion barriers. Several electrodes of the stopping part are perforated, allowing the gas to diffuse into the inner trap part. The high buffer gas pressure in the stopping part provides the energy loss power necessary to trap the injected ions. The gas flow is directed towards the outer parts of the system following the pressure gradient produced by the vacuum pumps. Special attention must be paid to the pressure value in the trapping and ejection part. On the one hand it must be sufficiently high to ensure a suitable cooling performance and on the other hand it must be as low as possible to prevent ion re-heating during the extraction process. Therefore, several electrodes are again perforated for a better evacuation of the ejection part.

The buffer gas pressure in the gas reservoir is of course higher than the one in the trap. In order to understand the pressure distribution of the buffer gas in all stages, gas flow calculations have been carried out, assuming Knudsen flow in the teflon tube and molecular flow in all other stages [Umr97]. Additionally, the vacuum gauge readings have been corrected for different gas types. The results of the calculations are shown in several figures. In Fig. 4.10 the buffer gas pressure normalised by the pressure at the high pressure region at several points is shown. The distribution over the complete trap structure is given in Fig. 4.20.

An important point of interest is the buffer gas pressure in the stopping part of REXTRAP as a function of the pressure in the reservoir, or in other words as a function of the control voltage. The correlation of both values is given in Fig. 4.11. The linear approximation

$$p_{0[\mathrm{mbar}]} = \exp\left\{\overline{U} \cdot U_{\mathrm{control\,[V]}} - \overline{p}\right\} \tag{4.1}$$

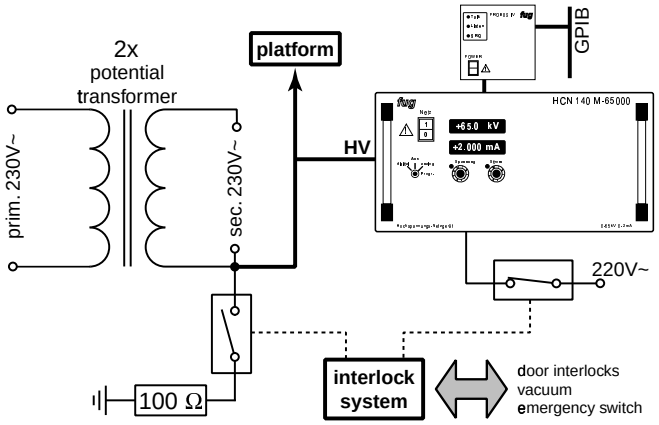

Figure 4.12: Schematic of the circuit used to provide line power and high voltage to the REXTRAP platform.

has been adjusted to the calculated points in order to describe the curve in the interesting working region. The constants $\overline{U}$ and $\overline{p}$ for the different gases can be found in the table of Fig. 4.11.

The gas flow conductance of the different parts of REXTRAP can be estimated only roughly. For instance the distance between the pumping stops and the vacuum tube was taken to be 0.1 mm. However, since the tube is slightly bent this value could easily be too small by a factor of two. Therefore, the pressure values obtained by the calculations should only be taken as approximations valid within a factor of two.

4.6 Electronics

4.6.1 The High-Voltage System

A schematic overview of the high-voltage and the line power supply for the high-voltage platform is given in the left part of Fig. 4.12. Two oil-free 2 kVA isolation transformer (PowerSources) deliver the line power needed at the platform. The platform potential is provided by a remote controlled power supply from fug (FUG HCN 140M-65000). The high voltage outlet is directly connected to the secondary winding of the potential transformer as well as to the high voltage platform. Several grounding band connections prevent any potential differences between installations on the platform. Varistors protect the electronic equipment from high-voltage transients caused by occasional spark overs.

A complex interlock systems which includes interlock contacts at the cage doors, for the platform grounding rods, for the vacuum system, and a master key ensures a safe operation of the high voltage platform and prevents the unwanted contact of trap operators and users with any kind of the high voltage installation. The system has been approved by the local CERN authorities in charge of the safety of HV installations.

Although stability and reproducibility of the HV power supply are specified to be better than 10^{-5} the manufacturer gives for the absolute calibration of the power supply a value of 0.5 %. The operation of the trap requires the calibration of the REXTRAP high-voltage power supply with respect to the accelerating voltage of the ISOLDE ion source. This has been achieved by a procedure described in Sec. 6.5.2. In conclusion, the voltage read back of the REXTRAP high-voltage power supply is at maximum 10 V off, which is an excellent value.

4.6.2 Electrode Supply

All static voltages needed for the beam optical elements like lenses and trap electrodes are provided by remote-controlled power supplies (FUG, CERN).

From the trap centre towards the trap exit all electrodes must be pulsed down for ejecting the ion bunches from REXTRAP. Voltages up to a few hundred volt must be switched in microseconds from one polarity to the other. There are two possibilities to achieve this. On one hand one can use fast high-voltage switches in connection with high-voltage powers supplies. A more elegant way has been chosen for REXTRAP illustrated schematically in Fig. 4.13.

An analog control voltage delivered from a channel of a self-made switch box is amplified by high voltage amplifiers (TREK Model 750/50, electronics lab (E-lab) University Mainz) depending on the response time and the dynamic range needed. The E-LAB amplifiers have a dynamic range of ± 100 V and a switching time less than 1 µs. They are used for the inner trap electrodes (electrode24...electrode29). For the outer electrodes (electrode29...electrode36), where the response time is uncritical, TREK amplifiers are used because of their higher dynamic range (± 750 V).

The self-made switch box contains 16 independent switching channels. Each channel consists of fast-switching stage followed by a fast line driver. The first bases on fast CMOS analog switches (TEMIC semiconductors DG 403). A TTL trigger signal switches the output voltage of this stage between two analog voltages. The line driver was added in order to drive resistive loads. A driving capability of ± 10 V into 50 Ω at switching times in the order of 1 µs is provided by a high speed, high power operational amplifier (National Semiconductor LM 6313).

The manipulation of the ion motion requires oscillating dipole and quadrupole fields. The radio frequency voltages are provided by two arbitrary function generators (Stanford Research Systems DS 345). The supply of the radio frequency to the four-fold split centre electrodes is schematically shown in Fig. 4.14. There are two disadvantage associated with this kind of "poor men" coupling. Firstly, one looses a factor of two in the amplitude of the rf field at the trap centre. Sec-

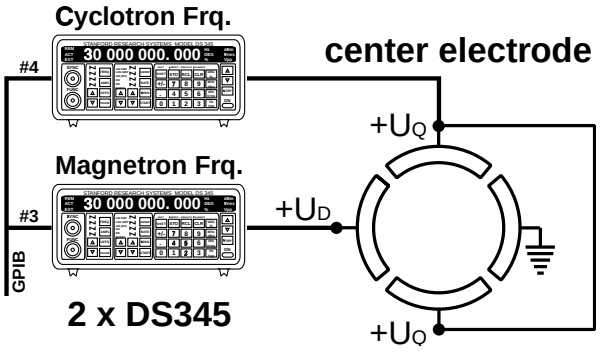

Figure 4.14: Schematic of the generation of rf dipole and quadrupole fields in the trap centre.

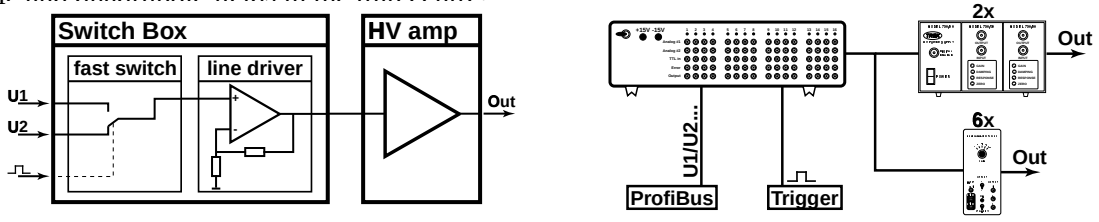

Figure 4.13: Principle of fast voltage switching for REXTRAP electrodes. **Left:** Principle sketch of one switching channel. **Right:** Schematic of the complete electrode switching system. The analog control voltages for each are provided by the PROFIBUS. The output of the switch box is controlled by TTL compatible trigger signals and finally amplified by a total of 6 E-lab and 2 TREK high voltage amplifiers.

ondly, one creates an additional DC offset at the trap centre. However, these drawbacks are by far compensated by its odds. This is on one hand the rather simple design of this circuit. In addition, it avoids broad band mixing stages and amplifiers, which are difficult in design and fragile during operation.

4.7 Beam Diagnostics and Ion detection

Several tools are available for the optimisation and diagnosis of the performance of REXTRAP and its team play with ISOLDE and the further stages of the trap system.

A standard ISOLDE diagnostic box is situated in front of REXTRAP at the end of the RA0 beam line. It contains a Faraday cup and a needle scanner which allow the beam intensity and spatial density of the incident beam to be determined.

For the study of beam injection and ejection two simple plates made of stainless steel can be inserted into the beam path. The plates are situated in between the gap of transfer potential and electrode01 and transfer potential and electrode40, respectively. They provide the possibility of current measurements in order to optimise the injection into REXTRAP. Although the construction is quite simple it ensures exact measurements since the electrical potential distribution at the position of the plates prevents the escape of secondary particles created by the ion impact, which normally falsify the current determination. The readout of the plates is achieved by pico-ampere meters (Keithley 485).

At the ejection side on ground potential three different beam diagnostic tools have been placed for the optimisation and characterisation of the ion pulses delivered by REXTRAP for the test measurements. A Faraday cup connected to a pico-ampere meter (Keithley 485) allowed the measurement of the beam current extracted from REXTRAP. For the recording of time-of-flight spectra a particle multiplier system and a commercial beam viewing system have been used. These set-ups are illustrated in Fig. 4.15.

An electron multiplier tube (Hamamatsu R2362), sometimes also referred to as particle multiplier, was used for numerous test measurements. Normally such systems are quite reliable and provide a wide dynamic range. Unfortunately this type of multiplier did not reach its performance with respect to gain. So it was only useful for the detection of rather high intensities and replaced by the Colutron beam viewing system. Although the multiplier was specified to work properly in the magnetic field of a few Gauss it is believed that its improper behaviour is caused by permanent damage caused by operation in the stray fields of the REXTRAP magnet.

The beam viewing system (Colutron BVS-2), which is mounted an a flange with

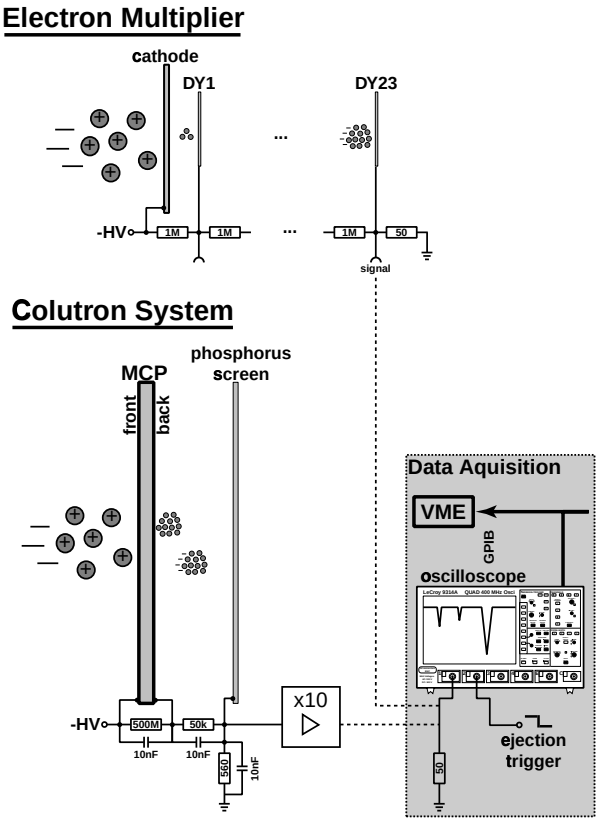

a view port, consists of a micro-channel plate with a phosphor screen behind. This system an deliver pictures of the spatial density of ion beams. The fluorescent light of the phosphor screen originated from secondary electrons emitted by the MCP after ion impact can be viewed through the window by a CCD camera. However, the lack of a triggerable camera and frame grabber card made this operation mode impossible during the work described here. The MCP was used only to record time-of-flight spectra of extracted ion bunches from REXTRAP.

The signals coming from the electron multiplier can be grabbed either by a standard oscilloscope (LeCroy 9314A) or a multi-channel scaler (Stanford Research Systems SR 430). The latter is most suitable for low count rates up to a few ions per pulse. At higher count rates the scaler starts to miss events due to the limited bandwidth of its discriminator stage. Therefore, it was used only occasionally.

4.8 The Control System

The REXTRAP control system bases on a system originally developed for the ISOLTRAP experiment [Emm93, Roh93, Bec97]. The central position is hold by a VME-bus computer running the real-time operating system OS/9. A graphical user interface is provided by several programs running on standard WINDOWS based personal computers, which communicate with the VME-bus computer via network connections.

An overview of the control system as it is used for REXTRAP is shown in Fig. 4.16. In the following it will be shortly described, including aspects concerning hardware as well as software.

4.8.1 Hardware

All parameters necessary for the operation of REXTRAP are remote controlled via three different channels. All intelligent devices, i.e. devices which need a certain amount of programmed information, are managed by a General Purpose Interface Bus (GPIB). A fieldbus system, i.e. a PROFIBUS system, serves for equipment which require less attention. Logical trigger signals coordinate the team play of all components of the system.

GPIB

As already mentioned, the GPIB controls all intelligent devices. This includes the Memory module responsible for timing (see paragraph trigger signals further down), the Probus control unit for the high-voltage power supply, the arbitrary function generators, the pico-ampere meters, the oscilloscope, and the multi-channel scaler. The bus transfers programming and status information as well as recorded data. It is controlled by VME-bus interface card (Janz Electronic). A fibre optic link system (GPIB 140-A, National Instruments) bridges the potential difference to the high-voltage platform.

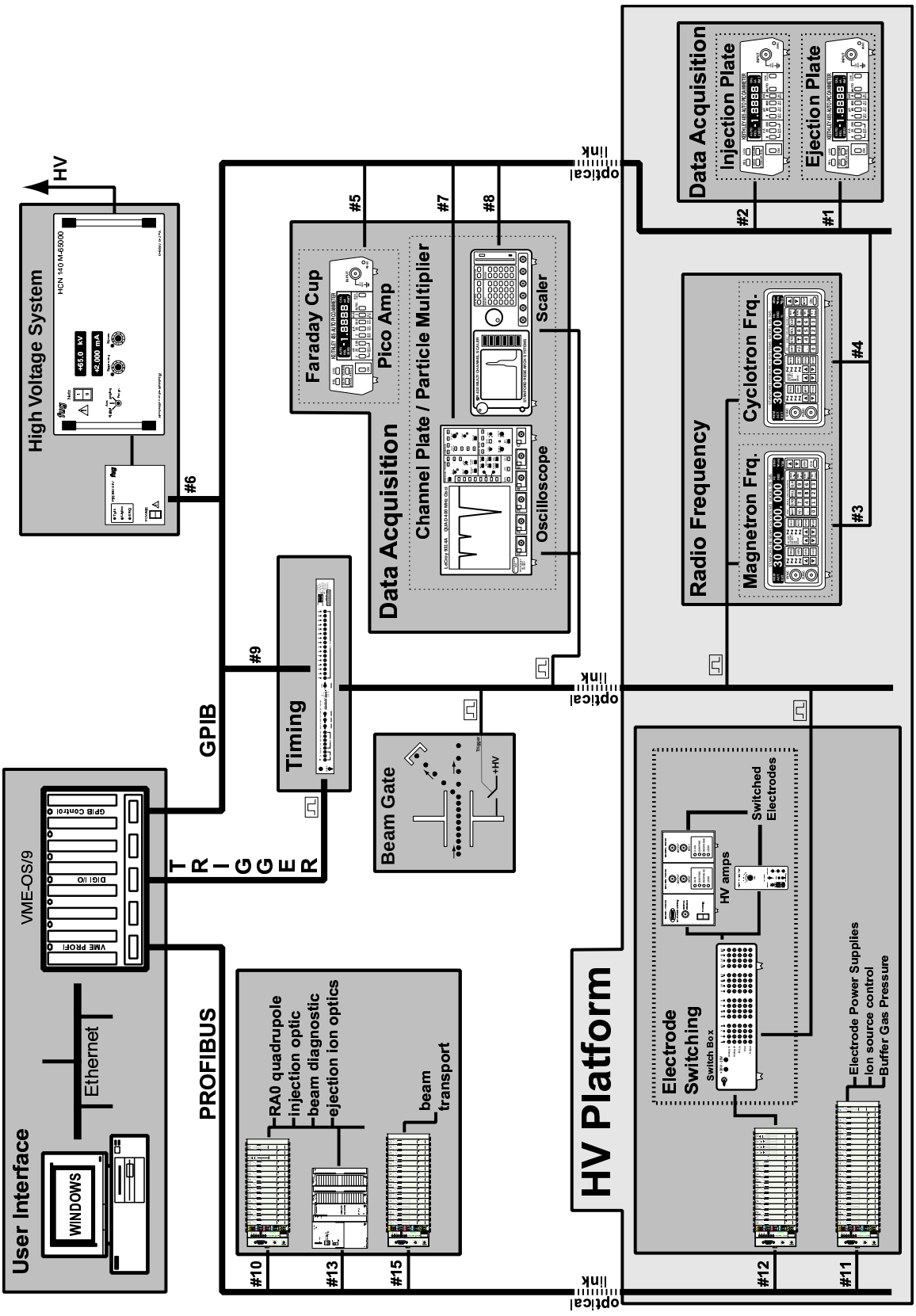

Figure 4.16: Overview of the REXTRAP control system.

PROFIBUS

PROFIBUS is a vendor-independent, open fieldbus standard developed for a wide range of applications in manufacturing, process and building automation [Pro00]. The bus protocol PROFIBUS-DP, chosen for the application at REXTRAP, is optimised for high speed communication and inexpensive hookup. It is designed especially for communication between a control system and distributed input/output devices matching exact the requirements for most of the larger physics experiments.

An overview of the topology of the PROFIBUS, designed for REXTRAP, is given in Fig. 4.17. The system consists of a bus master which determines the data communication on the bus and five slave units (Siemens ET200M with SIMATIC S3 and WAGO I/O system), equipped with DACs, ADCs, logical in and outputs, as well as serial interfaces, which allocate a total number of about 180 control signals. The slaves are spread over a large area of the experimental hall or are placed on the high voltage platform.

The PROFIBUS transmission bases on the RS 485 protocol, i.e. the bus signals are transported by shielded twisted pair cables to all slaves at ground potential. In order to bridge the potential difference to the high voltage platform, an optical link system consisting of an optical link module (OLM, Siemens) and an optical link plug (OLP, Siemens) connected via an plastic fibre loop is used. The transmission technology ensures simple cost-effective cabling. The used equipment allows data transfer rates up to 1.5 MBit/s, a performance which is far beyond the experimental demands.

The bus is controlled by a VME-PROFI master card (Dorsch Mikrosystem) [Chr98]. This card has its own CPU which handles the complex PROFIBUS protocol. The VME-bus system can read or write the I/O-bytes of the distributed peripheral stations by reading or writing of the dual ported memory of the card which is mirrored to the VME-bus memory. Low level debugging, configuration of the PROFIBUS, as well as inspection can be done using the WINDOWS based program DPKonfig [Chr96]. It interacts with the VME-PROFI card via an internal RS 232 interface or via TCP/IP connection. For this purpose several demon programs have been installed on the OS/9 system.

In order to integrate the PROFIBUS in the existing software package, several service programs as well as a library containing low level functions and procedures needed to implement high level code have been programmed.

REXTRAP and REXEBIS establish a functional unit with respect to ion preparation for the REX-ISOLDE LINAC. Therefore, in an early design phase both systems it has been considered to have a common control system. However, during the commissioning phase of each systems it turned out to be useful to have two independent sub-systems. When the tests of both REXTRAP and REXEBIS are completed both systems will be merged again.

The REXEBIS-PROFIBUS has been found very reliable since its implementing. It needed nearly no maintenance and during its operation period of about three years only one analog output module broke due to a high voltage spark.

Trigger Signals

The coordination of the trap operation cycle is provided by TTL-trigger signals. A programmable logical pattern generator, the so-called memory module (E-LAB University Mainz), creates the appropriate logical pulses. The logical pattern is programmed via the GPIB interface of the

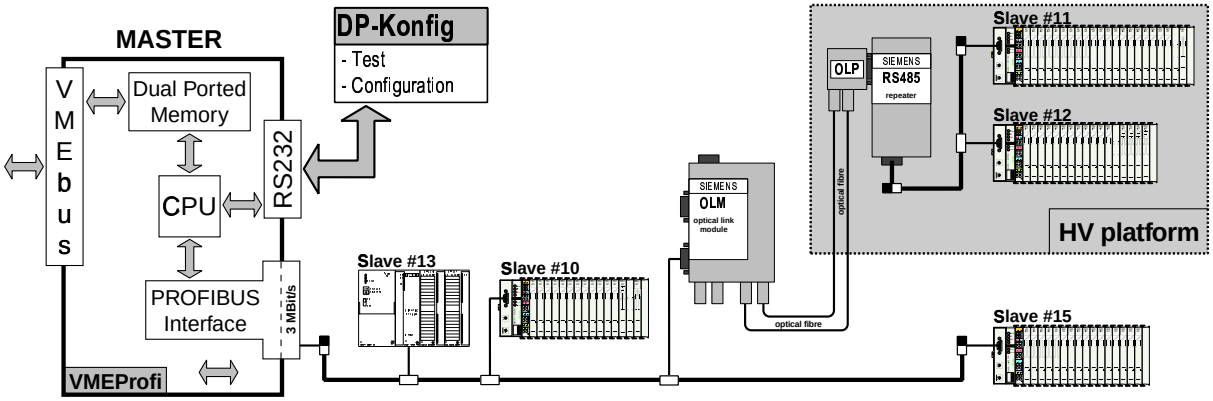

Figure 4.17: Topology of the REXTRAP PROFIBUS.

module. Synchronisation with the VME-bus processes is ensured via a VME-bus digital I/O interface card (Janz). Devices which demand trigger pulses are the beam gate in front of the trap, the function generators, and the data acquisition (the oscilloscope and the multi-channel scaler). A special optical link system has been developed to bring the fast trigger signals to the high voltage platform. They are based on optical receiver and transmitter components from Harting [Har98a, Har98b, Har98c].

4.8.2 Software

In order to provide a stable and reliable control system, which can be easily integrated in the complex accelerator chain of REX-ISOLDE, tremendous programming work has been carried out both on the WINDOWS user interface as well as on the VME computer side. This included the porting of the complete source code of the VME project to a cross compiler platform, bug fixing, and integration of new hardware. For the first time the system has been integrated in a well defined tree structure. The cross compiler system Hawk [Haw98] creates a complete and easy-to-use development environment, which should reduce the period of vocational adjustment for newcomers drastically. The description of all changes and additions is wide beyond the scope of this thesis and will be given in detail in [For01].

The following section will give a short introduction into the software project. Only very basic aspects can be treated. More information can be found in the references mentioned above.

An overview of the software part of the REXTRAP control system is shown in Fig.4.18. Both the PC as well as the VME side are shown. Inter process communication between the programs on PC and VME side is provided by a TCP/IP based network protocol.

VME Project

The real trap operation is controlled by a number of programs running on the VME-bus computer. This includes *DevServer*, *ProcServer*, and *DataServer*. They are coordinated by the *SuperVisor* process. Furthermore, it administrates a number of project tables (*DevTable*, *ProcTable*, *DataTable*, *ConnTable*), where important run-time information about the status of the system are stored and where they can be accessed by other processes. Real hardware equipment is represented by device drivers. Such a driver has information about the hardware addresses,

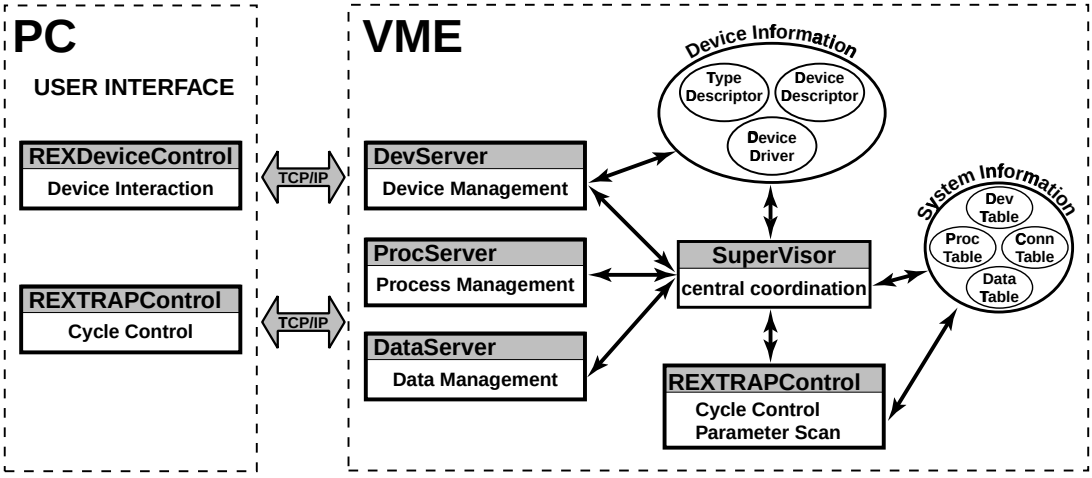

Figure 4.18: Overview of the software project of the REXTRAP control system.

initialisation and limit values as well as how to access the functionality of the equipment. All devices are managed by the *DevServer*. The *ProcServer* demon is responsible for correct initialisation and termination of all processes connected with the control system. The *DataServer* manages large portions of memory, so-called data modules where processes can store important data and information. Inter process communication is provided by a complex messaging system. The process *REXTRAPControl* controls the trap measurement cycle.

User Interface

Most of the functionality of the REXTRAP control system can be directly accessed via utility programs on the VME-bus computer. However, for a better visualisation and in order to have a well known system for new and unexperienced users a WINDOWS based graphical user interface exists. It consists of two programs. The program *REXDeviceControl* manages all static devices. `REXTRAPControl` at the PC side provides a well structured interface for the control of the trap cycle. Beside the possibility of controlling the time structure of the cycle it allows parameter to be scanned and the visualisation of the acquired data.

4.8.3 The Control of the Trap Timing

The control of the trap cycle includes hardware as well as software. The interaction between both will be shortly described in the following.

The principle of controlling the trap timing is illustrated in Fig. 4.19.

REXTRAPControl is started by the *SuperVisor* process after request by the user. The first action of the program is to set the time structure of the desired cycle in the memory module. For optimisation of the trap performance it is possible to scan parameters of certain devices. These devices are initialised in the second step. Now the control is handed over to the *RexMemHandler*. The signal `StartEnable` is generated that starts the memory module. `StartEnable` is cleared after receiving the signal `StartDone`. This avoids unwanted re-triggering. Now, the memory generates its pattern of trigger signals. After finishing the signal `CycleFinished` is generated. This re-activates the *RexMemHandler*. If the number of Memory cycles

has not reached its desired value, the Memory is restarted. Otherwise, the control is given back to *REXTRAPControl*. In this case data from the data acquisition system are written to a data module, where they can be accessed from the data evaluation program on the PC side. When the complete scan is finished the user is notified via the appropriate PC programs.

4.9 Basic Operational Procedures of REXTRAP

4.9.1 Functional Overview

After passing the beam gate in front of he system the incident ion beam reaches the REXTRAP setup. In the following the ion optical functionality of the different stages of REXTRAP is discussed. The denomination of the different parts and electrodes corresponds to the ones used in Fig. 4.8.

Deceleration and Injection

The incoming ion beam is focused through a first diaphragm by a lens system formed by the retardation potential and the first lens at transfer potential. The ion beam has now an energy corresponding to the transfer potential. After this first focus the expanding beam is refocused with an einzel lens consisting of electrode01 and two electrodes at transfer potential. The potential at electrode01 is chosen in order to focus the beam towards the injection diaphragm. Longitudinal ion energy is partly transfered to radial energy while travelling trough the fringe fields of the solenoid, referred to as radial energy pick up. There a part of the magnetic field vector is perpendicular to the direction of movement of the ion. This results in Lorentz force which is therefore responsible for the energy transfer. At the same time the ions have to climb the potential wall at the trap entrance, created by electrode02 to electrode05. The longitudinal energy spread has now reached its maximum, mainly determined by the ion species and the parameters of the incident beam. Typically the values range from 30 eV to more than 100 eV. In order not to reflect the beam partly, the potential applied to electrode05 has to be lower than the corresponding minimum axial energy of the incident ion beam. After this point, when the

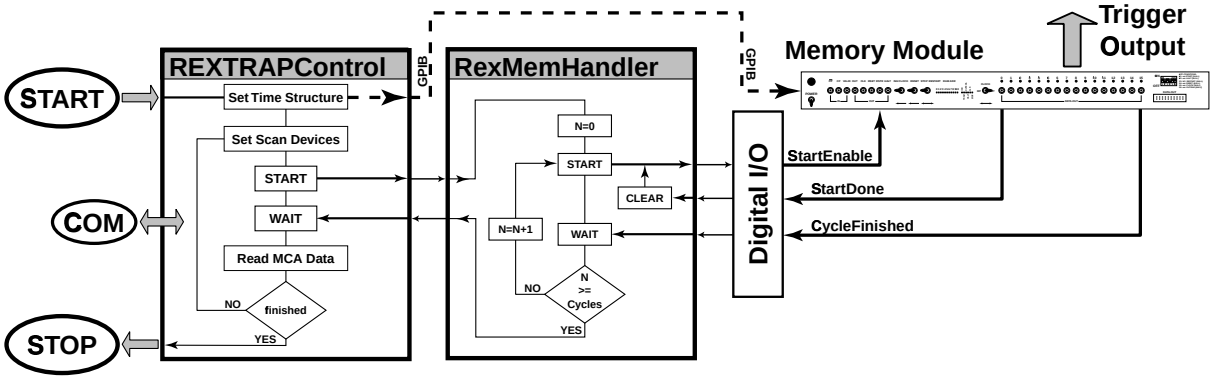

Figure 4.19: Overview of the part of the hardware and software that manages the trap cycle.

ions have reached the strong magnetic fields, they follow the magnetic field lines guiding them to the central region of the magnet.

Stopping and Trapping

The central part of REXTRAP is divided into two subunits. The stopping part with its high buffer gas pressure provides a sufficiently high energy loss to trap the ions. The pressure in the trapping part where the potential minimum is situated is kept lower in order to ensure good cooling performance and to prevent heating of the ions by collisions with the buffer gas, when they are ejected out of the trap. After injection the ions are allowed to cool during a few oscillations in the trap centre. There they are exposed to the radio frequency field used for the rf-sideband cooling (see Sec. 3.3.2). After finishing the cooling procedure the voltages of electrode24 to electrode36 is pulsed down in order to accelerate the ion bunch towards the trap exit.

Ejection and Acceleration

As already discussed in Sec. 4.4. The ejection and acceleration stage of REXTRAP is similar to the deceleration and injection part, except that the ions pass through in opposite direction, i.e. after passing the extraction diaphragm the ion pulse is refocused by the einzel lens system formed by transfer potential and electrode40 towards the final acceleration.

4.9.2 Operational Parameters

REXTRAP has been operated with two beam energies of the incident ion beam. When operating with the test ion source a beam energy of 30 keV has been chosen in order to avoid frequent spark-overs, whereas for on-line measurements with ISOLDE an ion energy of about 60 keV was used. Table 4.2 gives a compilation of all trap operation parameter but the timing for this two cases. For the different beam energies remarkable differences can be found for the following voltages: RA0 quadrupole, retardation potential, injection kicker, and acceleration potential, electrode05. The different values for electrode01 and electrode40 are due to the fact that different ion masses have been used to obtain these optimised settings. The argon buffer gas pressure in the high pressure area was $p_0 = 0.9 \cdot 10^3$ mbar for the off-line case and $p_0 = 1.2 \cdot 10^3$ mbar for the on-line case.

The voltages and buffer gas distribution along the trap axis resulting from applying the values for the on-line measurements are shown in Fig. 4.20.

4.9.3 Timing

For the exact coordination and trap synchronisation four trigger signals are necessary. They control the switching of the beam gate, the switching of the output of the arbitrary function generators for dipole and quadrupole excitation, and they trigger the pulsing of the potentials at the trap exit for ion extraction.*

*The latter consist in fact of two signals, which are delayed by 13 µs in order to compensate the different rise times of the high-voltage amplifiers (compare Sec. 4.6.2). However, thats of no importance for the understanding

device name	OFF-LINE operation		ON-LINE operation	
IonSource	heating:	4.6	—	
	offset:	300.0	—	
HV		30000.0		59730.0
TransferPotential		−1500.0		−1500.0
GasInlet		5.5		5.75
RA0.QP20		1355.0		2150.0
RA0.QP30		1812.0		3130.0
RA0.QS40	quad:	1292.0	quad:	2205.0
	offset:	600.0	offset:	300.0
	horiz:	80.0	horiz:	10.0
	vert:	−30.0	vert:	30.0
InjectionLens		−500.0		0.0
RetarationPot		−2900.0		−6500.0
InjectionKicker	horiz:	495.0	horiz:	815.0
	vert:	0.0	vert:	80.0
InjectionSteerer	horiz:	0.0	horiz:	50.0
	vert:	50.0	vert:	5.0
Electrode01		−135.0		−270.0
Electrode02		−2000.0		−1800.0
Electrode03		−1400.0		−1400.0
Electrode05		285.0		185.0
Electrode16		100.0		80.0
Electrode17		42.0		42.0
Electrode18		14.0		14.0
Electrode20		0.0		0.0
	injection	ejection	injection	ejection
Electrode24	14.0	−3.5	14.0	−3.5
Electrode26	42.0	−6.0	42.0	−6.0
Electrode27	80.0	−9.2	80.0	−9.2
Electrode28	100.0	−13.6	100.0	−13.6
Electrode29	120.0	−18.0	120.0	−18.0
Electrode32	185.0	−31.4	185.0	−31.4
Electrode33	212.0	−35.8	212.0	−35.8
Electrode36	310.0	−50.0	310.0	−50.0
Electrode37		−300.0		−300.0
Electrode38		−1000.0		−1000.0
Electrode39		−2000.0		−1800.0
Electrode40		−80.0		−380.0
AccelerationPot		−5000.0		−10000.0
EjectionKicker	horiz:	0.0	horiz:	0.0
	vert:	50.0	vert:	60.0
EjectionSteerer	horiz:	−130.0	horiz:	−50.0
	vert:	−25.0	vert:	−10.0
EjectionLens		−500.0		0.0

Table 4.2: Typical operational parameters of REXTRAP for a 30 keV ion beam (off-line operation) from the test ion source and for a 60 keV ion beam from ISOLDE (on-line operation). All voltages are given in volts.

There are a number of different timing schemes which have been used during the commissioning phase of REXTRAP. They are shown in Fig. 4.21 and will be described in the following. The enumeration of the following list corresponds to the one used in the figure.

(a) The beam gate is opened for the collection time T_{coll}, allowing an appropriate number of ions to enter the trap. A short waiting time T_{wait} has been introduced in order to ensure a similar conditions if T_{coll} changes over a wide range during a series of measurements. Afterwards the ions are centred by rf sideband cooling for a period T_{center}. Finally, they are ejected by opening the exit side of the trap for a period T_{ex}. This is one of the standard time schemes used. It has been employed for the determination and optimisation of important parameters of REXTRAP.

(b) This time scheme is similar to (a), except that after ion centring, dipole excitation for a period T_{excite} is carried out. This allows magnetron and cyclotron frequency as well as the appropriate amplitudes for the manipulation of the ion motion via rf dipole fields to be determined.

(c) In contrast to case (b) ions are recentred for a period $T_{recenter}$ after dipole excitation for a period T_{excite}. With this time scheme it is possible to clean the trap from unwanted ion species, since the ion centring process is mass dependent.

(d) This case is similar to (c) except that ion centring and dipole excitation take place at the

of the following discussion and will be neglected.

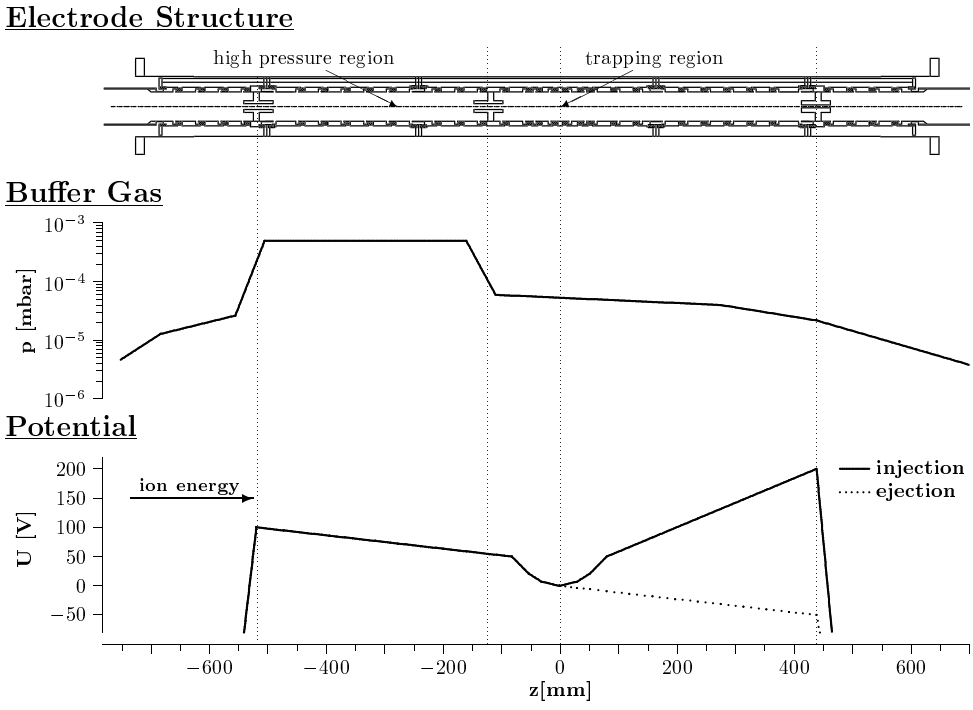

Figure 4.20: Electrode structure, buffer gas pressure distribution inside of REXTRAP, and potential along the trap axis. The potential is given relative to the platform potential.

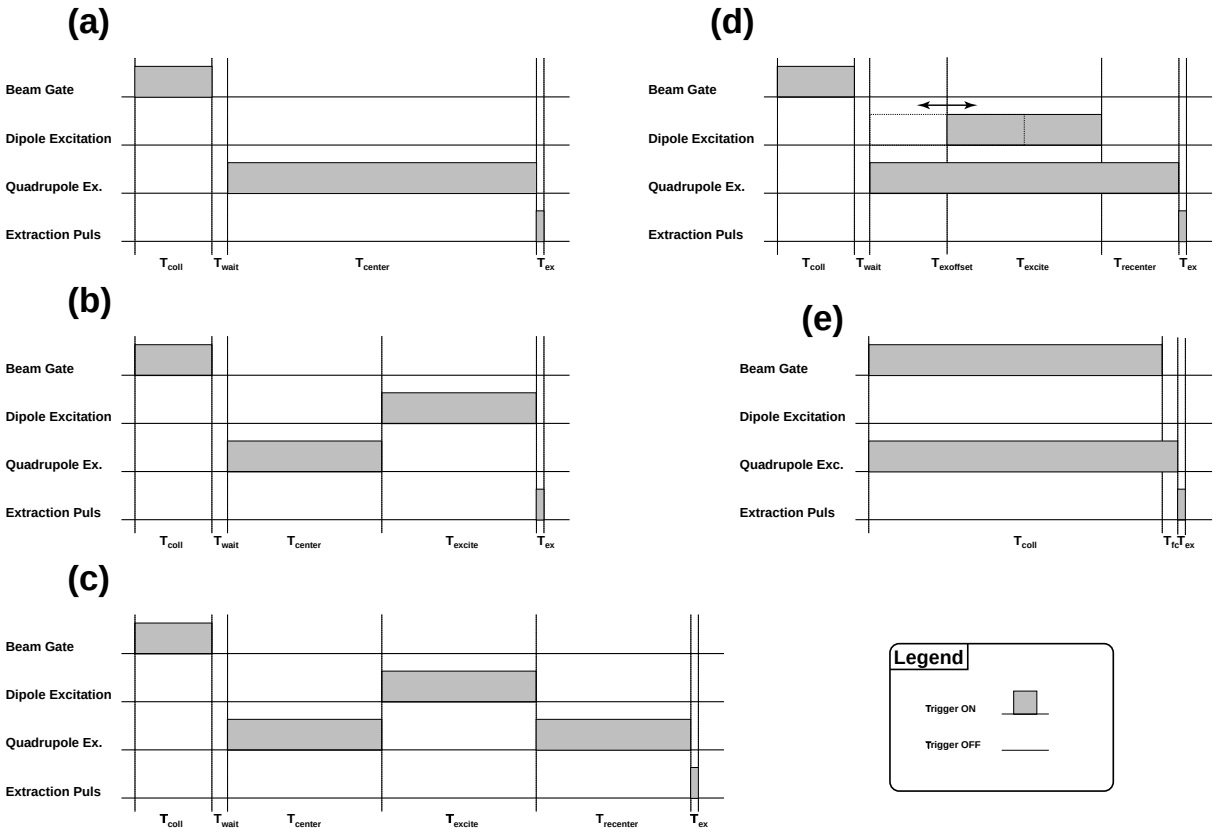

Figure 4.21: Schematic overview of the timing schemes used during the commissioning of REXTRAP. The different cases are discussed in the text.

same time. It has the advantage that overall time the ions have to spent in the trap is significantly reduced.

(e) Ion injection (T_{coll}) and cooling ($T_{coll}+T_{fc}$) takes place almost simultaneously. This time scheme has been rarely and only used for weak ion beams.

The individual times varied particularly over a wide range. Especially the collection time T_{coll} ranged from 1 µs to 100 ms. It depended on the strength of the incident ion beam and the desired number of ions to be injected into REXTRAP. Typical centring times T_{center} have been in the order of 10 to 40 ms, whereas for ion decentring excitation periods T_{excite} of 5 to 10 ms have been sufficient.

5 Simulation of REXTRAP Parameters

In general the features and the performance of an ion-optical system can be determined theoretically by employing matrix optics up to a sufficiently high order or via ray-tracing in numerically determined fields. Especially for larger systems it is obvious that copious simulations describing the system as realistic as possible should be done in the final stages of the construction process. They may circumvent later efforts in pretended error finding, redesigning, and expensive hardware work.

The main parts of REXTRAP have been constructed on the basis of calculations, estimations, and projections by my colleagues Friedhelm Ames, Ismael Martel-Bravo, and Harald Raimbault-Hartmann using the experiences gained with the cooler trap of the ISOLTRAP experiment [Rai97]. However, during the commissioning phase of the trap the efficiency stayed behind the expected value. In order to understand this phenomenon a complete set of "more realistic" and detailed simulations have been carried out. It turned out that indeed these calculations describe the experimental performance of REXTRAP very well. If done beforehand they could have influenced its design significantly. Now they may serve as input parameters for further improvements. In the following simulation will be presented which cover acceptance, efficiency, cooling performance of REXTRAP, as well as properties of the extracted ion bunches.

5.1 General Introduction

There are numerous codes for the simulation of particle optical systems. These codes fall into two categories. The matrix codes compute Taylor expansions to describe the action of the system on the phase space. They are very useful for the understanding of beam line like systems, where each element can easily be represented by a matrix. These matrices are combined to an overall transfer matrix, characterising the ion-optical properties of the system. Such codes are usually very fast and the expansion coefficients often provide a detailed insight of the system. However, they fail to describe special effects, e.g. dissipative forces or simple ion loss at electrodes. The other category of codes includes ray tracing codes which use numerical integrators to determine the trajectories of individual rays through numerically determined electromagnetic fields. Their advantage is that the electromagnetic fields produced by the electrodes can be fully taken into account even for complex configurations and effects like damping can easily be integrated.

For the simulation of the properties of REXTRAP and the beam transport from ISOLDE both approaches have been used. The ISOLDE beam line system has been analysed by the matrix systems COSY INFINITY [Ber00] and GIOSP [Wol87]. The trap and accompanying optics had been investigated with the program SIMION [Dah95] and a self-made software package. The latter are based on the ray tracing approach.

The commercial available program SIMION is a very powerful tool for calculation and visualisation of particle rays through arbitrary two and three-dimensional electromagnetic systems. It is well suited for a first look at an ion-optical system. However, very detailed simulations and

calculations are not manageable if a huge amount of ion trajectories needs to be calculated and additional forces be taken into account. Reasons are that user programs may have to be included in a FORTH like programming language which is rather difficult to learn and to maintain, limited in functionality, and slow in execution. It was therefore necessary to develop a dedicated program package which will be lined out in the following.

5.2 The Program Package

A SIMION like approach is in principle very favourable to trace rays through the desired systems. Such an ansatz had already been proven its excellence by the simulation of a large Paul trap as it was used in the ISOLTRAP experiment [Sch98]. However, that code was tailored for this special purpose only. Nevertheless, it served as a useful basis for the design of the new program package. This package consists of the main programs *IonFly* and *PennDamp*, as well as a number of auxiliary routines and tools. The programs are of object-oriented design This prevents to a large extent problems that occur in software that evolves over many iterations.

One of the best implementations of object-oriented programming is the C++ language [Str98]. Consequently, all programs have been coded in that language.

In order to carry out the extensive calculations as required in the present work the use of a batch service has been inevitable. A total of more than 10 000 jobs running from less than one minute up to several days have gulped a total CPU time of nearly four years on the CERN public batch service LXBATCH. The LXBATCH computer farm consist of about 100 INTEL Pentium II 600 MHz dual processor computer systems running LINUX as operating system and lsf as batch scheduler.

5.2.1 *IonFly*

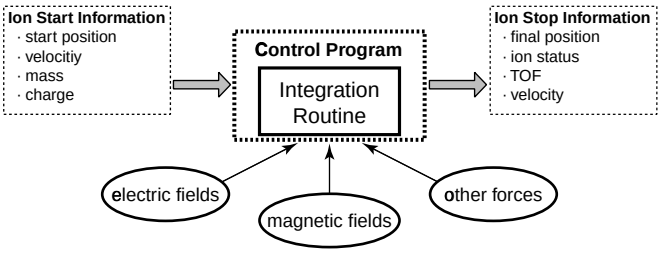

Figure 5.1: Flow chart of the program *IonFly* used for simulation of ion trajectories through the REXTRAP system.

A flow chart, which illustrates the working principle of the program *IonFly*, is shown in in Fig. 5.1. *IonFly* is based on a Runge-Kutta integration routine which numerically solves the equation of motion for an ion experiencing several forces simultaneously.

Following the SIMION concept the program incorporates the concept of a workbench. A workbench is an imaginary volume in space, where ion manipulating instances (for example an einzel lens) are placed. Instances are defined by their size, their place in the workbench, and their action of ions. In comparison to SIMION, where instances are always associated with a potential array, *IonFly* is more universal, i.e. every action on the particles are represented by instances that can be superimposed. These instances can be for instance a damping force or ion-ion interaction. The implementation of a new type of instances only requires the coding of some basic functions like initialisation and the action on an ion.

Computation of Ion Trajectories

The trajectories of a set of N ions is simply obtained by the integration of the equation of motion for every ion

$$\frac{\mathrm{d}\mathbf{r}_i}{\mathrm{dt}^2} = \frac{\mathbf{F}_i}{\mathrm{m}_i} \qquad i = 0 \ldots \mathrm{N} \; , \tag{5.1}$$

where $\mathbf{r}_i$ denotes the position of the ith particle. The force $\mathbf{F}_i$ incorporates all forces, e.g. Coulomb and Lorenz force, acting on that specific particle. This set of second order differential equation can be simplified by introducing the velocity $\mathbf{v}_i$. One obtains the following first order equations

$$\frac{\mathrm{d}\mathbf{r}_i}{\mathrm{dt}} = \mathbf{v}_i \qquad \text{and} \qquad \frac{\mathrm{d}\mathbf{v}_i}{\mathrm{dt}} = \frac{\mathbf{F}_i}{\mathrm{m}_i} \qquad i = 0 \ldots \mathrm{N} \; . \tag{5.2}$$

Although the number of equations has doubled it is now directly accessible for standard integration methods. In the case of *IonFly* a Runge-Kutta method of fourth order with adaptive step-wise error correction according to ref. [Pre97] has been implemented.

The major task during the integration of the equation of motion is the interpolation of the electric and magnetic fields at the actual point of integration to calculate the forces on the particle.

Computation of Electric Fields

The information about the electric fields are stored in so-called potential arrays. They represent a uniform grid overlaid the system of interest. The resulting matrices are two or three dimensional depending on the symmetry degree of the structure. The electric field at a certain point is obtained by interpolating between potential points of the grid. The complex interpolation routine has been adapted from ref. [Dah95, Pre97].

The potential arrays have been created with SIMION. The electrode structure is expressed in a special geometry programming language that comes with that program. In doing so the electrode surfaces are defined by a set of fixed potentials in a potential array. The potentials at all points surrounded are then successively approximated by a "relaxation" procedure, called "refining", i.e. by solving the Laplace equation. The generated files containing the field information serve as input parameter for *IonFly*.

• Off-line ion source

The mechanical set-up of the REXTRAP test ion source has been discussed in Sec. 4.2. The complicated geometrical shape of the ioniser demands a high resolution grid to reflect the electrical field distribution at the ion start point as good as possible. Therefore, the complete structure was modelled with a resolution of 0.1 mm. The SIMION geometry file used can be found in the appendix (Fig. B.7).

• REXTRAP electrode structure

The case of REXTRAP is a little bit more complicated. The internal capacity of SIMION is limited to 40 electrodes for the refining procedure. Thus the electrode structure of REXTRAP

can not be refined in one session. Instead, it has been divided into several sub-tasks for the refining procedure and joined again for the calculations. Natural points of division are the five diaphragms since there is no electrical field inside (see Sec. 4.4). The SIMION geometry files used to generate the potential arrays used can be found in the appendix (Fig. B.1–B.6). The REXTRAP electrode structure was modelled in rotational symmetry. A grid spacing of 1 mm has been chosen, which is a good compromise between adequate accuracy and size of the generated files.

The injection- and ejection kicker systems break the rotational symmetry of REXTRAP and would demand to model several parts of the trap fully three dimensional. On the computational workbench however, no beam steering is necessary, since the ion-optical elements are per definition perfectly aligned. Therefore, in the simulation the kicker systems are approximated by a cylinder electrode.

Computation of the Magnetic Field

The magnetic potential generated by the solenoid was calculated using the mechanical and electric data available for the REXTRAP solenoid. The data were converted to the appropriate SIMION file format. The information about the magnetic field at any point in space is obtained by the same algorithm as it has been applied in the case of the electrical fields. The magnetic field created by the REXTRAP magnet changes very smoothly (see Sec. 4.3). Therefore, it was sufficient to use a grid spacing of 5 mm for the magnetic potential.

Damping Forces

In addition to the forces resulting from the electric and magnetic fields, a velocity depending damping force according to Sec. 3.4 has been included in *IonFly*. A buffer gas pressure distribution along the trap axis according to Sec. 4.5 has been used.

5.2.2 *PennDamp*

The program *PennDamp* has been adapted from the already mentioned program library created by Stefan Schwarz in order to run in connection with *IonFly*. It allows the investigation of the ion motion in a Penning trap with a buffer gas atmosphere. A flow chart illustrating the working principle is shown in Fig. 5.1. In contrast to *IonFly* the algorithm of the program *PennDamp* is not based on a numerical integration algorithm. It uses the equation of motion in an ideal Penning trap derived in Sec. 3.3.2. Collisions with buffer gas atoms are treated by incorporating known realistic ion-neutral interaction potentials. The theory of ion-neutral collisions will not be discussed here. It can be found in detail in [Sch98, Kim97].

5.2.3 Data Evaluation

The numerical simulations would be of little use if the results cannot be easily extracted and interpreted. The program package uses a special text based file format to store ion related information. This allows easy extraction of desired information by standard UNIX tools like grep, awk, gnuplot etc. Over the time a numerous amount of scripts and programs for diverse purposes have been written, which are very reliable and fast in operation.

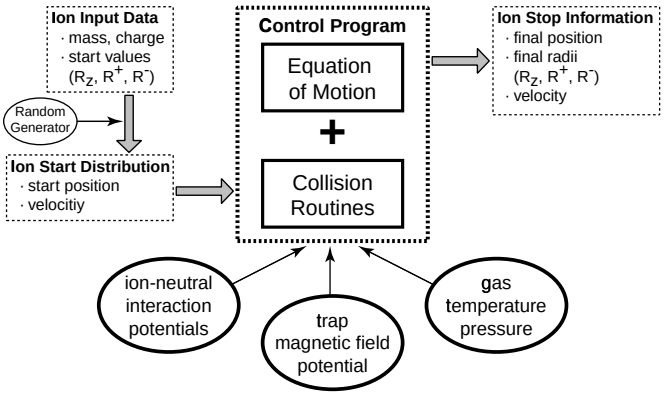

Figure 5.2: The principle of the program *PennDamp* used for simulation of ion motion in the trapping region of REXTRAP.

Emittance Definitions

The clearest picture of the evolution of a dynamic collection of particles can be obtained by combining its momentum and spatial coordinates p_i and x_i ($i = x \ldots z$) on an equal level. The six-dimensional volume represented by $\prod_{i=x,y,z} p_i x_i$ is called "phase space". Phase space is difficult to visualise in its full six dimensions. In order to obtain pictures that are easy to understand, it is projected into two-dimensional planes, the so called "emittance diagrams". This transition is described in an excellent way in ref. [Moo95]. Since the confusion about emittance and its property are widespread here are a few remarks concerning the numbers given in the present work.

Emittance plots of typical ion beams are of elliptical shape. The emittance value is the area of this ellipse. Nevertheless, for practical reasons, this definition is not completely unambiguous since a real beam has no well defined and sharp border line envelope in phase space. A practical definition is to define the emittance as the area of the smallest ellipse containing 95 % of all the particles in its interior.

Due to the radial symmetry of the REXTRAP system, the horizontal and vertical emittance are in principal identical. In the following they are referred to as the transverse emittance ϵ_{trans}. It is represented by

$$\epsilon_{trans} = \Delta x \cdot x' \qquad \text{with} \qquad \tan x' = \frac{p_x}{p_z} \,, \tag{5.3}$$

where Δx and x' denote the displacement coordinate and the beam divergence, respectively. The transverse emittance is measured in π mm·mrad.

Instead of using momentum and space for defining the phase space of a beam also energy and time can be used. This is of particular advantage for the description of the evolution of ion pulses. This is referred to as longitudinal emittance. The area of the emittance ellipse ϵ_{long} for a beam pulse is given by

$$\epsilon_{long} = \pi \Delta E \cdot \Delta t \,, \tag{5.4}$$

where ΔE and Δt correspond to energy spread and time duration, respectively. It is measured in eV·µs.

5.3 Simulations

Most of the calculations carried out are related to experimental results, which are presented in Sec. 6. The simulations have been restricted to the alkaline ions $^{7}Li^{+}$, $^{23}Na^{+}$, $^{39}K^{+}$, $^{87}Rb^{+}$, and $^{133}Cs^{+}$. This choice covers the entire mass range of experiments REX-ISOLDE is dedicated to. Furthermore, the interaction potentials of these ions with noble gas atoms are known. The REXTRAP set-up can be of course operated with several buffer gases. For instance helium, neon, or argon are possible choices. For time reasons the calculations have been restricted to the case of argon.

An overview of all simulations performed is shown in Fig. 5.3. Three groups can be distinguished. Firstly, calculations to understand the injection of ions into REXTRAP. Secondly, the modelling of the cooling performance and finally, the simulation of properties of the ejected ion bunches. Fig. 5.3 shows the different tasks which have been carried out and the programs used for this purpose. They will be described in detail in the appropriate sections.

5.3.1 Generation of Realistic Ion Ensembles for the Investigation of the Ion Injection

For the simulation of the ion injection process into REXTRAP it was necessary to generate ion ensembles at the focal plane in front of REXTRAP. In order to have them as realistic as possible it was necessary to investigate the ion optical properties of the test ion source and ISOLDE. The first has been done with *IonFly*. For the latter GIOSP and COSY have been used.

Ion Ensembles for the Off-line Case

Realistic ion ensembles at the focal plane have been generated by tracing ions from the place of creation at the surface of the ioniser of the test ion source to the focal plane in front of REXTRAP. This process consists of two steps. In the first step the creation and acceleration of the ions in the ion source is performed. For this purpose *IonFly* has been used. As a side effect the properties of an ion beam from the test ion source are obtained. The second step is the transfer of the ions through the injection beam line towards the focal plane in front of REXTRAP. This has been carried out using COSY.

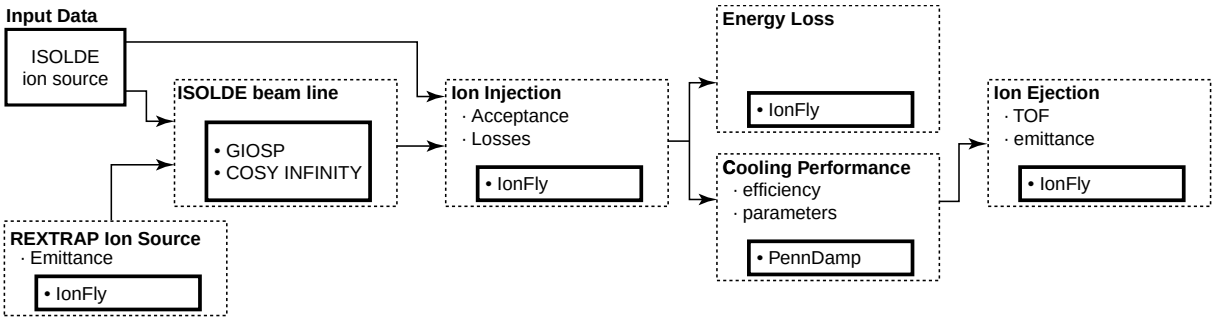

Figure 5.3: Overview of the simulations performed in order to investigate the experimental behaviour of REXTRAP.

For the simulation of creation and acceleration in the ion source the ions have been equally distributed over the front side of the ioniser hole. The active area was a circle with a radius of 0.95 mm. A Maxwell velocity distribution (T=1 000 K) reflects the thermal energy of the ions. Then the ions were extracted by the field produced by the electrodes and their properties were studied at a plane 250 mm downstream the ioniser. The results of the calculation for typical operation values of the ion source (acceleration voltage 30 300 V, voltage at extraction electrode 30 000 V) are shown in Fig. 5.4.

From these calculations the transverse emittance has been determined to 5 π mm·mrad (@30 kV). This value is about 4 times larger than it was estimated in [Dez96]. However, a reconstruction of scanner pictures downstream the beam line as well as the experimental performance of REX-TRAP when operated with beams from the test ion source give strong evidence that this value is in good agreement with reality. The longitudinal energy distribution is about 7 eV wide. This reflects exactly the potential gradient over the hole in the ioniser and proves that the integration routine is performing well.

For further processing the ions towards the focal plane in front of REXTRAP the injection beam line has been analysed with COSY. The source file used can be found in the appendix (Fig. C.3). The resulting transfer matrix provides an elegant way to generate the desired ion ensembles. Horizontal and vertical ion density distributions have been extracted from the result. They have been in good agreement with experimental recorded scanner pictures which gives evidence that the ion ensembles obtained for this case are suitable for the simulation of the ion injection process.

Ion Ensembles for the On-line Case

A commonly accepted value for the ISOLDE beam emittance is 34 π mm·mrad [Let00]. Based on this number the ISOLDE beam line was analysed with GIOSP and COSY. The source code of the COSY input file can be found in the appendix (Fig. C.2). Although the calculated voltages are in good agreement with the experimental values (see Table 6.3) a perfect reconstruction of the real conditions at the focal plane in front of REXTRAP has not been achieved.

Thus, suitable ion ensembles for the injection calculations have been obtained by another

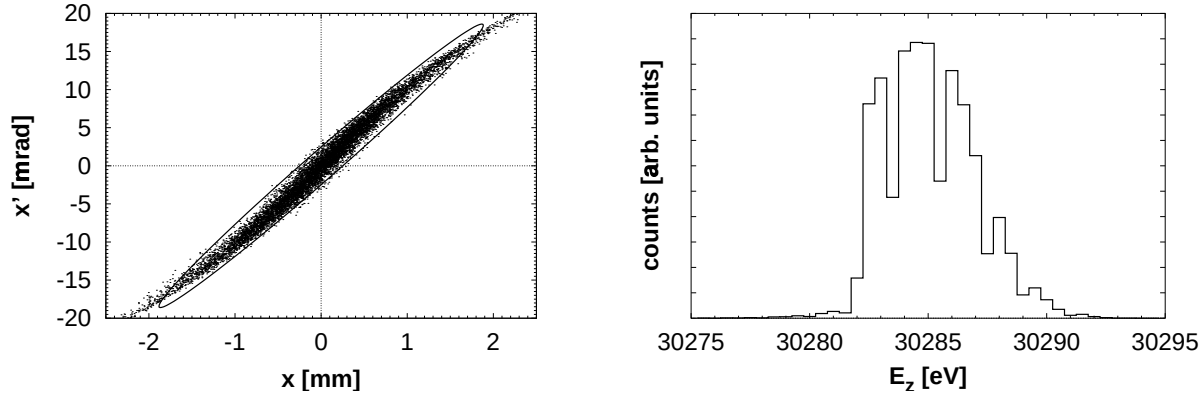

Figure 5.4: Simulated transverse emittance (left) and longitudinal energy distribution (right) of the REXTRAP test ion source for an acceleration voltage of 30 300 V.

method. Numbers about the spatial distribution of the ion beam can be extracted from experimental scanner pictures. Combining it with the emittance of the ISOLDE ion source gives all information required to create the desired distributions. For the simulations, reported in the following, the spatial as well as the angular ion distribution have been assumed to be Gaussians, with a full width at half maximum of 2.2 mm and 15 mrad wide.

5.3.2 Ion Injection into REXTRAP

The simulation of the ion injection process into REXTRAP has been performed with *IonFly* using the ion ensembles obtained above as input conditions. The simulation can be divided into two subtasks. Firstly, the parameters used for the simulations have been optimised. Secondly, the injection performance has been determined using the optimal parameters obtained in the first step. The results of both steps is discussed in detail in the following.

Optimisation of Retardation and Transfer Potential

The ion trajectories in the deceleration part of REXTRAP are determined by the retardation and transfer potentials. A proper adjustment of both voltages is necessary in order to achieve a high trapping efficiency. The voltage at the electron suppression electrode (injection lens) is uncritical and was set to zero for the calculations reported.

During the commissioning phase of REXTRAP the transfer potential has been limited to a value of 1.5 kV for technical reasons. However, improvements are planned which will allow higher values at a later date. Therefore, simulations have been carried out for beam energies of 30 keV and 60 keV and for transfer potentials of 1.5 keV, 3 keV, and 4 keV. The results are shown in Fig. 5.5. The percentage of particles detected after the first diaphragm in the deceleration stage (see Fig. 4.8) is plotted as function of the retardation potential.

For a beam energy of 30 keV the percentage of detected particle shows a common maximum for a retardation potential of about 3250 V. This is practically independent of the transfer voltage. However, the trend of these transmission curves changes as the retardation potential increases. It remains nearly constant for a transfer potential of 1.5 kV whereas it decreases in the case of 3 kV and 4 kV.

A different trend can be noted for a beam energy of 60 keV. All curves show the same tendency. The percentage of ions surviving the first diaphragm growths as the retardation potential increases until it reaches a maximum. In contrast to the case of a 30 keV beam energy when a one hundred percent efficiency can be reached at all transfer potential values, a maximum of only 95 % is achieved in the case of 1.5 keV. For further calculations retardation potentials of 9000 V with 1.5 kV transfer potential and of 6500 V with 3 kV and 4 kV transfer potential have been chosen. These values are marked by arrows in Fig. 5.5.

Optimisation of the Potential of Electrode01

The einzel lens formed by electrode01 and the two electrodes at transfer potential determines the ion injection into the magnetic field. Hence, a careful adjustment is necessary to ensure best injection performance. The optimum voltage applied to electrode01 depends mainly on the transfer voltage. Simulations with $^{7}Li^{+}$, $^{23}Na^{+}$, $^{39}K^{+}$, $^{87}Rb^{+}$, and $^{133}Cs^{+}$ have been performed

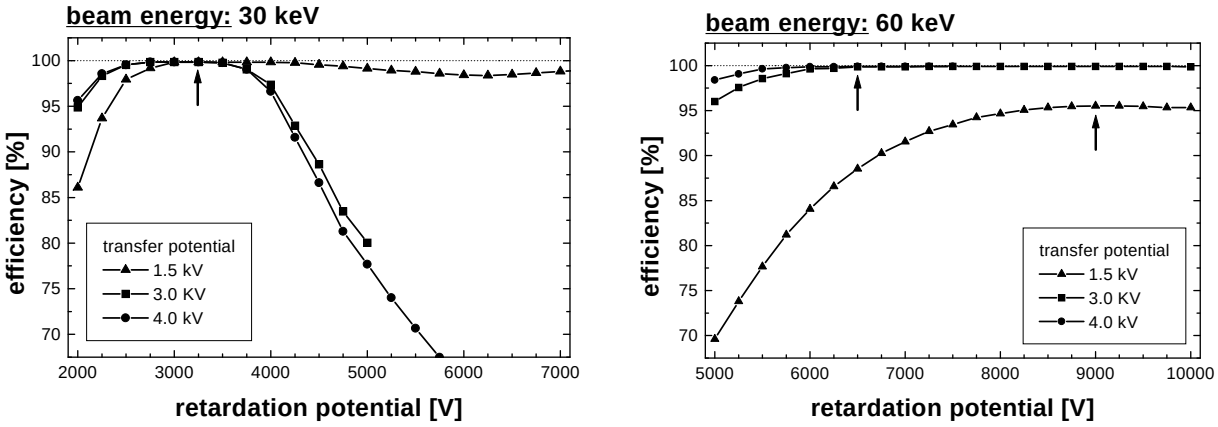

Figure 5.5: Percentage of particles detected after the first diaphragm as function of the retardation potential for different transfer potential voltages and beam energies (left: 30 keV, right: 60 keV). The plots results from simulations. The arrows mark the points chosen for further calculations.

ion energy	30 300 eV	60 000 eV
high voltage	30 300 eV	59 730 eV
injection lens	0 V	0 V
retardation pot.	3250 V	⊗
transfer pot.	1500 V	
electrode01	225 V	
electrode02	−2000 V	−1800 V
electrode03	−1400 V	−1400 V
electrode04	0 V	0 V
electrode05	285 V	185 V

⊗

transfer pot.	1500 V	3000 V	4000 V
retardation pot.	9000 V	6500 V	6500 V
electrode01	225 V	625 V	800 V

Table 5.1: Compilation of parameters used to simulate ion injection into REXTRAP.

in order to test the dependency on the ion mass. Such a dependency could occur since the ions cross the fringe field region of the solenoid. However, no effect was observed in the investigated mass region. The results of the optimisation process are summarised in Table 5.1. This lists also the optimum parameters of other electrodes used in further calculations.

Injection with 30 keV Beam Energy

The 30 keV injection calculations have only be carried out for a $^{133}Cs^{+}$ beam, traced from the test ion source into REXTRAP, as described above. For this simulation injection parameters as given in Table 5.1 have been used. The aim of this simulations has been to test how far it is possible to reproduce the experimental performance.

A total of 41 % of the ions reached a virtual detector, placed behind the trap entrance diaphragm. This value is in very good agreement with the experimentally observed one. Therefore, it was concluded that the simulation process proposed is well suited for these kind of studies.

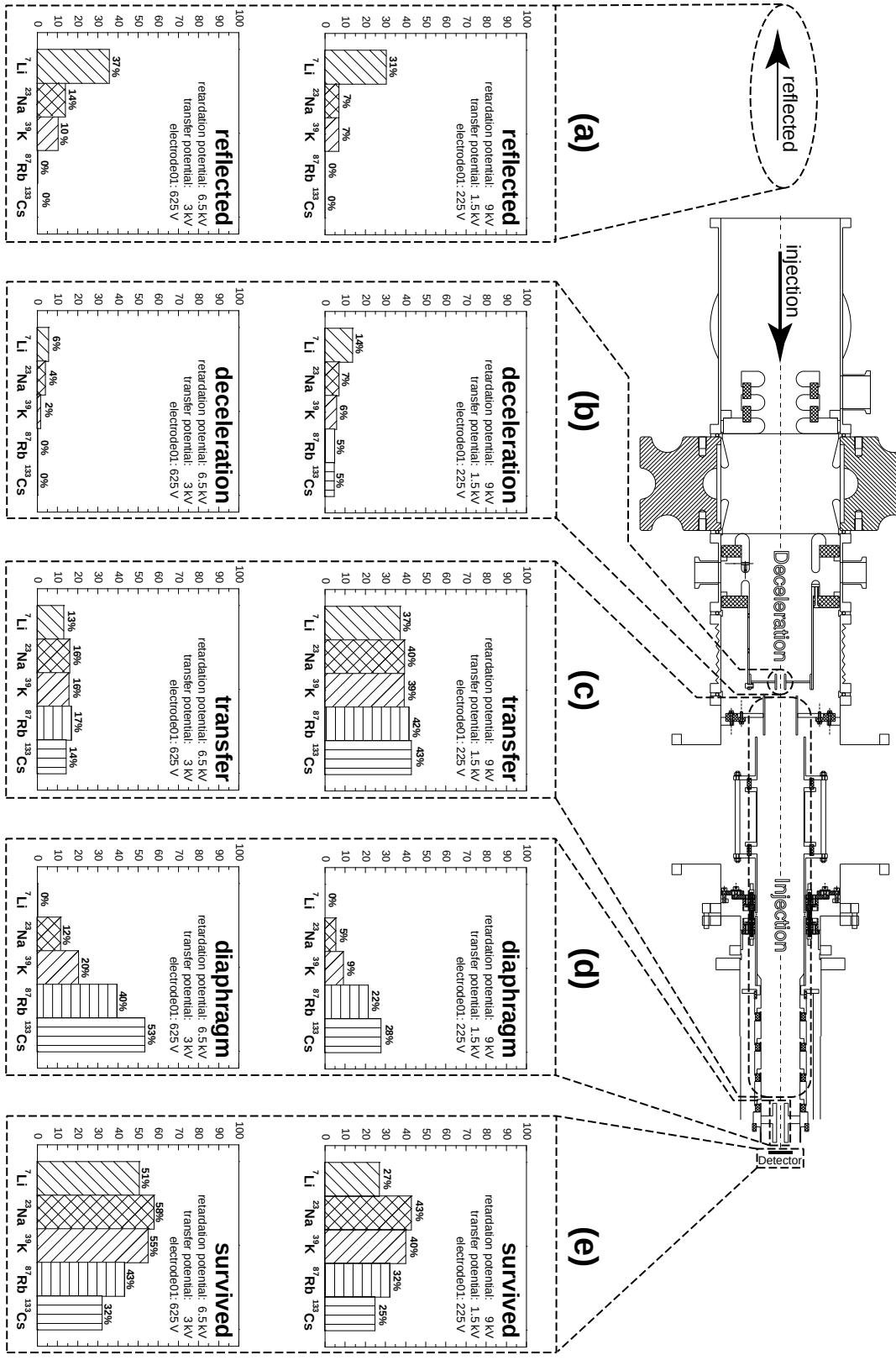

Figure 5.6: Overview of the results of injection simulations of typical ISOLDE ion beams. Plotted are the percentage of ions being reflected (a), being lost in the deceleration stage (b), injection stage (c), and at the trap entrance diaphragm (d) as well as reaching a virtual detector behind the trap entrance diaphragm (e). The top and bottom row of diagrams were obtained for a transfer potential of 1.5 kV and 3 kV, respectively.

Injection with 60 keV Beam Energy

The results of the injection simulations of typical 60 keV ISOLDE ion beams of $^{7}Li^{+}$, $^{23}Na^{+}$, $^{39}K^{+}$, $^{87}Rb^{+}$, and $^{133}Cs^{+}$ are shown in Fig. 5.6. The calculations have been performed for transfer potentials of 1.5 kV (top row of Fig. 5.6) and 3 kV (bottom row of Fig. 5.6).

Case (a) of Fig. 5.6 shows the percentage of ions being reflected, i.e. these ions leave the trap in opposite direction and are lost. Losses due to reflection can be noted for $^{7}Li^{+}$, $^{23}Na^{+}$, and $^{39}K^{+}$. They increase as the ion mass decreases. Absolute values range from 7 % to 31 % for a transfer voltage of 1.5 kV and 10 % to 37 % a transfer voltage of 3 kV. The reason for ions being reflected is a combined action of the electric potentials and the magnetic field. Longitudinal ion energy is partly transfered into radial energy when the ions enter the magnetic field. This process is called “radial energy uptake”. It is caused by the components of the magnetic field which are perpendicular to the ions direction of movement since these fields generate a Lorentz force. The absolute amount of energy transfered depends on the ion mass, velocity, and its inclination with respect to the magnetic field. If the radial energy pick-up exceeds a certain limit an ion is reflected at the entrance potential wall of the trap. The total amount of radial energy pick up as a function of the ion mass will be discussed more detailed further down.

Fig. 5.6 (b) shows the percentage of ions being lost at the diaphragm in the deceleration stage of REXTRAP. 5 % of the ions hit the diaphragm for a transfer potential of 1.5 kV, whereas no losses are found for a transfer potential of 3 kV. These numbers correspond to the ones obtained during the optimisation process of this stage described above.

The percentage of ions being lost in the injection stage of the trap is shown in case (c) of Fig. 5.6. The numbers found are practically mass independent. The losses in this stage are about 40 % for a transfer potential of 1.5 kV and about 15 % for a transfer potential of 3 kV.

Case (d) of Fig. 5.6 shows the percentage of ions hitting the trap injection diaphragm. In contrast to the case (c) here a clear mass dependency is noticed. For a transfer potential of 1.5 KV the ion losses rises gradually from 0 % for $^{7}Li^{+}$ to 28 % for $^{133}Cs^{+}$. This is even more dramatic for 3 kV transfer potential. In this case the a rise from 0 % for $^{7}Li^{+}$ to 53 % for $^{133}Cs^{+}$ occurs.

The percentage of ions reaching a virtual detector placed behind the entrance diaphragm of the trap are shown in case (e) of Fig. 5.6. The general trend is independent of the transfer potential. It peaks for $^{23}Na^{+}$. This is not astonishing since the set-up was originally designed and optimised for a mass-number around thirty. However, the strong dependence on the ion mass was not properly taken care of during that period. Remarkable lower injection efficiency can be noted for the cases of lower and higher ion masses, i.e. $^{7}Li^{+}$ on the one side and $^{87}Rb^{+}$ as well as $^{133}Cs^{+}$ on the other side. Another important observation is that the number of ions surviving the injection process is considerably higher in the case of a transfer potential of 3 kV. The absolute values of ions reaching the inner part of the trap range from 25 % (Cs^{+}) to 43 % ($^{23}Na^{+}$) for a transfer potential of 1.5 kV and from 35 % (Cs^{+}) to 58 % ($^{23}Na^{+}$) for a transfer potential of 3 kV.

As it has been seen, a large number of ions is being lost at the trap entrance diaphragm. Thus, an increase of the diaphragm radius should increase the number of ions surviving the injection process into REXTRAP. The results of calculations with an enlarged diaphragm and for different transfer potentials are shown in Fig. 5.7. Indeed, the number of ions reaching the detector increases as expected. Nearly twice as many ions survive if one increases the radius of

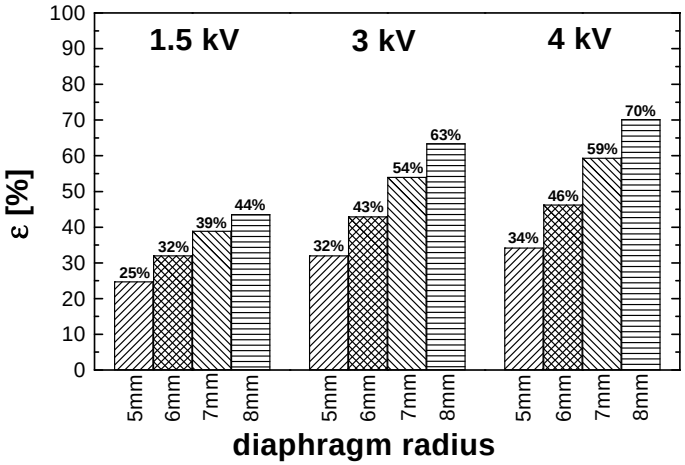

Figure 5.7: Percentage of a simulated ISOLDE $^{133}Cs^{+}$ ion beam reaching a virtual detector behind the trap entrance diaphragm as a function of the diaphragm radius and for several transfer potentials.

the diaphragm from 5 mm to 8 mm. This trend is independent of the transfer potential. However, even such an increase of the radius of this diaphragm does not yield to hundred percent capture efficiency. Depending on the transfer potential losses between 30 % and 56 % are still present.

Ion Capturing

The radial energy uptake determines not only if ions are reflected at the the potential wall at the trap entrance or not. It contributes to a large amount of energy which must be dissipated in the buffer gas of REXTRAP in order to trap the ions. It will be therefore discussed briefly in the following.

Histograms showing the longitudinal energy distribution for several ion species are shown in Fig. 5.8. These plots contain the information of all ions reached the virtual detector after the trap injection diaphragm. Please note that in the case of $^{23}Na^{+}$ the voltage at electrode05 has been lowered by 10 V for the calculation in order to see the complete longitudinal energy distribution.

The most important value to be extracted from these plots is the total width ΔE_z of the distribution. One immediately realizes that this value increases as the ion mass decreases. The following dependency has been fitted to data points (bottom right diagram of Fig. 5.8)

$$\Delta E_z \sim \frac{1}{\sqrt{A}} , \tag{5.5}$$

where A denotes the mass number.

Such a dependency is expected when considering a particle flying with constant velocity through a magnetic field perpendicular to its direction of moving. Similar trends have been found analytically when studying the injection process into an EBIS [Wen98] and the ejection out of an ECR source [KV88].

Surviving the injection stage is necessary to be captured into REXTRAP, but not sufficient. The energy loss during one oscillation in the trap must be high enough in order to not allow the ions to again overcome the potential barrier at the trap entrance. Simulations have been carried out in order to determine the maximum energy an incident ion may have with respect to the voltage applied to electrode05 in order to be captured in the REXTRAP potential.

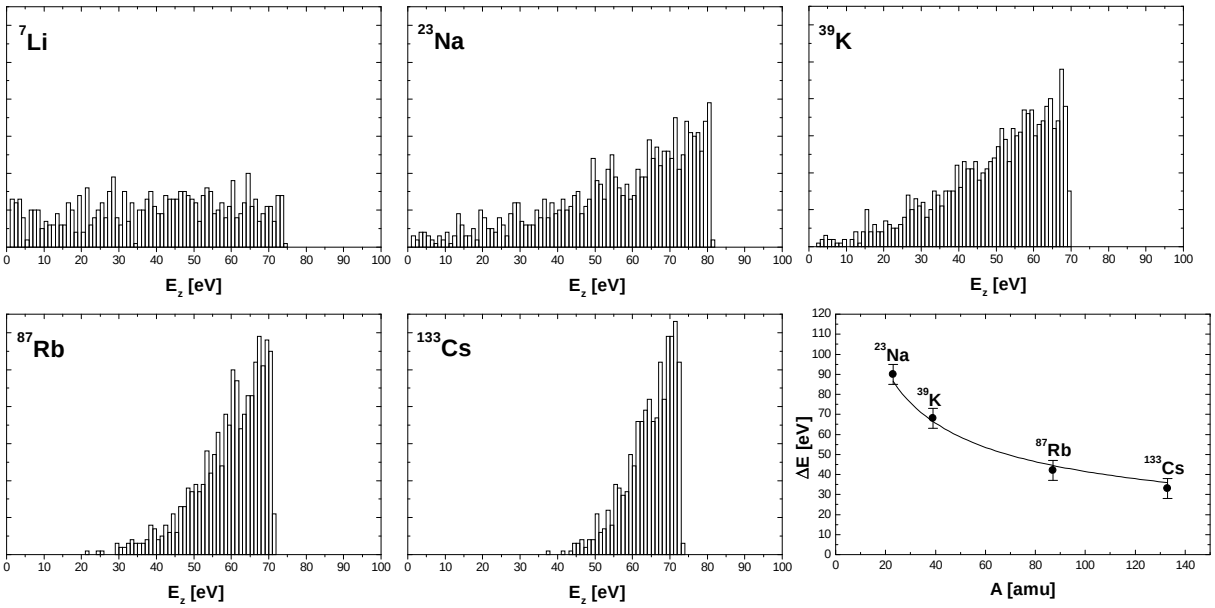

Figure 5.8: Histograms showing the longitudinal energy distribution for $^{7}Li^{+}$, $^{23}Na^{+}$, $^{39}K^{+}$, $^{87}Rb^{+}$, and $^{133}Cs^{+}$ behind the trap entrance diaphragm (electrode05). The width of the distributions is shown as function of the mass number at the bottom right diagram.

The following procedure has been used in order to determine the maximum tolerable energy for the different buffer gas pressure values inside the trap. An ion of the desired species was started in the middle of the entrance diaphragm with a certain energy. Its motion was recorded with *IonFly*. The start energy was step wise increased as long as the ion was not able to overcome the entrance potential barrier after its first oscillation. This value is the maximum tolerable energy $\widetilde{\Delta \mathsf{E}}$.

The results of the simulations are shown in Fig. 5.9. For clarity only the cases $^{133}Cs^{+}$ and $^{39}K^{+}$ have been plotted. The points follow a straight line in this double-logarithmic plot. Hence, $\widetilde{\Delta \mathsf{E}}$ can be described by the following equation

$$\widetilde{\Delta \mathsf{E}} = \epsilon_l \cdot \mathsf{p}^{\kappa} \ . \tag{5.6}$$

The constants ϵ_l and κ have been adapted to the individual cases. The appropriate values are listed in Fig. 5.9.

5.3.3 Cooling Performance

In the following the reduction of the amplitudes of the ion motion after being captured in REXTRAP will be discussed. Both cooling of the axial and the radial motion will be discussed separately in the following.

Cooling of the Axial Motion

A typical example of cooling of the axial motion in REXTRAP is shown in Fig. 5.10. The picture illustrates the evolution of the axial amplitude for a 60 keV $^{133}Cs^{+}$ ion entering the trap

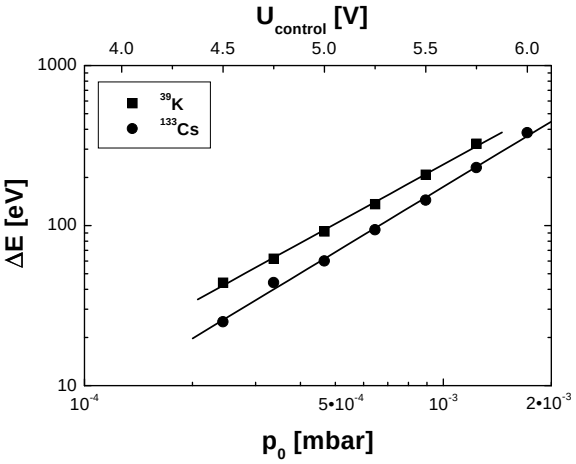

$$\widetilde{\Delta E} = \epsilon_l \cdot p^{\kappa}$$

	$\epsilon_l \left[\frac{\text{eV}}{\text{mbar}}\right]$	κ	$\widetilde{\Delta E}$ for 10^{-3} mbar
^{7}Li	$6.31{\cdot}10^{5}$	1.20	159
^{23}Na	$1.07{\cdot}10^{6}$	1.24	204
^{39}K	$1.17{\cdot}10^{6}$	1.23	239
^{87}Rb	$1.35{\cdot}10^{6}$	1.27	209
^{133}Cs	$2.04{\cdot}10^{6}$	1.36	170

Figure 5.9: The maximum ion energy $\widetilde{\Delta E}$ which can be dissipated in REXTRAP as a function of the argon buffer gas pressure p_0 in the high pressure region of the trap. **Left:** Plot of simulated values for $^{133}Cs^{+}$ and $^{39}K^{+}$. **Right:** Constants of the functional correlation adapted to the simulated sampling points according to Eq. (5.6). In addition $\widetilde{\Delta E}$ for an argon buffer gas pressure of $p_0 = 10^{-3}$ mbar is given.

system. A buffer gas pressure of of $p_0 = 10^{-3}$ mbar of argon in the high pressure region has been assumed. The electrode voltages are the same as been used for the injection calculation, reported above.

The ion was started at the tome origin at the focal plane in front of REXTRAP. It passes the trap entrance diaphragm after a few micro-seconds. Its total energy at this point is about 85 eV. This is about half of the maximum tolerable energy $\widetilde{\Delta E}$ to be captured in the trap. The oscillation amplitude of the motion reduces from about 400 mm to less than 100 mm during the first 1.5 ms. Then the ion oscillation is limited to the trapping part. The further damping of the oscillation amplitude is noticeable smaller since the buffer gas pressure in this region is about one order of magnitude smaller. After about 10 ms the amplitude has reached 25 mm. At this level the amplitude reduces only slightly because of the low velocity the ion has in the potential near the trap centre.

Ion Centring

• Simulation Parameters

The calculations carried out in order to investigate the ion centring process have been performed with *PennDamp*. The initial conditions for the simulations have been set to meet the realistic REXTRAP conditions as close as possible. *PennDamp* uses the magnetron frequency ν_{-} and cyclotron frequency ν_c to determine the characteristic Penning trap parameter. For the first a value of $\nu_{-} = 1014$ Hz has been used. The latter was adapted to the ion species by scaling according to the mass number using 343 kHz for $^{133}Cs^{+}$.

The start distributions for an ion ensemble chosen for the simulation of the centring process was mainly based on the experiences gained during the calculations reported above. After an ion has passed the trap entrance diaphragm it has a certain distance to the trap centre. This distance is the initial magnetron radius. The initial magnetron radii for the ion cloud were

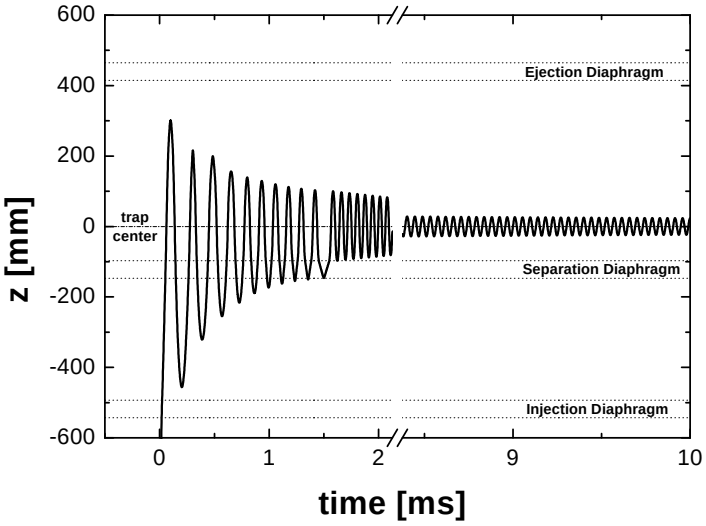

Figure 5.10: Simulation of cooling the axial motion of $^{133}Cs^{+}$ in REXTRAP assuming an argon buffer gas pressure of $p_0 = 10^{-3}$ mbar in the trap high pressure region. The evolution of the axial ion position is shown as a function of time. The position of the diaphragms separating the different pressure regions of the traps are indicated.

equally distributed over the radius of the diaphragm. Since the remaining amplitude of the cyclotron motion is rapidly cooled the initial value for this motion was set to zero. A value of 50 mm was used as initial amplitude for the axial motion. Such a value is reached after few milli-seconds of confinement in the trap.

After finishing the calculations it has to be decided if an ion may be extracted from the trap, e.g. whether the ion passes the extraction diaphragm or gets lost at this electrode. Further barriers on the way to the final detection do not exist in the REXTRAP set-up. An ion is regarded as survived if the sum of magnetron and cyclotron radius does not exceed the radius of the ejection diaphragm (2.5 mm). Applying this criteria to the start distribution of the ions would mean that 25 % could be extracted. This is simply the ratio of the areas of the injection and ejection diaphragm. This value corresponds quite well to experimental results. In the experiment such a number is measured by setting the trap is set to the non-trapping mode, i.e. the voltages at the trap exit part are permanently set to the values used for extraction. The direct comparison between the ion intensity in front of the trap with that measured behind gave typical values between 20 and 30 %.

• Centring efficiency

Simulations have been performed for $^{7}Li^{+}$, $^{23}Na^{+}$, $^{39}K^{+}$, $^{87}Rb^{+}$, and $^{133}Cs^{+}$ in order to determine the percentage of ions which can be centred as a function of the argon buffer gas pressure, excitation time and amplitude. The results are depicted in contour line plots in Fig. 5.11.

For $^{7}Li^{+}$ no ion centring was observed. The reason for this is the large mass difference between the ion and the neutral collision partner and additional rf heating. These effects are described further down. The according contour plots have not been included in this case.

In the case of $^{133}Cs^{+}$ the time needed for centring a certain percentage of ions decreases as the buffer gas pressure increases. This can be easily seen from the increasing density of the vertical contour lines. On the first view it might be astonishing that the number of centred ions shows no dependency on the excitation amplitude. However, this is an artifact due to the step size chosen to produce this plots. Already the first amplitude step of 800 V/m^2 exceeds the optimal saturation amplitude needed for the according buffer gas pressure (see Sec. 3.3.2). For typical cycle times of REXTRAP (20 ms) nearly hundred percent efficiency can be expected for

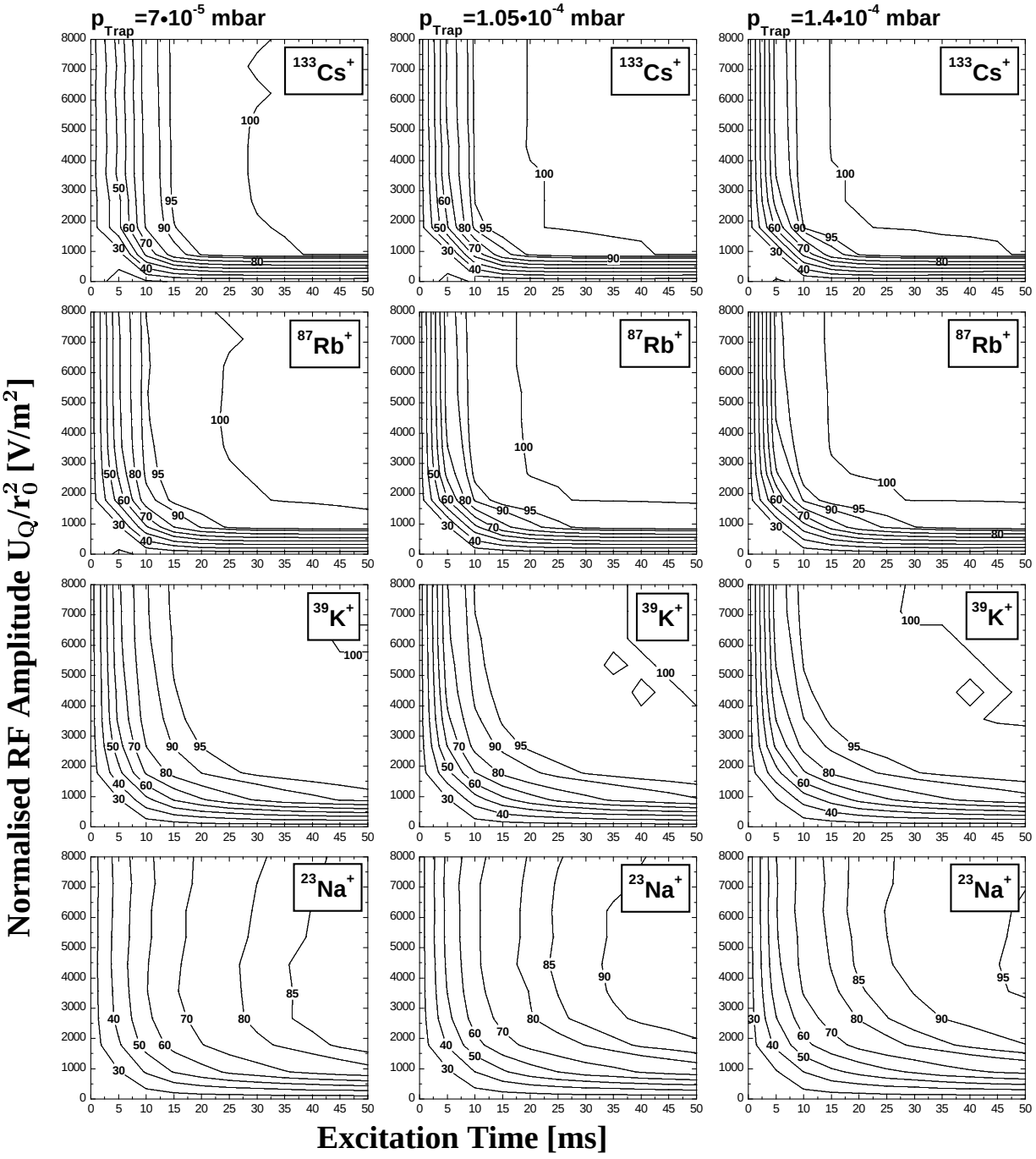

Figure 5.11: Percentage of centred ions as a function of excitation time and normalised radiofrequency amplitude for different ion species and for different argon buffer gas pressures.

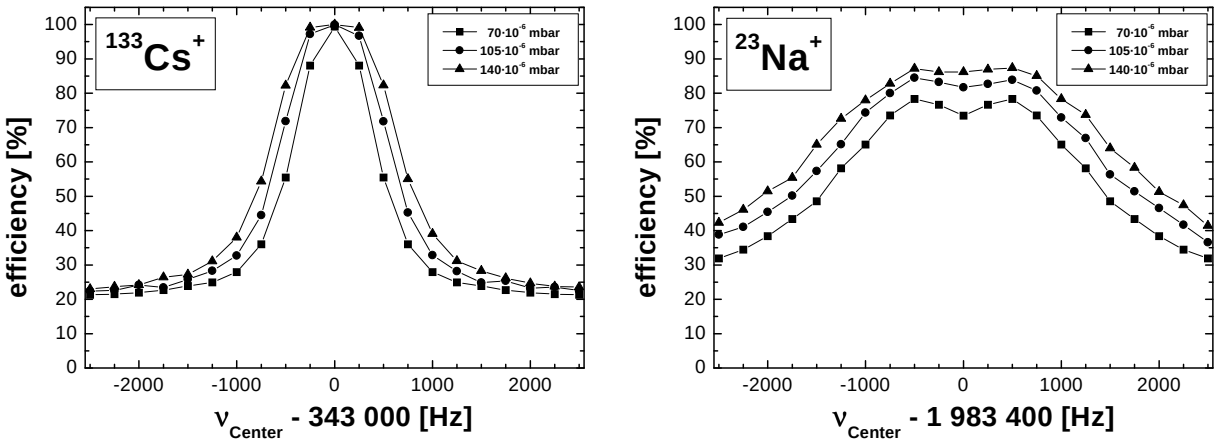

Figure 5.12: Simulated cooling scans for $^{133}Cs^+$ (left) and $^{23}Na^+$ (right) in REXTRAP. The plots show the number of particle being centred in between 20 ms and an excitation amplitude of 4000 V/m^2 as a function of the applied centring frequency ν_{center} for different argon buffer gas pressures.

buffer gas pressures of $p_{Trap} = 1.05 \cdot 10^{-4}$ mbar.

The results obtained for $^{133}Cs^+$ can be easily projected to case of $^{87}Rb^+$. The centring times are even slightly shorter.

However, in the case of $^{39}K^+$ and $^{23}Na^+$ this is not possible. Hundred percent efficiency is not reached within 20 ms cooling time. Losses of about 5 % and between 15 and 30 % must be noted for $^{39}K^+$ and $^{23}Na^+$, respectively. These results can be explained by the fact that nature of the ion-neutral interaction changes dramatically. The energy carryover to the ion increases as well as the corresponding displacement as the ratio of the ion mass to the mass of the buffer gas atom decreases. Additionally, in the case of $^{23}Na^+$ the effect of rf-heating can be noticed. At higher excitation amplitudes the percentage of ions being centred decreases again. This effect has already been described in Sec. 3.4.

• Mass Resolving Power

Beside the number of ions being centred information about the width of the cool resonances are important. A cooling resonance describes the number of ions being centred as function of the applied centring frequency ν_{center}. Its width $\Delta\nu_{FWHM}$ determines the mass resolving

$$R = \frac{\nu_c}{\Delta\nu_{FWHM}} \tag{5.7}$$

power since the cool process is mass selective.

Simulations of cooling scans have been performed for $^{23}Na^+$, $^{39}K^+$, $^{87}Rb^+$, and $^{133}Cs^+$ in REXTRAP. A cooling time of 20 ms and an excitation amplitude of 4000 V/m^2 has been chosen. Several diagrams visualise a few examples of the scans in Fig. 5.12. Table 5.2 gives important numbers obtained.

In the case of $^{133}Cs^+$ typical resonance curves are shown. The width of the resonances $\Delta\nu_{FWHM}$ increases from 0.9 to 1.35 kHz as the buffer gas pressure increases from $7 \cdot 10^{-5}$ to $1.4 \cdot 10^{-4}$ mbar. The corresponding mass resolving power decreases from $R = 380$ to 250.

The cases of $^{87}Rb^+$ and $^{39}K^+$ show similar behaviour. The width of the resonances increases to from 1.3 kHz to 1.8 kHz for $^{87}Rb^+$ and from 1.8 kHz to 2.65 kHz for $^{39}K^+$. This corresponds to a mass resolving power of about 400 to 300 and 650 to 450, respectively.

	p_{Trap} [mbar]	efficiency	ν_c [kHz]	$\Delta\nu_{FWHM}$ [kHz]	$R = \frac{\nu_c}{\Delta\nu_{FWHM}}$
$^{23}Na^+$	$70 \cdot 10^{-5}$	73 %	1983.4	3.0	670
	$105 \cdot 10^{-6}$	82 %		3.25	610
	$140 \cdot 10^{-6}$	86 %		3.55	560
$^{39}K^+$	$70 \cdot 10^{-6}$	98 %	1170.0	1.8	650
	$105 \cdot 10^{-6}$	99 %		2.3	510
	$140 \cdot 10^{-6}$	99 %		2.65	440
$^{87}Rb^+$	$70 \cdot 10^{-6}$	100 %	524.4	1.3	405
	$105 \cdot 10^{-6}$	100 %		1.35	390
	$140 \cdot 10^{-6}$	100 %		1.8	290
$^{133}Cs^+$	$70 \cdot 10^{-6}$	100 %	343.0	0.9	380
	$105 \cdot 10^{-6}$	100 %		1.2	290
	$140 \cdot 10^{-6}$	100 %		1.35	250

Table 5.2: Compilation of important parameter of simulated cooling scans in REXTRAP. Centring efficiency, centring frequency ν_c, width of the resonance $\Delta\nu_{cFWHM}$, and the corresponding mass resolving power R are given for different ion types and argon buffer gas pressure p_{Trap}.

In the case of $^{23}Na^+$ these trends continue. The resonance width varies between 3 kHz and 3.5 kHz for the different gas pressures. This corresponds to a mass resolving power of 560 to 670. However, a complete different line shape occurs. The resonance shows two maxima which are symmetrically shifted up and down with respect to the theoretical resonance frequency. A plausible explanation of this unexpected attitude has not been found and must be kept for the next generation of REXTRAP explorers. Nevertheless, several self-evident possibilities have already been ruled out. The program routines have been double-checked for obvious bugs. Errors of the integration routine have been excluded by a change to a well tested Runge-Kutta algorithm. Different ion-neutral interaction potentials have been used. However, the line shape remained constant. This leads to the conclusion that detailed calculations have to be carried out in order to understand this line shape occurring if a buffer gas much heavier than the ion mass is used.

5.3.4 Properties of Ejected Ion Bunches

An exact knowledge of the parameters of the ejected ion bunches is of great importance for their transfer towards the REXEBIS system. The ejection simulations have been carried out with *Ion-Fly* using ion ensembles as start distributions which have been obtained with *PennDamp*. The parameter used for the calculations are the experimentally optimised values given in Table 4.2. Additional optimisations of voltages at the ejection and acceleration part of the system have not been performed. This has not been necessary since the spatial extension of the extracted beam is remarkably smaller in the case of ejection. Correspondingly, no ion losses have been detected behind the trap exit diaphragm. Ion trajectories have been recorded at a virtual detector placed behind the acceleration part of REXTRAP. In fact it has been placed exactly at the position of the multi-channel plate of the Colutron beam viewing system (see Sec. 4.7).

The phase space of an ion bunch extracted from REXTRAP is mainly determined by the

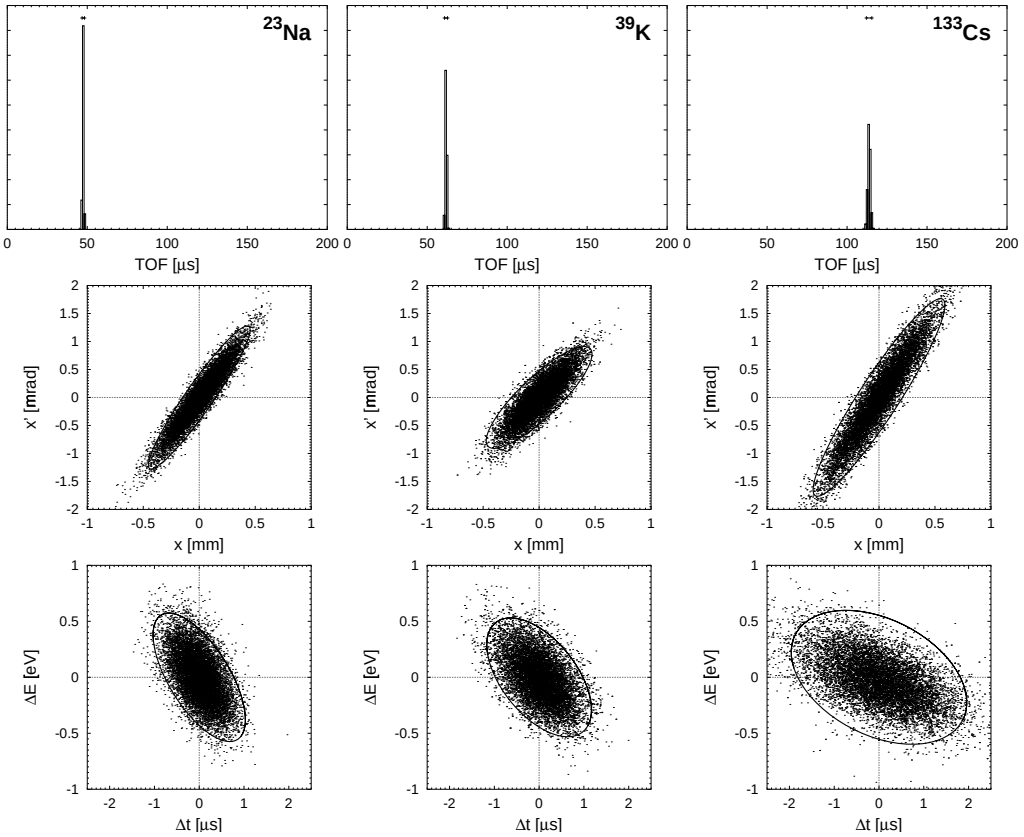

Figure 5.13: Time-of-flight histograms, transversal, and longitudinal emittance plots of ejected ion bunches from REXTRAP assuming start distributions with an equilibrium temperature of $T = 300\,K$. The line in the TOF histograms gives the width of the distribution containing 95 % of the ions. The emittance plots contain appropriate emittance ellipses.

volume the ion cloud occupies after the cooling process. To which extent this phase space is distributed transversely and longitudinally is discussed in the following.

Equilibrium Distributions

The smallest phase space for the ejected ion bunches can be expected if the ion start distribution is in thermical equilibrium with the buffer gas. Thus the distributions obtained in Sec. 3.4 have been used.

Time-of-flight histograms, transversal, and longitudinal emittance plots visualising the results are shown in Fig. 5.13. The emittance plots contain appropriate emittance ellipses, which are tilted since the pictures have neither been taken in a spatial nor in a time focus. A compilation of important numbers is given in Table 5.3. This includes the mean time-of-flight $\langle \mathrm{TOF} \rangle$, transversal emittance $\epsilon_{\mathrm{trans}}$, and longitudinal emittance ϵ_{long}. A width $\Delta\mathrm{TOF}$ of the time-of-flight histograms has been introduced. According to the emittance definition it is defined as the smallest time interval including 95 % of the ion bunch. Beside the values for the present case also values for different initial conditions are given. They are discussed further down.

The mean time-of-flight $\langle \mathrm{TOF} \rangle$ increases according to the ion mass. $\Delta\mathrm{TOF}$ growths as the mass increases. Values for the latter range from 1.5 to 3.4 µs.

Both ϵ_{trans} as well as ϵ_{long} increases for higher masses due to the larger volume the ion cloud occupies after the cooling process. Values of 0.19 to 0.37 π mm·mrad are obtained for the transversal emittance. The longitudinal emittance ranges from 1.39 to 3.41 eV·µs.

	T_{cool} [ms]	p_{Trap} [mbar]	⟨TOF⟩ [µs]	ΔTOF [µs]	ϵ_{trans} [π mm·mrad]	ϵ_{long} [eV·µs]
$^{23}Na^+$			47.4	1.5	0.19	1.39
$^{39}K^+$	Equilibrium		61.8	1.9	0.23	1.63
$^{133}Cs^+$			113.8	3.4	0.37	3.41
$^{133}Cs^+$	20	$70 \cdot 10^{-6}$	112.6	18.6	8.4	340
	20	$105 \cdot 10^{-6}$	113.6	10.5	3.4	68.6
	20	$140 \cdot 10^{-6}$	114.0	6.5	1.5	20.5
$^{23}Na^+$	20	$70 \cdot 10^{-6}$	45.6	18.0	*12.0	*407
	20	$105 \cdot 10^{-6}$	46.4	13.7	*8.0	*188
	20	$140 \cdot 10^{-6}$	46.9	11.8	*5.4	*140
$^{133}Cs^+$	cont.	$140 \cdot 10^{-6}$	114.0	6.5	*1.5	*20.5

*The emittance ellipse for this cases contains only 80 % of the appropriate ion number.

Table 5.3: Mean time-of-flight ⟨TOF⟩, width of the TOF peaks ΔTOF, transversal emittance ϵ_{trans}, and longitudinal emittance ϵ_{long} of ejected ion bunches from REXTRAP for different initial conditions. The top part gives the numbers assuming start distributions with an equilibrium temperature of T = 300 K. Parameters obtained with realistic start distribution are compiled in the middle part whereas to last line gives numbers for the case of continuous injection. A detailed description of the different cases is given in the text.

Realistic Start Distributions

Considering real trap operation parameters it is not possible to reach the thermodynamic equilibrium state since the cooling times are not sufficient. Thus the characteristics of the ion bunches obtained above does not reflect reality. In order to improve the ability to predict the beam quality of REXTRAP more realistic start distribution for the ejection calculations have been used.

• Injection and Cooling

The final ion distribution obtained in Sec. 5.3.3 have been used as appropriate input for the ejection calculations. Thus this test is based on the time scheme corresponding to case (a) in Fig. 4.21. An appropriate number of ions is injected, cooled, and finally ejected. A cooling time of 20 ms has been chosen. Simulations have been carried out for $^{23}Na^+$ and $^{133}Cs^+$ and three different buffer gases. The results are depicted in Fig. 5.14. The corresponding numbers are given in Table 5.3.

At both cases the TOF distributions change their width as well as their shape for the different buffer gas pressures. The narrow distributions smear out as the pressure decreases. This is well reflected by the width ΔTOF, which increases from 6.5 to 18.6 µs and from 11.8 to 18.0 µs in the case of $^{133}Cs^+$ and $^{23}Na^+$, respectively. In addition ⟨TOF⟩ decreases by more than 1µs in both cases.

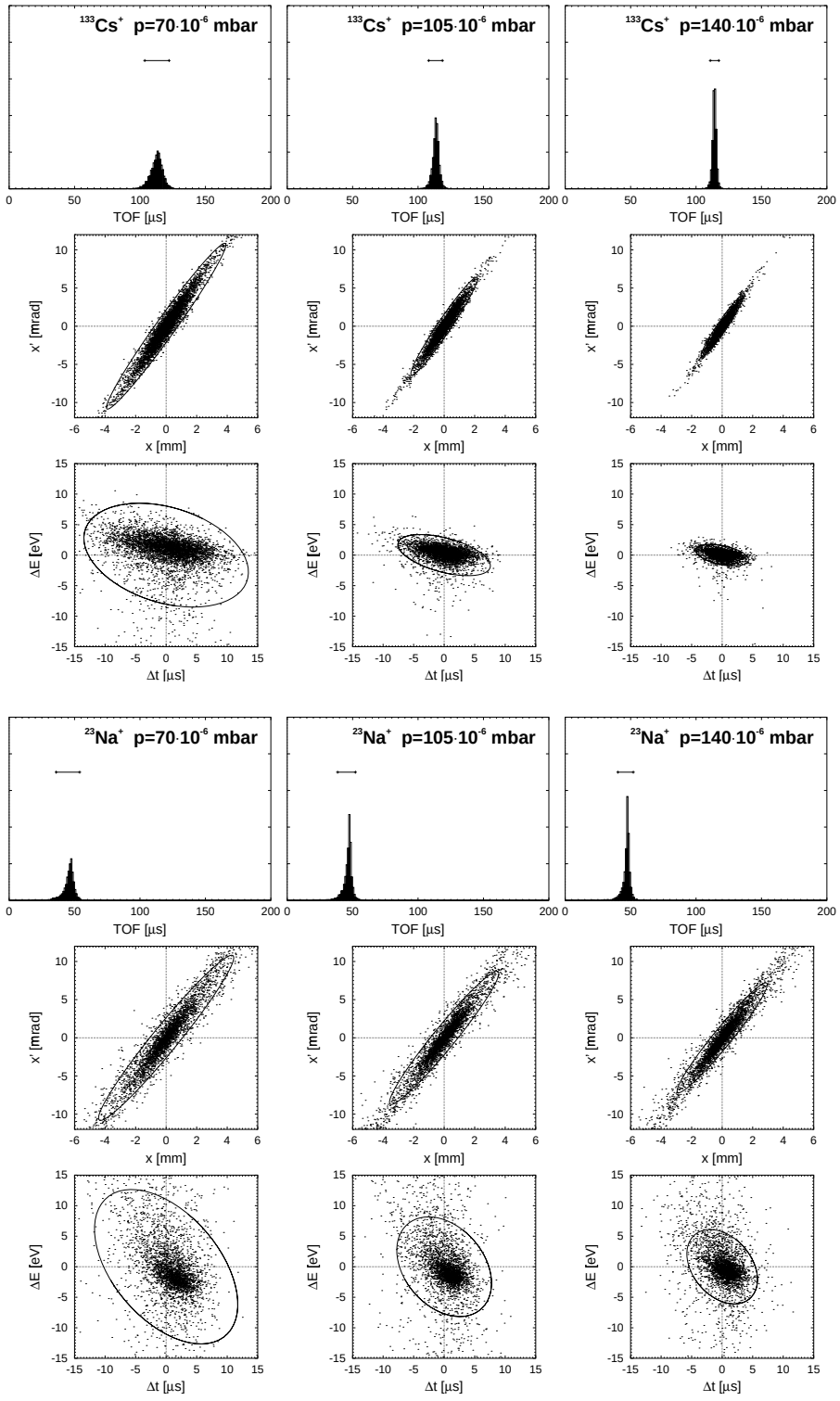

Figure 5.14: Time-of-flight histograms, transversal, and longitudinal emittance plots of ejected ion bunches from REXTRAP assuming realistic start distribution (explanation see text). The line in the TOF histograms gives the width of the distribution containing 95 % of the ions. The emittance plots contain emittance ellipses containing 95 % ($^{133}Cs^{+}$) and 80 % ($^{23}Na^{+}$) of the ions.

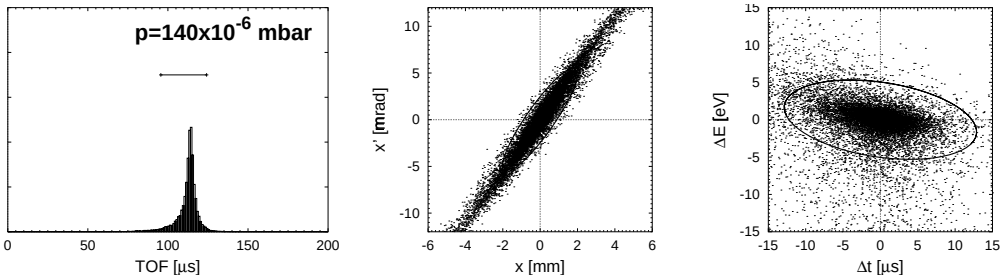

Figure 5.15: Time-of-flight histograms, transversal, and longitudinal emittance plots of ejected ion bunches from REXTRAP assuming realistic start distribution and continuous injection (explanation see text). The line in the TOF histograms gives the width of the distribution containing 95 % of the ions. The emittance plots contain emittance ellipses containing 80 % ($^{133}Cs^{+}$).

The emittance plots show a common feature. A dense core of already centred ions is surrounded by a halo. This is more pronounced in the case of lower gas pressures and for $^{23}Na^{+}$. Especially in the latter case the emittance definition as it has been introduced in Sec. 5.2.3 looses its meaning partly. In order to counterbalance this the emittance ellipses adjusted to contain only 80 % of the ions. The corresponding numbers are marked in Table 5.3.

The transverse emittance increases from 1.5 to 8.4 π mm·mrad and 5.4 to 12.0π mm mrad for $^{133}Cs^{+}$ and $^{23}Na^{+}$, respectively. The increase is even higher for the longitudinal emittance with 20.5 to 340 eV·µs for $^{133}Cs^{+}$ and 140 to 407 eV·µs for $^{23}Na^{+}$.

• Continuous Injection

The influence of changing the time scheme from the sequential case given above to simultaneously injection and cooling on the beam properties is briefly discussed in the following.

The modelling of the ion start distribution for the ejection calculations is more difficult then in the previous case. The following approach has been used. Ion start distribution as in Sec. 5.3.3 have been "cooled" with *PennDamp* from 1 to 20 ms in 1 ms. The joined distribution has been used as input for the simulation of the ejection process.

Since this kind of simulation is extremely resource intensive it has been only carried out for $^{133}Cs^{+}$ and for a buffer gas pressure of $p_{Trap} = 1.4 \cdot 10^{-4}$ mbar. The corresponding parameter plots are given in Fig. 5.15, whereas the number can be found again in Table 5.3.

In comparison to the previous case the TOF distributions is remarkably wider. The emittance plots show similar halo structures as it has been seen for the case of $^{23}Na^{+}$. Therefore, the emittance numbers given refer to 80 % of the ions again.

6 Experimental Results

6.1 The Very First Tests

REXTRAP saw its "first light" on 19th July 1999 after four years of development, construction, assembly, and testing. For the first time $^{133}Cs^{+}$ ions from the test ion source were injected, accumulated, cooled, and finally identified in a time-of-flight spectrum shown in Fig. 6.1. This major break through was the beginning of the first commissioning phase of REXTRAP. The goal was the determination of the basic operational parameters of the system. This phase was completed by a first on-line test with stable beams from ISOLDE. Time-of-flight spectra for different ion species delivered by ISOLDE are shown in Fig. 6.2. In these spectra the injected ion species can be identified by their time-of-flight. The additional peaks are due to ionised argon and residual gas ions. The

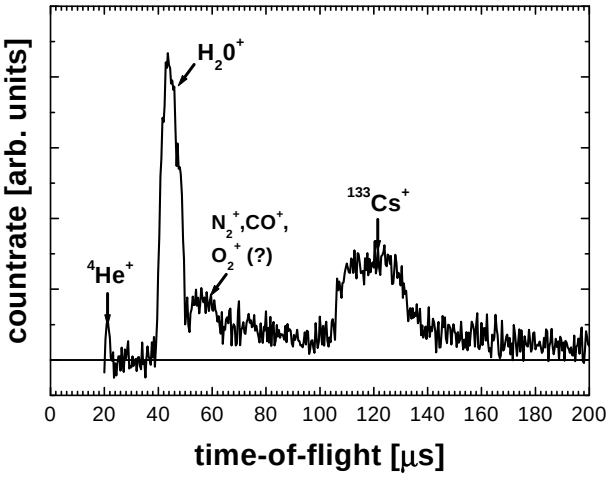

Figure 6.1: First time-of-flight spectrum containing a detectable amount of $^{133}Cs^{+}$ recorded using the REXTRAP set-up.

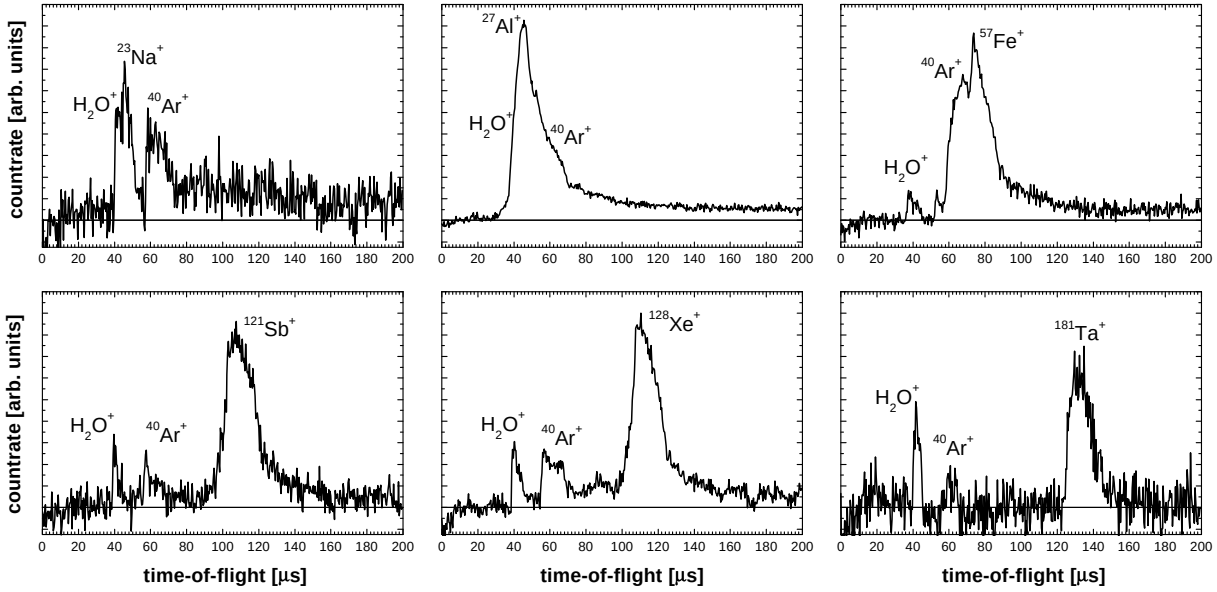

Figure 6.2: Time-of-flight spectra of $^{23}Na^{+}$, $^{27}Al^{+}$, $^{54}Fe^{+}$, $^{121}Sb^{+}$, $^{128}Xe^{+}$, and $^{181}Ta^{+}$ as obtained during a first on-line test. They ions were delivered by ISOLDE, accumulated, cooled in REXTRAP, and ejected.

	injected ions	ejected ions	efficiency
$^{23}Na^+$	$6.2 \cdot 10^6$	—*	—*
$^{27}Al^+$	$3.4 \cdot 10^8$	$1.2 \cdot 10^{7*}$	$3\,\%^*$
$^{54}Fe^+$	$7.5 \cdot 10^7$	$3.7 \cdot 10^{6*}$	$5\,\%^*$
$^{121}Sb^+$	$3.1 \cdot 10^7$	$8.7 \cdot 10^6$	$8\,\%$
$^{128}Xe^+$	$6.2 \cdot 10^6$	$1.2 \cdot 10^6$	$18\,\%$
$^{132}Xe^+$	$1.2 \cdot 10^8$	$8.7 \cdot 10^6$	$7\,\%$
$^{181}Ta^+$	$4.4 \cdot 10^8$	$2.5 \cdot 10^5$	$6\,\%$

* A determination of these values was not possible or is afflicted with a large uncertainty due to overlapping TOF peaks.

Table 6.1: Number of injected and ejected ions per trap cycle and the corresponding REXTRAP efficiency for different ion species. The numbers given were obtained during a first on-line test and correspond to the time-of-flight spectra given in Fig. 6.2.

width of the time-of-flight peaks is larger than expected. The reason for this is the low amplification of the particle multiplier used in these measurements (see Sec. 4.7) which required large ion numbers to be captured in the trap.

Nevertheless, already at this early commissioning stage and for the large ion number, efficiency values in the order of a few percent have been reached over nearly the entire mass range. They are listed in Table 6.1 together with the number of injected and ejected ions. In general, the efficiency increases as the injected ion number decreases. This indicates that a reduction of the injected number of ions is necessary in order to understand the performance of REXTRAP, not falsified by additional “space charge effects”.

After this test beam time a new ion detection system was installed. The Colutron beam viewing system described in Sec. 4.7 allows the detection of much lower ion intensities and was used for most of the subsequent measurements.

The results reported in the following have been obtained either with ions delivered by the off-line ion source or by ISOLDE. The origin of the ions is only explicitly mentioned if it is important for the respective case.

6.2 Signal Processing and Evaluation

Ions ejected from REXTRAP are detected either by direct current measurement using a Faraday cup or by using the multi-channel plate detector of the Colutron beam viewing system. In the first case the ion number is directly accessible. The latter, however, requires several manipulation processes in order to obtain final spectra. This procedure will be described in detail in the following.

6.2.1 Time-of-Flight Spectra

As described in Sec. 4.7 the ions reaching the multi-channel plate detector of the Colutron system generate a large number of secondary electrons. They are collected on an anode electrode and allowed to flow to ground via a load resistor R_L. R_L is determined by the $560\,\Omega$ resistor of

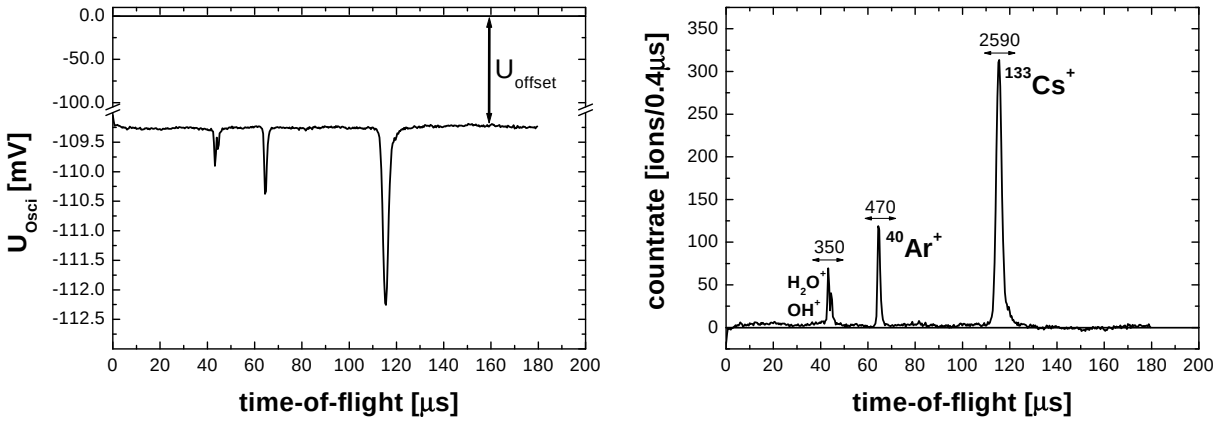

Figure 6.3: Left: Time-of-flight of flight spectrum recorded with the oscilloscope in its crude form. **Right:** The same spectrum after conversion into ion numbers. The numbers at the different time-of-flight peaks denote the total number of ions the peak contains as it is obtained by integrating over the peak are marked with arrows.

the high voltage divider and the $50\,\Omega$ input impedance of the pre-amplifier stage. This voltage is pre-amplified and recorded by an oscilloscope. A detailed sketch of the circuit is shown in Fig. 4.15. The dwell time Δt, i.e. the width of a single channel is determined by the time base of the oscilloscope.

Raw spectra are obtained by averaging over several cycles in order to improve the signal-to-noise. A typical raw spectrum is shown in the left part of Fig. 6.3. The oscilloscope voltage U_{osci} is shown as a function of the time-of-flight. The dwell time of the oscilloscope was $\Delta t = 40\,\text{ns}$. The amplitudes of the time-of-flight peaks is in the order of a few milli-volts. Due to the electrical circuit used (see Fig. 4.15) an offset voltage of $U_{offset} \approx -109\,\text{mV}$ is present.

The number N of ions per channel can be calculated via

$$N = \frac{\Delta t}{eVR_L}\left(U_{osci} - U_{offset}\right)\,, \tag{6.1}$$

where e denotes the elementary charge and U_{osci} is the voltage measured by the oscilloscope. The amplification $V = V_{MCP} \cdot V_{amp}$ of the system is determined by the amplification V_{MCP} of the MCP and V_{amp} of the pre-amplifier, respectively.

This formula allows the measured voltages to be converted into corresponding ion numbers. Except for the amplification V and the offset voltage U_{offset} all required parameters are known. The determination of the latter is straightforward. U_{offset} is obtained by averaging over a certain number of channels where no time-of-flight peak is present, preferably at the beginning or the end of the spectrum.

The determination of the amplification V of the detection system is more difficult. For this purpose the total charge Q ejected from the trap is directly measured using the Faraday cup and a pico-amperemeter and compared to the number of ions contained in the time-of-flight spectrum. Q is connected to the average current I_{avg} by

$$Q = I_{avg}T_{cycle} = Ne\,, \tag{6.2}$$

where T_{cycle} denotes the total time of one trap cycle. A comparison of Q with Eq. (6.1) allows

the amplification V to be determined. Thus one obtains

$$V = \frac{\Delta t}{R_L I_{avg} T_{cycle}} \sum_{\#} \left(U_{oszi} - U_{offset} \right) \tag{6.3}$$

for the amplification of the system. $\sum_{\#}$ symbolises the summation of all channels of the time-of-flight spectrum.

The average current is measured with the Faraday cup behind the trap for typical cycle times of 10 to 20 ms. Such short measurement intervals ensure reliable current values despite the pulsed nature of the beam because of the much larger integration time of the pico-ampere meter.

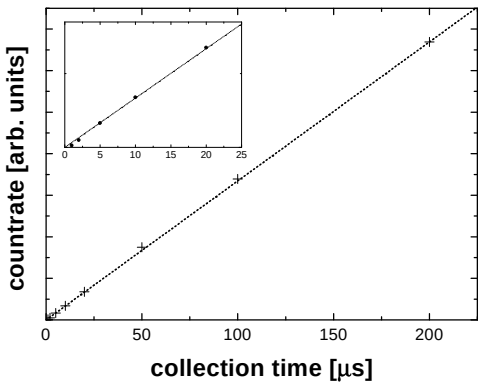

Figure 6.4: Number of ions detected as a function of the ion collection time. The dashed line corresponds to a linear fit.

The procedure above gives a value for the amplification of the system for a certain number of charges ejected. Due to the detection limit of the pico-amperemeter (about 1 pA) one has to use at least 10^5 to 10^6 ions per cycle for a trap repetition rate of 50 Hz. Depending on the MCP type such count rates can already mean that the MCP is in saturation, i.e. the amplification is lower than in the case of lower count rates. This has been excluded by measuring the number of ejected ions as a function of the injected number of ions. For this purpose the collection time in REXTRAP has been varied over several orders of magnitude while the incident ion current was kept constant. In the range of 10^2 to 10^6 ions/pulse the count rate is a linear function of the collection time indicating that the amplification V remains constant. This is illustrated in Fig. 6.4.

The limiting factor for the determination of the amplification V is the accuracy of the pico-ampere meter at this low currents. Fluctuations in the order of 20 to 30 % are noticed, which determine the uncertainty for V. The amplification of the complete system depends mainly on the high voltage applied to the MCP. For a MCP-voltage of 850 V the value for the amplification is typically $V = -5 \cdot 10^5$.

From a time-of-flight spectrum obtained by the oscilloscope the number of ions can now be calculated for each channel using to Eq. (6.1). For the raw spectrum shown in the left part of Fig. 6.3 a result as depicted on the right is obtained. The numbers given are obtained by integrating over the channels covering the range of the peak. They correspond to the total ion number a peak contains. This is the most useful number which can be extracted from the spectra. Therefore, in the following the ordinate of the time-of-flight spectra will not be labelled but the total number of ions in the interesting TOF peaks will be given.

The time-of-flight peaks can be assigned to a certain charge-to-mass ratio. Ions ejected from REXTRAP are in general singly charged due to the fact that higher charge states would recombine in the buffer gas. Thus time-of-flight peaks can be directly associated to a mass number.

6.2.2 Ion Signal as a Function of Trap Parameters

For optimising of REXTRAP operational parameters so called “parameter scans” have been carried out. In these scans the number of ions ejected from the trap is recorded time-resolved as a function of the parameter of interest. For that purpose the on-line measurement program has the possibility to set time gates on the time-of-flight spectrum, i.e. to mark a certain range of channels. Normally, a single TOF peak of the interesting ion species is selected. The voltage signals of these channels are then summed up to obtain a value U_{point} for a point in the parameter scan. U_{point} can be converted to ion numbers N_{point} via

$$N_{point} = \frac{\Delta t}{eVR_L}\left(U_{point} - n \cdot U_{offset}\right), \tag{6.4}$$

where n denotes the number of channels gated.

6.3 The Magnetic Field at the Trap Centre

The magnetic field at the trap centre is a very important parameter for the operation of the system. It defines directly the cyclotron frequency of the ions and therefore the centring frequency for the rf-sideband cooling technique. After installation and energizing of the magnet the magnetic field has been measured with a NMR probe to be 2.974911(1) T at the position of the trap centre. However, this measurement has been carried out without the trap electrodes in place. When inserting the electrode structure the field is expected to shift slightly due to the magnetic susceptibility of the used materials. Therefore, a re-determination of the field strength is necessary after all structures have been inserted. However, at this time the trap centre is not any longer accessible for a direct measurement and the magnetic field must be determined by an indirect method.

The knowledge of the cyclotron frequency ν_C of a trapped ion together with the ion mass m allows the determination of the magnetic field B_{center} at the trap centre using Eq. (3.3). An elegant method to measure ν_C is provided by the rf-sideband cooling technique since the optimum centring frequency is equivalent to the cyclotron frequency ν_C.

For the determination of B_{center} water molecule ions H_2O^+ were used. They are unintentionally created by ionization of residual gas molecules (see Sec. 6.6.2). These ions were captured in the trap region and centred via rf-sideband cooling in a helium buffer gas atmosphere. Cooling scans (see Sec. 6.4.2) resulted in a resonance frequency of $\nu_c = 2536345(45)$ Hz. This corresponds to a magnetic field of $B_{center} = 2.97478(5)$ T.

Based on this value cyclotron frequencies ν_c for different ion species are given in Table 6.2. The appropriate mass values were taken from [Aud97, Bra99].

6.4 Verification of Basic REXTRAP Functionality

The following section gives an overview about experiments which had the aim to prove the basic trap functionality. Dipole and quadrupole excitation as well as mass selective cooling will be discussed.

	ν_c [Hz]		ν_c [Hz]
$^{7}Li^{+}$	6 510 982(130)	$^{87}Rb^{+}$	525 618(11)
$^{23}Na^{+}$	1 987 018(40)	$^{133}Cs^{+}$	343 711(7)
$^{27}Al^{+}$	1 693 049(28)	$^{181}Ta^{+}$	252 454(5)
$^{39}K^{+}$	1 172 401(24)	$^{208}Pb^{+}$	219 645(4)
$^{85}Rb^{+}$	537 983(11)		

Table 6.2: Calculated cyclotron frequency ν_c for various ion species for the magnetic field $B_{center} = 2.97478(5)$ T of REXTRAP.

6.4.1 Dipole Excitation

It has been discussed in Sec. 3.3.2 that the radial motion of an ion in a Penning trap can be influenced by rf-dipole fields. Resonance effects are expected for the magnetron and cyclotron motion at the magnetron frequency ν_- and the reduced cyclotron frequency ν_+, respectively. In general, dipole excitation increases the amplitude of the motion. Therefore, a time structure for a REXTRAP cycle has been chosen in which the ions are firstly collected and centred, then excited by a radiofrequency dipole field, and finally ejected. This corresponds to case (b) in Fig. 4.21.

Magnetron Excitation

Magnetron excitation is needed for the first step for the application of the mass selective cooling technique which will be discussed in Sec. 6.4.3. Furthermore the determination of the magnetron frequency allows to verify the depth of the trapping potential U_0/d^2.

Fig. 6.5 depicts the number of ions ejected from the trap as a function of the excitation frequency ν_{Dipole}. The spectra have been obtained for an excitation time of $T_{Excite} = 10$ ms and excitation amplitudes of $A_{Dipole} = 50$ mV (left) and $A_{Dipole} = 200$ mV (right).

For an excitation amplitude of 50 mV a dip in the count rate can be recognised which indicates the resonance frequency ν_-. It was determined to be $\nu_- = 1014(10)$ Hz from this spectrum. This corresponds to a potential depth of $U_0/d^2 = 3.79(4) \cdot 10^4 \frac{V}{m^2}$. This value is slightly higher than $U_0/d^2 = 3.5 \cdot 10^4 \frac{V}{m^2}$ which has been obtained by fitting a parabola to the potential slope in the trap centre calculated with SIMION (see Sec. 5.2.1). The value corresponds to a magnetron frequency of $\nu_- = 940$ Hz. The difference of about 70 Hz results most likely from slightly different voltages applied to the inner trap electrodes due to the fact that the high-voltage amplifier used were not calibrated.

An increase of the excitation amplitude to 200 mV (right) broadens the resonance dip since the ions are driven further away from the trap centre. In addition, equidistant side bands become visible. The distance between the dips of 100 Hz is expected for an excitation time of 10 ms.

Once the magnetron frequency is determined, it is interesting to study which amplitude is required to drive all ions to orbits larger than the size of the extraction diaphragm. This is illustrated in Fig. 6.6. The number of ejected ions from the trap are shown as a function of the excitation amplitude A_{Dipole}. The excitation time was $T_{Excite} = 10$ ms. First the count rate decreases continuously to zero, but surprisingly ions come back for larger excitation amplitudes. A total of 75 % of the primary count rate is reached for $A_{Dipole} = 1.75$ V. For higher excitation

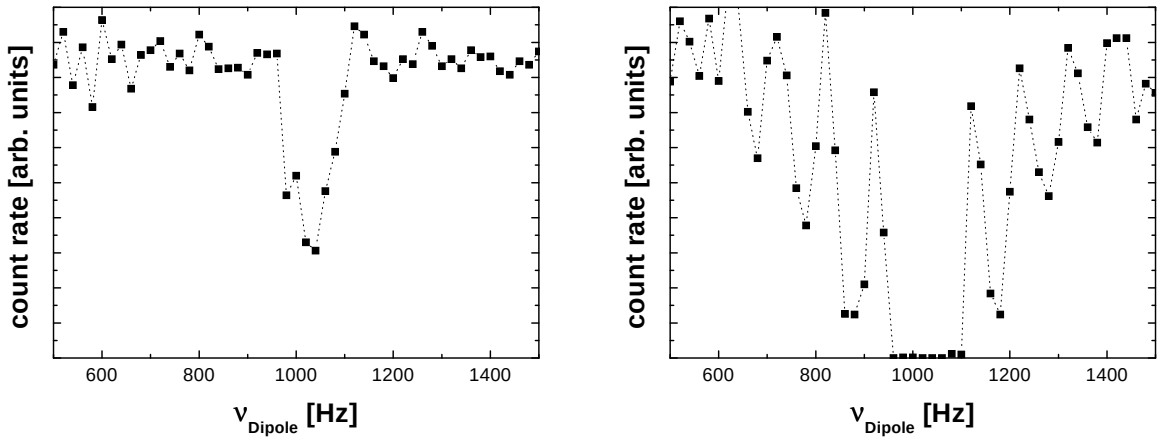

Figure 6.5: The number of ions ejected from REXTRAP as a function of the dipole excitation frequency ν_{Dipole} for an excitation time of $\mathsf{T}_{\mathrm{Excite}} = 10\,\mathrm{ms}$ and excitation amplitudes of 50 mV (left) and 200 mV (right).

amplitudes it decreases again to zero.

Such a peculiar dependency can be explained by trap imperfections. The magnetron radius increases during dipole excitation. The ions reach the outer regions of the trap. There the electric potential is not longer harmonic as required for Eq. (3.1) to be valid. As a consequence the magnetron frequency of the ion changes and the ion gets out of phase with the exciting rf field. For certain combinations of excitation amplitude and time the ions can then be recentred as it has been discussed in Sec. 3.3.2.

This observation is corroborated by results of further experiments. In these, the injected ions were centred ($\mathsf{T}_{\mathrm{center}} = 30\,\mathrm{ms}$). Secondly, they were magnetron excited for a variable time ($\mathsf{T}_{\mathrm{Excite}}$). In contrast to the experiment described above, they were finally recentred ($\mathsf{T}_{\mathrm{recenter}} = 30\,\mathrm{ms}$). The results for four different excitation times $\mathsf{T}_{\mathrm{Excite}}$ are shown in Fig. 6.7. The number of ejected ions is plotted as a function of the excitation amplitude.

For an excitation time of $\mathsf{T}_{\mathrm{Excite}} = 10\,\mathrm{ms}$ a recentring of the ions is possible up to an excitation amplitude of about 0.7 V. Then the count rate drops to zero. However, if $\mathsf{A}_{\mathrm{Dipole}}$ exceeds 1.4 V some ions are recentred again. A similar behaviour can be noted for all other excitation times. In these cases additional minima and maxima are observed shifted towards lower amplitudes.

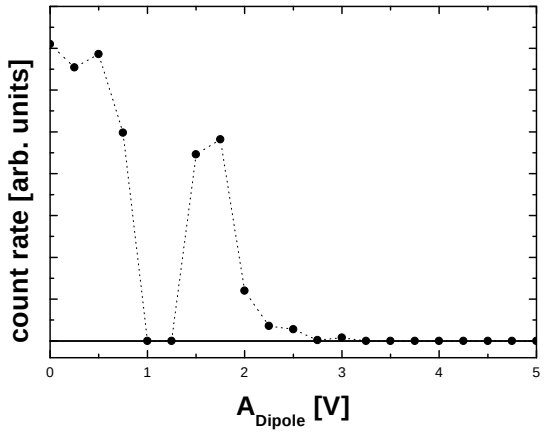

Figure 6.6: The number of ions ejected from REXTRAP as a function of the excitation amplitude $\mathsf{A}_{\mathrm{Dipole}}$ in the case of resonant dipole excitation with a frequency of ν_-. The excitation time was $\mathsf{T}_{\mathrm{Excite}} = 10\,\mathrm{ms}$.

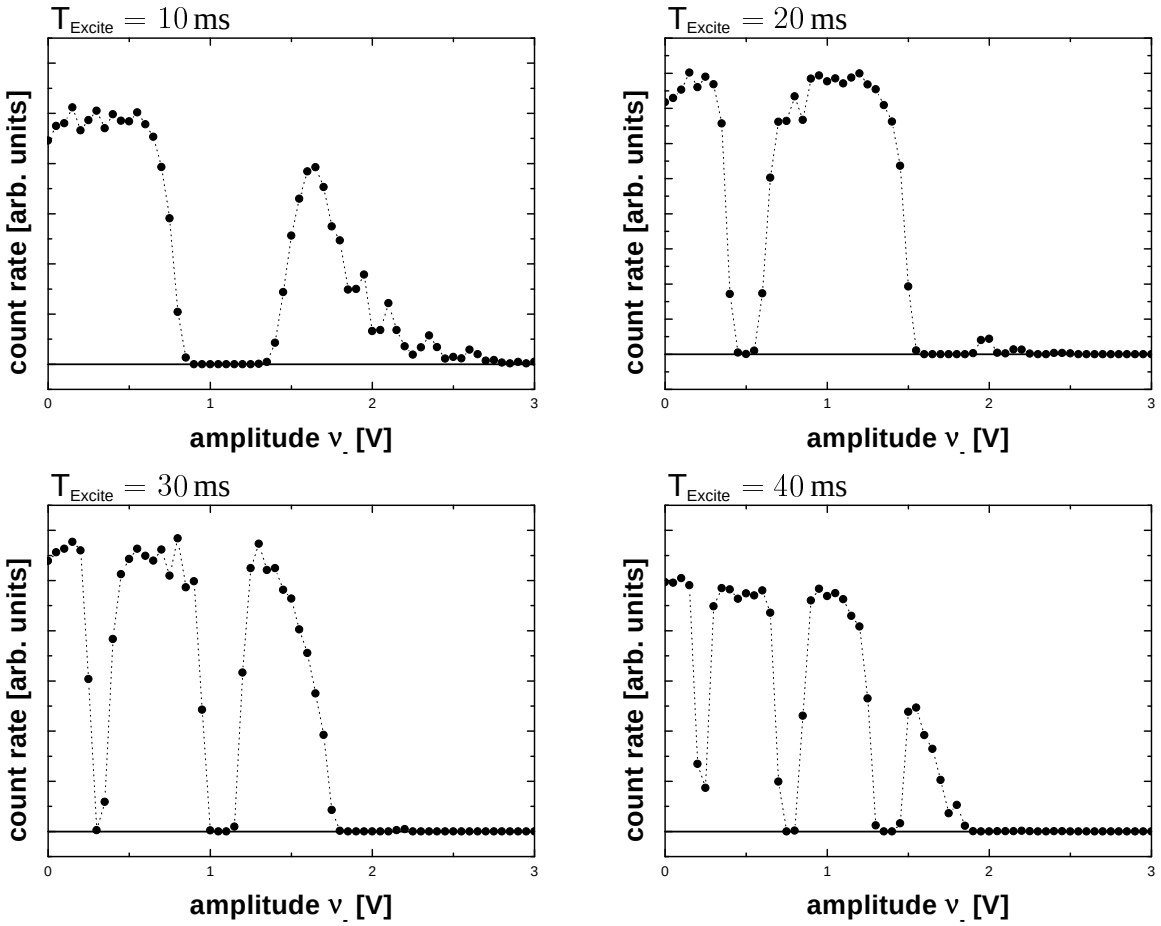

Figure 6.7: The number of ejected ions from REXTRAP as a function of the dipole excitation amplitude in the case of resonant dipole excitation with a frequency of ν_- and recentring with rf sideband cooling.

In general one finds that the extrema occur always at positions for which the term $\mathsf{A}_{\text{center}} \cdot \mathsf{T}_{\text{Excite}}$ has a fixed value. This is expected since the product $\mathsf{A}_{\text{center}} \cdot \mathsf{T}_{\text{Excite}}$ determines the final amplitude of the magnetron motion.

Cyclotron Excitation

Excitation of the ion motion at the reduced cyclotron frequency ν_+ is not required for the operation of REXTRAP. Nevertheless, it is interesting to verify that also in this case the trap works as expected.

Two typical spectra for the determination of ν_+ of $^{133}Cs^+$ ions in the REXTRAP system are given in Fig. 6.8. The plots depict the number of ions ejected from the trap as a function of the excitation frequency ν_{Dipole} in the vicinity of the expected frequency $\nu_+ = \nu_c - \nu_-$. Excitation amplitudes of $\mathsf{A}_{\text{Dipole}} = 100\,\text{mV}$ and 200 mV were used. The excitation time was $\mathsf{T}_{\text{Excite}} = 10\,\text{ms}$.

For an excitation amplitude of 100 mV (•) a dip in the count rate can be recognised which indicates the resonance frequency ν_+. An increase of the amplitude to 200 mV (○) broadens the resonance. The resonance frequency observed is in good agreement with the expected value of $\nu_+ = 342697(17)$ which is obtained by using $\nu_c = \nu_+ + \nu_-$ (see Eq. (3.8)). The cyclotron frequency $\nu_c = 343711\,\text{Hz}$ was taken from Table 6.2. For the magnetron frequency the experi-

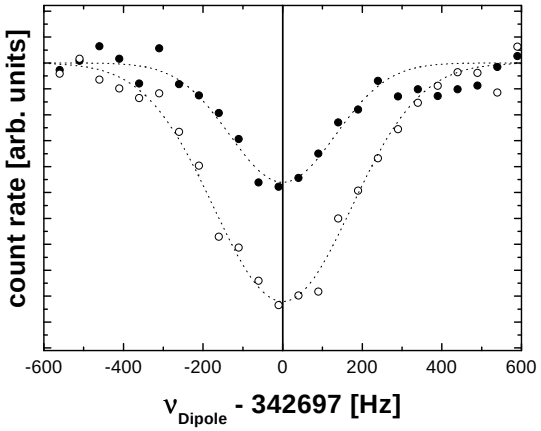

Figure 6.8: The number of ejected ions from REXTRAP as a function of the dipole excitation frequency ν_{Dipole} for different excitation amplitudes (•– $\mathsf{A}_{\text{Dipole}} = 0.1\,\text{V}$, ○– $\mathsf{A}_{\text{Dipole}} = 0.2\,\text{V}$). The excitation time was $\mathsf{T}_{\text{Excite}} = 10\,\text{ms}$. The were performed in the vicinity of the expected frequency $\nu_+ = \nu_c - \nu_-$.

mental value of $\nu_- = 1014(10)$ from above has been used. Thus, within the given uncertainty the frequency relation $\nu_c = \nu_+ + \nu_-$ is fulfilled in this case.

6.4.2 Quadrupole Excitation

Ions trapped in REXTRAP lose energy by collisions with the buffer gas. The dissipating force provided by the buffer gas leads to a reduction of the kinetic energy of the ions. This reduces the amplitudes of the axial and cyclotron motion, whereas the amplitude of the unstable magnetron motion increases (see Sec. 3.3.1). This can be circumvented by coupling of magnetron and cyclotron motion with an azimuthal radiofrequency quadrupole field at the cyclotron frequency. This sideband cooling technique was discussed in Sec. 3.3.2 and is decisive for the operation of REXTRAP.

During the commissioning phase of REXTRAP it turned out that the resonance curves obtained in cooling scans are more complex then expected. The left part of Fig. 6.9 shows a typical cooling scan for $^{133}Cs^+$. The number of ions is plotted as a function of the frequency ν_{center}. The scan was performed in the vicinity of the expected centring frequency ν_C listed in Table 6.2. REXTRAP was operated with a timing scheme corresponding to case (a) of Fig. 4.21. A centring amplitude of $\mathsf{A}_{\text{center}} = 3\,\text{V}$ and an excitation time of $\mathsf{T}_{\text{center}} = 25\,\text{ms}$ were used. The argon buffer gas pressure was $\mathsf{p}_0 = 0.9 \cdot 10^{-3}\,\text{mbar}$. One immediately realizes that the maximum of the resonance curve is shifted by about 90 Hz towards higher frequencies with respect to the expected frequency. Such a large shift cannot be explained by uncertainties of the determination of the magnetic field at the trap centre.

The right part of Fig. 6.9 gives a similar cooling scan of $^{133}Cs^+$. Compared to the case described above the buffer gas pressure in the trap was increased, the excitation amplitude was reduced to $\mathsf{A}_{\text{center}} = 1\,\text{V}$, and the centring time was increased to $\mathsf{T}_{\text{center}} = 100\,\text{ms}$. In addition, the voltages for the electrodes forming the harmonic potential in the trap centre have been reduced in order to lower the magnetron frequency ν_- to about 850 Hz.

The number of ions ejected reaches its maximum at the theoretical frequency value. However, there are additional "dips" in the count rate visible at frequency values close to ν_+ and $\nu_+ - \nu_-$. From the latter only about one half of the resonance can be seen. In the case of ν_+ the dip originates from an azimuthal dipole component of the excitation field, whereas the dip for $\nu_+ - \nu_-$ comes from an axially symmetric quadrupole component.

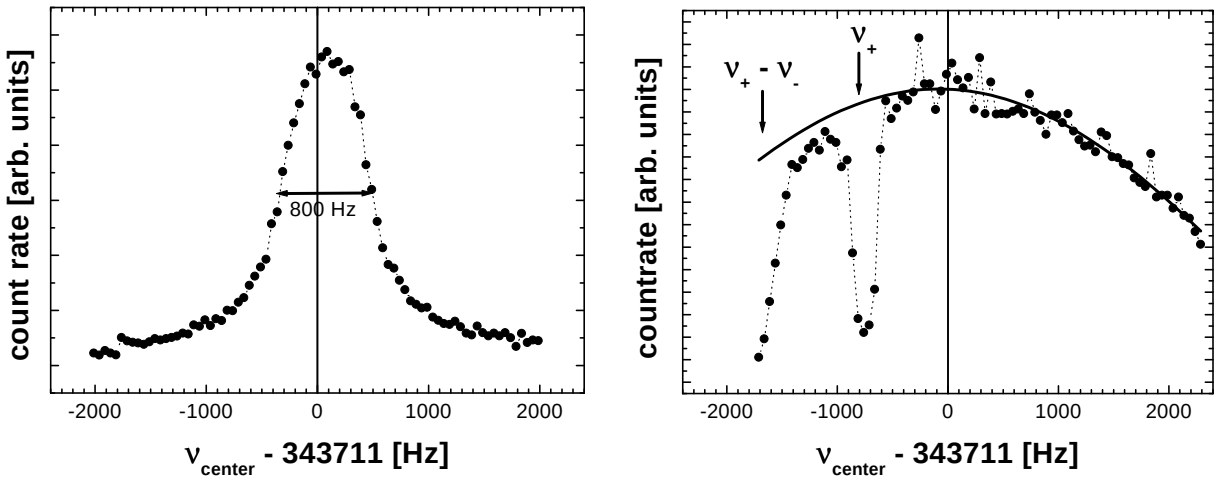

Figure 6.9: The number of ejected ions from REXTRAP as a function of the centring frequency ν_{center} for $^{133}Cs^{+}$. Two different sets of parameter were used in the left and right figure. The scans were performed in the vicinity of the expected resonance frequency $\nu_c = 343711\,\text{Hz}$. In the left spectrum the width of the resonance $\Delta\nu_{\text{FWHM}}$ is given. The solid line in the right spectrum indicates the expected shape of the cool resonance extrapolated from the right half of the spectrum.

The dipole components of the excitation field are not expected to occur. They rather result either from geometrical imperfections of the trap electrodes or from applying slightly different voltages to opposite electrodes of the four-fold split centre electrode. The latter can be caused by slightly different impedance values of the cables leading to the electrodes. The reason for the occurrence of the axially symmetric quadrupole component is the radiofrequency coupling scheme used (see Fig. 4.14). By feeding of the quadrupole radiofrequency voltages to only two opposite electrodes of the four-fold split centre electrode and grounding the others not only the desired azimuthal quadrupole field is generated but also an axially symmetric quadrupole field.

The effect of these additional excitation modes on a cooling resonance is schematically illustrated in Fig. 6.10. The individual modes are approximated by Gaussian shaped resonance curves. The width of the different resonance curves has been chosen for best visualisation of the resulting effects. The left part of Fig. 6.10 shows the curves of the individual resonances, whereas in the right part the undisturbed resonance is given in comparison to the final cool resonance. The latter is created by the superposition of the separate resonance curves. Its shape has dramatically changed in comparison to the undisturbed case. One recognises that the left shoulder of the resonance is now noticeable steeper, whereas its right side is hardly influenced. The result is a reduction of the width of the resonance and a shift of its centre towards higher frequencies. The total count rate is slightly reduced. An additional dip becomes visible at a frequency value of $\nu_+ - \nu_-$.

With this analysis Fig. 6.9 becomes better understandable. The shift of the optimal centring frequency towards higher frequencies observed in the left figure is the effect of the resonance at ν_+. The resonance at a frequency of $\nu_+ - \nu_-$ is hardly visible. It is adumbrated at the left end of the spectrum around -2 kHz by a slightly lower count rate.

The width of the cooling resonance is about $\Delta\nu_{\text{FWHM}} \approx 800\,\text{Hz}$. This value is somewhat smaller than expected from the simulations (see Fig. 5.2). However, this experimental value is not the true width of the ν_C resonance, but narrowed by the ν_+ resonance. Therefore, a good

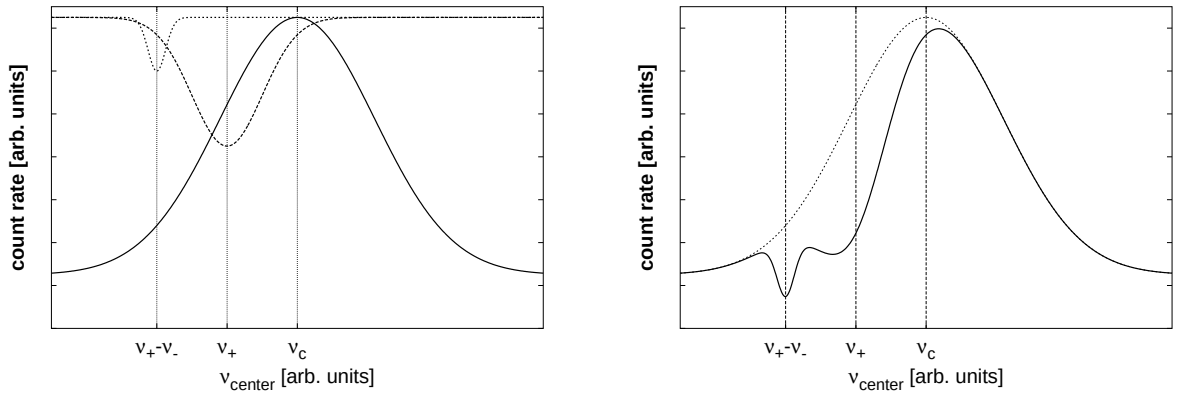

Figure 6.10: Principle line shape of a REXTRAP cooling resonance. The number of ejected ions is plotted as a function of the excitation frequency ν_{center}. **Left:** The three individual resonance curves for the resonances at ν_C (solid line) and ν_+, $\nu_+ - \nu_-$ (dotted line). **Right:** The superposition of the individual resonances (solid line) and the unperturbed ν_C resonance (dotted line).

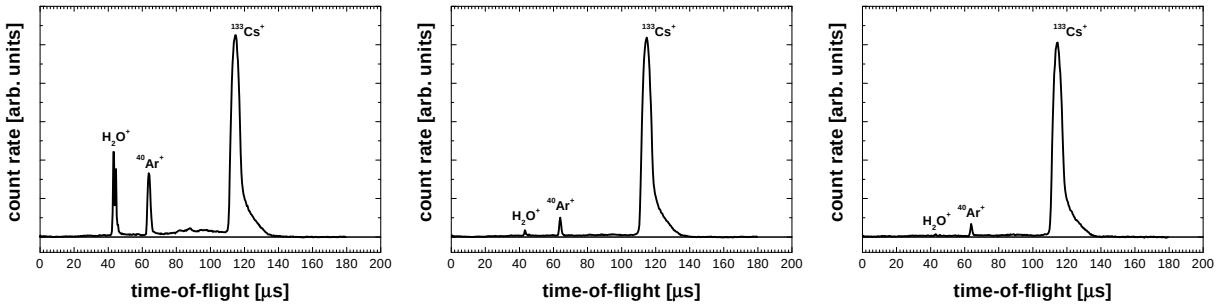

Figure 6.11: Time-of-flight spectra of ejected ions from REXTRAP in order to clean the ion bunches from contaminations. **Left:** Reference spectrum obtained without mass selective buffer gas cooling. **Middle:** TOF spectrum applying a sequential excitation procedure for the cleaning. **Right:** TOF spectrum applying a simultaneous excitation procedure for the cleaning.

agreement of the experimental and simulated data can be stated. A $\Delta\nu_{\text{FWHM}}$ value of 800 Hz corresponds to a mass resolving power of $\mathsf{R} \approx 400$ for $^{133}Cs^+$.

6.4.3 Mass Selective Cooling

A typical time-of-flight spectrum of $^{133}Cs^+$ is shown in the left figure of Fig. 6.11. It has been obtained using a timing scheme corresponding to case (a) of Fig. 4.21. A centring time of $\mathsf{T}_{\text{center}} = 15$ ms was used. The centring amplitude was $\mathsf{A}_{\text{center}} = 3$ V. In addition to time-of-flight peaks of injected ion species into REXTRAP those of "volitional" contaminants are found. They correspond to ionised argon buffer gas and residual water atoms. A detailed discussion of these time-of-flight spectra will be given in Sec. 6.6.2.

A selective removal of the unwanted ion species can be achieved by a mass selective cooling technique. In the first step the amplitude of the magnetron motion is increased by magnetron excitation. Since the magnetron frequency is practically mass independent all ions are driven

to significant large orbit. Subsequently, they would be hindered to be extracted from the trap by the ejection diaphragm. Afterwards only the desired ion species is recentred by quadrupole excitation with the cyclotron frequency ν_c of this ion species. Only these centred ions can then be extracted.

A timing scheme corresponding to case (c) of Fig. 4.21 has been used in order to apply a sequential excitation scheme for the cleaning of ions stored in REXTRAP. After being centred for $\mathsf{T}_{\text{center}} = 15\,\text{ms}$, the injected ions have been magnetron excited for $\mathsf{T}_{\text{excite}} = 10\,\text{ms}$, recentred for $\mathsf{T}_{\text{recenter}} = 15\,\text{ms}$, and finally ejected. The excitation amplitudes were $\mathsf{A}_{\text{center}} = 3\,\text{V}$ and $\mathsf{A}_{\text{excite}} = 0.6\,\text{V}$. The result is shown in the middle figure of Fig. 6.11. The time-of-flight peaks for the unwanted ion species are remarkably smaller in comparison to the left spectrum in Fig. 6.11 where no cleaning procedure was applied. In fact the fraction of $^{133}Cs^+$ in the ion bunch increased from 81 % to 96 %. The total number of $^{133}Cs^+$ ions remained constant, whereas $^{40}Ar^+$ and residual gas ions were reduced by 75 % and 90 %, respectively.

These results show that the standard procedure of mass selective cooling works with REXTRAP. Unfortunately, these sequential cleaning process has one important disadvantage. The overall cycle time of the trap is prolonged by magnetron excitation time $\mathsf{T}_{\text{excite}}$ and recentring time $\mathsf{T}_{\text{recenter}}$. In order to overcome this handicap a new procedure has been tested. Magnetron excitation was applied directly after the ion injection for a period of $\mathsf{T}_{\text{excite}} = 5\,\text{ms}$ starting at the same time as the quadrupole excitation, which was applied for $\mathsf{T}_{\text{center}} = 15\,\text{ms}$ (case (d) in Fig. 4.21). Excitation amplitudes of $\mathsf{A}_{\text{center}} = 3\,\text{V}$ and $\mathsf{A}_{\text{excite}} = 4\,\text{V}$ were used. The result is shown in the right figure of Fig. 6.11. An even better suppression of unwanted ion species was found compared to sequential cleaning. The number of $^{40}Ar^+$ and residual gas ions has been reduced by additional 7 % and 3 %, respectively. This increases the fraction of $^{133}Cs^+$ in the ejected ion bunch to 97 %. Also in this case no reduction of the overall number of ejected $^{133}Cs^+$ ions is observed.

Both types of applying mass selective buffer gas cooling have been proven to be extremely powerful methods to influence the composition of the ion bunches ejected from REXTRAP.

6.5 Determination of Optimum Operation Parameter

6.5.1 Cooling Parameters

The determination of optimal cooling parameters, i.e. buffer gas pressure, centring time and amplitude has been one of the most important tasks during the commissioning phase of REXTRAP. It was carried out with great care since it influences directly the overall performance of the system. These procedure is independent of the optimisation of the trap injection and ejection which will be described in Sec. 6.5.2.

The first point of concern is the buffer gas pressure the trap must be operated with in order to ensure high trapping efficiency and short cooling times. For this purpose the standard timing scheme corresponding to case (a) of Fig. 4.21 has been used, i.e. the ions are injected, centred, and finally ejected. The centring time was set to $\mathsf{T}_{\text{center}} = 20\,\text{ms}$ and an excitation amplitude of 3 V was used. In Fig. 6.12 the number of ejected ions from REXTRAP as a function of the argon buffer gas pressure is shown. The number of ions ejected increases linear up to a control voltage of $\mathsf{U}_{\text{control}} = 5.5\,\text{V}$ ($\mathsf{p}_0 = 0.9 \cdot 10^{-3}\,\text{mbar}$) applied to the buffer gas control unit.

For higher values it remains nearly constant, i.e. the saturation point is reached for the chosen centring time.

After having found a buffer gas pressure for trap operation a series of measurements was performed in order to study the amount of ejected ions as a function of centring time and amplitude. The same timing scheme as above was used but now with a variable excitation time $\mathsf{T}_{\text{center}}$. The results of the systematic investigation are shown in Fig. 6.13. The percentage of ejected $^{133}Cs^{+}$ ions is plotted in contour line plots as a function of excitation time $\mathsf{T}_{\text{center}}$ and the amplitude $\mathsf{A}_{\text{center}}$ for different argon buffer gas pressures. It was normalised to the highest count rate which occurred during this series of measurement, i.e. the percentage values do not correspond to the overall efficiency of the system. The error for the determination of the values is the short time fluctuation of the count rate. It was in the order of $5 \ldots 10\,\%$.

Except for the case of $\mathsf{U}_{\text{control}} = 5.25\,\text{V}$, where the excitation time was not sufficient, saturation of the number of ejected ions is reached. In the case of $\mathsf{U}_{\text{control}} = 5.5\,\text{V}$ it is achieved at an excitation time of $\mathsf{T}_{\text{center}} = 32.5\,\text{ms}$, whereas for $\mathsf{U}_{\text{control}} = 5.75\,\text{V}$ a centring time of around $\mathsf{T}_{\text{center}} = 17.5\,\text{ms}$ is sufficient. The corresponding excitation amplitudes $\mathsf{A}_{\text{center}}$ are about 2.5 V and 3 V, respectively. In order to be able to compare these experimental results with the numerical ones shown in Fig. 5.11 the excitation amplitudes $\mathsf{A}_{\text{center}}$ must be converted into quadrupole strength values V_Q. This can be achieved according to Eq. (3.18) via

$$V_Q = a\,\frac{\mathsf{A}_{\text{center}}}{r_0^2}\,, \tag{6.5}$$

where r_0 denotes the radius of the electrodes. The attenuation factor a is only approximately known for the configuration of the REXTRAP excitation electrodes and the radiofrequency coupling scheme used. Due to the fact that the rf-voltage for the generation of the rf field is only fed to one pair of electrodes the factor is close to $a = \frac{1}{2}$ if further attenuation factors can be neglected. After scaling the ordinates of Fig. 5.11 and Fig. 6.13 become directly comparable. The experimental excitation amplitude needed to reach saturation is slightly lower than the one obtained from the simulated plots, whereas for the excitation time an opposed behaviour is found. This indicates that the buffer gas pressure in the trap region p_{Trap} is slightly lower then postulated in Sec. 4.5.

Buffer gas pressure and excitation amplitude are two important values which determine the cooling performance of REXTRAP. Furthermore it is influenced by the cooling or centring time. The left part of Fig. 6.14 shows vertical sections through Fig. 6.13 for a buffer gas pressure

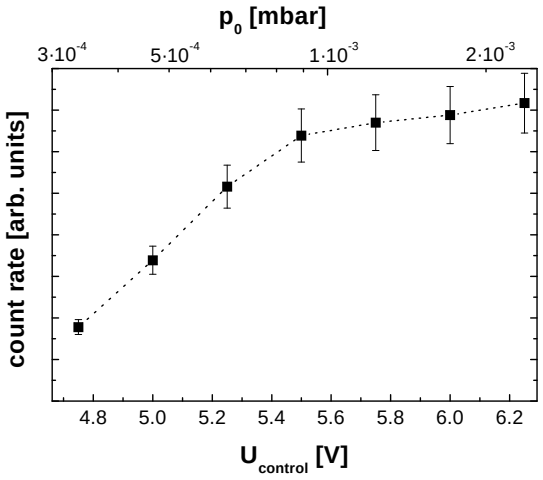

Figure 6.12: The number of ejected ions from REXTRAP as a function of the control voltage of the buffer gas regulator unit. The according argon gas pressure in the high pressure region was calculated using Eq. (4.1). An excitation time of $\mathsf{T}_{\text{center}} = 20\,\text{ms}$ was used.

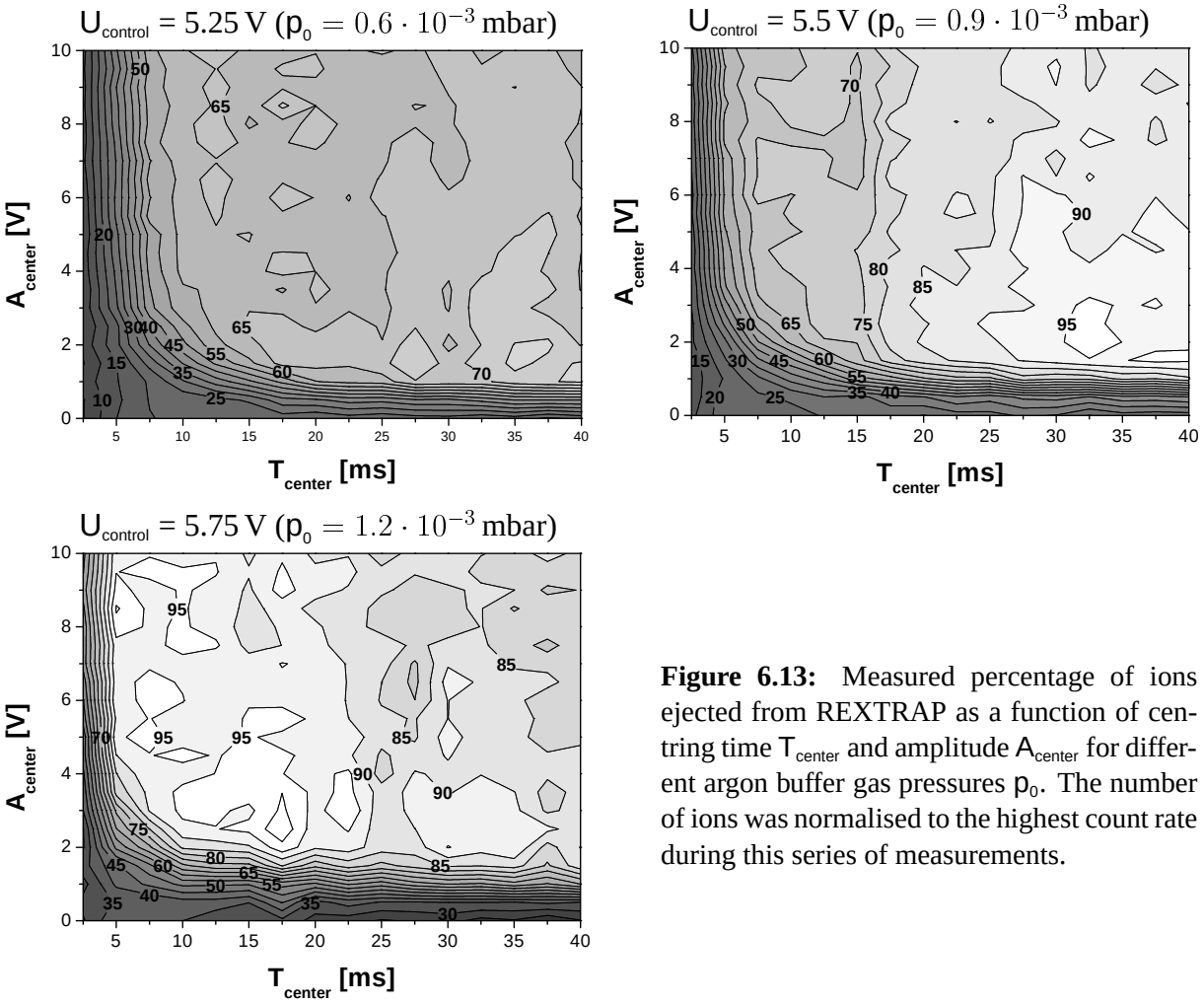

Figure 6.13: Measured percentage of ions ejected from REXTRAP as a function of centring time T_{center} and amplitude A_{center} for different argon buffer gas pressures p_0. The number of ions was normalised to the highest count rate during this series of measurements.

of $p_0 = 1.2 \cdot 10^{-3}$ mbar ($U_{control} = 5.75$ V). The number of ejected ions is plotted as a function of the excitation amplitude A_{center} for excitation times of $T_{center} = 5$ ms and $T_{center} = 15$ ms.

In both cases the number of ions ejected rises gradually for lower excitation amplitudes. At higher values saturation is reached. The corresponding amplitudes are $A_{center} = 8$ V for $T_{center} = 5$ ms and $A_{center} = 3$ V for $T_{center} = 15$ ms. The appropriate points are marked by arrows.

In the right part of Fig. 6.14 time-of-flight spectra are shown which have been obtained using the amplitudes where saturation is reached. The total number of ions extracted is slightly lower for the case of $T_{center} = 5$ ms. Additionally, the TOF peak for $^{133}Cs^+$ is remarkably broadened towards shorter time-of-flights. Both indicating that the centring process has not been finished for $T_{center} = 5$ ms. Thus, centring times of at least $T_{center} = 15$ ms are necessary to finish the cooling process.

The production of the raw data for contour plots like that of Fig. 6.13 is a very time consuming process and was therefore only carried out for the cases reported above. Due to the fact that the experimental results are in good agreement with the simulations performed it can be expected that for other ion species the behaviour is similar. In order to have short centring times an argon buffer gas pressure of $p_0 = 1.2 \cdot 10^{-3}$ mbar ($U_{control} = 5.75$ V) in the high pressure

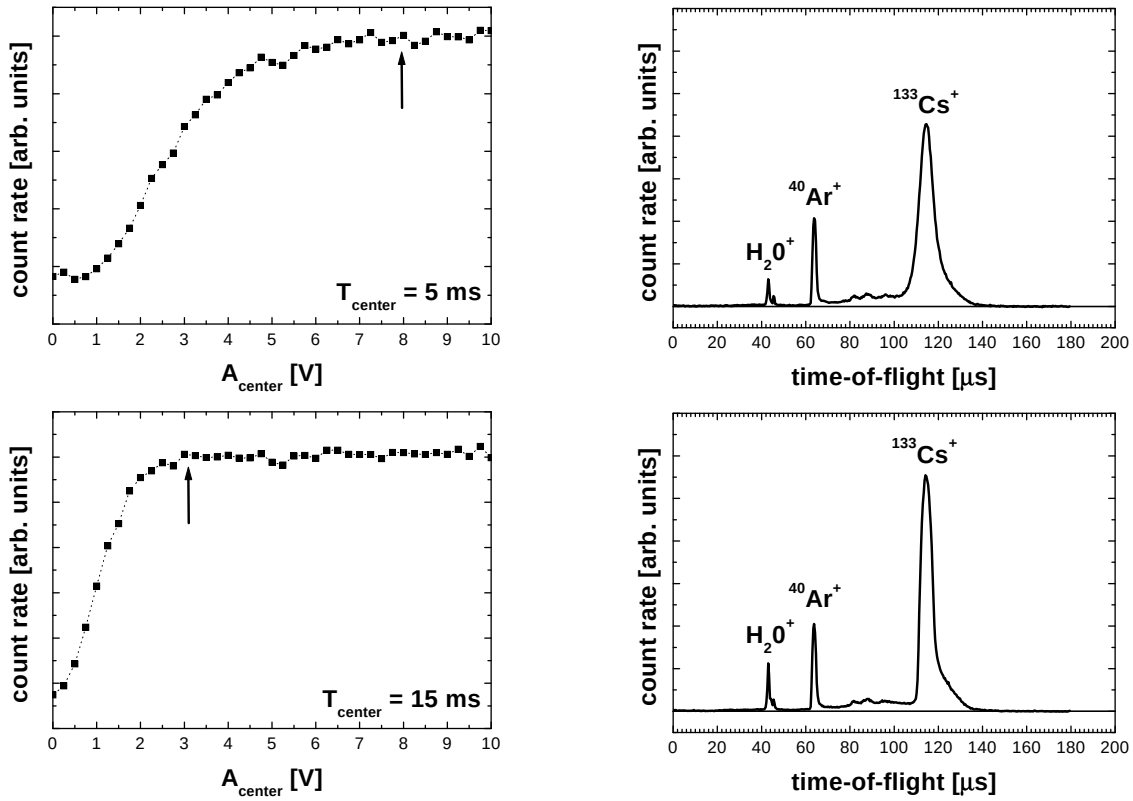

Figure 6.14: Left: The number of ions ejected from REXTRAP as function of the excitation amplitude A_{center} for rf side band cooling and excitation times $T_{center} = 5$ ms (top) and 15 ms (bottom). The amplitudes where saturation is reached are marked by arrows. **Right:** Time-of-flight spectra obtained for the saturation amplitudes.

region of the trap has been chosen for further measurements.

To ensure ensure short and cool ion bunches typical centring times of $T_{center} \approx 15 \ldots 25$ ms were used. For these cases only the optimum excitation amplitude for the centring process must be determined.

6.5.2 Injection and Ejection Parameters

In the following the procedure is described which must be carried out in order to optimise the injection and ejection parameter of REXTRAP. It can be divided into three parts. Firstly, the ion beam must be brought to a focal plane in front of REXTRAP either from the ISOLDE target or the test ion source. Secondly, the injection into the trap system has to be optimised for maximum ion transmission. Finally, the trap operation parameter must be adapted to the ion beam used and the demands of the particular experiments.

Normally, for on-line operation the tuning process is carried out with a stable ion beam from ISOLDE. Almost every target type offers a variety of different choices. For the tuning procedure a species should be chosen similar to the mass studied later.

Beam Transport to the Focal Plane in Front Of REXTRAP

A good starting point for the optimisation of the beam transport are the voltages given in Table 6.3 for the on-line and Table 4.2 for the off-line case. They have been found in a number of beam transport exercises. Then only moderate modifications should be necessary. In the diagnostic box in front of REXTRAP a beam focus should be achieved.

During the on-line tests an overall ISOLDE transmission of about 85 % to the beam line position RA0.FC90 has been reached. Although this is a standard transmission value of ISOLDE it turned out that the correct bending of the ion beam from the central beam line into the REXTRAP injection beam line was very crucial and sensitive to small deviations from the optimal transport voltages. A displacement of the bender in this switch yard by about 10 mm from its ideal position was later identified as the reason. The correction of this misalignment is planned which should make the beam transport less critical and yield even better transmission values.

Optimal Injection into REXTRAP

Optimal injection into REXTRAP requires a beam that is symmetric with respect to the magnetic field axis. In order to achieve this the trap timing is switched off and the ejection electrodes are set to the values used for extraction. The transmission through REXTRAP is optimised by measuring the beam current that arrives on the ejection plate (see Sec. 4.7) and by varying the voltages of the beam line elements of CA0.KI70, RA0.BE10, the RA0-quadrupole, injection kicker, and injection steerer. As an intermediate step the ISOLDE beam can first be optimised on the injection plate (see Sec. 4.7).

Fine Tuning

The fine tuning of injection and ejection parameters is carried out with trapped and cooled ions by optimising the count rate of the ejected ion bunches with respect to the different parameter. It normally starts with the injection stage. Parameters to be optimised are the voltages of the quadrupole RA0, injection kicker, injection steerer, retardation potential and electrode01. When an optimum has been found the procedure is continued with the ejection part. Parame-

	Calculated	Experimental		Calculated	Experimental
	Value [V]			Value [V]	
GPS.QS030	−1634	−1500	CA0.QS40	−2131	−2062
GPS.QP040	3474	3420	CA0.QP50	2218	2531
GPS.QP050	−1666	−1820	RA0.QP20	−2052	−1955
GPS.QP170	−120	−105	RA0.QP30	2873	3045
GPS.QP180	439	451	RA0.QP40	−1731	−1890
GPS.QP520	2290	2240			
GPS.QP530	−2840	−2800			
GPS.QP540	−2502	−2670			
GPS.QS550	2681	2700			

Table 6.3: Calculated and experimental voltages of ISOLDE beam-line elements for optimal beam transport from the target of the General Purpose Separator area towards the focal plane in front of REXTRAP.

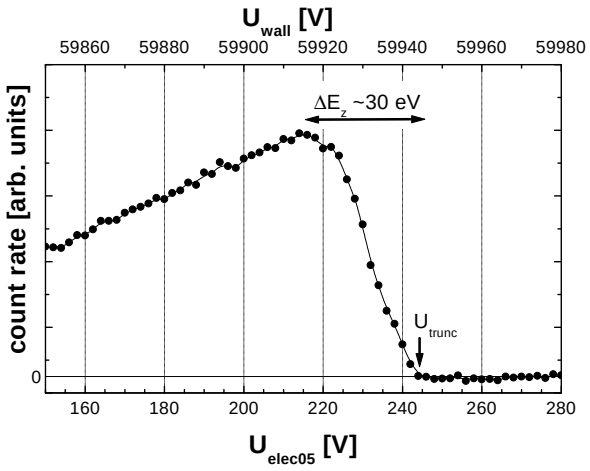

Figure 6.15: Number of ejected $^{133}Cs^{+}$ ions from REXTRAP as function of the voltage applied to electrode05 U_{elec05}. The top scale shows the height of the potential wall U_{wall}. Additionally, the truncation voltage U_{trunc}, the corresponding ISOLDE acceleration voltage, and the radial energy uptake ΔE_z are marked.

ters concerned are the voltages applied to electrode40, ejection kicker, and ejection steerer, and the acceleration potential. Optimised values both for off-line as well as on-line operation are compiled in Table 4.2.

An ion beam delivered by ISOLDE or by the test ion source is practically mono-energetic. If it enters the magnetic field longitudinal energy is partly transferred into radial energy. This process of radial energy uptake has been discussed in Sec. 5.3.2. Thus, the longitudinal energy spread ΔE_z of the ion beam can reach several ten eV (see Fig. 5.8). Accordingly, the potential wall at the trap entrance has to be low enough in order to not reflect ions. At the same time it must be so high that the energy loss of the ions during one oscillation in the trap is sufficient not to overcome it again (see Sec. 5.3.2). Therefore, the determination of the height of the potential wall U_{wall} is a critical parameter during the optimisation of the injection process. Its absolute value is given by $U_{wall} = U_{elec05} + U_{HV}$, where U_{elec05} and U_{HV} denote the voltages applied to the high-voltage platform and to electrode05, respectively.

For a scan over U_{wall} one expects a constant count rate as long as U_{wall} is smaller than a voltage which corresponds to $E_{beam} - \Delta E_z$. E_{beam} denotes the ion beam energy delivered by ISOLDE or the test ion source. For higher voltages the count rate should fall until it reaches zero at a value for U_{wall} which corresponds to a beam energy E_{beam}.

A typical scan of the voltage applied to electrode05 is shown in Fig. 6.15. The top scale of the spectrum shows U_{wall}. It was obtained with a REXTRAP high-voltage of $U_{HV} = 59\,700$ V. The ISOLDE beam energy was $E_{beam} = 59\,937(2)$ eV. The number of $^{133}Cs^{+}$ ions ejected from the trap increases until it reaches a maximum at 215 V. For higher values it decreases to zero which is reached for a voltage of $U_{trunc} = 244$ V. The curve looks as it was expected but for the fact that the count rate increases for lower values of U_{elec05}. The reason for this is that electrode05 has a small focusing effect for the incoming ions. The value for the radial energy uptake of $\Delta E_z = 30$ eV is in perfect agreement with the one obtained numerically (see Fig. 5.8).

Furthermore this measurement allows the calibration of the REXTRAP high-voltage power supply with respect to voltage supply used for the ISOLDE ion sources and front-end. Collinear laser spectroscopy has proven that that the error of the ISOLDE high-voltage read-back does not exceed 2 V [Gei99]. Comparing the total height of the potential wall $U_{wall} = 59\,944$ V with the ISOLDE acceleration voltage of 59 937(2) V leads to the conclusion that the REXTRAP high-voltage power supply has a maximal systematic error of 10 V.

6.6 Summary of REXTRAP Performance

The final investigations of the on-line performance of REXTRAP was carried out in the beginning of December 1999. A simple test target equipped with a tungsten surface ioniser was used (ISOLDE test target #119). It contained two independent target material reservoirs filled with cesium and aluminium compounds, respectively. Thus, beams of $^{133}Cs^+$, and $^{27}Al^+$ with currents up to a few nano-amperes were available. In addition, a wide variety of beams of surface-ionised target impurities were observed and used. This included stable isotopes from lithium, sodium, potassium, rubidium, and barium. The currents of these impurity beams had an intensity several orders of magnitudes less than the cesium and aluminium beams.

Fig. 6.16 shows cooling scans (left) and time-of-flight spectra (right) for $^{23}Na^+$, $^{27}Al^+$, $^{39}K^+$, $^{85}Rb^+$, and $^{133}Cs^+$ obtained during this on-line test. Most of the parameters used can be found in Table 4.2. A timing scheme corresponding to case (a) of Fig. 4.21 has been applied. The collection time $T_{collection}$ was varied to inject $10^4 \ldots 10^5$ ions/pulse in all cases. The centring time was $T_{center} = 15\,\text{ms}$. The trap set-up was carefully optimised for the different cases. This included the optimisation of ion injection (see Sec. 6.5.2) as well as the optimisation of the centring process (see Sec. 6.5.1) for every ion species. The optimum centring amplitudes A_{center} obtained during this procedure are listed in Table 6.4. One observes that A_{center} reduces as the mass number increases. The reason for this is that larger excitation amplitudes are needed to counterbalance the higher damping coefficient for the lighter ion species (see Fig. 3.9 and Table 3.1). Furthermore, larger amplitudes are needed to compensate the attenuation of the rf feeding lines which rises significantly for the higher rf frequencies.

6.6.1 Cooling

The cooling scans shown in Fig. 6.16 have been performed in the vicinity of the expected resonance frequencies for the different ion species. The line shapes of the observed resonance curves are equivalent to the ones discussed Sec. 6.4.2. The resonance frequencies indicated by arrows are shifted towards higher values due to the ν_+ resonance for all cases but for $^{85}Rb^+$. For the latter the statistics is not sufficient to observe an occurring shift. Absolute values range from about 80 Hz in the case of $^{133}Cs^+$ to nearly 2 kHz for Al^+. For the cases of $^{23}Na^+$ and $^{27}Al^+$ a substantial reduction of the maximum possible count rate can be seen.

The width of the cooling resonances increases as the ion mass decreases. It is not reasonable to give values for the mass resolving power of the centring process but for $^{133}Cs^+$ (Sec. 6.4.2). This has two reasons. Firstly, the quadrupole resonances are strongly influenced by the additional resonances and secondly, in most of the cases the base line of the resonance was not recorded. Thus, a reasonable comparison with the simulated cooling resonances (see Sec. 5.3.3) is not possible.

6.6.2 Characteristics of Ejected Ion Bunches

The time-of-flight spectra shown in the right column of Fig. 6.16 have been obtained by applying the optimum centring amplitudes and frequencies described above for the centring procedure.

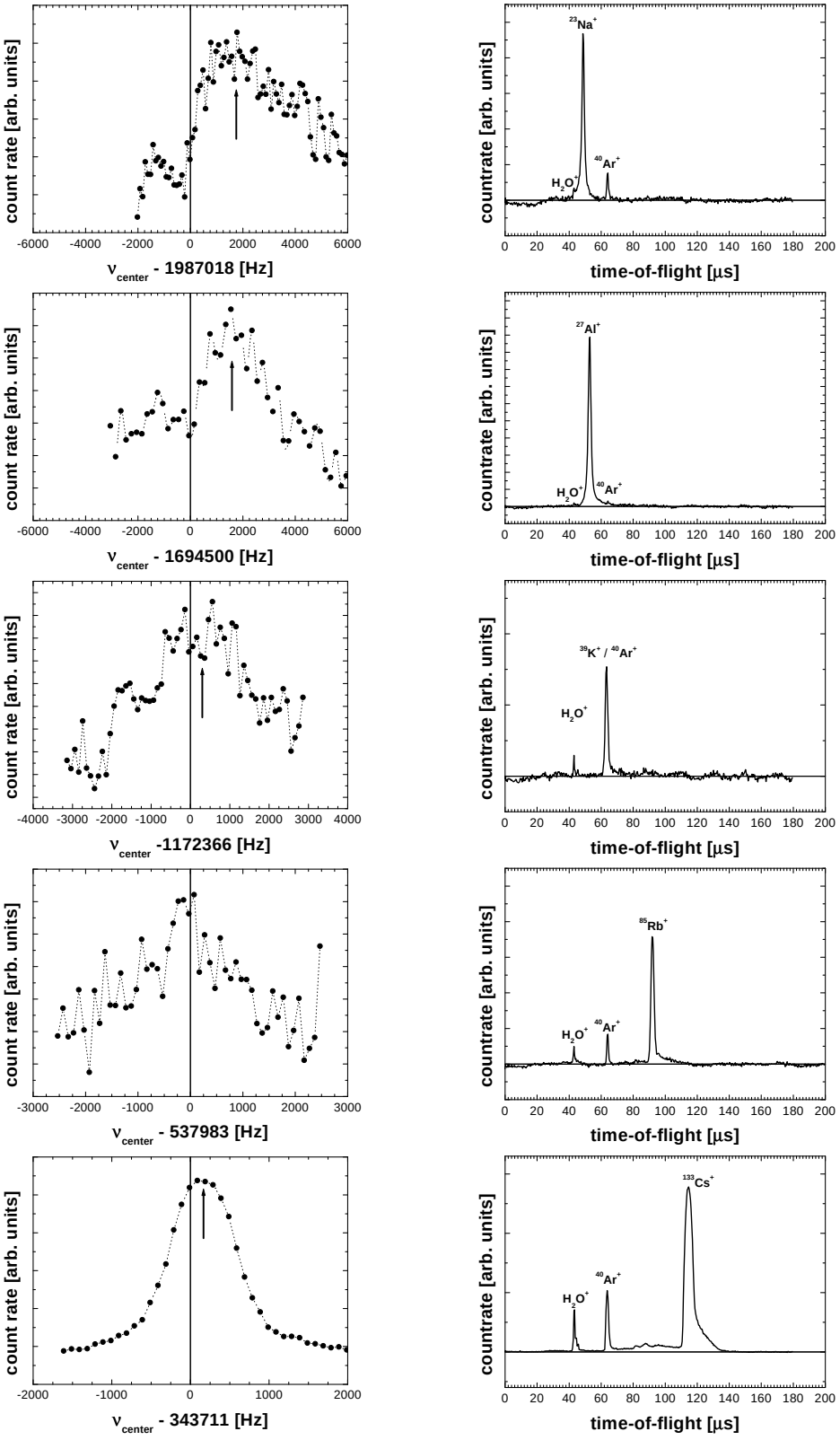

Figure 6.16: Cooling scans (left) and time-of-flight spectra (right) for $^{23}Na^+$, $^{27}Al^+$, $^{39}K^+$, $^{85}Rb^+$, and $^{133}Cs^+$ (top to bottom). The cooling scans have been performed in the vicinity of the expected frequency. The optimal centring frequencies are indicated by arrows.

Pulse Shape of the Time-Of-Flight Peaks

The time-of-flight for the ejected ion pulses is in good agreement with the calculated values. However, the pulse shape exhibits remarkable differences. The simulations described in Sec. 5.3.4 predict symmetric peaks. In the experimental spectra the rising edge is well reproduced. The falling edge on the other hand does not drop as sharp as expected. A long tail can be observed. This is in particular true for the cases of $^{133}Cs^{+}$, and $^{85}Rb^{+}$. The reason for this long tail is not completely understood. A most likely reason is that a small fraction of the ions collides with buffer gas atoms during the extraction process. This decelerates the particle and finally leads to a longer time-of-flight. For the buffer gas pressure used the mean free path for the extracted particles is in the order of one metre in the ejection and accelerating part of the trap system. Thus, ion neutral collision can occur during extraction.

Contaminations

In addition to time-of-flight peaks of "volitional" ions contaminations are found in the TOF spectra. They can be assigned to mass number 17, 18, and 40, corresponding to water molecule ions (H_2O^{+}), hydroxide ions (OH^{+}), and ionised buffer gas atoms (^{40}Ar). As origin for the creation of these unwanted ion species secondary electrons have been identified. These electrons are produced by ions hitting the surface of electrodes. Two different locations are mainly affected: the beam gate in front of REXTRAP and the injection diaphragm at the trap entrance. After creation the secondary electrons are trapped in Penning trap like regions formed by maxima in the electric potential and the magnetic field present at this location. The corresponding energy minimum for electrons can be found at the einzel lenses around electrode01 and electrode40, as well as at electrode05 and electrode36. Once trapped the electrons have sufficient energy to ionise buffer gas atoms and residual gas atoms and to crack water molecules to hydroxide ions. Ions produced at the injection diaphragm are especially dangerous since they can enter the ion trapping region of the system and are then trapped, cooled, and finally ejected. However also ions created at other points can have large effects since they are accelerated and possibly strike a surface again producing secondary electrons.

In addition to ionization by electron impact unwanted ions could also be created by charge exchange reactions. However, this can practically be ruled out for the reported cases. Alkali elements have a very low ionization potential compared to noble buffer gases.

There are several measures that allow to reduce or even suppress the unwanted ion species. One is to position small tungsten wires across all endangered electrodes. This has been done and proven to absorb a large fraction of the secondary electrons. Additionally, a finishing of the surface of critical electrodes with a graphite compound is planned. Such a treatment reduces the emission of secondary electrons by increasing the work function of the surface [Sol00]. Furthermore, tests confirmed that the count rate of the unwanted ion species can be reduced significantly if the the ISOLDE ion beam is not swept over the electrode surfaces in front of REXTRAP. Therefore, in all future on-line experiments the beam gate of the ISOLDE mass separator will be used.

The selective removal of the unwanted ion species can also be achieved by the mass selective cooling technique which has been discussed in Sec. 6.4.3.

	A_{center} [V]	Count Rate [ions per pulse]	Efficiency measured	Efficiency calculated
$^{23}Na^+$	10	$3.0 \cdot 10^3$	20(6) %	30 %
$^{27}Al^+$	10	$1.5 \cdot 10^4$	28(8) %	—
$^{39}K^+$	5	$1.5 \cdot 10^4$	28(8) %	36 %
$^{85}Rb^+$	6	$2.9 \cdot 10^3$	*14(4) %	32 %
$^{133}Cs^+$	3	$4.3 \cdot 10^4$	27(8) %	25 %

* The injection stage was optimised for $^{27}Al^+$ for that measurement.

Table 6.4: Measured and calculated efficiency for different ion species accumulated, cooled, and bunched in REXTRAP. In addition the centring amplitude A_{center} and the count rate is given.

Emittance

The emittance of the ejected ion bunches has not been investigated experimentally during the work presented here. However, it is an important characteristics of the ion bunches since it determines directly the transfer and injection process of the REXTRAP ion bunches into REXEBIS. It turned out that the simulations described in Sec. 5 reproduce the experimental performance of REXTRAP quite well. Consequently, the emittance of the ion bunches delivered by REXTRAP should be in the order of the values derived in Sec. 5.3.4. For the values given a transport and injection into REXEBIS without difficulty should be feasible. The according test will be carried out if the set-up of the transport beam line and REXEBIS are finished.

6.6.3 Efficiency

One of the most important questions of the performance of REXTRAP is the overall efficiency of the system, i.e. which amount of the injected ion beam can be extracted as ion bunch. A compilation of the efficiency values for on-line operation is given in Table 6.4. The appropriate numbers have been extracted from the time-of-flight spectra shown in Fig. 6.16. They have a relative large absolute error, which is due to the uncertainty of the determination of the amplification V of the ion detection system (see Sec. 6.2.1). However, the proportion among themselves remains unaffected. For comparison the calculated efficiencies are listed too. These values have been obtained by combining injection efficiency (Fig. 5.6) and centring efficiency (Table 5.2) for the different ion species.

An experimental efficiency of nearly 30 % has been found for all cases but $^{85}Rb^+$ and $^{23}Na^+$. For the case of $^{133}Cs^+$ the experimental value of 27(8) % is in good agreement with the simulated value of 25 %. For all other cases the experimental values are considerably smaller than the simulated ones. This is not astonishing for $^{85}Rb^+$ since for this test the injection stage of REXTRAP was not optimised due to the limited amount of on-line time available. The settings for $^{27}Al^+$ were used instead. This proves again that a careful adjustment of all stages of REXTRAP for each ion species is necessary for an optimal performance of the system. One reason for the reduced experimental efficiency for $^{23}Na^+$ and $^{39}K^+$ results from the fact that the voltage applied to electrode05 which was optimised for Cs^+ (see Fig. 6.15) was not re-optimised when a new isotope was chosen. Thus ions with a radial energy uptake of more than 30 eV were reflected by the potential wall at the trap entrance. According to the simulations a fraction of 20 %

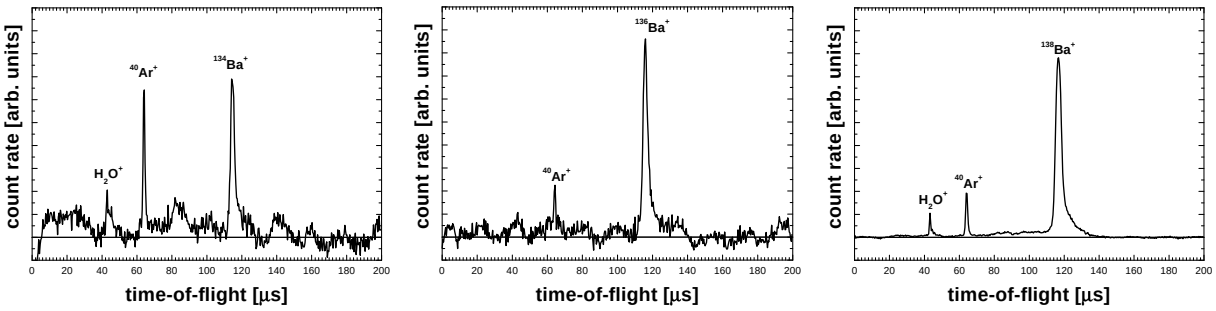

Figure 6.17: Time-of-Flight spectra of ejected $^{134}Ba^{+}$ (left), $^{136}Ba^{+}$ (middle), $^{138}Ba^{+}$ (right) from REXTRAP. The relative scale of the ordinates of the different spectra is 1:2:20.

to 30 % of $^{23}Na^{+}$ and $^{39}K^{+}$ is expected to be affected (see Fig. 5.8). Taking this into account the expected efficiencies become 21 % for $^{23}Na^{+}$ and 29 % for $^{39}K^{+}$, respectively. Then both values are in very good agreement with experimental observed efficiencies.

Furthermore for the case of $^{23}Na^{+}$ it can not be excluded that a substantial fraction of ions is lost due to the influence of the decentring ν_{+} resonance (see Fig. 6.16).

Constancy of Efficiency

An important characteristics of REXTRAP is up to what extent the efficiency depends on the number of injected ions. Investigations were carried out using stable barium beams from ISOLDE. Barium offers seven different stable isotopes covering a wide abundance range [Pfe98]. Thus, isotopical clean beams of $^{132}Ba^{+}$, $^{134}Ba^{+}$, $^{136}Ba^{+}$, and $^{138}Ba^{+}$ with intensities varying over several orders of magnitude were used.

^{138}Ba is the most frequent barium isotope with a natural abundance of 71 %. The average current of this isotope delivered by ISOLDE was well below the detection limit of the ISOLDE ion detection systems of about 1 pA. Nevertheless, a time-of-flight peak can be found in the corresponding TOF spectrum of Fig. 6.17. The count rate was 11 100 ions/pulse. Even for ^{134}Ba, and ^{132}Ba where the natural abundance drops to 7.854 %, and 2.417 %, respectively time-of-flight peaks are clearly visible. Count rates of 1000 ions/pulse for ^{136}Ba and 410 ions/pulse for ^{134}Ba have been recorded for these cases. Although for the latter the TOF peak is still above the noise level it is obvious that one approaches the detection limit of the used combination of MCP and oscilloscope. Thus it is not astonishing that an identification of ^{132}Ba in a corresponding time-of-flight spectra was not possible since the expected count rate would have been again reduced by a factor of 25. However, it is believed that also for this count rate the trap is still well performing.

Due to the fact that it was not possible to measure the current of the injected beams an absolute efficiency value of the trap system can not be given for these cases. Nevertheless, it is possible to compare the count rates obtained for the different isotopes according to their natural abundance. The result of this is given in Table 6.5. The relative abundances have been normalised to that of ^{138}Ba. The experimental values of 9 % for ^{136}Ba and 4 % for ^{134}Ba are in good agreement with the expected ones of 11 % and 3.4 %, respectively. It can therefore be concluded that the performance of REXTRAP does not change when working with a very low

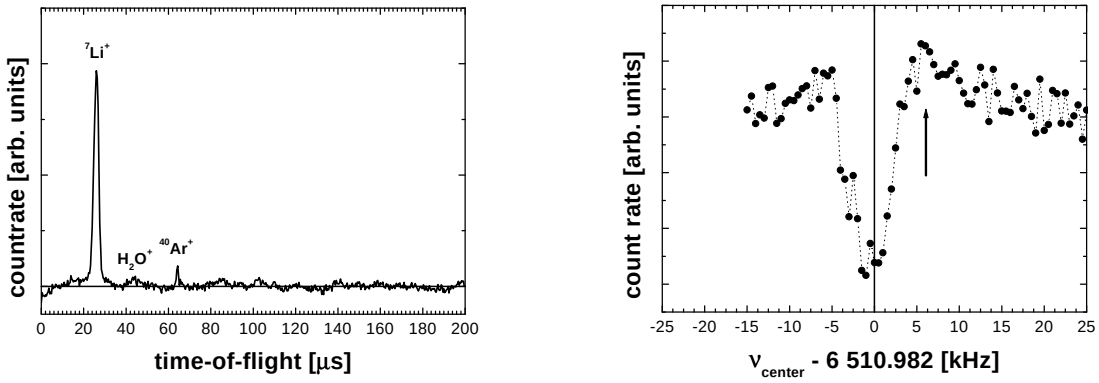

Figure 6.18: Left: Time-of-flight spectrum for $^7Li^+$ ion bunches ejected from REXTRAP. **Right:** Cooling scan for $^7Li^+$. The scan was performed in the vicinity of the expected frequency $\nu_c = 6\,510\,982$ Hz. The optimum centring frequency is marked with an arrow.

number of ions. The implementation of a new more sensitive ion detection system is planned which will allow to verify that the system can be operated even with single ions.

If the number of injected ions is substantially increased a decline of the efficiency of REXTRAP is expected. This is due to the fact that the size of the ion cloud increases which is due to electrostatic repulsion among the ions. If the radial dimension of the cloud becomes larger than the opening of the extraction diaphragm the ions are lost during extraction. The effects of larger ion numbers in the trap will be discussed in detail in Sec. 6.6.5.

6.6.4 $^7Li^+$ — What a surprise!

While checking the ion beams produced by the target it was looked for $^7Li^+$. Lithium is like sodium a frequent contaminant of various chemicals and it is therefore not unusual to find lithium beams from different ISOLDE targets.

There was no evidence for the presence of a lithium ion beam neither from the scanner pictures nor from current measurements from the ISOLDE Faraday cups. Nevertheless, the ISOLDE mass separator was set to mass number seven and the beam gate was opened. A time-of-flight spectra shown in Fig. 6.18 has been obtained. A timing scheme according to case (a) in Fig. 4.21 was used. In contrast to all other cases reported no centring quadrupole field

	literature abundance	count rate [ions/pulse]	relative abundance natural	relative abundance experimental
^{132}Ba	0.101 %	—*	0.1 %	—*
^{134}Ba	2.417 %	410	3.4 %	4 %
^{136}Ba	7.854 %	1000	11.0 %	9 %
^{138}Ba	71.700 %	11000	100.0 %	100 %

*detection sensitivity too low

Table 6.5: Literature abundance, recorded count rate as well as relative natural and experimental abundance of investigated stable barium isotopes. The relative abundance is normalised to that of ^{138}Ba.

was applied. The ions was only allowed to cool for $T_{center} = 15\,\text{ms}$. The time-of-flight spectra shows clearly a peak which corresponds to mass number seven. This is not surprising since the REXTRAP ion detection system is much more sensitive than the ISOLDE ones. However, cooling of $^7Li^+$ with argon buffer gas seems to be very unlikely due to the large difference in mass. This is supported by cooling simulations carried out where no ion cooling effect was found for this ion-neutral combination (see Sec. 5.3.3). Therefore, the only cooling method that can be imagined is that the lithium ions have been cooled either by residual gas atoms or ions.

In addition to the time-of-flight spectra a cooling scan of $^7Li^+$ is shown in Fig. 6.18. The scan was performed in the vicinity of the expected frequency $\nu_c = 6\,510\,982\,\text{Hz}$. A centring amplitude of $A_{center} = 10\,\text{V}$ was used. Only a slight increase of the number of ejected ions can be noticed which results from a very broad resonance. The optimal centring frequency is marked with an arrow. It is shifted towards higher frequencies due to the ν_+ resonance. The latter is visible as a several kilo-Hertz wide dip. The reason for the large width of both resonances is not completely understood. It results most likely from the combination of the large amplitude used and a high damping constant for $^7Li^+$.

6.6.5 Effects at High Ion Numbers

The characteristics of REXTRAP has also been investigated for very large ion numbers. For this purpose the number of $^{133}Cs^+$ ions injected into the trap has been controlled by varying the collection time T_{coll} over several orders of magnitude. Fig. 6.19 gives an overview of the results. Time-of-flight spectra, and scans in order to determine the optimal frequencies for magnetron and cyclotron excitation as well as cooling scans are shown for a count rate of $1.2 \cdot 10^4$, $1.7 \cdot 10^5$, $7.2 \cdot 10^5$, and $1.6 \cdot 10^6$ ions/pulse. The different cases will be discussed in the following.

Shape of Time-Of-Flight Spectra and Ion Numbers

In order to obtain the time-of-flight spectra shown in the left column of Fig. 6.19 a timing scheme corresponding to case (a) in Fig. 4.21 was used. Centring time and amplitude were $T_{center} = 15\,\text{ms}$ and $A_{center} = 3\,\text{V}$, respectively. The centring frequency was adapted to the number of ions for optimum centring efficiency. This was necessary since a shift of the optimum frequency for the centring process was observed which will be discussed further down.

The $^{133}Cs^+$ peak in the time-of-flight spectra changes significantly with increasing ion numbers. It becomes broader and moves towards shorter times. Especially for the highest count rate the peak ranges over about 40 µs. The explanation for this is an axial expansion of the ion cloud due to the internal electrostatic repulsion among the ions.

The number of ions ejected from the trap has been determined assuming a constant amplification of the ion detection system. However, there are indications that this is not the case. Firstly, the efficiency of the whole system decreases for the two cases with the highest count rate to one third and one fourth, respectively, in comparison to the case of $1.2 \cdot 10^4$ ions/pulse ejected ions. Assuming constant injection efficiency, the reason for this could be that due to electrostatic repulsion among the ions the radial extension of the ion cloud is larger than the opening of the extraction diaphragm. Furthermore, in the case of $1.6 \cdot 10^6$ ions/pulse the base line of the TOF spectrum starts to oscillate indicating that the ion detection system is saturated. The origin of that reduction of the experimentally observed efficiency remains unclear. Thus

in the two cases with the highest count rate the number of ions ejected from the trap could in reality be up to three to five times higher.

To how far the transfer and subsequent capture process in REXEBIS is influenced by the change of the width of the ejected ion bunches must be evaluated in further experiments.

Resonance Shapes and Frequency Shifts in the Case of Dipole Excitation

The dipole excitation scans, i.e. the scans in order to determine the magnetron and reduced cyclotron frequency are shown in the middle columns of Fig. 6.19. They have been carried out using a timing scheme corresponding to case (c) in Fig. 4.21. The ions were firstly centred applying a centring amplitude of $\mathsf{A}_{\text{center}} = 3\,\text{V}$ for a period of $\mathsf{T}_{\text{center}} = 15\,\text{ms}$. For the subsequent excitation an amplitude of $\mathsf{A}_{\text{excite}} = 200\,\text{mV}$ was used for a period of $\mathsf{T}_{\text{excite}} = 10\,\text{ms}$.

The magnetron excitation scans exhibits clearly the reduction of the count rate for the case of resonance. Sidebands expected for an excitation time $\mathsf{T}_{\text{excite}} = 10\,\text{ms}$ are visible. At lower count rates the number of ions can be reduced to zero for the case of resonance, whereas for the two cases with the highest count rate, the amplitude is not any longer sufficient to excite all ions. The reason for the latter is unclear. One possible explanation is that the inner part of the ion cloud is shielded from the excitation field by the outer ions. The resonance frequency shifts towards higher values for an increase of the ion number. This shift reaches about 80 Hz in the case of $1.6 \cdot 10^6$ ions/pulse. Such a frequency shift of the magnetron frequency can be explained when taking into account the electric potential created by the ion cloud. This potential enlarges the radial part of the potential generated by the trap electrodes and results in a change of the potential depth of the trap ($\frac{U_0}{d^2}$ of Eq. (3.1)). Consequently, the magnetron frequency is increased.

The cyclotron excitation scans were performed in the vicinity of the expected frequency $\nu_+ = 342\,597\,\text{Hz}$. Also in this case the the reduction of the count rate is clearly visible but for the highest number of ions. The resonance frequency shifts towards lower frequencies with a higher absolute frequency shift value. In the case of $7.2 \cdot 10^5$ ions/pulse the shape of the resonance curve becomes asymmetric and for $1.6 \cdot 10^6$ ions/pulse it seems that the resonance even splits. The reduction of the reduced cyclotron frequency is again because of the eigen potential of the ion cloud. However according to Eq. (3.3) and Eq. (3.5) ν_+ is now shifted to lower frequency values. The splitting of the resonance curve for the highest count rate is not fully understood. It shows similarities to results obtained for non-neutral plasma in Penning traps [Sar95]. There it was found that at high particle densities the ion cloud shows several cyclotron excitation modes with slightly different excitation frequencies. However, more detailed studies must be carried out to understand this phenomenon.

Resonance Shapes and Shifts of the Cooling Resonance

Cooling scans were performed in the vicinity of the expected frequency $\nu_C = 343\,711\,\text{Hz}$. A timing scheme corresponding to case (a) in Fig. 4.21 was used. Centring time and amplitude were $\mathsf{T}_{\text{center}} = 15\,\text{ms}$ and $\mathsf{A}_{\text{center}} = 3\,\text{V}$, respectively. The scans are shown in the right column of Fig. 6.19.

The cooling scans for lower ion numbers look like it was discussed in Sec. 6.4.2. The resonance curve is a superposition of three separate resonances, the centring quadrupole resonance

and the two decentring resonances at frequencies of ν_+ and $\nu_+ - \nu_-$, respectively. Due to the cyclotron resonance the optimal centring frequency is slightly higher than expected. However, as the ion number increases this frequency is shifted towards higher frequencies. In the case of $1.6 \cdot 10^6$ ions/pulse a total shift of 2.5 kHz can be found. Such a large shift can not be explained by the broadening of the ν_+ resonance as it was possible for the other cases. In fact up to now no satisfying explanation of this phenomenon has been found.

The results reported above indicate that at high ion numbers in REXTRAP one leaves the scope of single particle Penning trap theory. Plasma physics phenomena start to play an important role. Investigations about the effects related to a larger amount of ions in the trap are going on both experimentally as well as theoretically [Ame00, Ame01]. Especially, simulations seem to be very promising since frequency shifts of dipole as well as quadrupole excitation could be confirmed [Bec01]. However, these calculations are very time consuming and not yet finished.

6.6.6 Tests with Radioactive Ion Beams

In order to investigate how far radioactive ions influence the performance of REXTRAP a second on-line test has been carried out in spring 2000. A standard tantalum foil target (ISOLDE target #139) equipped with a tungsten surface ioniser was used. Such a target ion source combination delivers normally strong beams of the neutron deficient alkali and rare earth isotopes. Unfortunately, this has not been the case for this target since it had nearly expired its desired life-time after intensive use for nuclear physics experiments over several weeks. Therefore, only low beams of sodium and rubidium isotopes were available.

Time-of-flight spectra of $^{25}Na^+$, $^{26}Na^+$, $^{87}Rb^+$, and $^{88}Rb^+$ extracted from REXTRAP are shown in Fig. 6.20. All of these isotopes are unstable β^--emitters but ^{87}Rb which is stable. The half lives are 1.07 s, 59.6 s, and 17.8 min for ^{26}Na, ^{25}Na, and ^{88}Rb, respectively [Pfe98].

The time-of-flight spectra were obtained by applying a timing scheme corresponding to case (a) in Fig. 4.21. Collection times used were $\mathsf{T}_{\text{collection}} = 50$ ms for the sodium isotopes and $\mathsf{T}_{\text{collection}} = 20$ ms for the rubidium isotopes, respectively. In both cases the centring time was $\mathsf{T}_{\text{center}} = 20$ ms. The centring amplitude was $\mathsf{A}_{\text{center}} = 6$ V.

Time-of-flight peaks according of the injected ions are clearly visible. Beside the already known peaks of $^{40}Ar^+$ and residual gas ions no new peaks can be observed. This is a good indication that the decay of ions in the trap or of those ions implanted in the electrodes does not result in a significant increase of back ground ions. The count rates have been determined to be 11 000 ions/pulse for $^{25}Na^+$, 650 ions/pulse for $^{26}Na^+$, and 4700 ions/pulse for $^{88}Rb^+$.

The long half live of $^{88}Rb^+$ allowed the determination of the location of ion losses in REXTRAP. For this purpose the trap was run continuously for about one hour. After this period it was immediately dismantled. The different pieces were checked for radiation. Smaller hot spots were found along the injection section of the trap. However, most activity was located at the entrance diaphragm of the trap. Hence, these results are in perfect agreement with the predictions from the calculations.

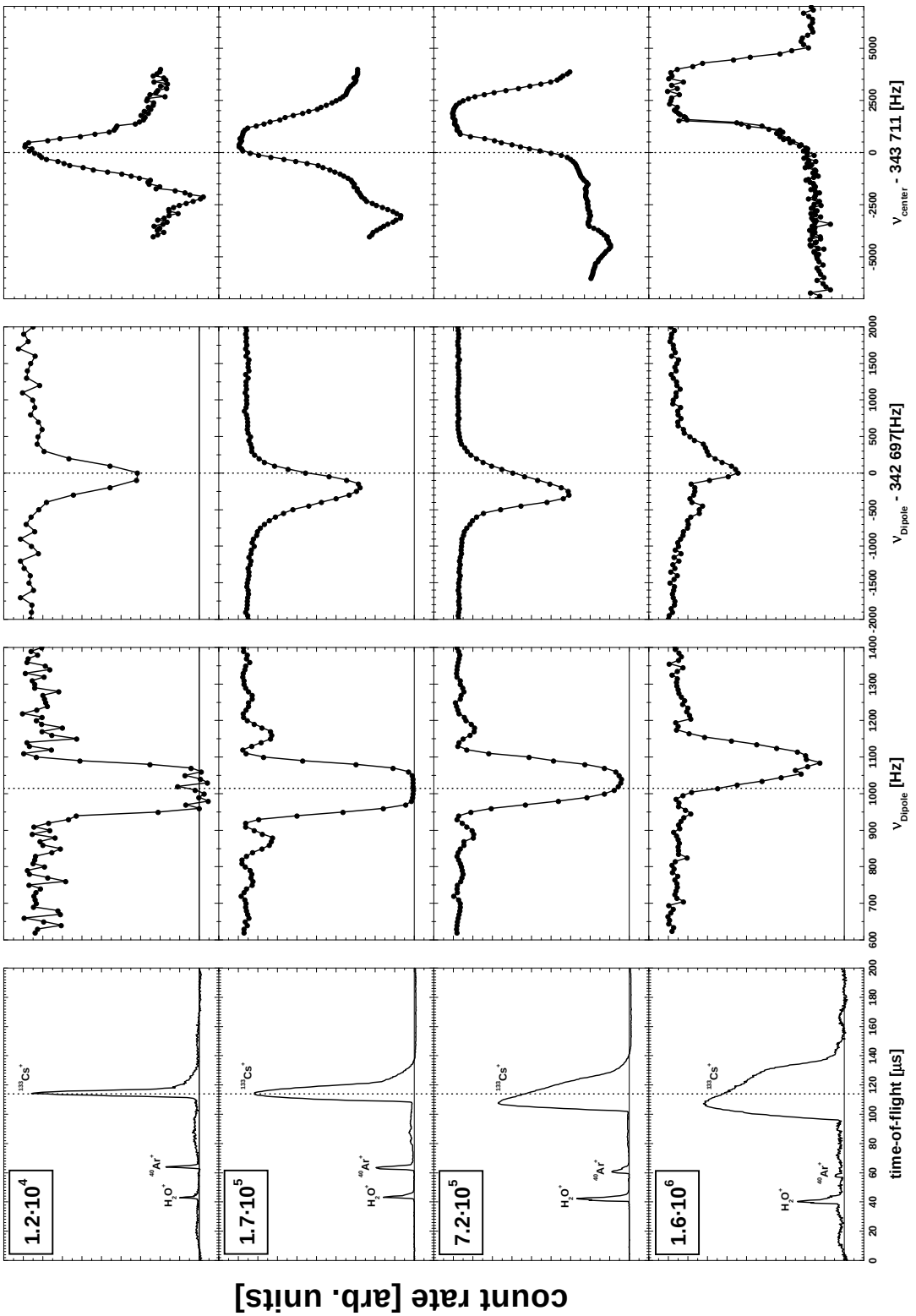

Figure 6.19: Time-of-flight spectra (left) and scans in order to determine the magnetron ν_- and reduced cyclotron ν_+ (middle) frequency as well as a cooling scan (right) for $^{133}Cs^+$ ions and for different ion numbers in REXTRAP. The ν_+ scan as well as the cooling scan were performed in the vicinity of the expected frequencies.

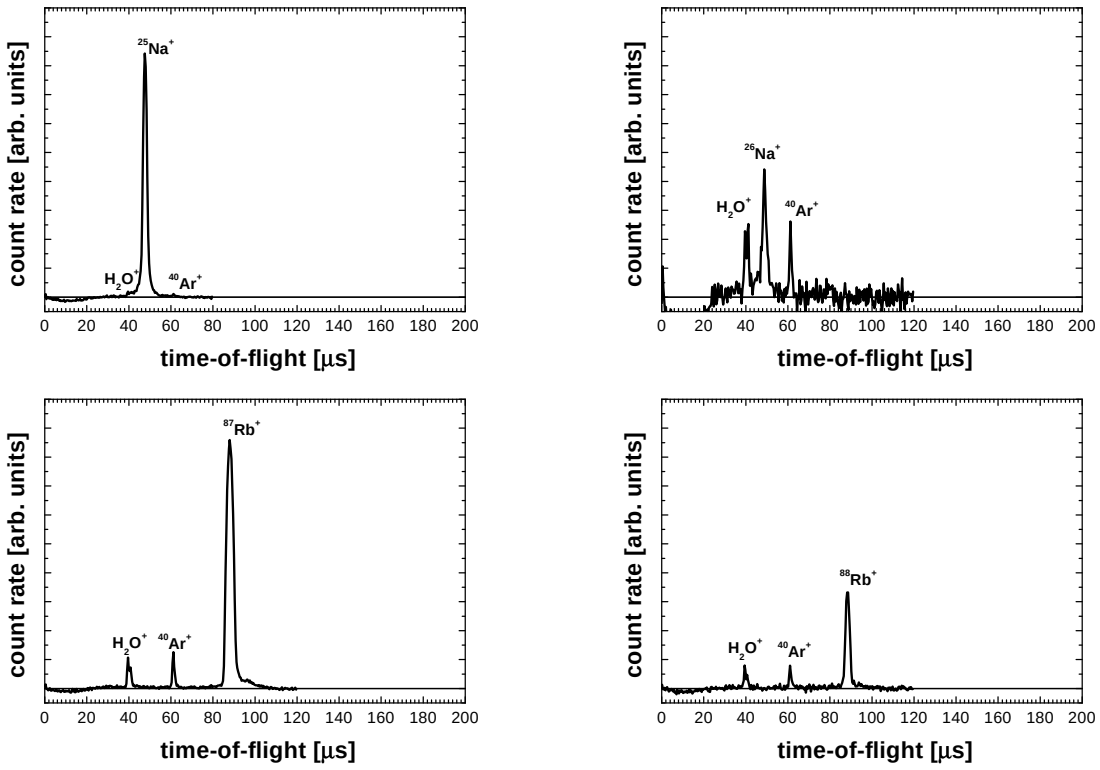

Figure 6.20: Time-of-flight spectra of $^{26}Na^+$ (top left), $^{25}Na^+$ (top right), $^{87}Rb^+$ (bottom left), and $^{88}Rb^+$ (bottom right) ejected from REXTRAP. Please note that the ordinate in the case of $^{25}Na^+$ has been stretched by a factor of 10 in comparison to the other spectra.

7 Comparison of REXTRAP to Other Cooling and Bunching Concepts

With REXTRAP it has been demonstrated for the first time that it is possible to accumulate, cool, and bunch a continuous ion beam from an ISOL facility by the means of a large gas-filled Penning trap. In the following the performance of REXTRAP is compared to other cooling and bunching techniques.

The only technique REXTRAP can be reasonably compared with is the beam accumulation and bunching with linear radiofrequency traps. This technique is a further development of Paul traps as for example the one described in [Sch98]. A typical outline of such a linear trap system is shown in Fig. 7.1 [Her00]. After electrostatically decelerating the incoming beam it is injected into the trap which is filled with a buffer gas. The trap system consists of four segmented rods. A radiofrequency voltage applied to the rods results in a transversely focusing force. The segmentation of the rods allows the creation of a DC electric field along the axis of the system. The ions entering the linear trap will lose transverse and longitudinal energy by collisions with the buffer gas. They are finally accumulated in the potential minimum and can be extracted as bunches by lowering the potential wall at the trap exit.

At the moment two of these radiofrequency cooler and buncher are operational at ISOL type facilities. There is the ISOLTRAP cooler and buncher at ISOLDE [Her00] and the ion beam cooler-buncher at the IGISOL facility in Jyväskylä (JYFL) [Nie00a, Nie00b]. A compilation of

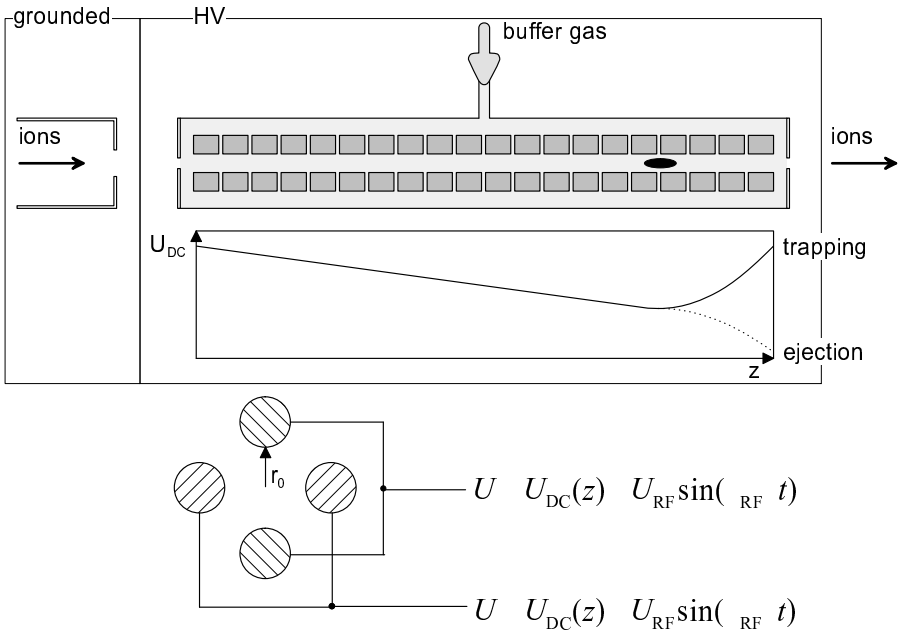

Figure 7.1: Basic scheme of a radiofrequency ion beam cooler and buncher. **Top:** Schematic side view of the system together with the potential along the symmetry axis. **Bottom:** The four rods and their supply with radiofrequency and DC voltage. The figure was taken from [Her00].

	beam energy	ϵ_{beam} [π mm·mrad]	efficiency	T_{cool}	# of ions
REXTRAP	60 keV	34	30 %	15 ms	$< 10^5$
ISOLTRAP	60 keV	34	10 %	10 ms	$< 1\,000$
JYFLTRAP	40 keV	5	80 %	10 ms	$< 1\,000$

Table 7.1: Comparison of the REXTRAP performance with radiofrequency cooler and buncher devices used at ISOL facilities for cooling and bunching of radioactive beams. The initial ion beam energy, the transversal emittance ϵ_{beam}, the bunching efficiency, the cooling time T_{cool}, and the number of ions per bunch are listed.

the performance of both systems in comparison to REXTRAP is shown in Table 7.1.

Both facilities differ in the beam quality delivered. ISOLDE has a transversal beam emittance of 34 π mm·mrad (@60 keV) while the IGISOL beam emittance is about one order of magnitude smaller. This has a direct effect on the efficiencies reached which is about 10 % for the ISOLTRAP and up to 80 % for the JYFL cooler. The efficiency of REXTRAP is with 30 % about three times higher than the one for the ISOLTRAP cooler.

The bunching efficiency values for the radiofrequency cooler and buncher devices has been determined for ion numbers of 10 to about 1 000 per bunch. The latter is already at the upper limit for these devices since the effective radial trapping potential provided by the radiofrequency field is relatively low. In contrast, the effective radial potential created by the magnetic field for the Penning trap is noticeable higher. This gives REXTRAP a natural advantage and explains that the good bunching performance is conceived over several orders of magnitude more.

Typically cooling times of about 10 ms are achieved in radiofrequency cooler and buncher devices. This is slightly lower than the average cooling times achieved with REXTRAP. The reason for this is that the centring process is not as complex.

Comparing both techniques leads to the conclusion that they are rather similar except for the number of ions per bunch. A Penning trap based buncher and cooler is first choice if short pulses with intensities of more than thousand ions per pulse must be delivered. In the case of REX-ISOLDE when the experiments require a large dynamic range of operation, this will be decisive.

8 Technical Improvements and New Applications

Within this work REXTRAP has been brought into reliable and smooth operation. The present performance of the system will allow the first REX-ISOLDE experiments to be carried out. Nevertheless, there are a number of improvements that can still be made. They will be discussed in the following.

8.1 Efficiency Improvement

8.1.1 Injection Efficiency

The first step to improve the injection efficiency is an enlargement of the diameter of trap entrance diaphragm by several millimetre. As shown in Sec. 5.3.2 this has to be accompanied by an increase of the transfer potential to at least 3 kV. This will improve the injection efficiency by at least a factor of two.

For very light ions, as for instance lithium isotopes, the radial energy uptake during the ion injection turned out to be an important limiting factor. For this case only a redesign of the injection section of REXTRAP or an improvement of the ISOLDE beam quality will result in a larger efficiency. A new injection stage of the trap must be constructed in order to minimise the radial energy pick up of the ion beam, which is mainly determined by the energy of the incident ion beam, its emittance, and the shape of the fringe fields of the magnet. The simulation programs developed in the present work are appropriate to find an improved design. A second alternative for increasing the injection efficiency of REXTRAP is the reduction of the radial emittance of the ISOLDE ion beam. For this purpose devices similar to that shown in Fig. 7.1 can be used. Operated in a continuous ion guide mode they have proven to be efficient and fast DC beam cooler devices [Kim97]. Such an ion-guide could be either placed in front of REXTRAP or close to the ISOLDE targets before the separation magnets. From the latter possibility even other ISOLDE experiments would profit.

8.1.2 Centring Efficiency

Ion losses during the cooling process occur due to the presence of decentring excitation modes (see Sec. 6.4.2) and due to radiofrequency heating. Lighter buffer gases like neon and helium will increase the ion-neutral mass ratio and minimise rf-heating.

For the reduction of ion losses due to the decentring excitation modes several possibilities exist. On one hand a new coupling scheme for the radiofrequency will extinguish the $\nu_+ - \nu_-$ resonance mode, which occurs in REXTRAP due to the simple coupling circuit (see Fig. 4.14). For this purpose the quadrupole field is obtained by applying voltages with a phase shift of 180° to neighbouring electrodes of the four-fold split centre electrode (see Fig. 3.4). An additional possibility would be to increase the depth of the trapping potential. This will shift the cyclotron frequency ν_+ towards lower frequencies and will reduce the influence of the decentring resonance due to their larger separation from ν_c.

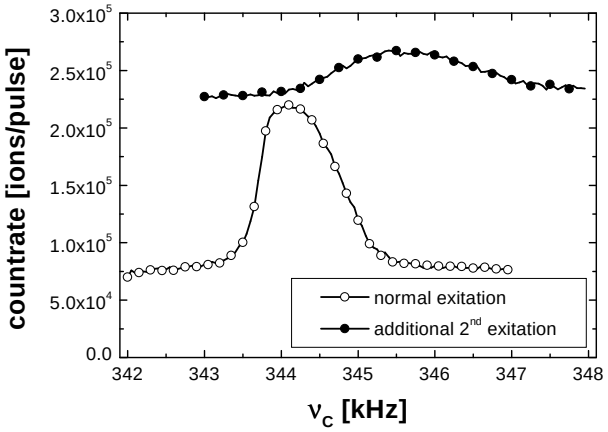

Figure 8.1: Number of extracted ions as function of the applied centring frequency ν_c for a single (○) and a double (●) excitation scheme.

A new excitation scheme promises to increase the efficiency of the trap in particular for a larger number of ions. The optimum value of the centring frequency ν_c increases with the number of ions in the trap as discussed in Sec. 6.6.5. So a continuous change of that frequency during the ion centring process should improve the efficiency. First results of a test are shown in Fig. 8.1. It shows the number of ejected ions as a function of the centring frequency. In addition to a normal cooling scheme the result of a cooling scan performed after the ions were already centred is shown. The optimum centring frequency is shifted to higher frequencies and an increase of the count rate of up to 20 % is observed. On the basis of this result a new excitation scheme will be developed [For01]. During the excitation period he centring frequency will be varied in order to follow this shift.

Another interesting technique for the centring of large number of ions is the rotating wall technique. It is routinely used for the storage of non-neutral plasma in Penning traps [Hua97]. Recently it was shown that this technique can also be used to increase the density of a plasma cloud up to a factor of 20 [Gre00]. The technique is based on the fact that for a large number of charged particles in a Penning trap the interaction between the particles can not be neglected. In such a case the ion cloud starts to rotate [Dub99]. The rotation frequency increases with the particle density. The application of a rotating electric field with a frequency always slightly higher than the rotation frequency of the cloud can compress the latter further. Heating of the particles due to the rotating fields can be counteracted by collisions with a buffer gas. Up to now this this technique has only be proven to work with a positron plasma [Gre00]. However, there are no obvious reasons that it should not work with ions.

8.2 REXTRAP as a Precision Conversion Electron Spectroscope

In the following a new interesting application of ion traps will be presented which was tested with REXTRAP. The limiting factor of high-resolution spectroscopy of low-energy electrons emitted by radioactive nuclei is the thickness of the source material in which electrons are scattered. The detection of conversion electrons from the decay of trapped ions may provide new opportunities for spectroscopy since the trapped ions form a source of nearly zero thickness and therefore the electrons do not suffer energy loss due to scattering.

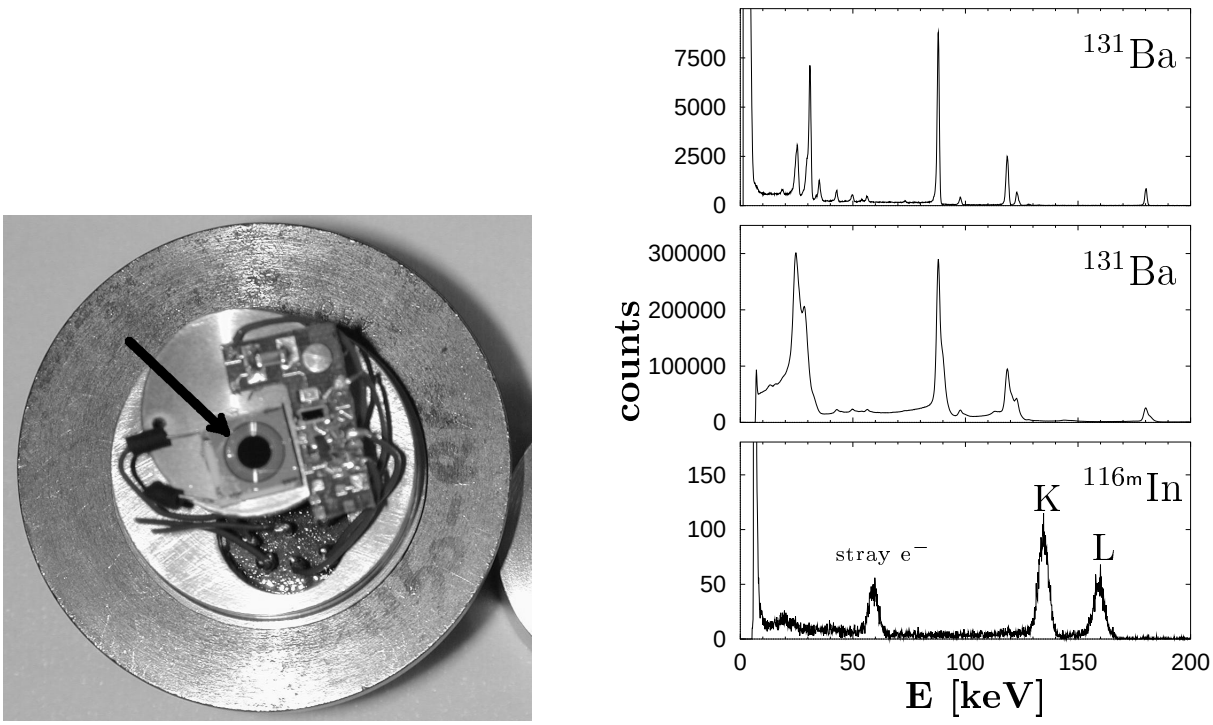

Figure 8.2: Left: The conversion electron detector setup used for the electron spectroscopy experiments. The detector (Canberra, RD ED10GC-500P, marked with an arrow) is placed together with the pre-amplifier FET on a Peltier element for cooling. **Right:** Conversion electron spectra: (top) Off-trap ^{131}Ba (massive source) spectrum recorded in a test chamber. (middle) In-trap ^{131}Ba (massive source) spectrum recorded in REXTRAP. (bottom) In-trap ^{116m}In (trapped ions) spectrum recorded in REXTRAP.

The electrons emitted by radioactive nuclei confined in the trap travel along the magnetic field lines. Starting in the strong centre field of the solenoid nearly all emitted electrons in forward direction are guided to the trap exit direction in a very limited solid angle. This allows the use of a small-area high-resolution silicon detector with high efficiency. In order to test this approach a special detector setup was developed by L. Weissman [Wei00] which is shown in the left part of Fig. 8.2. The detector (Canberra, RD ED10GC-500P, marked with an arrow) is placed together with the pre-amplifier FET on a Peltier element for cooling to ensures low noise operation. The performance of the detector system has been tested in several experiments which are summarised in the right parts of Fig. 8.2.

The top spectrum was obtained with a massive ^{131}Ba source. The source was prepared by implanting ^{131}Ba from ISOLDE into a thin capton foil. Source and detector were mounted in a test chamber for this experiment. The spectrum shows good energy resolution but it suffers from from background due to electron scattering in the target material.

The spectra in the middle and bottom of the right part of Fig. 8.2 show in-trap measurements. The detector was positioned directly after the extraction diaphragm of REXTRAP. The middle spectrum was obtained with the same source as it was used for the measurements above placed in the trap centre. A decrease of the energy resolution and an increase of the background is observed. A reason for that is the fact that the detection solid angle is increased due to the electron guidance the magnetic field provides. Thus also scattered electrons are detected. The

results of first on-line measurements for ^{118m}In are shown in the bottom spectrum. An ISOLDE beam of that ion species was injected into REXTRAP, accumulated, and trapped. Conversion electrons emitted from the nuclei were then investigated. In addition to the K- and L-transitions of the 159 keV isomer of ^{116m}In and the 20.1 keV Auger transition a strong peak around 60 keV is observed. It results from stray electrons accelerated by the platform potential. In comparison to the spectra of ^{131}Ba a better background to noise ratio can be noted, as expected if scattering of electrons in the source is avoided. The energy resolution seems to become worse but it turned out that this was caused by the strong electronic noise produced by the copper vapour laser setup for the ISOLDE laser ion source running in parallel during this measurements and had nothing to do with the fact that trapped ions were used.

9 Summary and Conclusion

REX-ISOLDE is a pioneering project for the post-acceleration of radioactive beams and, if successful, will provide the opportunity for a new generation of experiments at the on-line mass separator facility ISOLDE. An important part of the REX-ISOLDE concept is the efficient conversion of a continuous low-energy radioactive beam into short ion bunches with excellent beam properties. The development, test and successful commissioning of REXTRAP, a beam accumulator, cooler and buncher was the topic of the present work.

REXTRAP is based on a large gas-filled Penning trap. Ions from ISOLDE are decelerated, injected and accumulated in a Penning trap by employing energy loss via collisions with buffer gas atoms. A mass selective centring technique is used to concentrate all ions in the trap centre. From there they can be extracted as cooled short ion bunches, ready to be delivered to the next stage of REX-ISOLDE, an electron beam ion source.

With REXTRAP new territory of ion trap physics was entered. Never before a Penning trap of such size had been constructed and nor the injection of several keV continuous ion beams was ever attempted. With the demanded storage of large ion numbers new effects were expected to show up and it was not clear to which extend they would affect the performance of REXTRAP.

Much time during this thesis work was spent to bring REXTRAP into an operational state before any test could be performed. The operation of an ion trap on a high voltage platform, the demand of a high repetition rate and a high reliability required in particular the development of a robust and versatile control and electronics system.

Already the first tests of REXTRAP revealed that the concept was successful. Ions from an external ion source could be trapped and bunched successfully. A large number of subsequent tests were carried out both with stable and radioactive ISOLDE beams as well as with beams from the test ion source. The properties of REXTRAP were investigated in a systematic manner. This allowed optimum parameters for a routine operation to be found and resulted in the following performance:

- A total efficiency of 30 % for accumulation, cooling and bunching of ion beams from ISOLDE can be realized.
- REXTRAP is applicable to practically the whole mass range available at ISOLDE.
- Up to 10^5 ions per ion pulse can be ejected without a noticeable deterioration of its properties due to space charge effects.
- These pulses can be delivered with a repetition rate up to 100 Hz.

The studies also revealed the limits of the technique with respect to the usage of large ion numbers, which for example result in large shifts of resonance frequencies of the stored ions. These interesting effects need still to be fully understood. The experimental investigation of REXTRAP properties was accompanied by a large number of numerical simulations. These

simulations confirmed the experimental results and show that the behaviour of the systems can be understood from first principles. Furthermore, the simulations helped to understand observed deficiencies in the system. It is now clear how to raise the efficiency well above 30 %, and required modifications of the apparatus are presently pursued.

In conclusion, REXTRAP, the decisive first component of REX-ISOLDE is working. The concept of using a large gas-filled Penning trap has proven to be successful. Practically all other REX-ISOLDE components are assembled and most of them installed at ISOLDE and under test. First experiments with post-accelerated radioactive beams at ISOLDE will start soon.

Appendix

First Capture and Storage of $^{5.5kg}$Drillium in a Magnetic Trap

Pitch Mid for the REX-ISOLDE collaboration

August 1997

Abstract

First capture and storage of a single mega-heavy $^{5.5kg}$Drillium has been observed in a superconducting magnetic trap at the ISOLDE facility at CERN. The observed storage time so far has been determined to be $T_{1/2} > 10\,d$. The specific particle is made visible by scattering of photons in visible spectrum and can be stored without further cooling.

At REX-ISOLDE the radioactive isotopes produced at PS-ISOLDE will be accumulated and bunched in a magnetic trap, multiple ionized to charged states with $q=4^+ \ldots 5^+$ in an EBIS-source and postaccelerated by RFQs to energies up to 2.2 MeV/nucleon.
Still under construction the already operational first stage of this chain, the superconducting magnetic trap, has already shown its capability. Having a maximum magnetic flux of B=3.0 T and an aperture of r=0.07 m the apparatus was able to attract and capture a single mega-heavy $^{5.5kg}$Drillium which was passing the so called "drilltrap" at a right angle in a distance of approx. 0.5 m in a walking-like velocity. Stored in a deep potential to prevent tunneling effects the $^{5.5kg}$Drillium — for which decays neither in $^{0.5kg}$Corkscrewium nor in $^{0.001kg}$Toothpickium are known so far — is supposed to stay in this status for a very long time.
Encouraged by this success further experiments with mega-heavies are foreseen with clusters of $^{0.1kg}$Keyons, more prolate like $^{0.3kg}$Screwdriveriums and $^{0.1kg}$Watchiums, which may serve as stored clocks to test the twin paradoxon in special relativity.

References

[1] CERN-Security. How to handle Mega-Heavies near Strong Magnetic Fields.

[2] BOSCH company. $^{5.5kg}$Drillium electronic-super-450E.

[3] P. Mid. If i had a hammer... Heavy Metal Dreams in Lyrics.

[4] M. War. How to become a Ghostwriter for the REX.

A Ion-Neutral Interaction Potentials

Buffer gas cooling at lower ion energies bases on the long range ion buffer gas interaction.

The ion-neutral interaction potentials consist of two parts, namely a short range repulsive and a long range attractive part. One of simplest form is given by:

$$V(r) = \frac{B}{r^n} - \frac{C_6}{r^6} - \frac{C_4}{r^4} \; . \tag{A.1}$$

The so called (n,6,4)-potentials contain the parameter n, B, C_6, and C_4. The C_4/r_4 and C_6/r_6-terms describe the attracting force of the ion interaction with the induced dipole and quadrupole polarisation of the neutrals, respectively. The empirical B/r^n represents the short range repulsion of the interaction. In the literature one often finds Eq. (A.1) in the form of:

$$V(r) = \frac{n\epsilon}{n(3+\gamma) - 12(1+\gamma)} \left[\frac{12}{n}(1+\gamma) \left(\frac{r_m}{r}\right)^n - 4\gamma \left(\frac{r_m}{r}\right)^6 - 3(1-\gamma) \left(\frac{r_m}{r}\right)^4 \right], \tag{A.2}$$

where r_m and ϵ denotes position and depth of the potential minimum. γ gives the relative strength of the r^6-term in comparison to the r^4-term.

The knowledge of the ion neutral interaction potential allows the determination of the ion mobility K. Three succesive integrations are needed to obtain K. The first integration determines the deflection angle in an ion-neutral collision as a function of the impact parameter b and the center of mass energy E:

$$\theta(b, E) = \int_{r_a}^{\infty} \frac{1}{\sqrt{1 - \frac{b^2}{r^2} - \frac{V(r)}{E}}} \frac{dr}{r^2} \; , \tag{A.3}$$

where the distance of closest approach r_a is the outermost root of:

$$1 - \frac{b^2}{r_a^2} - \frac{V(r_a)}{E} = 0 \; . \tag{A.4}$$

The second and third over energy E and impact parameter b yields the collision integrals as a function of temperature T:

$$\Omega(T) = \frac{4\pi}{(kT)^3} \int_0^{\infty} E^2 \exp\left\{-\frac{E}{kT}\right\} \int_0^{\infty} b(1 - \cos(\theta(b, E))) \, db \, dE \; . \tag{A.5}$$

The ion mobility K is then given by:

$$K = \frac{3qE}{16N} \sqrt{\frac{2\pi}{kT_{eff}} \frac{m+M}{mM}} \frac{1}{\Omega(T_{eff})} \; , \tag{A.6}$$

where m and q denote ion mass and charge, M the mass of the gas particle and N the gas number density, respectively. The effective temperature T_{eff} is connected to the ion drift velocity v_d and the gas temperature via:

$$\frac{3}{2} kT_{eff} = \frac{3}{2} kT_{gas} + \frac{1}{2} M v_d^2 \; . \tag{A.7}$$

ion/buffer gas	B $\left[\frac{\text{eV}}{\text{Å}^n}\right]$	n	C_6 $\left[\frac{\text{eV}}{\text{Å}^6}\right]$	C_4 $\left[\frac{\text{eV}}{\text{Å}^4}\right]$
$^{7}Li^{+}$—Ar	371.80	8	41.58	13.03
$^{23}Na^{+}$—Ar	1288.41	8	215.62	4.39
$^{39}K^{+}$—Ar	9134.31	10	171.46	3.60
$^{87}Rb^{+}$—Ar	23747.30	10	211.36	8.38
$^{133}Cs^{+}$—Ar	21010.70	10	138.15	12.57

Table A.1: Parameter of the interaction potential of alkali ions and argon atoms.

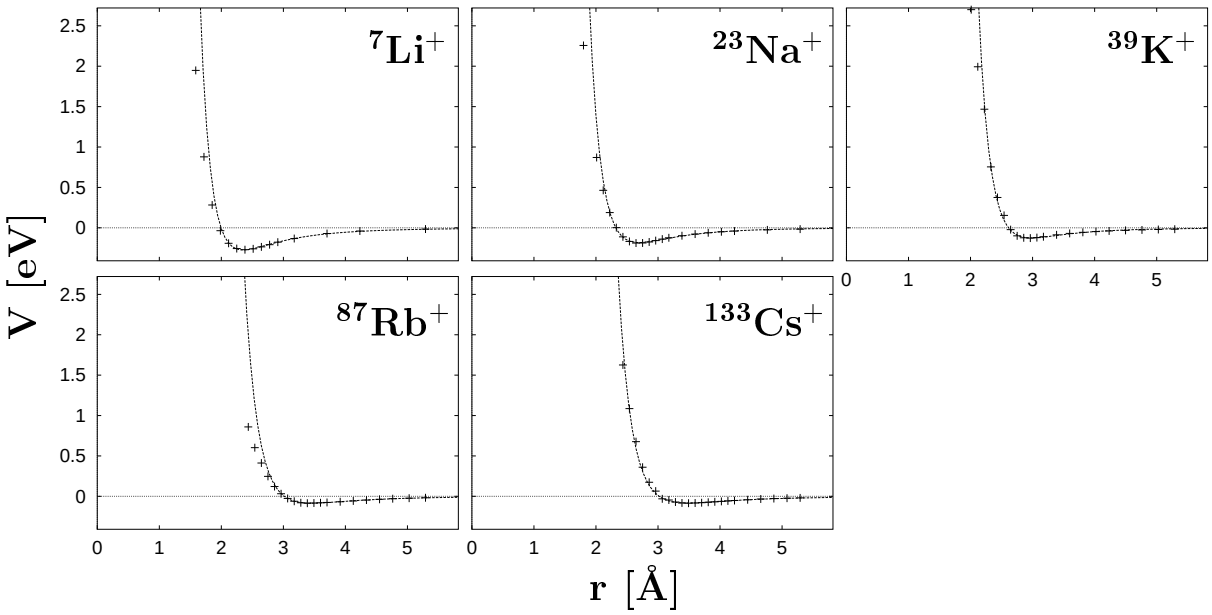

Figure A.1: Interaction potentials of alkali ions and argon atoms.

B SIMION Listings

Printed by Pit Schmidt

Sep 12, 00 23:54 **electr01.gem** Page 1/1

```
;************************
;* REXTRAP Version 12 *
;************************
;
;
; standard electrodes for REXTRAP
;
; place:
;
; grid spacing: 1mm
;
; last change: 26.07.2000 by Pit Schmidt
;
fill
{
  within
  {
    box(6,25,40,26)     ; inner plate
  }
  within
  {
    box(6,26,29,30)     ; massive middle part
  }
  within
  {
    box(0,30,29,33)      ; outer plate
  }
}
```

Saturday December 09, 2000 1/1

Figure B.1: SIMION geometry file modelling a REXTRAP standard electrode. This file is included by other geometry files.

Printed by Pit Schmidt

Sep 12, 00 23:54 **decel.gem** Page 1/3

```
;*********************
;* REXTRAP Version 12 *
;*********************
;
;
; deceleration part rotated by 180 degrees
;
; place:
;
; trap center at 510mm
; grid spacing: 1mm
;
; Electrode 1: transfer potential
; Electrode 2: electrode01
; Electrode 3: deceleration potential
; Electrode 4: beam tube gnd & injectionlens gnd
; Electrode 5: injection lens
; Electrode 6: beam tube hv
;
; last change: 01.08.2000 by Pit Schmidt

PA_define(860, 91, 1, Cylindrical, Y, Electrostatic, 1)

; transferpotential
Electrode(1)
{
  fill
  {
    within
    {
      box(0,30,140,34)
    }
    within
    {
      box(235,30,342,34)
    }
    within
    {
      box(348,40,483,45)
    }
    ; shielding
    within
    {
      box(333,47,363,49)
    }
    within
    {
      circle(483,45,5,5)
    }
    within
    {
      box(352,40,354,10)
    }
    within
    {
      box(348,10,358,12)
    }
  }
}

; lens
Electrode(2)
{
fill
  {
    within
    {
```

Saturday December 09, 2000 1/3

Printed by Pit Schmidt

Sep 12, 00 23:54 **decel.gem** Page 2/3

```
      box(150,30,225,34)
    }
  }
}

; 1. deceleration stage
Electrode(3)
{
fill
  {
    within
    {
      circle(503,45,5,5)
    }
    within
    {
      box(503,40,539,50)
    }
    within
    {
      circle(539,49,9,9)
    }
  }
}

; injection lens/beam tube ground part
Electrode(4)
{
;injection lens part I
fill
  {
    within
    {
      circle(686,30,10,10)
    }
    within
    {
      box(676,30,696,73)
    }
  }
;injection lens part II
fill
  {
    within
    {
      circle(746,30,10,10)
    }
    within
    {
      box(736,30,756,50)
    }
  }
;beam tube
fill
  {
    within
    {
      box(645,75,678,77)
    }
    within
    {
      circle(645,72,5,5)
    }
    within
    {
      box(672,77,676,90)
```

2/3 Saturday December 09, 2000

Printed by Pit Schmidt

Sep 12, 00 23:54 **decel.gem** Page 3/3

```
    }
    within
    {
      box(676,77,688,90)
    }
    within
    {
      box(688,77,859,79)
    }
  }
}

; injection lens
Electrode(5)
{
fill
  {
    within
    {
      circle(716,30,10,10)
    }
    within
    {
      box(706,30,726,50)
    }
  }
}

;beam tube - platform potential
Electrode(6)
{
  fill
  {
    within
    {
      box(547,75,580,77)
    }
    within
    {
      circle(580,72,5,5)
    }
    within
    {
      box(549,77,553,90)
    }
    within
    {
      box(536,77,548,90)
    }
    within
    {
      box(0,77,536,79)
    }
  }
}
```

Saturday December 09, 2000 3/3

Figure B.2: SIMION geometry file modelling the REXTRAP deceleration part.

Printed by Pit Schmidt

Sep 12, 00 23:54 **injec.gem** Page 1/2

```
;**********************
;* REXTRAP Version 12 *
;**********************
;
;
; trap injection part rotated by 180 degrees
;
; place:
;
; Electrode 1 --- Electrode05
; Electrode 2 --- platform ground
; Electrode 3 --- Electrode03
; Electrode 4 --- Electrode02
; Electrode 5 --- transfer potential
;
; trap center at 510mm
; grid spacing: 1mm
;
; last change: 26.07.2000 by Pit Schmidt

PA_Define (211, 35, 1, Cylindrical, Y, Electrostatic, 1)

;injection diaphragm 1st half
Electrode(1)
{
  Fill
  {
    within
    {
      box(0,6,25,10)
    }
    within
    {
      box(0,10,1,25)
    }
    within
    {
      box(0,25,25,26)
    }
    within
    {
      box(0,26,6,33)
    }
  }
}

; acceleration electrodes
Electrode(2)
{
  locate( 24) { include(Electr01) }
}

Electrode(3)
{
  locate( 63) { include(Electr01) }
}

Electrode(4)
{
  locate(102) { include(Electr01) }
}

; transferpotential
Electrode(5)
{
  fill
  {
```

Saturday December 09, 2000 1/2

Printed by Pit Schmidt

Sep 12, 00 23:54 **injec.gem** Page 2/2

```
    within
    {
      box(141,30,210,33)
    }
    within
    {
      box(147,25,186,30)
    }
  }
}
```

2/2 Saturday December 09, 2000

Figure B.3: SIMION geometry file modelling the REXTRAP injection part.

Printed by Pit Schmidt

Sep 12, 00 23:54 **stop.gem** Page 1/2

```
;**********************
;* REXTRAP Version 12 *
;**********************
;
; stopping part --- high pressure region
;
; place:
;
; trap center at 510mm
; grid spacing: 1mm
;
; Electrode  1 --- electrode05
; Electrode  2 --- electrode06
; Electrode  3 --- electrode07
; Electrode  4 --- electrode08
; Electrode  5 --- electrode09
; Electrode  6 --- electrode10
; Electrode  7 --- electrode11
; Electrode  8 --- electrode12
; Electrode  9 --- electrode13
; Electrode 10 --- electrode14
; Electrode 11 --- electrode15
;
; last change: 02.08.2000 by Pit Schmidt

PA_Define(397, 35, 1, Cylindical, Y, Electrostatic, 1)

; half of entrance diaphragm
Electrode(1)
{
  fill
  {
    within
    {
      box(0,6,25,10)
    }
    within
    {
      box(0,10,1,25)
    }
    within
    {
      box(0,25,25,26)
    }
    within
    {
      box(0,26,6,33)
    }
  }
}

; 9. field electrode
Electrode(2)
{
fill
  {
    within
    {
      box(24,30,70,33)
    }
    within
    {
      box(31,25,64,30)
    }
  }
}
```

Saturday December 09, 2000 1/2

Printed by Pit Schmidt

Sep 12, 00 23:54 **stop.gem** Page 2/2

```
Electrode(3)
{
  locate (109,0,0,1,180,0,0) { include(electr01) }
}

Electrode(4)
{
  locate (148,0,0,1,180,0,0) { include(electr01) }
}

Electrode(5)
{
  locate (187,0,0,1,180,0,0) { include(electr01) }
}

Electrode(6)
{
  locate (226,0,0,1,180,0,0) { include(electr01) }
}

Electrode(7)
{
  locate (265,0,0,1,180,0,0) { include(electr01) }
}

Electrode(8)
{
  locate (304,0,0,1,180,0,0) { include(electr01) }
}

Electrode(9)
{
  locate (343,0,0,1,180,0,0) { include(electr01) }
}

Electrode(10)
{
  locate (382,0,0,1,180,0,0) { include(electr01) }
}

;half of 2. diaphragma
Electrode(11)
{
  locate (421,0,0,1,180,0,0) { include(Electr01) }
  fill
  {
    within
    {
      box(405,25,395,10)
    }
    within
    {
      box(396,10,371,5)
    }
  }
}
```

2/2 Saturday December 09, 2000

Figure B.4: SIMION geometry file modelling the REXTRAP stopping part.

Printed by Pit Schmidt

Sep 12, 00 23:54 **ejec.gem** Page 1/2

```
;*********************
;* REXTRAP Version 12 *
;*********************
;
;
; trap ejection part
;
; place:
;
; Electrode 1 --- Electrode36
; Electrode 2 --- Electrode37
; Electrode 3 --- Electrode38
; Electrode 4 --- Electrode39
; Electrode 5 --- transfer potential
;
;
; trap center at 510mm
; grid spacing: 1mm
;
; last change: 02.08.2000 by Pit Schmidt

PA_define (211, 35, 1, Cylindrical, Y, Electrostatic, 1)

; ejection diaphragm 2nd half / injection diaphragm 1st half
Electrode(1)
{
  fill
  {
    within
    {
      box(0,3,25,10)
    }
    within
    {
      box(0,10,1,25)
    }
    within
    {
      box(0,25,25,26)
    }
    within
    {
      box(0,26,5,33)
    }
  }
}

; acceleration electrodes
Electrode(2)
{
  locate( 24) { include(Electr01) }
}

Electrode(3)
{
  locate( 63) { include(Electr01) }
}

Electrode(4)
{
  locate(102) { include(Electr01) }
}

; transferpotential
Electrode(5)
{
  fill
  {
```

Saturday December 09, 2000 1/2

Printed by Pit Schmidt

Sep 12, 00 23:54 **ejec.gem** Page 2/2

```
    within
    {
      box(141,30,210,33)
    }
    within
    {
      box(147,25,186,30)
    }
  }
}
```

2/2 Saturday December 09, 2000

Figure B.5: SIMION geometry file modelling the REXTRAP ejection part.

Printed by Pit Schmidt

Sep 13, 00 0:10 **accel.gem** Page 1/3

```
;*********************
;* REXTRAP Version 12 *
;*********************
;
;
; deceleration part rotated by 180 degrees
;
; place:
;
; grid spacing: 1mm
;
; Electrode 1: transfer potential
; Electrode 2: electrode40
; Electrode 3: acceleration potential
; Electrode 4: beam tube gnd & ejectionlens gnd
; Electrode 5: ejection lens
; Electrode 6: beam tube hv
;
; last change: 01.08.2000 by Pit Schmidt

PA_Define(820, 91, 1, Cylindrical, Y, Electrostatic, 1)

; transfer potential
Electrode(1)
{
  fill
  {
    within
    {
      Box(0,30,140,34)
    }
    within
    {
      Box(235,30,342,34)
    }
    within
    {
      Box(348,40,483,45)
    }
    within
    {
      Circle(483,45,5,5)
    }
    within
    {
      Box(352,40,354,10)
    }
    within
    {
      Box(348,10,358,12)
    }
  }
}

; lens
Electrode(2)
{
fill
  {
    within
    {
      Box(150,30,225,34)
    }
  }
}

; 1. acceleration
```

Saturday December 09, 2000 1/3

Printed by Pit Schmidt

Sep 13, 00 0:10 **accel.gem** Page 2/3

```
Electrode(3)
{
fill
  {
    within
    {
      Circle(503,45,5,5)
    }
    within
    {
      Box(503,40,539,50)
    }
    within
    {
      Circle(539,49,9,9)
    }
  }
}

; ejection lens/beam tube ground part
Electrode(4)
{
;injection lens part I
fill
  {
    within
    {
      Circle(646,30,10,10)
    }
    within
    {
      Box(636,30,656,59)
    }
;injection lens part II
    within
    {
      Circle(706,30,10,10)
    }
    within
    {
      Box(696,30,716,59)
    }
;beam tube
    within
    {
      Box(615,75,638,77)
    }
    within
    {
      Circle(615,72,5,5)
    }
    within
    {
      Box(632,77,636,90)
    }
    within
    {
      Box(636,77,648,90)
    }
    within
    {
      Box(648,77,819,79)
    }
  }
}
```

2/3 Saturday December 09, 2000

Printed by Pit Schmidt

Sep 13, 00 0:10 **accel.gem** Page 3/3

```
; ejection lens
Electrode(5)
{
fill
  {
    within
    {
      Circle(676,30,10,10)
    }
    within
    {
      Box(666,30,686,59)
    }
  }
}

; beam tube - platform potential
Electrode(6)
{
fill
  {
    within
    {
      Box(547,75,570,77)
    }
    within
    {
      Circle(570,72,5,5)
    }
    within
    {
      Box(549,77,553,90)
    }
    within
    {
      Box(536,77,548,90)
    }
    within
    {
      Box(400,77,536,79)
    }
  }
}
```

Saturday December 09, 2000 3/3

Figure B.6: SIMION geometry file modelling the REXTRAP acceleration part.

Printed by Pit Schmidt

Sep 12, 00 23:02 **source.gem** Page 1/2

```
;*********************************************************
;*  REXTRAP Ion Source                                   *
;*                                                       *
;*  units: 1/10 mm                                       *
;*                                                       *
;*  SIMION definition file                               *
;*  contains: Ionizer, Skimmer, Extraction lens, and     *
;*  vacuum tube                                          *
;*                                                       *
;*  Pit Schmidt, 05/20/2000                              *
;*********************************************************

PA_Define(3000,800,1,Cylindrical,Y,Electrical,1)


; Ionizer (part 10)
;*********************************************************
Locate(200,0,0,1,0,0,0)
{
  Electrode(1)
  {
    fill
    {
      within {Box(0,50,300,0)}
       notin {Box(0, 9,300,0)}
       notin {Polyline(301,50,291,9,300,9)}
       notin {Polyline(290,20,0,50,290,50)}
    }
  }
}


; Lens 1 (parts 4 & 5)
;*********************************************************
Locate(0,0,0,1,0,0,0)
{
  Electrode(2)
  {
    fill
    {
      within {Box(   0,200,800,300)}
      within {Circle(800,250,50,50)}
      within {Box(   0,300, 40,380)}
      notin  {Box(   0,200,560,230)}
    }
  }
}

; Skimmer (part 6)
;*********************************************************
Locate(460,0,0,1,0,0,0)
{
  Electrode(3)
  {
    fill
    {
      within {Box (   0, 30, 70,210)}
      notin  {Box (   0, 30, 60,150)}
      notin  {Box (  20, 30, 60,170)}
      notin  {Box (  20,190, 60,210)}
    }
  }
}

; Extraction Electrode and Vacuum Tube
```

Saturday December 09, 2000 1/2

Printed by Pit Schmidt

Sep 12, 00 23:02 **source.gem** Page 2/2

```
;*********************************************************
Locate(0,0,0,1,0,0,0)
{
  Electrode(4)
  {
    fill
    {
      ; tube
      within {Box (620,770,3000,779)}
      ; lens
    }
    ; lens
    Locate(2650,0,0,1,0,0,0)
    {
      fill
      {
        ;part 3
        within {Box(0,100,-120,770)}
      }

      Locate(-880,0,0,1,0,0,0)
      {
        ; part 1
        fill
        {
          within {Circle(50,100,50,50)}
          notin {Box(0,50,100,99)}
          within {Box(50,100,760,150)}
        }
        Locate(-460,0,0,1,0,0,0)
        {
          ; part 2
          fill
          {
            within{Box(25,50,800,100)}
            within{Circle(25,75,25,25)}
          }
        }
      }
    }
  }
}
```

2/2 Saturday December 09, 2000

Figure B.7: SIMION geometry file modelling the REXTRAP test ion source.

C ISOLDE Beam Line

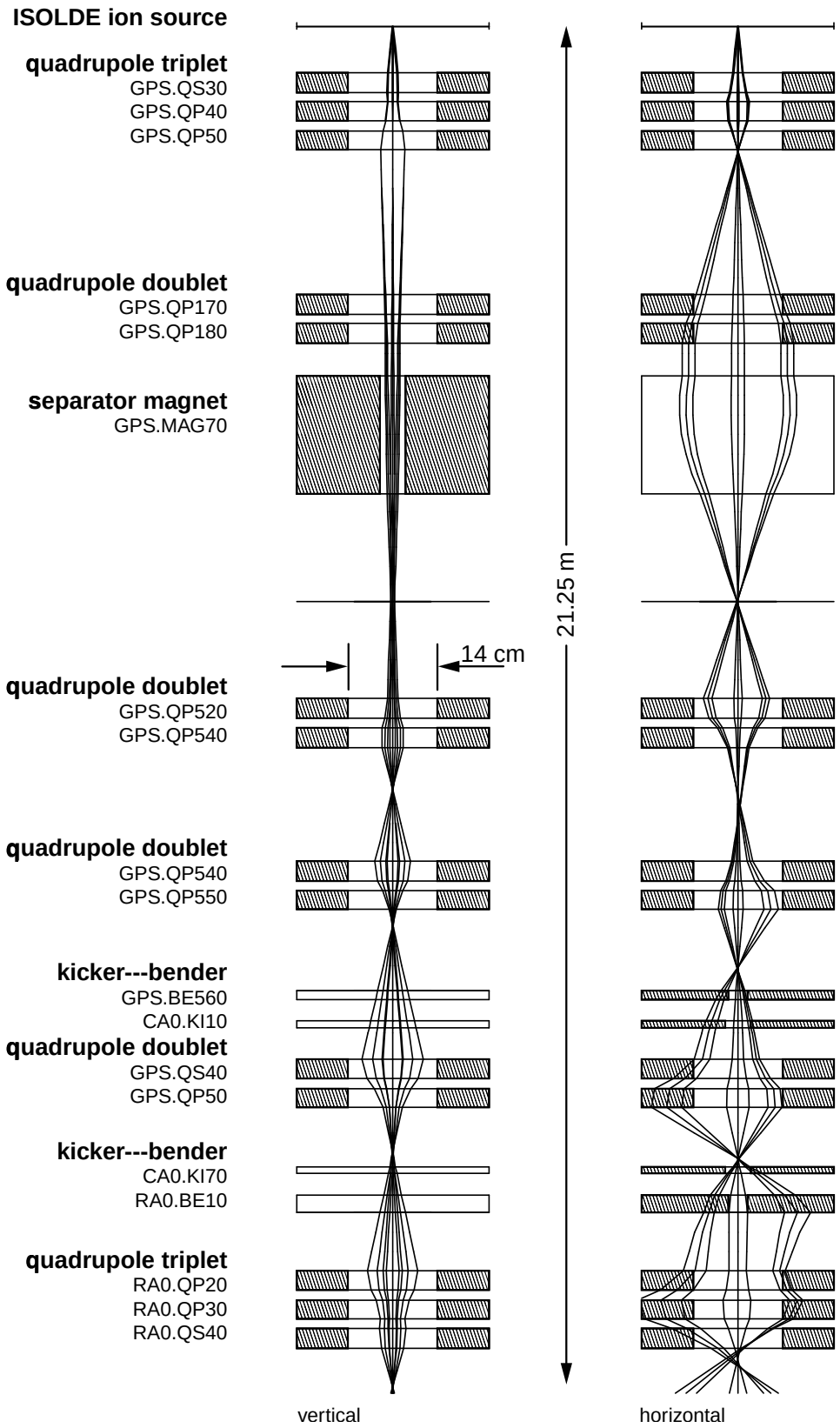

Figure C.1: Ion-optical elements of the ISOLDE beam line from the target area to the focal plane in front of REXTRAP.

Figure C.2: COSY source file to analyze the ISOLDE beam line system from the target area to the focal plane in front of REXTRAP. See also next page.

```
    CB ;                                { change bending direction          }
    ISOLDEBENDER 12.582 ;               { GPS.BE560 angle: 12.582 deg       }

  {*********************************}
  {* CA0 section                   *}
  {*********************************}

    DL 0.32759 ;                        { drift length                      }
    ISOLDEKICKER ;                      { CA0.KI10                          }
    DL 0.0879 ;                         { drift length                      }
                                        { CA0.SC20, CA0.FC30                }
    DL 0.400257 ;                       { drift length                      }
    ISOLDEDOUBLET CA0_QS40 CA0_QP50 ;   { CA0.QS40, CA0.QP50                }
    DL 0.792 ;                          { drift length                      }
                                        { CA0.SC66, CA0.FC68                }
    DL 0.12 ;                           { drift length                      }
    CB ;                                { change bending direction          }
    ISOLDEKICKER ;                      { CA0.KI70                          }
    DL 0.1 ;                            { drift length                      }
                                        { CA0.SC80, CA0.FC90                }
    DL 0.22759 ;                        { drift length                      }

  {*********************************}
  {* RA0 section                   *}
  {*********************************}

    ISOLDEBENDER 27.5 ;                 { RA0.BE10 angle: 27.5 deg          }
    DL 0.9 ;                            { drift length                      }
    ISOLDETRIPLET RA0_QP20 RA0_QP30     { RA0.QP20, RA0.QP30, RA0.QS40      }
      RA0_QS40 ;
    DL 1.10 ;                           { drift length                      }
                                        { RA0.SC80, RA0.FC90                }
  EP ;                                  { stop output for graphic           }
{*************************************************************************}
{ END OF BEAM LINE                                                        }
{*************************************************************************}

  PRINTMATRIX ;                         { print transfer matrix             }

  PG -101 -102 ;                        { print beam evelope                }
  READ 5 STOP ;                         { wait until RETURN is pressed      }

ENDPROCEDURE ;                          { end of RUN procedure              }

RUN ; END ;
```

Figure C.3: COSY source file to analyze the REXTRAP injection beam line from the test ion source to the focal plane.

Bibliography

[Ade93a] E. G. Adelberger. Erratum: “Improved limits on scalar weak couplings”. *Physical Review Letters* **71**, 469 (1993).

[Ade93b] E. G. Adelberger. Improved limits on scalar weak couplings. *Physical Review Letters* **70**, 2856–2859 (1993).

[All92] B. W. Allardyce, K. Elsener, D.C. Fiander, E. Kugler, C. Metzger, A. Pace, H. Ravn, K. Schindl, H. Schonauer, G. Shering, D.J. Simon, and E. Wildner. Isolde at the PS booster. CERN PS Divisional Report 92-46 (1992).

[Ame00] F. Ames. Plasma Effects in REXTRAP. Internal Group Report (2000).

[Ame01] F. Ames, P. Schmidt, O. Forstner, G. Bollen, O. Engels, D. Habs, G. Huber, and the REX-ISOLDE collaboration. Space-charge effects with REXTRAP. *Hyperfine Interactions* (2001), in press.

[And97] M. V. Andrés, M. J. G. Borge, and M. D. Cortina. Dipole coulomb polarizability in the scattering of halo nuclei. CERN ISC97-10, ISC I21 (1997).

[Arf71] George Arfken. *Mathematical Methods for Physicists*. Academic Press (1971).

[AS88] F. Ajzenberg-Selove. Energy levels of light nuclei A=5–10. *Nuclear Physics* **A490**(1), 1–225 (1988).

[Asp86] A. Aspect, J. Dalibard, A. Heidmann, C. Salomon, and C. Cohen-Tannoudji. Cooling atoms with stimulated emission. *Physical Review Letters* **56**, 1688 (1986).

[Aud97] G. Audi, O. Bersillon, J. Blachot, and A. H. Wapstra. The NUBASE evaluation of nuclear and decay properties. *Nuclear Physics* **A624**, 1–124 (1997).

[Axe96] L. Axelsson, M. J. G. Borge, S. Fayans, V. Z. Goldberg, S. Grévy, D. Guillemaud-Mueller, B. Jonson, K.-M. Källman, T. Lönnroth, M. Lewitowicz, P. Manngård, K. Markenroth, I. Martel, A. C. Mueller, I. Mukha, T. Nilsson, G. Nyman, N. A. Orr, K. Riisager, G. V. Rogatchev, M.-G. Saint-Laurent, I. N. Serikov, O. Sorlin, O. Tengblad, F. Wenander, J. S. Winfield, and R. Wolski. Study of the unbound nucleus ^{11}N by elastic resonance scattering. *Physical Review* **C54**(4), R1511–R1514 (1996).

[Axe98] L. Axelsson, U. C. Bergmann, M. J. G. Borge, G. Chubaryan, G. Crawley, C. Forssèn, L. M. Fraile, H. Fynbo, V. Z. Goldberg, P. Hornshøj, B. Jonson, T. Lönnroth, K. Markenroth, M. Meister, I. Mukha, T. Nilsson, G. Nyman, K. Riisager, G. V. Rogachev, M. V. Rojkov, G. Schrieder, I. N. Serikov, H. Simon, S. Tabor, O. Tengblad, W. Trzaska, F. Wenander, and M. V. Zhukov. Proposal to the ISOLDE committee: Investigations of neutron-rich nuclei at the dripline through their analogue states: The cases of ^{10}Li–^{10}Be (T=2) and ^{17}C–^{17}N (T=5/2). CERN ISC98-23, ISC P105 (1998).

[Axe99] J. Axelsson, M. Björkhage, P. Carlé, L. Liljeby, K. G. Rensfelt, B. Jonson, G. Nyman, and F. Wenander. REXEBIS : a charge breeder for the REX-ISOLDE post accelerator. In S. Myers, L. Liljeby, and C. Petit-Jean-Genaz (eds.), *6th European Particle Accelerator Conference Stockholm*, pages 1412–1414. IOP Bristol (1999).

[Bah92] J. N. Bahcall and M. H. Pinsonneault. Standard solar models, with and without helium diffusion, and the solar neutrino problem. *Reviews of Modern Physics* **64**(4), 885–925 (1992).

[Bah98] J. N. Bahcall, Basu S., and M. H. Pinsonneault. How uncertain are solar neutrino predictions? *Physics Letters* **433**(1–2), 1–8 (1998).

[Bau98] T. Baumann, M. J. G. Borge, H. Geissel, H. Lenske, K. Markenroth, W. Schwab, M. H. Smedberg, T. Aumann, L. Axelsson, U. Bergmann, D. Cortina-Gil, L. Fraile, M. Hellström, M. Ivanov, N. Iwasa, R. Janik, B. Jonson, G. Münzenberg, F. Nickel, T. Nilsson, A. Ozawa, A. Richter, K. Riisager, C. Scheidenberger, G. Schrieder, H. Simon, B. Sitar, P. Strmen, K. Sümmerer, T. Suzuki, M. Winkler, H. Wollnik, and M. V. Zhukov. Longitudinal momentum distributions of ^{16,18}C fragments after one-neutron removal from ^{17,19}C. *Physics Letters* **B439**(3–4), 256–261 (1998).

[Bec97] Dietrich Beck. *Massenbestimmung instabiler Isotope der Seltenen Erden um ^{146}Gd mit dem ISOLTRAP-Spektrometer*. Dissertation, Johannes Gutenberg-Universität Mainz (1997).

[Bec99] D. Beck, M. Beck, T. Phalet, P. Schuurmans, N. Severijns, A. van Geert, B. Vereecke, S. Versyck, J. Deutsch, R. Prieels, G. Bollen, O. Forstner, J. Dilling, W. Quint, F. Ames, and P. Schmidt. Proposal to the ISOLDE scientific committee: search for new physics in β-neutrino correlations using trapped ions and a retardation spectrometer. CERN ISC99-13, ISC P111 (1999).

[Bec00] D. Beck, F. Ames, M. Beck, G. Bollen, B. Delauré, J. Deutsch, J. Dilling, O. Forstner, T. Phalet, R. Prieels, W. Quint, P. Schmidt, P. Schuurmans, N. Severijns, B. Vereecke, and S. Versyck. Search for new physics in beta-neutrino correlations with the WITCH spectrometer. *Hyperfine Interactions* (2000), submitted for publication.

[Bec01] D. Beck, F. Ames, G. Bollen, B. Delauré, P. Schuurmans, S. Schwarz, P. Schmidt, N. Severijns, and O. Forstner. Space charge effects in a gas filled Penning trap. *Hyperfine Interactions* (2001), in press.

[Ber00] M. Berz. *COSY INFINITY, Version 8, User's Guide and Reference Manual*. NSCL, Michigan State University, East Lansing, MI 48824, USA (2000).

[Ble89] W. Bleuel, B. Langenbeck, U. Ratzinger, and R. Stenner. GSI Scientific Report 90-1 (1989).

[Bol90] G. Bollen, R. B. Moore, G. Savard, and H. Stolzenberg. The accuracy of heavy-ion mass measurements using time of flight-ion cyclotron resonance in a Penning trap. *Journal of Applied Physics* **68**(9), 4355–4374 (1990).

[Boo84] A. I. Boothroyd, J. Markey, and P. Vogel. Status of the standard vector-axial-vector model for nuclear beta decay. *Physical Review* **C29**(2), 603–617 (1984).

[Bra99] M. P. Bradley, J. V. Porto, S. Rainville, J. K. Thompson, and D. E. Pritchard. Penning trap measurements of the masses of ^{133}Cs, ^{87,85}Rb, and ^{23}Na with uncertainties ≤ 0.2 ppb. *Physical Review Letters* **83**(22), 4510–4513 (1999).

[Bro86] L. S. Brown and G. Gabrielse. Geonium theory: Physics of a single electron or ion in a Penning trap. *Reviews of modern Physics* **58**(1) (1986).

[Cam97] A. Campajola, L. D'Onofrio, L. Gialanella, et al. Measurement of the ^{7}Be(p,γ)^{8}B absolute cross section in inverse kinematics. CERN ISC97-1, ISC I20 (1997).

[Chr96] R. Christophersen. *DPKonfig — Technical Manual*. DMS Dorsch Mikrosystem GmbH, Steinbergkirche (1996).

[Chr98] R. Christophersen. *VMEProfi — Technical Manual*. DMS Dorsch Mikrosystem GmbH, Steinbergkirche (1998).

[Cor89] E. A. Cornell, R. M. Weisskoff, K. R. Boyce, R. W. Flanagan Jr., G. P. Lafyatis, and D. E. Pritchard. Single-ion cyclotron resonance measurement of m(CO^+)/m(N_2^+). *Physical Review Letters* **63** (1989).

[Cub00] J. Cub, C. Gund, D. Pansegrau, G. Schrieder, and H. Stelzer. A position sensitive parallel plate avalanche counter for single-particle and current readout. *Nuclear Instruments and Methods in Physics Research* **A 453**, 522–524 (2000).

[Cut85] L. S. Cutler, R. P. Giffard, and M. D. McGuire. Thermalization of ^{199}Hg ion macromotion by a light background gas in an rf quadrupole trap. *Applied Physics* **B36**, 137–142 (1985).

[Cut86] L. S. Cutler, C. A. Flory, R. P. Giffard, and M. D. McGuire. Doppler effects due to thermal macromotion of ions in an rf quadrupole trap. *Applied Physics* **B39**, 251–259 (1986).

[Dah95] David A. Dahl. *SIMION 3D Version 6.0 Users Manual*. Princeton Electronic Systems, Princeton, NJ (1995).

[Dal89] J. Dalibard and C. Cohen-Tannoudji. Laser cooling below the doppler limit by polarization gradients: simple theoretical models. *Journal of the Optical Society of America* **6**(11) (1989).

[Deh67] H. G. Dehmelt. Radiofrequency Spectroscopy of Stored Ions I: Storage. *Advances in Molecular and Atomic Physics* **3**, 53–72 (1967).

[Deh69] H. G. Dehmelt. Radiofrequency Spectroscopy of Stored Ions II: Spectroscopy. *Advances in Molecular and Atomic Physics* **5**, 109 (1969).

[Dez96] A. M. Ghalambor Dezfuli, R. B. Moore, and P. Varfalvy. A compact 65 keV stable ion guide for radioactive beam experiments. *Nuclear Instruments and Methods in Physics Research* **A386**, 611–616 (1996).

[Dob94] J. Dobaczewski, I. Hamamoto, W. Nazarewicz, and J. A. Sheikh. Nuclear shell structure at particle drip lines. *Physical Review Letters* **72**(7), 981–984 (1994).

[Dub99] Daniel H. E. Dubin and T. M. O'Neil. Trapped noneutral plasmas, liquids, and crystals (the thermal equilibrium state). *Reviews of Modern Physics* **71**(1) (1999).

[Dyc85] R. S. van Dyck, F. L. Moore, D. L. Farnham, and P. B. Schwinberg. New measurement of the proton-electron mass ratio. *International Journal of Mass Spectrometry* **66**, 327–337 (1985).

[Ebe96] J. Eberth, H. G. Thomas, P. v. Brentano, R. M. Lieder, H. M. Jäger, H. Kämmerling, M. Berst, D. Gutknecht, and R. Henck. Encapsulated Ge detectors: development and first tests. *Nuclear Instruments and Methods in Physics Research* **A369**, 135–140 (1996).

[Ell76] H. W. Ellis, R. Y. Pai, E. W. McDaniel, E. A. Mason, and L. A. Viehland. Transport properties of gaseous ions over a wide energy range. *Atomic Data and Nuclear Data Tables* **17**, 177–210 (1976).

[Ell78] H. W. Ellis, E. W. McDaniel, D. L. Albritton, L. A. Viehland, S. L. Lin, and E. A. Mason. Transport properties of gaseous ions over a wide energy range. Part II. *Atomic Data and Nuclear Data Tables* **22**, 197–217 (1978).

[Ell84] H. W. Ellis, M. G. Thackston, E. W. McDaniel, and E. A. Mason. Transport properties of gaseous ions over a wide energy range. Part III. *Atomic Data and Nuclear Data Tables* **31**, 113–151 (1984).

[Emm93] J. Emmes. *Präzissionsmassenspektrometrie in der Penningfalle*. Diplomarbeit, Johannes Gutenberg-Universität Mainz (1993).

[Fis59] E. Fischer. Die dreidimensionale Stabilisierung von Ladungsträgern in einem Vierpolfeld. *Zeitschrift für Physik* **156**, 1–26 (1959).

[For94] D. Forkel-Wirth, N. Achtziger, and A. Burchard. Energetic radioactive ion beam studies of hydrogen in semiconductors. CERN ISC94-27, ISC I13 (1994).

[For99] D. Forkel-Wirth. Exploring solid state physics properties with radioactive isotopes. *Reports on Progress in Physics* **62**, 527–597 (1999).

[For01] Oliver Forstner. *REXTRAP*. Dissertation, TU Wien (2001), to be published.

[Fri91] J. Friedrichs et al. In *Proceedings of the IEEE PAC*, page 3044 (1991).

[Fuj97] S. Fujitaka, M. Wada, H. Wang, J. Tanaka, H. Kawakami, I. Katayama, K. Ogino, H. Kaksuragawa, S. Ohtani, K. Okada, and T. Nakamura. Accumulation of ions from a recoil mass separator in a new type of linear ion trap. *Nuclear Instruments and Methods in Physics Research* **B126**, 386–391 (1997).

[Gab89] G. Gabrielse, X. Fei, L. A. Orozco, R. L. Tjoelker, J. Haas, H. Kalinowsky, and T. A. Trainor. Cooling and slowing of trapped antiprotons below 100 meV. *Physical Review Letters* **63**, 1360 (1989).

[Gei97] W. Geithner, S. Kappertz, G. Katko, G. Kotrotsios, R. Neugart, S. Wilbert, M. Keim, P. Lievens, R. E. Silverans, L. Vermeeren, F. Buchinger, and B. A. Brown. Measurement of nuclear moments and radii by collinear fast-beam laser spectroscopy. CERN ISC97-29, ISC P9, Add.2 (1997).

[Gei99] W. Geithner, K. M. Hilligsoe, S. Kappertz, G. Katko, M. Keim, S. Kloos, G. Kotrotsios, P. Lievens, K. Marinova, R. Neugart, L. Vermeeren, and S. Wilbert. Accurate isotope shift measurements on short-lived neon isotopes. *Hyperfine Interactions* **127**(1–4), 117–120 (1999).

[Gla97] T. Glasmacher, B. A. Brown, M. J. Chromik, P. D. Cottle, M. Fauerbach, R. W. Ibbotson, K. W. Kemper, D. J. Morrissey, H. Scheit, D. W. Sklenicka, and M. Steiner. Collectivity in ^{44}S. *Physics Letters* **395**(3–4), 163–168 (1997).

[Glü98] F. Glück. Order-α radiative correction to ^{6}He and ^{32}Ar β-decay recoil spectra. *Nuclear Physics* **A628**(3), 493–502 (1998).

[Gre00] R. G. Greaves and C. M. Surko. Inward transport and compression of a positron plasma by a rotating electric field. *Physical Review Letters* **85**(9), 1883–1886 (2000).

[Haa94] H. Haas, J. P. Biersack, D. Fink, et al. Diffusion in highly immiscible systems. CERN ISC94-29, SC I15 (1994).

[Haa97] H. Haas and M. Lindroos. Beam energy boosting for experiments at ISOLDE using a high-voltage platform. *Nuclear Instruments and Methods in Physics Research* **B126**(1–4), 250–252 (1997).

[Hab97] D. Habs, D. Rudolph, O. Kester, P. Thirolf, P. Reiter, D. Schwalm, G. Walter, P. van Duppen, and J. Eberth. Physics with REX-ISOLDE and MINIBALL. *Zeitschrift für Physik* **A358**(2), 161–162 (1997).

[Hab00] D. Habs et al. The REX-ISOLDE project. *Hyperfine Interactions* (2000), in press.

[Hah92] R. von Hahn, M. Grieser, D. Habs, C.-M. Kleffner, J. Liebmann, R. Repnow, D. Schwalm, M. Stampfer, E. Jaeschke, and S. Papureanu. The 7-gap resonators for the high current injector of the Heidelberg Test Storage Ring TSR. In H. Henke and P. J. Homeyer Genaz (eds.), *EPAC92 — Third European Particle Accelerator Conference, Berlin*, volume 2. Editions Frontieres, Gif-sur-Yvette (1992).

[Han87] P. G. Hansen and B. Jonson. The neutron halo of extremely neutron-rich nuclei. *Europhysics Letters* **4**(4), 409–414 (1987).

[Han95] P. G. Hansen. Nuclear halos: structure and reactions. *Nuclear Physics* **A588**(1), 1C–10C (1995).

[Har98a] Harting Elektronik GmbH. Data sheet: TB 2050 000 1121, LED 850 nm (1998).

[Har98b] Harting Elektronik GmbH. Data sheet: TB 2050 000 2222, LWL-Empfänger FH-ST (1998).

[Har98c] Harting Elektronik GmbH. Schaltungsbeispiel für LWL Sender und Empfänger mit Repeaterfunktion. private communication (1998).

[Has96] H. Haseroth and C. E. Hill. Multicharged ion sources for pulsed accelerators. *Review of Scientific Instruments* **67**(3), 945–949 (1996).

[Haw98] Microware Hawk 1.0. Microware Systems Corporation (1998).

[Her00] F. Herfurth, J. Dilling, A. Kellerbauer, G. Bollen, S. Henry, H.-J. Kluge, E. Lamour, D. Lunney, R. B. Moore, C. Scheidenberger, S. Schwarz, G. Sikler, and J. Szerypo. A linear radiofrequency ion trap for accumulation, bunching, and emittance improvement of radioactive ion beams. *Nuclear Instruments and Methods in Physics Research* (2000), submitted for publication.

[Hey92a] K. Heyde, C. De Coster, J. Jolie, and J. L. Wood. Intruder analog states: new classification of particle-hole excitations near closed shells. *Physical Review* **46**(2), 541–547 (1992).

[Hey92b] K. Heyde, C. De Coster, J. L. Wood, and J. Jolie. Proton 2p-2h intruder excitations and the modified vibrational intensity and selection rules. *Physical Review* **46**(5), 2113–2116 (1992).

[Hua97] X.-P. Huang, F. Anderegg, E. M. Hollmann, C. F. Driscoll, and T. M. O'Neil. Steady-state confinement of non-neutral plasmas by rotating electric fields. *Physical Review Letters* **78**(5), 875–878 (1997).

[Ibb98] R. W. Ibbotson, T. Glasmacher, B. A. Brown, L. Chenand M. J. Chromik, P. D. Cottle, M. Fauerbach, K. W. Kemper, and H. Scheit D. J. Morrissey and. Quadrupole Collectivity in ^{32,34,36,38}Si and the n=20 Shell Closure. *Physical Review Letters* **20**(10), 2081–2084 (1998).

[Ibb99] R. W. Ibbotson, T. Glasmacher, P. F. Mantica, and H. Scheit. Coulomb excitation of odd-a neutron-rich π(s-d) and ν(f-p) shell nuclei. *Physical Review* **C59**(2), 642–647 (1999).

[Ita95] W. M. Itano, J. C. Bergquist, J. J. Bollinger, and D. J. Wineland. Cooling methods in ion traps. *Physica Scripta* **T59**, 106–120 (1995).

[Jon93] B. Jonson, H. L. Ravn, and G. Walter. ISOLDE PS boster facility at CERN: experiments with slow radioactive beams. *Nuclear Physics News* **3**(2) (1993).

[Jon98a] B. Jonson, T. Nilsson, and L. Axelsson. Proposal to the ISOLDE committee: Study of the unbound nuclei ^{10}Li and ^{7}He at REX-ISOLDE. CERN ISC98-11, ISC P100 (1998).

[Jon98b] B. Jonson and K. Riisager. Halos and halo excitations. *Philosophical Transactions of the Royal Society, London* **356**(1744), 263–281 (1998).

[Kim97] T. Kim. *Buffer gas cooling in an RF ion guide: A study of the cooling process and cooled beam properties*. PhD thesis, McGill University, Montreal (1997).

[Kle92] C.-M. Kleffner, M. Grieser, D. Habs, R. von Hahn, J. Liebmann, R. Repnow, M. Stampfer, H. Deitinghoff, A. Schempp, E. Jaeschke, and S. Papureanu. The RFQ-accelerator for the high current injector of the TSR. In H. Henke and P. J. Homeyer Genaz (eds.), *EPAC92 — Third European Particle Accelerator Conference, Berlin*, volume 2, pages 1340–1342. Editions Frontieres, Gif sur Yvette, France (1992).

[Kni79] R. D. Knight and M. H. Prior. Laser scanning measurement of the density distribution of confined $^6Li^+$ ions. *Journal of Applied Physics* **50**(5), 3044 (1979).

[Kön95] M. König, G. Bollen, H.-J. Kluge, T. Otto, and J. Szerypo. Quadrupole excitation of stored ions motion at the true cyclotron frequency. *International Journal of Mass Spectrometry and Ion Processes* **142**, 95–116 (1995).

[Kra92] K. L. Kratz, H. Gabelmann, P. Möller, B. Pfeiffer, H. L. Ravn, A. Wöhr, and F. K. Thielemann. Nuclei far from stability and the r-process waiting-point concept. In M. Vergnes, J. Sauvage, P. H. Heenen, and Tuan Duong Hong (eds.), *Nuclear Shapes and Nuclear Structure at Low Excitation Energies. Proceedings of a NATO Advanced Research Workshop, Cargese, France*. Plenum, New York (1992).

[Kra95] K. L. Kratz. Nuclear properties far from stability and the r-process. In *Nuclei in the COSMOS III. Third International Symposium on Nuclear Astrophysics, Assergi, Italy*, volume 327, pages 113–124. AIP-Conference-Proceedings (1995).

[Kra96] K. L. Kratz, B. Pfeiffer, and F. K. Thielemann. The astrophysical r-process: a stellar laboratory for nuclear physics near the neutron drip line. In H. Feldmeier, J. Knoll, and W. Noerenberg (eds.), *24. international workshop on gross properties of nuclei and nuclear excitations: Extremes of nuclear structure, Hirschegg, Austria*, pages 177–188 (1996).

[Kra98a] K. L. Kratz. New experiments on r-process nuclei in the 132 82 region. In M. Buballa, W. Norenberg, J. Wambach, and A. Wirzba (eds.), *HIRSCHEGG '98 Nuclear Astrophysics. Proceedings of the International Workshop XXVI on Gross Properties of Nuclei and Nuclear Excitations, Hirschegg, Austria*, page 304 (1998).

[Kra98b] K. L. Kratz, B. Pfeiffer, M. Hannawald, F. K. Thielemann, J. Gorres, H. Schatz, and M. Wiescher. Nuclear physics far from stability and explosive nucleosynthesis processes. *Nuovo Cimento A* **111**(8–9), 1043–1054 (1998).

[Kud98] Y. Kudryavtsev, S. Franchoo, J. Gentens, M. Huyse, R. Raabe, I. Reusen, P. van Duppen, P. van den Bergh, L. Vermeeren, and A. Wöhr. Status of the laser ion source at the Leuven isotope separator online. *Review of Scientific Instruments* **69**, 738–740 (1998).

[Kug92] E. Kugler, D. Fiander, B. Jonson, H. Haas, A. Przewloka, H. L. Ravn, D. J. Simon, and K. Zimmer. The new CERN-ISOLDE on-line mass-separator facility at the PS-Booster. *Nuclear Instruments and Methods in Physics Research* **B70**, 41–49 (1992).

[KV88] W. Krauss-Vogt, H. Beuscher, H. L. Hagedoorn, J. Reich, and P. Wucherer. Emittance and matching of ECR sources. *Nuclear Instruments and Methods in Physics Research* **A268**, 5–9 (1988).

[Let88] P. D. Lett, C. I. Westbrook R. N. Watts, W. D. Phillips, P. L. Gould, and H. J. Metcalf. Observation of atoms laser cooled below the Doppler limit. *Physical Review Letters* **61** (1988).

[Let98] J. Lettry, R. Catherall, G. J. Focker, O. C. Jonsson, E. Kugler, H. L. Ravn, C. Tamburella, V. N. Fedoseyev, V. I. Mishin, G. Huber, V. Sebastian, M. Koizumi, and U. Köster. Recent developments of the ISOLDE laser ion source. *Review of Scientific Instruments* **69**(2), 761–763 (1998).

[Let00] Jacques Lettry. private communication (2000).

[Lin95] M. Lindroos, C. Broude, G. Goldring, H. Haas, M. Hasss, P. Richards, and L. Weissmann. Tilted foil polarization of radioactive ions. *Nuclear Instruments and Methods in Physics Research* **A361**(1–2) (1995).

[Lin97] M. Lindroos, J. Billowes, C. Broude, G. Goldring, H. Haas, M. Hass, L. Müller, M. R. Pearson, and L. Weissman. Measurement of the magnetic moment of ^{23}Mg using the tilted-foil polarization technique. *Nuclear Instruments and Methods in Physics Research* **B126**(1–4), 423–426 (1997).

[Maj68] F. G. Major and H. G. Dehmelt. Exchange-collision technique for the rf spectroscopy of stored ions. *Physical Review* **170**(1), 91 (1968).

[MAR00] http://www.bl.physik.uni-muenchen.de/marabou/html/marabou.html (2000).

[MBS00] http://www-gsi-vms.gsi.de/daq/home.html (2000).

[Met99] H. J. Metcalf and P. van der Straten. *Laser Cooling and Trapping*. Springer Verlag (1999).

[Mis93] V. I. Mishin, V. N. Fedoseyev, H. J. Kluge, V. S. Letokhov, H. L. Ravn, F. Scheerer, Y. Shirakabe, S. Sundell, and O. Tengblad. Chemically selective laser ion-source for the CERN-ISOLDE on-line mass separator facility. *Nuclear Instruments and Methods in Physics Research* **B73**, 550–560 (1993).

[Moh00] P. J. Mohr and B. N. Taylor. CODATA recommended values of the fundamental physical constants 1998. *Reviews of Modern Physics* **72**(2) (2000).

[Moo92] R. B. Moore and G. J. Rouleau. In flight capture of an ion beam in a Paul trap. *Journal of Modern Optics* **39**, 361 (1992).

[Moo95] R. B. Moore, A. M. Ghalambor Dezfuli, P. Varfalvy, and H. Zhao. Production, transfer and injection of charged particles in traps and storage rings. *Physica Scripta* **T59**, 93–105 (1995).

[Mor92] Y. Moriwaki, M. Tachikawa, Y. Maeno, and T. Shimizu. Collision cooling of ions stored in quadrupole radio-frequency trap. *Japanese Journal of Applied Physics* **31**(11B), L1640–L1643 (1992).

[Mot95] T. Motobayashi, Y. Ikeda, Y. Ando, K. Ieki, M. Inoue, N. Iwasa, T. Kikuchi, M. Kurokawa, S. Moriya, S. Ogawa, H. Murakami, S. Shimoura, Y. Yanagisawa, T. Nakamura, Y. Watanabe, M. Ishihara, T. Teranishi, H. Okuno, and R. F. Casten. Large deformation of the very neutron-rich nucleus ^{32}Mg from intermediate-energy Coulomb excitation. *Physics Letters* **B346**(1–2), 9–14 (1995).

[Nie00a] A. Nieminen, J. Huikari, A. Jokinen, and J. Äystö. Time charcteristics of the ion beam cooler-buncher at JYFL. *Hyperfine Interactions* (2000), submitted for publication.

[Nie00b] A. Nieminen, J. Huikari, A. Jokinen, J. Äystö, P.Campbell, and E. C. A. Cochrane. Beam cooler for low-energy radioactive ions. *Nuclear Instruments and Methods in Physics Research* **A** (2000), in print.

[Nil96] T. Nilsson, F. Humbert, W. Schwab, H. Simon, M. H. Smedberg, M. Zinser, Th. Blaich, M. J. G. Borge, L. V. Chulkov, Th. W. Elze, H. Emling, H. Geissel, K. Grimm, D. Guillemaud-Mueller, P. G. Hansen, R. Holzmann, H. Irnich, B. Jonson, J. G. Keller, H. Klingler, A. A. Korsheninnikov, J. V. Kratz, R. Kulessa, D. Lambrecht, Y. Leifels, A. Magel, M. Mohar, A. C. Mueller, G. Münzenberg, F. Nickel, G. Nyman, A. Richter, K. Riisager, C. Scheidenberger, G. Schrieder, B. M. Sherrill, K. Stelzer, J. Stroth, O. Tengblad, W. Trautmann, E. Wajda, M. V. Zhukov, and E. Zude. ^{6}He and neutron momentum distributions from ^{8}He in nuclear break-up reactions at 240 MeV/u. *Nuclear Physics* **A598**(3), 418–434 (1996).

[Nol79] E. Nolte, G. Geschonke, K. Berdermann, R. Oberschmid, R. Zierl, M. Feil, A. Jahnke, M. Kress, and H. Moringa. The Munich heavy ion postaccelerator. *Nuclear Instruments and Methods* **158**(2–3), 311–324 (1979).

[Ost97] A. N. Ostrowski and P. van Duppen. Proposal to the ISOLDE committee: Structure features of ^{6}He from direct reactions on light target nuclei. CERN ISC97-25, ISC P93 (1997).

[Pau58] W. Paul, H. P. Reinhard, and U. von Zahn. Das elektrische Massenfilter als Massenspektrometer und Isotopentrenner. *Zeitschrift für Physik* **152**, 143–182 (1958).

[Pen36] F. M. Penning. Die Glimmentladung bei niedrigem Druck zwischen koaxialen Zylindern in einem Magnetfeld. *Physica* **3**, 873 (1936).

[Pen97] H. Penttilä, P. Dendooven, A. Honkanen, M. Huhta, P. P. Jauho, A. Jokinen, G. Lhersonneau, M. Oinonen, K. Peräjärvi, J.-M. Parmonen, and J. Äystö. Status report of the jyväskylä ion guide isotope separator on-line facility. *Nuclear Instruments and Methods in Physics Research* **B126**, 213–217 (1997).

[Pfe98] G. Pfennig, H. Klewe-Nebenius, and W. Seelmann-Eggebert. Chart of the nuclides. Forschungszentrum Karlsruhe (1998).

[Pie48] J. R. Pierce. *Theory and Design of Electron Beams*, chapter 3. D. van Nostrand Co., New York (1948).

[Pod98] H. Podlech, M. Grieser, R. von Hahn, S. Papureanu, R. Repnow, and D. Schwalm. The 7-gap-resonator-accelerator for the REX-ISOLDE-experiment at CERN. *Nuclear Instruments and Methods in Physics Research* **B139** (1998).

[Pod99a] H. Podlech, M. Grieser, R. von Hahn, R. Repnow, and D. Schwalm. The 7-gap-resonator-accelerator for the REX-ISOLDE-linac. In A. Luccio and W. MacKay (eds.), *Proceedings of the 1999 Particle Accelerator Conference*, volume 5, pages 3543–3545 (1999).

[Pod99b] Holger Podlech. *Entwiclung des 7-Spalt-Resonatorbeschleunigers für das REX-ISOLDE-Project am CERN*. PhD thesis, University of Heidelberg (1999).

[Pos66] A. M. Poskanzer, S. W. Cosper, and Earl K. Hyde. New isotopes: ^{11}Li, ^{14}B, and ^{15}B. *Physical Review Letters* **17**(1271) (1966).

[Pre91] J. D. Prestage, G. J. Dick, and L. Maleki. Linear ion trap based atomic frequency standard. *IEEE Transactions on Instrumentation and Measurement* **40**(2), 132 (1991).

[Pre97] W. H. Press, S. A. Teukolsky, W. T. Vetterling, and B. P. Flannery. *Numerical Recipes in C: The art of scientific computing*. Cambridge University Press, 2$^{\mathrm{nd}}$ edition (1997).

[Pri99] B. V. Pritychenko, T. Glasmacher, P. D. Cottle, M. Fauerbach, R. W. Ibbotson, K. W. Kemper, V. Maddalena, A. Navin, R. Ronningen, A. Sakharuk, H. Scheit, and V. G. Zelevinsky. Role of intruder configurations in ^{26,28}Ne and ^{30,32}Mg. *Physics Letters* **461**(4), 322–328 (1999).

[Pro00] http://www.profibus.com (2000).

[Rai97] H. Raimbault-Hartmann, D. Beck, G. Bollen, H.-J. Kluge, E. Schark, J. Stein, S. Schwarz, and J.Szerypo. A cylindrical penning trap for capture, mass selective cooling, and bunching of radioactive ion beams. *Nuclear Instruments and Methods in Physics Research* **B126**, 378–382 (1997).

[Rao98] R. Rao and F. Wenander. A preliminary design of the electron beam optics of the electron beam ion source for REX-ISOLDE. *Nuclear Instruments and Methods in Physics Research* **A 416**(2–3), 210–220 (1998).

[Rao99] R. Rao, O. Kester, T. Sieber, D. Habs, and K. Rudolph. Beam optics design of the REX-ISOLDE q/m-separator. *Nuclear Instruments and Methods in Physics Research* **A 427**, 170–176 (1999).

[Rav74] H. L. Ravn and S. Sundell. The ISOLDE target and ion-source unit. In H. P. Blok and A. E. L. Dieperink (eds.), *International Conference on Nuclear Structure and Spectroscopy*, Amsterdam (1974). Scholar's Press.

[Rav76] H. L. Ravn. Progress in targets and ion source for on-line separators. *Nuclear Instruments and Methods* **139**, 281 (1976).

[REX94] Proposal to the ISOLDE scientific committee: Radioactive beam experiments at ISOLDE — Coulomb excitation and neutron transfer reactions of exotic nuclei. CERN ISC94-25, ISC P68 (1994).

[Roh93] W. Rohde. *Erste Massenmessungen mit ISOLTRAP an der neuen PS-Booster ISOLDE und Entwicklung eines neuen Experimentsteuerungssystems*. Diplomarbeit, Johannes Gutenberg-Universität Mainz (1993).

[ROO00] http://www.root.cern.ch (2000).

[Sar95] E. Sarid, F. Anderegg, and C. F. Driscoll. Cyclotron resonance phenomena in a non-neutral multispecies ion plasma. *Physiscs of Plasmas* **2**(8), 2895–2907 (1995).

[Sav91] G. Savard, St. Becker, G. Bollen, H.-J. Kluge, R. B. Moore, Th. Otto, L. Schweikhard, H. Stolzenberg, and U. Wiess. A new cooling technique for heavy ions in a Penning trap. *Physics Letters* **A158**, 247–252 (1991).

[Sch81] H. Schaaf, U. Schmeling, and G. Werth. Trapped ion density distribution in the presence of He-buffer gas. *Applied Physics* **25**, 249–251 (1981).

[Sch85] A. Schempp, H. Deitinghoff, Ferch M., Junior P., and Klein H. Four-rod-λ/2-rfq for light ion acceleration. *Nuclear Instruments and Methods in Physics Research* **B10–11**, 831–834 (1985).

[Sch88] A. Schempp. Design of compact RFQs. In *Proceedings of the EPAC I*, page 464 (1988).

[Sch93] D. Schardt and K. Riisager. Beta-neutrino recoil broadening in beta-delayed proton emission of ^{32}Ar and ^{33}Ar. *Zeitschrift für Physik* **345**(3), 265–271 (1993).

[Sch96] H. Scheit, T. Glasmacher, B. A. Brown, J. A. Brown, P. D. Cottle, P. G. Hansen, R. Harkewicz, M. Hellström, R. W. Ibbotson, J. K. Jewell, K. W. Kemper, D. J. Morrissey, M. Steiner, P. Thirolf, and M. Thoennessen. New Region of Deformation: The Neutron-Rich Sulfur Isotopes. *Physical Review Letters* **77**(19), 3967–3970 (1996).

[Sch97] H. Schatz, A. Aprahamian, B. A. Brown, J. Goerres, H. Herndl, K. L. Kratz, P. Moeller, B. Pfeiffer, T. Rauscher, J. F. Rembges, F. K. Thielemann, M. Wiescher, and L van Wormer. The endpoint of the rp-process. *Nuclear Physics* **A621**(1–2), 417–420 (1997).

[Sch98] Stefan Schwarz. *Manipulation radioaktiver Ionenstrahlen mit Hilfe einer Paulfalle und direkte Massenmessungen an neutronenarmen Qecksilberisotopen mit dem ISOLTRAP-Experiment*. Dissertation, Johannes Gutenberg-Universität Mainz (1998).

[Sch99] H. Scheid, C. Gund, H. Lenske, I. Mukha, D. Pansegrau, A. Richter, G. Schrieder, and D. Schwalm. Proposal to the ISOLDE committee: Investigation of the single particle structure of the neutron-rich sodium isotopes $^{27-31}$Na. CERN ISTC99-20, ISC P114 (1999).

[Sch00] Stefan Schwarz. private communication (2000).

[Seb96] V. Sebastian, T. Budiman, and G. Huber. Laser preparation of bunched ion beams. *Nuclear Instruments and Methods in Physics Research* **B126**(1–4), 73–75 (1996).

[Sel91] P. J. Sellin, P. J. Woods, D. Branford, T. Davinson, N. J. Davis, D. G. Ireland, K. Livingston, R. D. Page, A. C. Shotter, S. Hofmann, and A. N. James. A strip detector system for proton radioactivity studies on the Daresbury recoil separator. In Ikeda K. and Y. Suzuki (eds.), *Proceedings of International Symposium on Structure and Reactions of Unstable Nuclei, Niigata, Japan*, pages 70–75. World Scientific, Singapore (1991).

[Sha94] M. M. Sharma, G. A. Lalazissis, W. Hillebrandt, and P. Ring. Shell effects in nuclei near the neutron-drip line. *Physical Review Letters* **72**(10), 1431–1434 (1994).

[Sol00] Torsten Soldner. private communication (2000).

[Sor95] P. Sortais. Recent progress in making highly charged ion beams. *Nuclear Instruments and Methods in Physics Research* **B98**, 508–516 (1995).

[Ste94] Johannes Stein. Untersuchungen zum puffergasgestützten Ionen-Einfang in eine Penningfalle. Diplomarbeit, Universität Mainz (1994).

[Str98] B. Stroustrup. *Die C++-Programmiersprache*. Addison Wesley, 3rd edition (1998).

[Sun92] S. Sundell and H. L. Ravn. Ion-source with combined cathode and transfer line heating. *Nuclear Instruments and Methods in Physics Research* **B 70**, 160–164 (1992).

[Tan96] I. Tanihata. Neutron halo nuclei. *Journal of Physics* **22**(2), 157–198 (1996).

[Thi75] C. Thibault, R. Klapisch, C. Rigaud, A. M. Poskanzer, R. Prieels, L. Lessard, and W. Reisdorf. Direct measurement of the masses of ^{11}Li and $^{26-32}$Na with an on-line mass spectrometer. *Physical Review* **C12**(2), 644 (1975).

[Thi94] F. K. Thielemann, K. L. Kratz, B. Pfeiffer, T. Rauscher, L. van Wormer, and M. C. Wiescher. Astrophysics and nuclei far from stability. *Nuclear Physics* **A570**(1–2), 329–343 (1994).

[Thi98] F. K. Thielemann, C. Freiburghaus, T. Rauscher, E. Kolbe, B. Pfeiffer, K. L. Kratz, and J. J. Cowan. Explosive nucleosynthesis and the astrophysical r-process. In *ENAM 98. Exotic Nuclei and Atomic Masses, Bellaire, MI, USA*, volume 455, pages 837–48. AIP-Conference-Proceedings (USA) (1998).

[Umr97] W. Umrath. Grundlagen der Vakuumtechnik. Leybold Vakuum (1997).

[Ved83] F. Vedel, J. André, M. Vedel, and G. Brincourt. Computed energy and spatial statistical properties of stored ions cooled by a buffer gas. *Physical Review* **27**(5), 2321 (1983).

[Vie95] L. A. Viehland and E. A. Mason. Transport properties of gaseous ions over a wide energy range, IV. *Atomic Data and Nuclear Data Tables* **60**, 37–95 (1995).

[War93] D. J. Warner, N. Angert, M. P. Bourgarel, É. Brouzet, R. Cappi, D. Dekkers, J. Evans, G. Gelato, H. Haseroth, C. E. Hill, G. Hutter, J. E. Knott, H. Kugler, A. Lombardi, H. D. Lustig, E. Maalwitz, F. Nitsch, G. Parisi, A. Pisent, U. Raich, U. Ratzinger, L. Riccati, A. Schempp, K. Schindl, H. O. Schönauer, P. Têtu, H. H. Umstätter, M. van Rooij, and M. Weiss. CERN heavy-ion facility design report. CERN Yellow report 93-01 (1993).

[Wei00] L. Weissman, F. Ames, J. Äystö, O. Forstner, S. Rinta-Antila, and P. Schmidt. Feasibility of in-trap conversion electron spectroscopy. *Hyperfine Interactions* (2000), submitted for publication.

[Wen98] Fredrik Wenander. *REXEBIS — An Electron Beam Ion Source for the REX-ISOLDE project*. Licentiate thesis, Chalmers Univerity of Technology and Göteborg University (1998).

[Wen00] Fredrik Wenander. private communication (2000).

[Wey94] K. Weyer, G. Bonde Nielsen and M. Fanciulli. Defects studies in high-energy ion implanted semiconductors. CERN ISC94-24, ISC I12 (1994).

[Wie97] M. Wiescher, F. K. Thielemann, K. L. Kratz, et al. A radioactive-ion beam experiment for the study of the astrophysical rp-process at CERN-ISOLDE. CERN ISC94-21, ISC I11 (1997).

[Win79] D. J. Wineland. Laser-to-microwave division using synchrotron radiation. *Journal of Applied Physics* **50**(4), 2528 (1979).

[Wol87] H. Wollnik. *Optics of Charged Particles*. Academic Press (1987).

[Woo92] J. L. Wood, K. Heyde, W. Nazarewicz, M. Huyse, and P. van Duppen. Coexistence in even-mass nuclei. *Physics Reports* **215**(3–4), 101–201 (1992).

[Yod92] J. Yoda and K. Sugiyama. Determination of characteristics of Yb^+ ion cloud trapped in a rf trap with He buffer gas. *Japanese Journal of Applied Physics* **31**(11), 3750–3753 (1992).

[Zhu94] M. V. Zhukov, A. A. Korsheninnikov, and M. H. Smedberg. Simplified α+4n model for the ^{8}He nucleus. *Physical Review* **C50**(1), R1–R4 (1994).

Danksagung

An dieser Stelle möchte ich all jenen Dank aussprechen, die mich in der Zeit, in der diese Arbeit entstanden ist, begleitet und unterstützt haben, also all denen, die mich und meine Launen ertragen durften und mußten. Selbstverständlich gilt mein Dank auch jenen, die hier nicht namentlich aufgeführt sind und die zum Gelingen der Arbeit beigetragen haben.